ON NANOSIZED PRECIPITATES IN STEELS FOR ADVANCED NUCLEAR REACTORS

THOMAS PAUL DAVIS

A thesis submitted for the degree of

Doctor of Philosophy

at the Department of Materials

and Saint Anne's College

University of Oxford

Trinity Term 2020

This DPhil thesis is dedicated to my Grandfather
Stanley James Davis
who could not be here to read the final product.

1927 – 2020

Preface

The research described in this thesis was carried out by the author whilst at the Department of Materials, University of Oxford, between October 2016 and October 2020, under the supervision of Prof. D. E. J. Armstrong, Prof. M. P. Moody, Dr. P. A. J. Bagot and Dr. M. A. Auger. This research was part of the Science and Technology of Fusion Energy (Engineering and Physical Sciences Research Council (EPSRC) Fusion Centre for Doctoral Training (Fusion CDT)). All the work is original and clear acknowledgements and references are given where work by others has been included. All figures and tables reproduced from journal articles and books have been used with permission from the respective copyright owner. No part of this thesis has been submitted or accepted for any other degree at this university or elsewhere. Parts of this work have been published in peer reviewed journals or presented at conferences and workshops; these are:

Publications

- T. P. Davis, M. A. Auger, C. Hofer, P. A. J. Bagot, M. P. Moody, and D. E. J. Armstrong, 'Nanocluster evolution and mechanical properties of ion irradiated T91 ferritic-martensitic steel', Journal of Nuclear Materials, 2021, 547, 152842, https://doi.org/10.1016/j.jnucmat.2021.152842

- T. P. Davis, M. A. Auger, N. Almirall, P. A. J. Bagot, P. Hosemann, M. P. Moody, G. R. Odette, and D. E. J. Armstrong, 'Atom Probe Characterisation

of Segregation Driven Cu and Mn-Ni-Si co-precipitation in neutron irradiated T91 tempered-martensitic steel', Materialia, 14, 2020, 100946, https://doi.org/10.1016/j.mtla.2020.100946

- T. P. Davis, J. Haley, S. Connolly, M. A. Auger, M. J. Gorley, P. S. Grant, P. A. J. Bagot, M. P. Moody, and D. E. J. Armstrong, 'Electron microscopy and atom probe tomography of nanoindentation deformation in oxide dispersion strengthened steels', Materials Characterization, 167, 110477, 2020, https://doi.org/10.1016/j.matchar.2020.110477

- T. P. Davis, 'Dispelling misconceptions of nuclear energy technology: How Generation IV nuclear reactors could become the key to achieving the Paris Agreement and the United Kingdom's net zero CO_2 emissions target by 2050', Saint Anne's Academic Review 9, 2019, http://st-annes-mcr.org.uk/staar/publications/staar-9-2019/davis-2019-dispelling-misconceptions-of-nuclear-energy-technology/

- T. P. Davis, 'Review of the iron-based materials applicable for the fuel and core of future Sodium Fast Reactors (SFR)', Office for Nuclear Regulation, ONR-RRR-088, 2018, URL: http://www.onr.org.uk/documents/2018/onr-rrr-088.pdf

Conference Presentations

- Oral, 'Microstructural evolution of neutron irradiated T91 ferritic-martensitic steel in the advanced test reactor', 3rd Postgraduate Research Symposium of Ferrous Metallurgy, London, UK, 25 February 2020.

- Oral, 'Microstructural Evolution of Neutron Irradiated T91 Steel in ATR', American Nuclear Society Winter Meeting 2019, Washington D.C., USA, 17 – 21 November 2019.

- Poster, ‘A microstructural investigation of ion and neutron damage in T91 ferritic-martensitic steel” 19th International Conference on Fusion Reactor Materials (ICFRM-19), San Diego, USA, Oct 28 – 1 November 2019.

- Oral, ‘Review of the iron-based materials applicable for the fuel and core of future Sodium Fast Reactors’, EUROMAT19, Stockholm, Sweden 2 – 6 September 2019.

- Oral, ‘Investigating the nanoscale segregation and characterisation of generation IV fission reactor core structural steels’, 2nd Postgraduate Research Symposium of Ferrous metallurgy, London, UK, 26 February 2019.

- Poster, ‘Understanding the nano-oxide particle nature of irradiated oxide dispersion strengthened steels’, Nuclear Materials Conference 2018 (NuMat2018), Seattle, USA, 14 – 18 November 2019.

- Oral, ‘A Microstructural and Mechanical Investigation of Neutron Damage in Oxide Dispersion Strengthened Steel’, Young Global Centre of Excellence in Advanced Steel (YCEAS), Stockholm, Sweden, 26 August – 7 September 2018.

- Poster, ‘A Microstructural and Mechanical Investigation of Ion vs Neutron Damage in Oxide Dispersion Strengthened Steel’, 7th European Atom Probe Workshop 2017, Göteborg, Sweden, 2 – 5 October 2017.

- Poster, ‘A Microstructural and Mechanical Investigation of Ion vs Neutron Damage in Oxide Dispersion Strengthened Steel’, 4th International Workshop on ODS, Helmholtz-Zentrum Dresden-Rossendorf, Dresden, Germany, 2 – 28 June 2017.

Acknowledgements

First I would like to thank my four supervisors, Prof. D. E. J. Armstrong, Prof. M. P. Moody, Dr. P. A. J. Bagot, and Dr. M. A. Auger, for their endless support in the pursuit of this research, attending free college dinners, and for pushing my academic abilities. Special thanks goes to Prof. D. E. J. Armstrong for his support with my seemingly endless travel to conferences, workshops, and national laboratories in the United States of America, United Kingdom, Germany, South Korea, France, Sweden, and Poland. Your generosity has made all the difference in the nucleation and evolution of my company which would not have happened otherwise (i.e. networking is key). The range of experiments conducted for this thesis could not have been possible without the following scholarships and grants provided by: the Clarendon Scholarship; Engineering and Physical Sciences Research Council (EPSRC) Fusion Centre for Doctoral Training [EP/L01663X/1]; post irradiation experiments on neutron irradiated samples at the Microscopy and Characterization Suite, Center for Advanced Energy Studies, Idaho National Laboratory under the US Nuclear Science User Facility Rapid Turnaround Experiment No 19-1721; supported by EPSRC grant EP/M022803/1 “A LEAP 5000XR for the UK National Atom Probe Facility.”; characterisation facilities within the David Cockayne Centre for Electron Microscopy, Department of Materials, University of Oxford. Lastly, thank you to my friends and family for the support, laughs, humility, coffee, and kindness throughout these years.

Abstract

Nuclear fission power is a reliable and zero carbon-dioxide emitting energy source and nuclear fusion is regarded as the ultimate terrestrial energy source. Both processes require radiation resistant structural reactor core materials. Atom probe tomography, nanoindentation, and electron microscopy were used to investigate a) radiation-induced precipitation of nanosized Mn-Ni-Si precipitates (MNSP) and nanosized copper-rich precipitates (CRP), and radiation-induced solute segregation to dislocations in neutron and ion irradiated T91 ferritic-martensitic steel and b) the effect of yttrium-titanium-oxygen (Y-Ti-O) nanosize precipitates on the grain structure and mechanical properties of Fe-14Cr-3W-0.25Ti-0.25Y_2O_3 (14YWT (wt%)) oxide dispersion strengthened steel. Two neutron irradiated T91 steel conditions were investigated: 2.14 dpa at 327 °C and 8.82 dpa at 377 °C. The MNSP compositions fell near the MnSi(Ni) phase field, which is distinctly different than the typically cited 'G-phase' ($Mn_6Ni_{16}Si_7$). MNSPs appeared as a co-precipitated appendage to CRPs. CRP-MNSP number densities, radii, and volume fractions agreed well with literature cluster dynamics model. Parallels were drawn between the limited database on MNSPs in neutron irradiated Fe-Cr alloy systems with the extensive literature on precipitate evolution in reactor pressure vessel steels. T91 was Fe^{4+} irradiated from 0.12 dpa to 4.1 dpa at $\sim$ 300 °C with the characterisation of MNSP and their impact on mechanical properties were discussed. 14YWT Y-Ti-O (7 – 15 nm diameter; number density $10^{23} - 10^{24}$ #/m^3) particles had a small effect on the hardness, suggesting that the dominant hardening mechanism was related to the grain boundary refinement rather than the dislocation pinning on the oxides.

Contents

List of Figures

List of Tables

Nomenclature

AS	As-Received
APT	Atom Probe Tomography
ASME BPVC	American Society of Mechanical Engineers Boiler & Pressure Vessel Code
BF	Bright-Field
CRP	Copper-rich Precipitate
CSM	Continuous Stiffness Measurement
DBTT	Ductile-to-Brittle Transition Temperature
dpa	Displacements-per-atom
EBSD	Electron Backscatter Detection
G-Phase	$Mn_6Ni_{16}Si_7$
HAADF	High-Angle Annular Dark-Field
MCF	Magnetic Confinement Fusion
MNSP	Mn-Ni-Si Precipitate
NRT	Norgett, Robinson and Torrens
NSUF	Nuclear Science User Facility
ODS	Oxide Dispersion Strengthened
PKA	Primary Knocked-on Atom
RIP	Radiation-induced Precipitation
RIS	Radiation-induced Segregation
RPV	Reactor Pressure Vessel
SEM	Scanning Electron Microscope
STEM	Scanning Transmission Electron Microscope
SFR	Sodium-cooled Fast Reactor
SRIM	Stopping and Range of Ions in Matter
TEM	Transmission Electron Microscope
TKD	Transmission Kikucki Diffraction
TMS	Tempered Martensitic Steels

Chapter 1

The Role of Nuclear Power in a Changing Climate

Human activity is attributed to be the major cause of recent climate change, as concluded with 95% certainty in the special report titled 'Global Warming of 1.5 °C' by The Intergovernmental Panel on Climate Change [1]. This conclusion is shared by 97.1% of scientific papers published on climate change [2]. Carbon dioxide (CO_2) levels have risen with the global temperature over the last 800,000 years [3], as shown in figure 1.0.1 through the measurement of trapped gasses within the Antarctica ice. Since the industrial revolution (1850s), the production of CO_2 compared to pre-industrial times has risen significantly. This is the fundamental scientific evidence that the climate change community uses as the basis for the concept that human activity is the leading cause of a changing climate [4–6].

The Paris Agreement was signed by the 195 'United Nations Framework Convention on Climate Change' member countries on 12 December 2015. The agreement commits all nations to undertake ambitious efforts for the first time to combat climate change. The United Kingdom (UK) Government enacted an amendment to the Climate Change Act 2008 in 2019 [7] that requires the UK to lower all greenhouse gas emissions (this includes CO_2 as one of these gases) to net zero by 2050. Thus, the

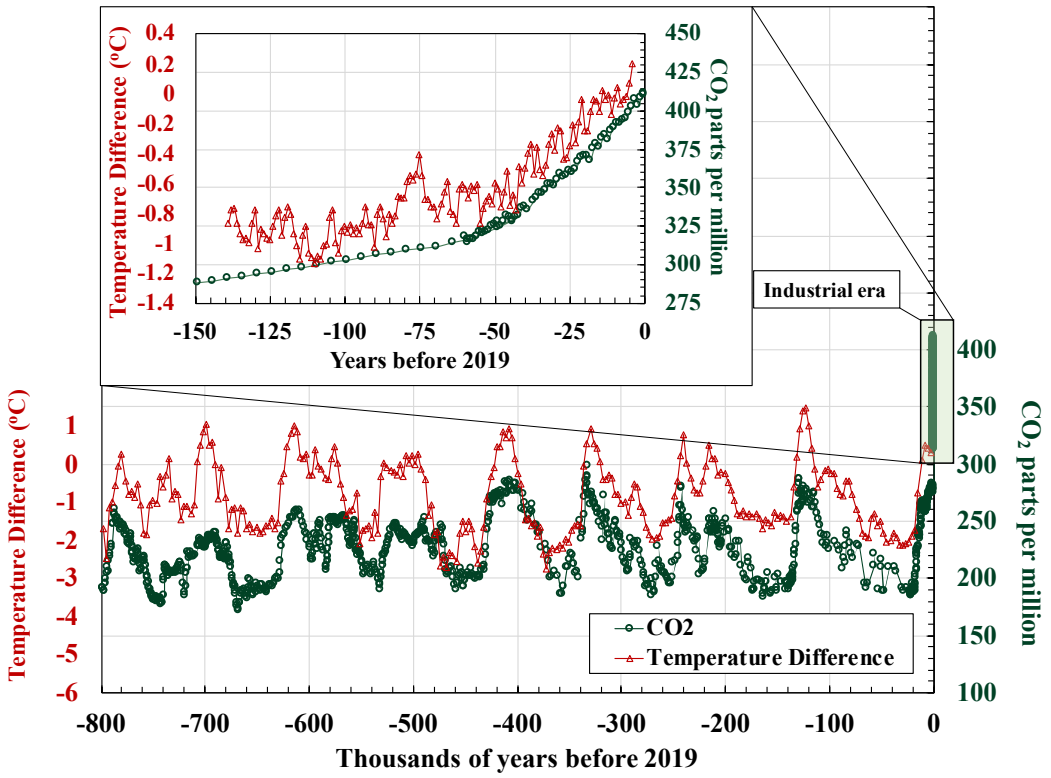

Figure 1.0.1: The measurements of CO_2 and temperature difference are achieved by monitoring the concentrations of various trapped gases in Antarctica's ice. Reproduced with permission from T.P. Davis [3].

current strategy for the world population is to meet these requirements and to reduce carbon emissions, whilst still improving the standard of living, is through a diverse, advanced and efficient portfolio of energy options, such as through the use of renewable, carbon capture, and nuclear power [8, 9], whilst still improving the standard of living.

The expansion of nuclear fission energy to tackle climate change is considered as a key stepping-stone to meet the Paris Agreement signed in December 2015, but its success will require increased governmental and public support [3]. This claim echoes statements made by the International Energy Agency [10], Bill Gates [11], the Intergovernmental Panel on Climate Change [1], and the MIT Energy Initiative [12].

Nuclear power has proven to be a reliable, safe and scalable energy source through its extensive operational history [3]. The drive to improve the reliability, safety, and scalability of future reactor designs by way of 'Generations' has lead to the 'Generation IV' type fission reactors [13]. In addition, nuclear fusion energy, which fuses atoms together rather than splitting them, has been in development since the 1960s and has been touted to become the ultimate terrestrial energy source [14].

1.1 Nuclear Fission Energy

1.1.1 The Fission Process

A nuclear engineer's endeavour is to employ radiation, radioactivity and the nuclear processes for the benefit of humankind. The basic function of any nuclear fission reactor is driven by the *nuclear fission* process; fission is the splitting of one atom into two, or more, lighter nuclei, called *fission products*. Fission generates: a) heat by the energy deposition from the fission products, b) gamma-rays emitted from decaying fission products, c) neutrons which induce further fission, and d) anti-electron-neutrinos. The easiest element to fission is Uranium-235 (^{235}U), which has 92 protons and 143 neutrons. A typical fission of this isotope is as follows:

$$^{235}_{92}\mathrm{U} + ^{1}_{0}\mathrm{n} \rightarrow ^{236}_{92}\mathrm{U} \rightarrow ^{92}_{36}\mathrm{Kr} + ^{142}_{56}\mathrm{Ba} + 2^{1}_{0}\mathrm{n} \tag{1.1.1}$$

This nuclear reaction produces a plethora of products known as fission product yields. The emission of two neutrons (or more), as shown in eq. 1.1.1, generally induces an additional event process (and so on), which creates a fission chain reaction, as shown in Fig. 1.1.1. Neutrons are emitted isotropically. Two fundamental principles characterise the control and operation of any nuclear reactor and these are as follows:

Principle 1: Control the neutron population. Neutron absorbing materials are

used to remove the neutron population from the system either by control rods, a coolant, and/or structural materials.

Principle 2: Remove the heat. This can be achieved by cooling the reactor core sufficiently.

However, neutrons do leak out of the reactor core because a) the neutron is neutrally charged, b) the interaction is a function of statistical mechanics and c) the fuel assembly is not infinite in size. The neutrons that do not interact with the fuel impinge on every single structural material that surrounds the reactor core.

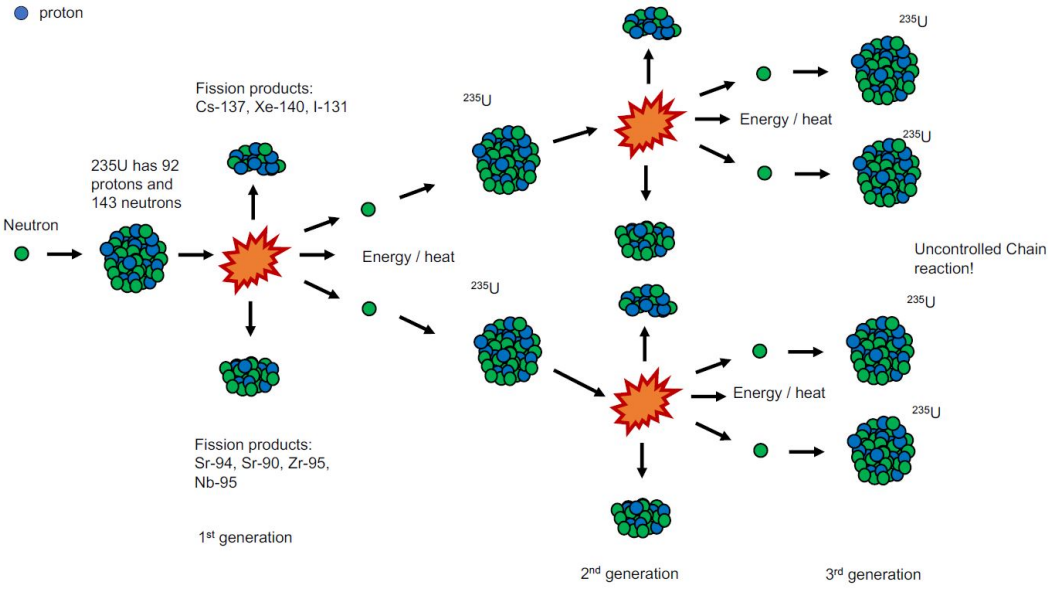

Figure 1.1.1: A schematic of the most common fission process, the fissioning of ^{235}U. The maximum probability of a neutron capture causing fission of ^{235}U is when the neutron's energy is thermalised. The fission products listed are examples.

Neutrons that interact with the structural materials can damage the materials' microstructure, which has detrimental consequences on the structural integrity of the fuel and core [9]. These consequences could affect the ability to maintain the two aforementioned principles to control a reactor core. Therefore, there has been a significant degree of scientific research, industrial development and governmental assistance to understand radiation damage of materials [9, 15–17].

1.1.2 Generation to Generation

The development of nuclear fission power has focused around six main factors: safety, security, non-proliferation, cost-effectiveness, commercialisation, and fuel cycle management. The development cycle can be categorised into 'generations' where each successive generation represents a significant improvement in one or more of the six main factors [17, 18]. A detailed history of the Generation I to III reactors can be found in reference [19]. Briefly, the four generations are:

- **Generation I:** the prototype power reactors that initiated the civil nuclear industry in the 1950s with the final reactor decommissioned in December 2012 (two Magnox reactors located at the Wylfa site in Wales, UK). These reactors were, in effect, 'proof-of-concept' for the commercialisation of nuclear energy.

- **Generation II:** the 400+ operational commercial reactors around the globe with a designed lifetime of 40 years (without extensions granted[1]). The reactor technologies that dominate Generation II include pressure water reactors (PWR), boiling water reactors (BWR), and advanced-gas reactors (AGR). The reactor technologies rely on active safety systems (which requires human interaction), are designed for large electrical grid systems, and have an open fuel cycle (the waste is not reprocessed or recycled).

- **Generation III/III+:** an evolutionary design from Generation II that focuses on a 60-year initial operational lifetime, improving the thermal efficiency, using passive (rather than active) safety systems, and improving on fuel technology. However, the fuel cycle remains open. These PWR designs are under construction today and such vendors are Rosatom (Russia), EDF Energy (France), and China General Nuclear (China).

[1] It should be noted that the US Nuclear Regulatory Commission has granted a lifetime extension of the Peach Bottom PWRs located in Pennsylvania (US) from 40 to 80 years. These PWRs will now close in 2054 [20]

- **Generation IV:** these have been in development since the 1950s, but under the 'advanced' reactor design term. The Generation IV term was defined in 2001 by the Generation IV International Forum (GIF) [13]. The term 'fast reactor technology' is sometimes used as a reference to Generation IV nuclear reactors. The aim of Generation IV reactors is to provide solutions for nuclear waste challenges [21], to improve safety [21], to decrease risk of proliferation [22], to optimise fuel utilisation [23], to widen the scope to include hydrogen production [24], enable heat production [25], and to increase the long-term operational lifetimes [17]. Recent research has evaluated how these reactors may be used to substantiate geopolitical influence [26]. There have been six proposed generation IV reactor types that have been categorised by technology. These are: [18]:
  - Very high temperature reactor (VHTR);
  - Molten-salt reactor (MSR);
  - Supercritical water cooled reactor (SWCR);
  - Gas-cooled fast reactor (GFR);
  - Sodium-cooled fast reactor (SFR);
  - Lead-cooled fast reactor (LFR).

It should be noted that 99% of all the commercial nuclear reactors that are under construction in 2020 fall within the Generation III/III+ classification. However, the recent advancements in Generation IV nuclear reactors have enabled privately funded Western corporations, such as Moltex Energy Ltd [27], Terrestrial Energy Inc [28] and Advanced Reactor Concepts, LLC [29], to develop credible reactor designs for eventual deployment in the 2030s and beyond. These reactors appear to address the shortcomings of Generation I, II and III/III+ technology, as well as providing possible credible solutions to the world's long-term energy supply [3], whilst emitting zero

CO_2. It is important to note that these companies, and the others that have not been listed, have yet to demonstrate the engineering feasibility, reliability, and economics advantages of using such technologies.

For the six Generation IV designs, SFR technology has the longest operational history [30]; therefore, the SFR reactor design will be the focus within this thesis.

1.1.3 Sodium-cooled Fast Reactors

SFRs have already operated in the UK, the United States, France, Russia and Japan with the power output ranging from 1.1 MW(th) to 3000 MW(th). A general layout of the reactor design is displayed in figure 1.1.2. The main advantages of using SFR technology are:

- The sodium coolant operates at atmosphere pressures, which reduces the overall system stresses;
- Utilisation of ^{235}U, ^{238}U, ^{239}Pu and ^{241}Pu as fuel;
- Able to transmute actinides, such as neptunium and americium [18];
- The liquid-metal sodium coolant flows through the core and has an effective heat transfer coefficient that is $\sim$ 100 times greater than water;
- The coolant is near transparent to neutrons (i.e. it does not thermalise them, as discussed below);
- The reactor can operate at high temperatures (> 500 °C),which increases thermal efficiencies of the reactor.
- The reactor core operates at atmospheric conditions and natural circulation can be sufficient to remove heat from the core under accident conditions [18].

The major disadvantage of the SFR design is that sodium explodes when in contact with water and burns in oxygen. However, these chemical reactions are severely

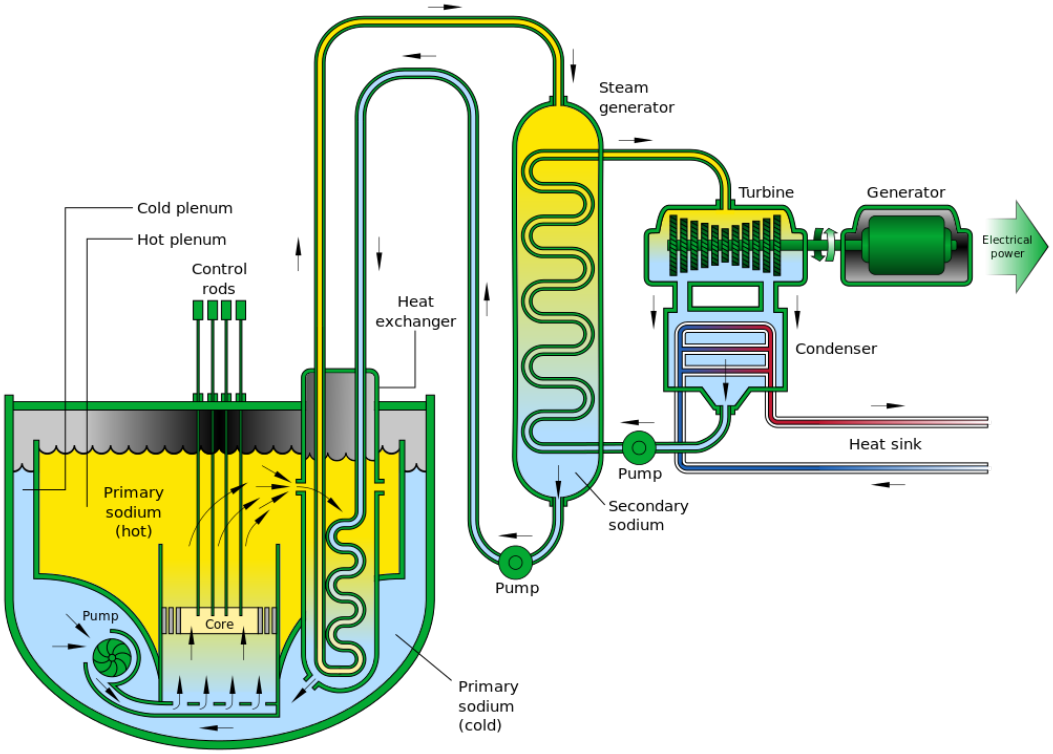

Figure 1.1.2: A typical schematic of a pool-type SFR. The reactor core is submerged in liquid-metal sodium (primary coolant) which is pumped to increase cooling efficiencies. A primary heat exchanger is submerged into the pool of primary coolant. This heat exchanger increases the temperature of a secondary liquid-metal coolant (which is isolated from the primary coolant so no radioactivity is transferred), where it goes to a secondary heat exchanger with water. The secondary heat exchanger converts the water into steam, which drives the turbines to generate electricity. Reproduced with permission from GIF [13].

mitigated in reactor designs and experience gained from operating such reactors (such as the BN-series SFR in Russia). SFR fission is based on utilising the fast neutron (1 MeV energy on average) rather than thermal neutron ($E < 10^{-8}$ MeV, or < 0.025 eV, where E is the neutron's energy) energy spectrum. The utilisation of ^{235}U, ^{238}U, ^{239}Pu and ^{241}Pu as fuel is key to the technology and is summarised below.

- To use ^{235}U (0.3 % natural abundance) the neutrons are required to have a thermal energy spectrum, as shown in figure 1.1.3's low energy portion ($E < 10^{-8}$ MeV). This can be achieved by passing the neutrons through water or

graphite, which moderates the neutron's energy (i.e. slows it down);

- The ^{238}U (99.7 % natural abundance) is not used (generally) as nuclear fuel in Generation III reactors due to the lack of high energy neutrons ($E < 1$ MeV) within the system, thus the interaction probability is just too low to maintain a fission chain reaction, as shown figure 1.1.3;
- SFR reactors have a greater portion of high energy neutrons ($E < 1$ MeV) and can now transmute ^{238}U to ^{239}Pu. The ^{239}Pu can now fission, as shown in figure 1.1.3.

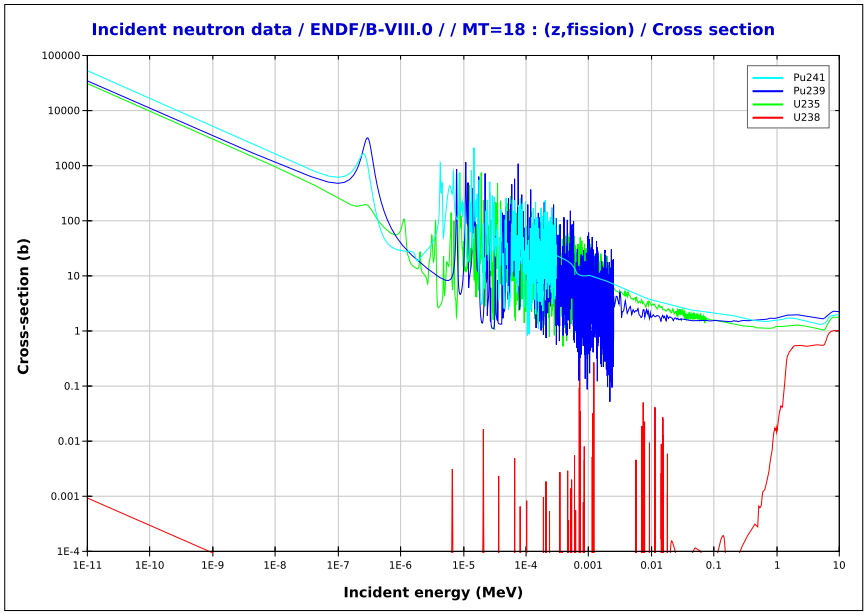

Figure 1.1.3: The neutron fission cross-section (the probability of a neutron inducing fission) as a function of the incoming neutron energy for ^{235}U, ^{238}U, ^{239}Pu and ^{241}Pu. The cross-section data is from the ENDF/B-VIII.0 nuclear database [31].

This latter point describes the potential of using up to 99.7 % world's supply of uranium as fuel [3, 18], which could improve the longevity of uranium supply.

The operating temperatures of SFRs have been shown to go to 550 °C [18]. Intense neutron irradiation [9] and liquid-metal sodium offers extra challenges when

considering the corrosion performance of materials [32]. The structural materials selection (such as fuel cladding and assembly) is vital to the safety and economics of any Generation IV design. The desirable characteristics for the selection are:

- Acceptable radiation damage resistance under the expected intense neutron damage and helium embrittlement [33];
- Sufficient mechanical properties before and after neutron exposure;
- Excellent dimensional stability (against irradiation creep; [34], void swelling [35] and thermal creep [9]);
- High resistance to irradiation-assisted stress corrosion cracking (IASCC) [36].

For SFR reactors (Prototype Fast Reactor in the UK, BN-series in Russia, Experimental Breeder Reactor II and Fast Flux Test Facility in USA, for example), the primary reactor core materials were based on ferritic-martensitic high chromium (9-12 % Cr) steels [37]; these steels have high temperature strength, high creep resistance, high strength and high resistance to irradiation induced swelling [38–40]. However, future reactor designs are increasing the fuel cladding's operating temperature to 650 °C to increase the efficiency and, hence, improve the economical outputs [41]. Ferritic-martensitic steels are unable to meet these demands [42], therefore, a new branch of steels, called Oxide Dispersion Strengthened (ODS) steels, are in development [41, 43–45], which could meet the structural demands of Generation IV nuclear reactors [44].

1.2 Nuclear Fusion Energy

For long-term (>2050) electricity production, it is widely perceived that nuclear fusion energy could be the ultimate terrestrial energy source [14]. Fusion has the potential of producing non-CO_2 emitting, near-limitless energy from the abundance of fuel with minimal radioactivity [46]. However, to achieve fusion the conditions required

to overcome the electrostatic repulsion of nuclei is on the order of millions of degrees Celsius [47]. As of today, there are two main fusion methods currently being pursued: Magnetic Confinement Fusion (MCF) and Inertial Confinement Fusion (ICF). MCF uses strong magnetic fields to confine a hot plasma, creating the conditions for fusion to occur, and ICF heats a fuel target via ultra-high-powered lasers to produce conditions for the fuel to fuse together [48].

MCF has received the most research and development. The тороидальная камера с аксиальным магнитным полем (**to**roidal'naya **kam**era s **ak**sial'nym magnitnym polem (toroidal chamber with axial magnetic field)), or commonly known as 'tokamak', fusion reactor concept has been the most successful at containing and controlling fusion plasmas [48]. The Eurofusion program [49, 50], the US 'National Strategic Plan for US Plasma Research' programme [51], the Japanese fusion research activities [52], the UK Atomic Energy Authority Spherical Tokamak for Energy Production (STEP) programme [53], and the Chinese fusion research activities [54] have all decided that the tokamak device configuration is the way forward. Due to the significant investment by Governments, industry, universities and national laboratories, the tokamak-based fusion reactor will be considered within this thesis. A consensus has been made surrounding the need for demonstration fusion power [55]. However, discussions have been ongoing since the 1980s regarding the feasibility and overhype nature of fusion energy [55–58];

1.2.1 Principles of Controlled Nuclear Fusion

The controlled fusion energy relies on the fundamental process of fusing two isotopes of hydrogen: deuterium ($^{2}_{1}$H) and tritium ($^{3}_{1}$H). The principal nuclear reaction is [59]:

$$^{2}_{1}\mathrm{H} +^{3}_{1} \mathrm{H} \rightarrow^{1}_{0} n +^{4}_{2} \alpha + 17.6 \text{ MeV} \tag{1.2.1}$$

where the neutron's, n, kinetic energy is 14.1 MeV and α's kinetic energy is 3.4 MeV.

To achieve fusion of ${}^{2}_{1}\mathrm{H}$ and ${}^{3}_{1}\mathrm{H}$, the nuclei must overcome the electrostatic Coulomb barrier, which is on the order of 10^{9} °C [14]. The break-even parameter that is used to describe the performance of a fusion reactor is called the Q-value, and this is defined as:

$$Q = \frac{E_{\text{fusion}}}{E_{\text{heat-in}}} \tag{1.2.2}$$

where E_{fusion} is the energy provided from the fusion reaction and $E_{\text{heat-in}}$ is the energy provided by the equipment to heat the plasma. For scientific break-even, $Q = 1$, and for ignition (where the reaction is self-sustaining) $Q \to \infty$ as $E_{\text{heat-in}} \to 0$.

${}^{3}_{1}\mathrm{H}$ is radioactive and has a half-life of 12.32 years [60], which indicates that there is little available in the world. ${}^{3}_{1}\mathrm{H}$ decays at a rate of 5.5 percent per year so half of the fuel (50% ${}^{3}_{1}\mathrm{H}$ and 50% ${}^{2}_{1}\mathrm{H}$) for fusion reactors must either be bred in nuclear fission reactors (through the use of tritium-producing burnable absorber rods (TPBARs) [61] or as a by-product with transmutation of deuterium in the Canadian heavy water reactor's coolant [62] (the former has been explored to supply fusion energy temporarily [62]). The most common ${}^{3}_{1}\mathrm{H}$ production reaction is :

$$^{6}\mathrm{Li} + n \to {}^{3}_{1}\mathrm{H} + \alpha \tag{1.2.3}$$

with the relative abundance of ${}^{6}\mathrm{Li}$ making up 7.4% of the natural Li [14]. Lithium extracted from land-based supplies could supply future fusion power plants for approximately 1000 years. Moreover, Li could be extracted from sea-water with the latest reserves estimated to last approximately 6 million years [46].

1.2.2 ITER Fusion Reactor

In the south of France, 35 nations are collaborating to build the latest tokamak fusion reactor, called ITER [2]. The goal for ITER is to produce 500 MW(th) power, to

[2] ITER used to be an abbreviation of International Thermonuclear Experimental Reactor, however, this name was dropped for 'Iter', which means 'the way' in Latin.

achieve $Q > 5$, to demonstrate the feasibility and effectiveness of breeder blanket technology, and to demonstrate the feasibility of all the fusion technologies working in unison. It will be the first fusion device to produce net energy (i.e. $Q > 1$) for up to 500 seconds per fusion pulse. It should be noted that ITER will not be a materials test reactor for fusion power stations but rather a technology demonstrator. The International Fusion Materials Irradiation Facility (IFMIF) is the facility that is currently under construction with a mission to test materials in fusion-like neutron damage environments [63]. For further details on the ITER project, refer to Ref. [47]. Figure 1.2.1 is a 2D model of the reactor, and figures 1.2.2 and 1.2.3 are the latest aerial construction and base of the cryostat photos, respectively.

1.2.3 DEMO Fusion Reactor

The European Fusion Development Agreement (EFDA) outlines the roadmap for demonstration, and eventual commercialisation, of fusion energy [49]. The European strategy is to build DEMO, a demonstration fusion power station, by 2050. The DEMO concept will meet the goal of generating electricity from fusion energy with construction starting in the 2030s. ITER will provide the physics, engineering and technology basis for DEMO. However, the transition from ITER to DEMO provides two major technical challenges to overcome:

- DEMO will need to breed its own tritium supply [62];
- DEMO will need suitable structural and functional materials that can resist the damage caused by the neutron flux [44, 49, 64].

The implications and consequences of the DEMO design strategy have been reviewed [65] and will be discussed in Chapter 2. The social-economical impact of the DEMO design strategy has been reviewed in context of renewable energy systems, radioactive material generation consequences, and discusses policy implications [58].

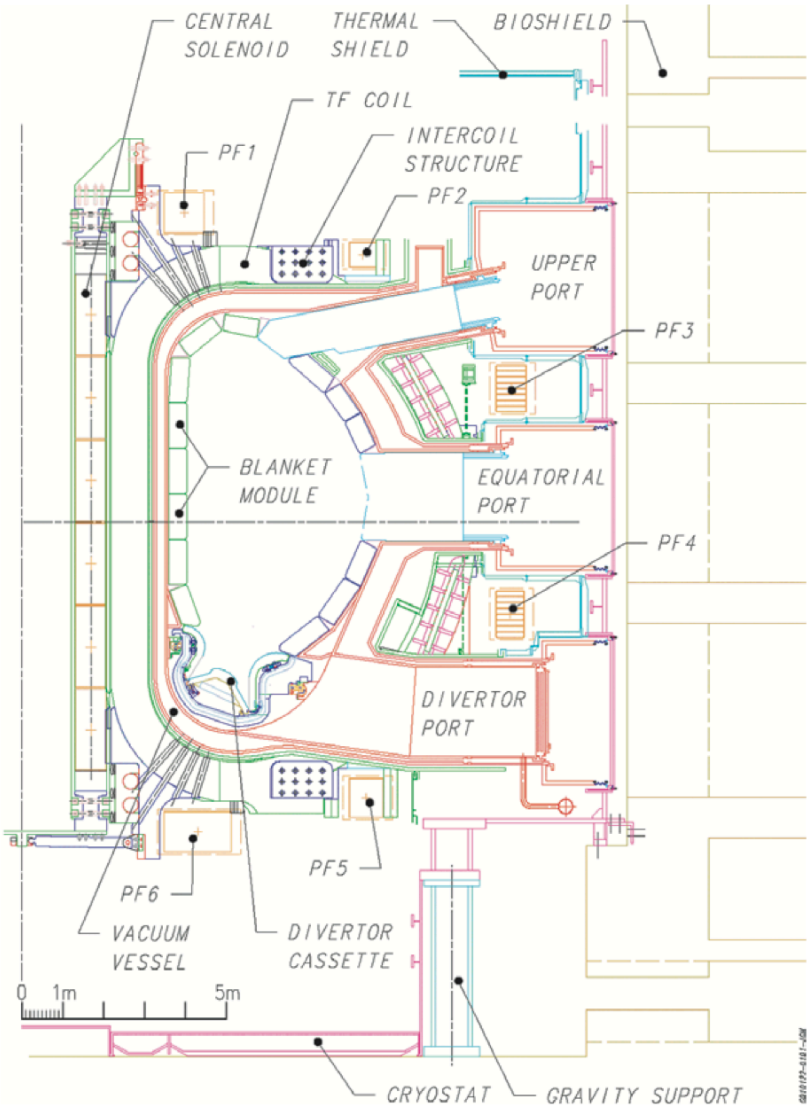

Figure 1.2.1: A 2D model of the ITER design with various components labelled. Reproduced with permission from [66].

Figure 1.2.2: An ITER construction site photo in the south of France. This photo was taken in February 2020. Reproduced with permission from [67].

Figure 1.2.3: The cryostat base being moved into place at the Tokamak pit's bottom. This photo was taken on 28 May 2020. Reproduced with permission from [68].

1.3 Summary

Nuclear power is a reliable, non-CO_2 emitting, and sustainable energy source, and is part of the world's strategy to combat climate change. Generation IV nuclear reactors are under development, which could provide improvements for the safety, security, non-proliferation, cost-effectiveness, commercialisation, and fuel cycle management of nuclear energy, and should be deployable during the 2030s [3]. Nuclear fusion energy is widely perceived to be the ultimate terrestrial energy source. Fusion holds the potential for producing non-CO_2 emitting, near-limitless energy from the abundance of fuel with minimal radioactivity. However, common engineering challenges remain for both energy systems and these need to be solved before commercialisation can occur such as the development of suitable structural materials for the reactor cores [9, 17, 18, 65] and, for fusion specifically, the demonstration of net gain energy (i.e $Q > 1$).

One such challenge is selecting suitable structural materials. This selection is vital to the operation, safety and economics of any future nuclear fission or fusion reactor. It is the job of nuclear engineers and material scientists to develop, select and demonstrate the feasibility of structural materials to maintain the integrity of the reactor core. Assessing the integrity of structural materials in a nuclear reactor core is a critical aspect of the regulator's efforts in maintaining public safety. Structural materials that are exposed to neutron irradiation alters the mechanical, thermomechanical, and microstructure of the material [9]. Safe reactor operation relies on the understanding of unirradiated properties (such as creep, fatigue, creep-fatigue, loading, and corrosion) and neutron irradiated properties (such as swelling, embrittlement, induced activation, and transmutation) during operation [42].

The major structural material candidates for both fission and fusion systems is based on steel. In particular, ferritic-martensitic 9 (weight %) chromium-based steels, such as T91 ferritic-martensitic steel, are generally selected for structure of the reac-

tor cores due to the materials good mechanical and thermal properties, and established manufacturing routes [38, 42]. However, this steel's properties are affected by neutron irradiation and these properties range from the nanoscale to macroscale [64]. Nanoscale solute precipitation is accelerated by neutron irradiation and has been shown to affect the mechanical properties of this steel [38, 69, 70]. Understanding the precipitation nature in steels used in nuclear reactors is of interest within this thesis.

1.4 Thesis Organisation

The thesis is organised as follows:

- Chapter 2 provides a literature review into the major challenges for structural steels of Generation IV fission and DEMO-type fusion environments.
- Chapter 3 discusses the experimental methods used within this thesis research.
- Chapter 4 discusses the first research study on the effect of neutron irradiation on T91 ferritic-martensitic steel;
- Chapter 5 discusses the second research study on the effect of ion irradiation on T91 ferritic-martensitic steel;
- Chapter 6 discusses the third and final research study on the microstructure inhomogeneity of oxide dispersion strengthened steels, a replacement of T91 ferritic-martensitic steels.
- Chapter 7 provides an overall contribution to science and future work suggestions.

Chapter 2

Reactor Core Structural Materials

2.1 Introduction

The selection of structural materials for nuclear engineering poses many challenges; a material that meets the combinational requirements of chemical, mechanical and nuclear properties must be found. Engineers often use material property maps when selecting a suitable material for the application [71]. Nuclear regulators require that reactor operators must understand the effect of radiation on the materials' properties at *operating and accidental* conditions [72, 73] .

The core conditions of SFRs could limit the use of structural materials due to the effect of radiation damage, liquid-metal corrosion and high temperature creep rupture [17, 38]. DEMO fusion reactors increase the degree of radiation damage, high temperature creep rupture and liquid-metal corrosion (if used) compared to SFRs; and in addition, due to the high neutron energy spectrum of fusion, the rate of helium production significantly impacts the materials' performance [44]. Steels have been used for all reactor core configurations [17, 18] due to the engineering maturity (i.e. deep understanding and extensive experience of fabrication routes), compatibility with coolants, and reasonable radiation resistance in PWR technology [64]. Therefore, this chapter will review the current literature on steels for use as a fuel

cladding material in SFRs and structural steels for the in-vessel components of fusion reactors. The chapter will begin with a review of the radiation damage mechanisms and candidate structural steels.

2.2 Radiation Materials Science

Radiation materials science is the study of how radiation interacts with matter and its effects on the material's microstructure and mechanical properties. Ions, neutrons, photons, and electrons all have the potential to displace an atom from its lattice site. Neutrons are emitted by the fission or fusion reactions, which bombard the surrounding materials and displace atoms from their lattice sites. The lattice atom that is displaced from its site is called the Primary Knock-on Atom (PKA) and (if the PKA has enough energy) it will continue to displace neighbouring atoms producing a damage cascade.

The displacement of atoms is the fundamental process driving microstructural change in metallic materials [69]. The displaced atom leaves an empty lattice site called a *vacancy* and once the displaced atom comes to rest, it becomes a self-interstitial [74]. In addition, neutron irradiation can lead to activation and transmutation of elements within the material [9, 75–77]. The most common effects from neutron irradiation are: the change of shape (swelling) [78, 79], increase in hardness [80, 81], radiation induced creep [79], radiation-induced segregation of alloying elements [82–86], severe reduction in ductility, embrittlement [87–89], and increased susceptibility to cracking from the environment [82, 84, 90].

2.2.1 The Damage Event

The PKA event occurs over $\sim 10^{-11}$ s [74]. This PKA creates a vacancy and interstitial, and together these are called a *Frenkel Pair*. For most incoming particles, the energy is generally orders of magnitude higher than the required energy to displace a

lattice atom [74]. Thus, the PKA has enough energy to displace further lattice atoms producing a damage cascade over 5-10 ps, as displayed in figure 2.2.1. The average fusion neutron energy is 14.1 MeV and provides an indication that the PKA atom will have enough energy to displace multiple atoms from their lattice site. This event is called a *damage cascade* or 'heat spike'. The concept was proposed by Brinkman (1954) [91] and is now established [92]. Most of these Frenkel Pairs will recombine, but a small concentration will remain as shown in figure 2.2.2, and it is these that lead to radiation damage [69, 74].

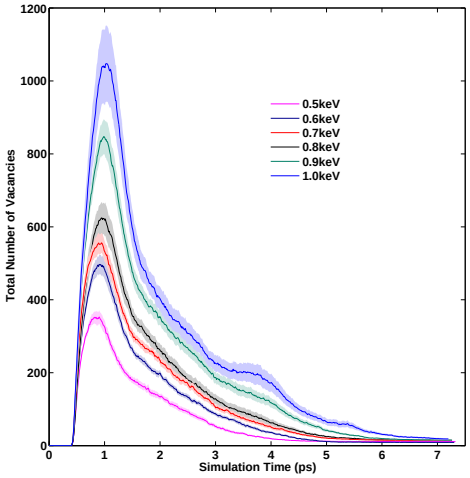

Figure 2.2.1: The number of vacancies produced from a single PKA cascade from neutron irradiation using molecular dynamics simulations. Reproduced with permission from Davis et al. (2015) [93].

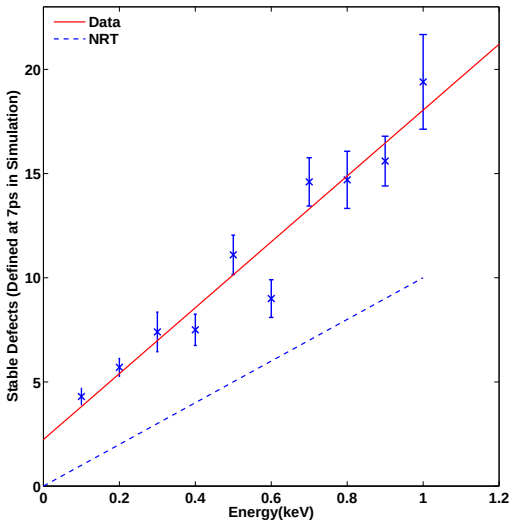

Figure 2.2.2: The number of stable vacancies remaining after 7 ps during a cascade as a function of PKA energy. The NRT model is provided for comparison [94]. Reproduced with permission from Davis et al. (2015) [93].

2.2.2 Displacement Threshold Energy

The displacement threshold energy, E_d, is defined as the minimum energy that must be transferred to the lattice atom for it to be displaced from the site. The threshold energies range between 10 – 90 eV [95, 96] and are dependent on the atomic weight. The parameter is generally considered to be fixed and independent of crystallography,

temperature, and velocity vector. ASTM E521 [97] recommends 40 eV should be the E_d value for iron. Contrary to this, the threshold energy has been shown to be heavily dependent on crystallography [95, 98] and the thermal state at the atomic scale [98]. It should be noted that there are inconsistencies in the standard threshold energy supplied by ASTM E521 to literature [99]. However, the standard is useful as provides a simplification for calculating the damage caused by radiation.

2.2.3 Kinchin and Pease Model

Kinchin and Pease (1955) [100] developed a model (now called the Kinchin-Pease model) that calculates the number of displacements produced per PKA. The authors assumed that the damage collisions were independent, and the displacements produced were linearly proportional to the PKA energy. This model calculated the average displacement of atoms per incident ion. The model was modified by Norgett, Robinson and Torrens (NRT) in 1975 [94] and is now part of the ASTM E521 [97] standard. This modification used binary collision approximation simulations and considered the possibility of ballistic process recombination. The full NRT equation is as follows:

$$\nu(T) = \begin{bmatrix} 0 & , & T_d < E_d \\ 1 & , & E_d < T_d < \frac{2E_d}{0.8} \\ \frac{0.8T_d}{2E_d} & , & \frac{2E_d}{0.8} < T_d < \infty \end{bmatrix} \tag{2.2.1}$$

where T_d is the energy available for damage production, $\nu(T)$ as the displacements of atoms per incident particle, E_d is the threshold displacement energy, and 0.8 factor was result of the NRT modification. Equation 2.2.1 can be used to calculate the number of displaced atoms in any material, given that E_d and T_d is known.

For neutron irradiation, the particle transport code Monte-Carlo N-Particle (MCNP) [101, 102] utilises the NRT model to calculate the energy transferred to lattice atoms by incident neutrons. For ion irradiation, the Stopping and Range of Ions in Materials (SRIM) Monte-Carlo code [103] simulates materials exposure to

ion radiation and calculates $\nu(T)$ through implementation of the NRT model.

2.2.4 Displacements per Atom (dpa) Unit

The ASTM E521-96 [97] states that the standard measurement unit of radiation damage is the displacement per atom (dpa). It represents the number of displacements for each atom from their original lattice sites. If the volume of material is known then the number of displacements in this volume can be calculated by normalising the number of displacements to the atomic density, which yields the dpa value. For example, 1 dpa is a representation which signifies that every atom within the lattice has been displaced at least once on average. The dose dpa unit can be used to compare with different radiation damage by radiation modes (neutron, proton, and ion) as the unit is independent of ion type. The determination of dpa in as follows:

$$R = N \int_{E_{\text{min}}}^{E_{\text{max}}} \phi(E_i)\sigma_D(E_i)dE_i \tag{2.2.2}$$

$$\text{dpa} = \int_0^t \frac{R}{N} dt \tag{2.2.3}$$

where R is the displacement rate per volume, E_{max} and E_{min} are the maximum and minimum energy of the incoming particle, respectively, N is the atom number density, $\phi(E_i)$ is the energy dependent displacement cross-section, $\sigma_D(E_i)$ is the energy dependent displacement cross section and t the irradiation time [16, 97]. An alternative view of the dpa value can be:

$$\text{dpa} = \frac{\text{number of displaced atoms in a unit volume}}{\text{number of (material) atoms in the same volume}} \tag{2.2.4}$$

The limitations of using the dpa value are:

- It uses averaged damage values across the whole irradiation experiment;
- It does not account for transmutation effects (a neutron is removed from the

system, thus this now-removed neutron cannot induce further damage);

- It does not consider the material's crystallographic structure;
- It does not consider the defects already present in the material (such as grain boundaries);
- It does not consider the incident radiation type;
- It does not consider the incident radiation directional angle.

Charged particles, photons, and neutrons cause radiation damage in materials. Neutrons are not charged, whereas ions are charged. For neutron irradiation dpa calculations, ASTM E693 [104] should be followed. To calculate dpa for ion (which includes proton) irradiation, the number of displacements per incident ion must be calculated. SRIM is the most used Monte Carlo code to calculate this displacements per incident ion [103, 105]. However, it is still not standard practice in the literature to find full descriptions of the explicit calculation of dpa using SRIM. It is important to know how the authors have calculated dpa, as the value is useful to compare with other irradiation studies.

Stoller et al. (2013) [99] investigated the use of SRIM for computing the radiation damage exposure. It has been known that the 'Detailed Calculation with full Damage Cascade' option in SRIM yields approximately twice the number of displacements produced per Angstrom per ion compared to the 'Ion Distribution and Quick Calculation of Damage' mode. From this discrepancy, the authors recommended the use of the standard NRT model and ASTM E521 [97] standards on the displacement threshold energy to calculate the number of displacements per ion. This is to provide a standard method for researchers to calculate dpa and to provide a comparison against other ion irradiation studies. Comparisons between neutron and ion dose should be taken with caution due to the difference in dose rates (neutron dpa/s ranges from $10^{-6} - 10^{-8}$ and ion dpa/s ranges from $10^{-2} - 10^{-5}$), charge deposition, nuclear reactions/transmutation rates, and penetration depth [106].

When literature reports describe neutron dpa results, the authors usually do not provide detailed calculation information, such as which model they used (Kinchin-Pease, half-Nelson, NRT and French model). Each of these models produce slightly different dpa values that will affect the interpretation of data when comparing between different spectra [107, 108]. The neutron energy spectrum should also be quoted, as outlined by Gilbert et al [76, 77, 109], transmutation rates are highly dependent on the energy spectrum of the incident radiation. A list of expected dose (dpa) values and temperature for nuclear reactors are listed in Table 2.2.1.

Table 2.2.1: Common radiation damage values and temperatures of fission and fusion reactors. DEMO values are highly dependent on the design and are subject to change.

Component	Temperature (°C)	Radiation damage (dpa)	Ref
Reactor Pressure Vessel steel (40 years)	230	0.1 – 0.4	[110]
Fuel cladding in a light-water reactor (2-5 years)	320	20 – 30	[18]
Fuel cladding in a SFR (2-5 years)	550 – 650	50 – 100	[17, 18]
Joint European Torus (JET) divertor tile	1000 – 1200	<0.001	[111]
ITER W divertor tile	800 – 1100	0.1	[112]
ITER first wall Be tile	600 – 1000	1	[113]
EU-DEMO1 first wall steel structure	400 – 500	∼50 – 100	[114]
EU-DEMO1 W first wall	1000 – 1500	∼30 – 80	[114]
EU-DEMO1 W divertor	1000 – 1500	∼30 – 50	[114]

2.2.5 Radiation Damage Dependence on Temperature

The survived point defects that are produced by the displacement cascade will diffuse though the atomic microstructure. The effects of point defects are highly dependent on operating temperature and can be generally categorised into these main types:

- Below 0.3–0.4 T_{M} (where T_{M} is the melting temperature of the material) radiation-induced defect clusters form, called radiation-induced precipitation (RIP), segregation of solute atoms or trace impurities [74]. These defects resist dislocation movement, increasing the hardness and yield strength of the material (as initially predicted by Makin et al. (1965) [115]). This occurs with a damage dose between 0.001 to 0.1 dpa [9, 44].

- Between 0.3–0.6 T_{M} there are three main mechanisms that become dominant: radiation-induced segregation (RIS) and RIP [40], void swelling [69], and radiation-induced creep [116, 117].

- At high temperatures, $> 0.5\ T_{\mathrm{M}}$, and applied mechanical stress, helium transmutation products migrate towards the grain boundaries, which can cause intergranular fracturing [9, 118]. These stages are represented in figure 2.2.3 compiled by Zinkle et al. (2017) [44]. In addition, at these temperatures creep rupture is a likely failure mechanism [34].

These temperatures may differ between material systems (such as nickel-based, refractory-based etc.) but the generalisation provides a useful insight into radiation damage of materials. Radiation damage is a complex, multifaceted phenomena that occurs from the nanometer to millimetre length scales and from picoseconds to decades timescale.

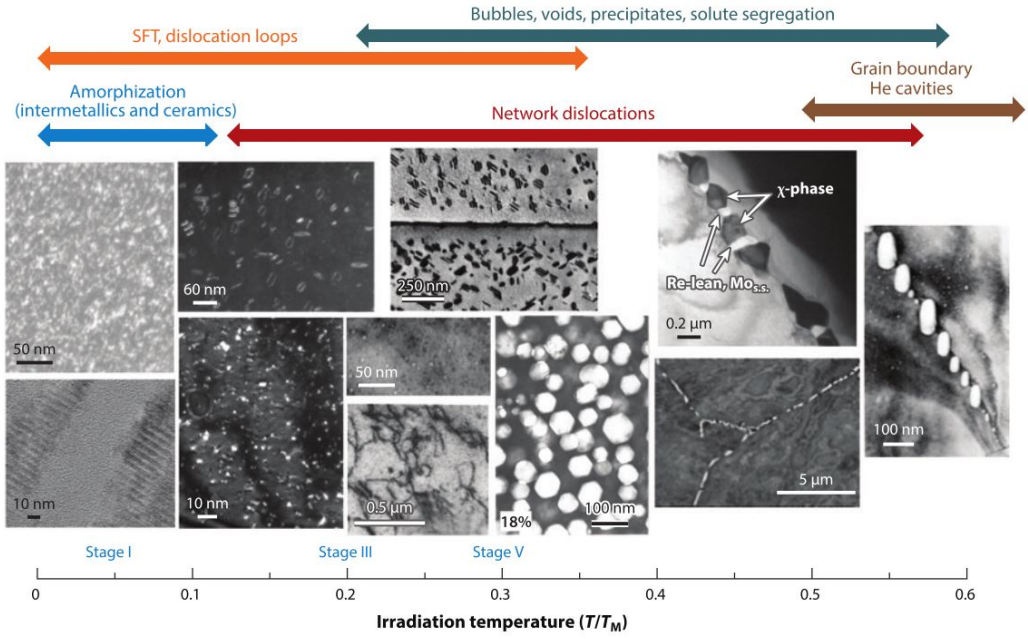

Figure 2.2.3: An example of irradiation damage as a function of temperature using transmission electron microscopy. The stages listed are determined by: Stage I, initiation of long-range self-interstitial migration; Stage III, monovacancy migration initiation; Stage V, thermal dissolution of small vacancy clusters. Reproduced with permission from Zinkle et al. [30].

2.2.6 Radiation-Induced Swelling

Radiation-induced swelling is a volume change mechanism and is shown in figure 2.2.4 for austenitic stainless steel. Radiation damage produces vacancies which cluster to form voids within the material at temperature ranges between $0.3 - 0.6T_{\mathrm{M}}$. Helium is produced by the (n, α) reaction, and it is these helium ions that stabilise the voids [35]. The most common source of α particles in materials is from the transmutation of ^{58}Ni by:

$$^{58}\mathrm{Ni}(n, \gamma) \rightarrow ^{59}\mathrm{Ni}(n, \alpha)^{56}\mathrm{Fe} \tag{2.2.5}$$

where α is a helium nucleus. The α stabilises the voids and forms bubbles with an associated internal pressure. This pressure expands the lattice producing a volume

change. Under constant irradiation and temperature, these voids start to grow and causes swelling. There are two main methods that reduce the swelling of a material:

- Remove the main source of alpha particles (i.e. remove nickel);
- Include a large dislocation density network to absorb the vacancies produced by radiation damage;

Radiation-induced swelling can can be a showstopper within a nuclear environment which experiences high flux neutrons (such as fast spectrum fission reactors and fusion reactors). The rates of swelling, as shown in figure 2.2.4, observed for certain materials are not possible to engineer out. The definition of a showstopper can be considered as the engineering elimination of a material based on swelling rates due to radiation [42].

2.2.7 Helium Embrittlement

As described in section 2.2.6, helium is generated by the $X(n,\alpha)Y$ nuclear reaction. Helium embrittlement is temperature dependent: if the temperature is >0.5 T_{M}, the helium diffuses towards the grain boundaries and embrittles them; if the temperature is <0.5 T_{M}, the helium forms bubbles and induces the swelling effect.

Helium embrittlement of grain boundaries is one of the major showstoppers in Generation IV nuclear reactor core materials [33, 119] and fusion structural steels [64, 120]. This type of embrittlement can cause the material to catastrophically fail [44].

Expanding on the nuclear reaction discussed in section 2.2.6 for the source of helium, the typical reactions for structural materials are: ^{10}B(n,α)^{7}Li, ^{58}Ni(n,γ) $\rightarrow^{59}$Ni(n,α)^{56}Fe and ^{58}Ni(n,α)^{55}Fe. The reactions are dependent on the neutron energy spectrum, as shown in figure 2.2.5. The ^{58}Ni(n,γ) $\rightarrow^{59}$Ni(n,α)^{56}Fe reaction is the most common reaction in structural materials, such as steels and nickel, due to the presence of nickel in the alloys. Furthermore, the reaction occurs across the entire

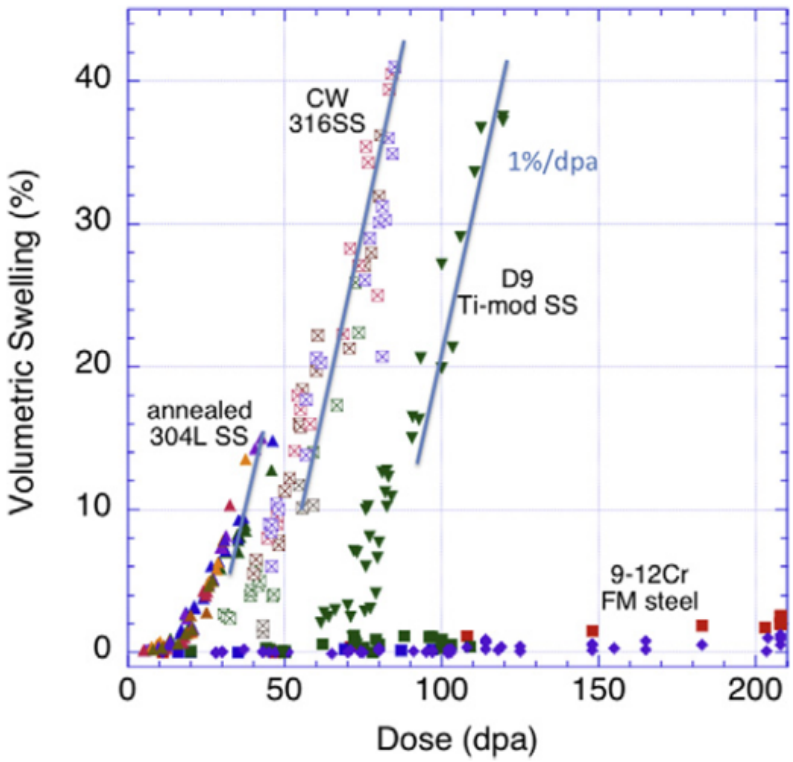

Figure 2.2.4: Comparison of the volumetric swelling behaviour of stainless steels (304L SS, CW 316SS, D9 Ti-mod SS; CW (coldwork), SS (stainless steel)) and ferritic-martensitic (FM) 9-12Cr Steels following fast neutron irradiation between 400-550 °C temperature in Phénix. This is a good example of the severity of the radiation-induced swelling experienced by austenitic steels compared to the swelling experienced by FM steel. Figure reproduced from Ref. [64].

neutron energy spectrum indicating that helium generation should be expected in all nuclear reactors.

The high neutron energies associated with fusion reactions generate, on average, 50 to 100 times the quantity of He per dpa in materials compared to the levels found in fission reactors, as shown in figure 2.2.6. The levels of helium embrittlement predicted in fusion structural materials are significantly higher than fission. Helium embrittlement is difficult to investigate because the He generation is dependent on the neutron energy spectrum dependence, as shown in figure 2.2.5.

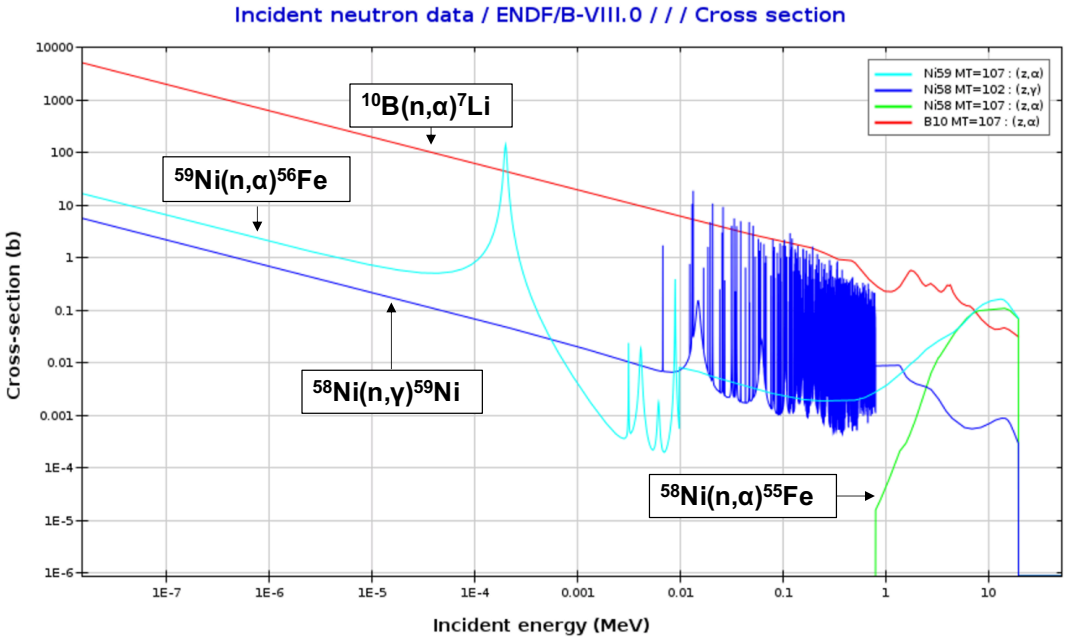

Figure 2.2.5: The neutron cross-section for the common helium generation reactions (^{10}B, ^{58}Ni and ^{59}Ni) as a function of neutron energy. The data is from the ENDF/B-VIII.0 nuclear database [121].

2.2.8 Simulating Neutron Irradiation

The motivation to use ion irradiation to study the effects of neutron irradiation began as a result of the fast breeder and fusion reactor programmes that occurred during the 1970s [97, 122]. Neutron irradiation experiments are time consuming (months to years), expensive and induce radioactivity. Thus, the main advantages of using ions to simulate neutron irradiation damage are as follows:

- It avoids a highly radioactive environment;
- There are a limited number of neutron irradiation facilities;
- It is economically advantageous to use ion irradiation over neutron irradiation;
- Ions can be accelerated with high currents achieving low irradiation times to reach the same damage dose (dpa) [123].

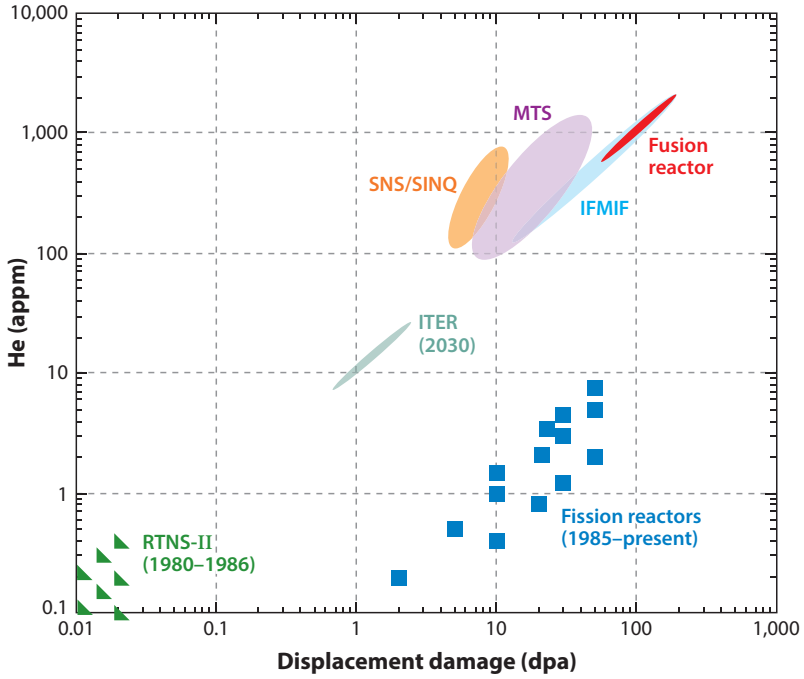

Figure 2.2.6: A summary of the dpa and He (appm) for structural steels in fusion reactors compared to fission reactors. IFMIF (International Fusion Materials Irradiation Facility); MTS (Materials Test Station) spallation source; RTNS (Rotating Target Neutron Source); SINQ (Swiss Spallation Neutron Source); SNS (Spallation Neutron Source). Reproduced with permission from Ref. [30].

There are four fundamental differences between ion and neutron irradiation. Firstly, the spectrum of energies for ions is mono-energetic as they are produced by accelerators, whereas neutron irradiation energies can occur over several orders of magnitudes [124], as shown in figure 2.2.7. Secondly, ions can only penetrate a limited depth into the target as they readily lose energy due to the Coulomb repulsion [103, 125], as shown in figure 2.2.8. This gives rise to non-uniform energy deposition throughout this penetration depth with most of the damage induced at the Bragg peak of energy deposition. It is impossible to extract any useful macroscopic mechanical properties from the ion or proton irradiated depths for design purposes [125]. The third difference is the transmutation rates and products are different. The fourth difference is the damage dose rate is on orders of magnitude. (neutron dpa/s ranges from

$10^{-6} - 10^{-8}$ and ion dpa/s ranges from $10^{-2} - 10^{-5}$).

Protons are extensively used in materials development as a surrogate for neutron damage [40, 83, 126–131] with limited success [106, 127, 131]. It has been shown that neutron PKA energy is clearly higher than proton PKA [132], which dictates the formation of damage cascades. Souidi et al. (2011) [133] have shown that cluster size distribution at 0.1 dpa (low dose) was virtually independent of the cascade energy. This suggests that the energy-dependent phenomena, such as sub-cascade formation, spatial extension, radial pair correlation functions do not influence the long-term cluster evolution. Therefore, it is these studies that have provided the basis for exploring whether proton irradiation could become a surrogate for neutron irradiation.

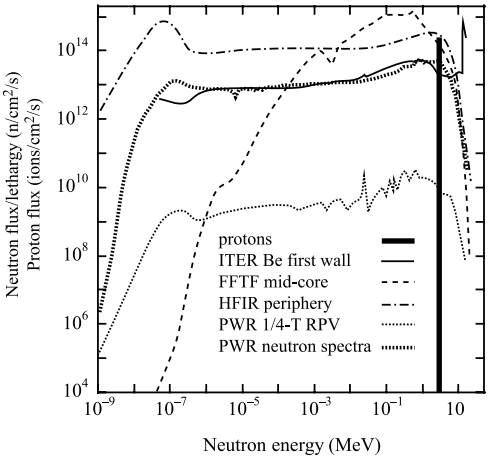

Figure 2.2.7: The energy spectra of neutrons from various reactor types and spectra of a mono-energetic proton beam Reproduced with permission from Ref. [16].

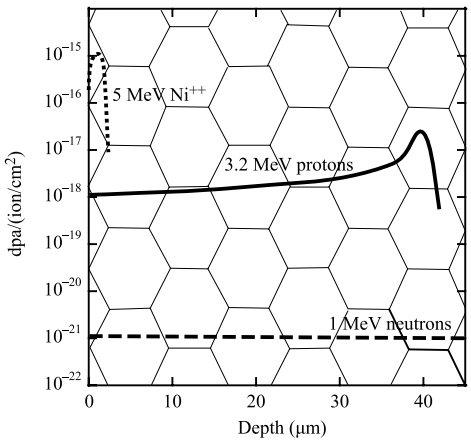

Figure 2.2.8: The damage profile of 1 MeV neutrons, 5 MeV Ni^{++} and 3.2 MeV protons in stainless steel. The Bragg peak for proton irradiation can be seen at the end of the penetration path ($\sim$ 40 μm). There is a superimposed 10 μm grain structure to give a sense of scale. Reproduced with permission from Ref. [124].

Heavy ions (normally self-ions, which, for example, would be Fe ions for a Fe matrix) are used to minimise chemical and compositional changes, high dose rates, and high damage in an efficient amount of time. Heavy ions have typical energies within the MeV range, which have been shown to have similar damage cascades with

neutrons [134]. However, the penetration depth is very shallow (typically between 200 nm – 2 μm, as shown in figure 2.2.8), which limits the volume of the effective damaged region. A significant consequence of high dose rates is that they produce a large temperature and dose rate shift along the penetration depth. It has been shown that void swelling has been suppressed at the Bragg peak and not at the initial damage dose near the surface [131, 135]. This is highlighted clearly in figure 2.2.10. The injected interstitials are in excess compared to vacancy production [135].

Was et al. (2002) [127] thoroughly investigated whether proton irradiation can actually emulate neutron irradiation effects, such as RIS. The authors showed direct comparisons between the same alloy heats (i.e neutron irradiation at 275°C and proton irradiation at 360°C); this is important to note on alloys, as it eliminates potential sources of discrepancy between heats. The shift in temperature was used to increase diffusion of solute elements. Dislocation loop size distributions and number density were in agreement with both irradiation types on 304 and 316 austenitic stainless steels. Grain boundary segregation (Cr, Ni, Si, and Mo) agreed well for both distances and percentage trends, as shown in figure 2.2.9.

Nonetheless, ion irradiation cannot emulate transmutation effects, especially within fusion reactors [76, 77, 109, 137], which is critical for the plasma-facing components [138–140]. Furthermore, ion irradiation cannot produce in-situ gas production, such as alpha emission from neutron capture, thus researchers have irradiated materials with ion and helium beams to simulate these effects [141]. It is evident that modelling neutron irradiation with ions will not be sufficient to provide realistic data in material properties and, more importantly, provide solid evidence to the nuclear regulators, which they ultimately determine whether the material could be safely used in a nuclear environment. Despite this, ion irradiation can provide a valuable insight and screening process for new materials (i.e. if they perform unsatisfactorily once ion irradiated, it can be safely assumed that the material will not perform satisfactorily under neutron irradiation [142]).

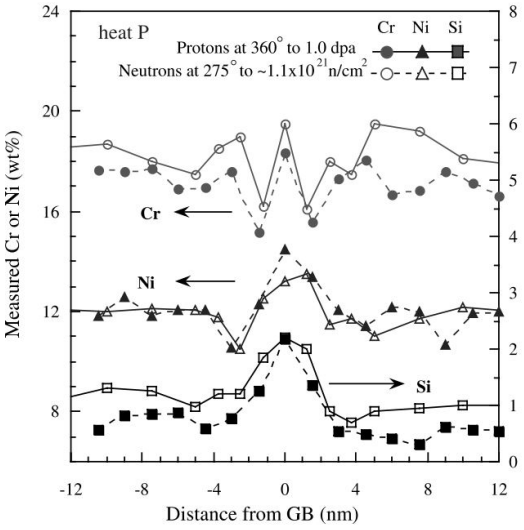

Figure 2.2.9: A direct comparison of radiation-induced segregation in Cr, Ni and Si in 316 stainless steel following an irradiation of 1.0 dpa with both protons and neutrons. Reproduced with permission from Ref. [127].

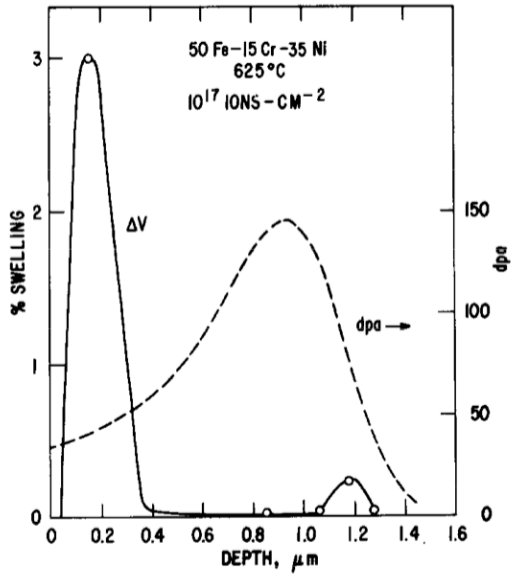

Figure 2.2.10: The swelling as a function of depth for Fe-15Cr-35Ni steel irradiated with Ni ions at 625 °C. The dotted profile is the dpa damage as a function of depth for comparison. It is clear that void formation is suppressed with heavy ions beyond the surface layer to the Bragg peak [136].

The use of ions to study radiation damage has received a significant amount of attention since the 1990s [142]. The main reason behind this was due to the US and UK shutting down their fast breeder test reactors so access to neutron sources was hard to come by. The academic debate for using ions as a surrogate for neutron irradiation has yet to be resolved [106, 122, 142]. To-date, no strong evidence has been provided which suggests that neutron irradiation could be replaced by any other technique [142].

2.3 Structural Materials Selection for Reactor Cores

The structural materials selection must not only consider the material properties, but also the overall system parameters of reactor cores [42, 71]. These parameters could

impact the acceptability and performance limits of the material (e.g. materials surpass the acceptable limit for radioactivity after use [109, 137]). Advanced materials can improve reactor performance via increased safety margins and design flexibility, in particular by increasing the tensile strength [64, 73], thermal creep resistance [64, 143], and superior neutron radiation damage resistance [44]. A balance must be obtained between the maturity of the material (standardisations, history etc.), safety margins, functionality, material properties, and consideration of the knowledge gaps [42].

Nuclear structural materials have both general and nuclear properties. These properties are:

- **General Properties:** factors such as mechanical strength, ductility, dimensional stability, fabricability, fracture toughness, cost, availability, heat transfer, etc.
- **Nuclear Properties:** factors such as neutron absorption, moderation and reflectivity characteristics, susceptibility to induced radioactivity, resistance to radiation damage, helium embrittlement, swelling etc.

Further the selection must also include specific parameters for fusion (if applicable):

- Tritium breeding performance [62];
- Neutron multiplier performance [54];
- Plasma facing, such as sputtering properties [138];
- Ferromagnetic behaviour for MCF [144];
- Residual activation [109, 137, 145].

This selection criteria does not consider every component; however, it provides a clear list of requirements that need to be considered when selecting a material in both Generation IV fission and fusion reactors.

In addition, there are two main nuclear design codes for Generation IV fission and fusion that will used for the construction of components for nuclear power plants. These are:

- American Society of Mechanical Engineers (ASME) Boiler and Pressure Vessel Code (BPVC) Section III Division 5 'High Temperature Reactors' [73] design code for Generation IV fission reactors, and is discussed in section 2.4.2.
- ASME BPVC Section III Division 4 'Fusion Energy Devices' [146] is under development.
- AFCEN (French) RCC-MRx 'Design and Construction Rules for Mechanical Components in high-temperature structures, experimental reactors and fusion reactors' nuclear design code [147].

The purpose of these codes is to establish national or international standards that consist of a set of rules based on state-of-the-art knowledge, experience and experimental feedback from nuclear facilities. The codes provide the bridge between different suppliers, participants, researchers, designers, manufacturers and regulators.

For a nuclear environment, steels can be segregated into two strands:

- Austenitic steels, which have a face-centred cubic (fcc) crystal structure at operating temperatures.
- Ferritic-martensitic steels, which have a body-centred cubic (bcc) crystal structure at operating temperatures.

2.3.1 Austenitic Stainless Steels

For any nuclear environment, steels are the chosen material for the pipework, reactor core structure, reactor pressure vessel (RPV) and all other major components [64]. For a fusion environment, steels are the primary candidate for the structural components (divertor, first wall, breeder blankets), cryostat, auxiliary systems, and robotics [148].

The major disadvantage when using austenitic stainless steels is that they are inherently susceptible to radiation-induced swelling, as discussed in section 2.2.6. The swelling of austenitic stainless steels is a showstopper (within the 450 – 600 ° [149]) when considering them as structural components for use within Generation IV fission and fusion reactors as these reactors will experience radiation damage beyond 30 dpa [38]. These factors indicates that these austenitic stainless steels life-limiting factor to be swelling.

2.3.2 Ferritic-Martensitic Steels

Ferritic-martensitic steels are based on 9-12 wt% Cr and were developed in the 1930s for use in the petrochemical industry, later gas turbines, and conventional fossil fuel plants [38]. After the discovery of radiation-induced swelling in the 1960s [34], ferritic-martensitic steels were chosen to replace austenitic stainless steel in the US fast breeder programme in the 1970s [150].

Ferritic-martensitic 9–12 %Cr steels have been shown to have excellent resistance to void swelling [34], high thermal conductivity [73], and high fracture toughness [42]. It is these properties which enable the material to become prime candidates for fuel cladding, reactor core internals, and pipework for lead-cooled fast reactors, SFRs and molten salt reactors [32, 38], and structural materials for fusion reactors [148].

As mentioned in Chapter 1 Section 1.1.3, novel SFR concepts are designed to operate at elevated temperatures (> 600 – 650 °C). During the 1970s, SFR fuel cladding

was generally constructed out of austenitic stainless steels [37], however these steels are prone to void swelling. For the US SRF programme (namely the Fast Flux Test Reactor (FFTF)), the fuel cladding and surrounding reactor core materials was chosen to be Sandvik HT9 ferritic 12Cr % steel [38] (see Table 2.3.1 for composition comparisons).

HT9 steel was designed for the petrochemical industry in the 1960s with a maximum operating temperature of 550 °C and is considered to be a first-generation structural steels. However, the reactor conditions (>450 – 500°C, 10 – 50 dpa, 100 – 150 MPa internal pressure due to fission gas products) require the cladding to be thicker or the gas plenum enlarged (to lower the internal pressure [119]). These are undesirables as they reduce neutron population within the core and therefore a larger enrichment of the fuel is required.

The desire to increase operating temperatures paved the way for second generation structural steels to be produced and codified against ASTM standards [151, 152]. The most developed steel in this category is the Grade 91 ferritic-martensitic steel. This steel was developed as part of the advanced creep resistant alloys for the US fast breeder program [153]. Niobium was added to produce strong carbides and nitrides to increase the creep rupture life at 600 °C to 100 MPa from 60 MPa [38].

In addition to this steel, low-activation steels are being developed for fusion energy. The overarching goal for low-activation steels is to build fusion energy with materials that either do not activate or, if activated, produce low-level radioactivity that can be handled after 100 years of a reactor shutting down [109, 145, 154]. EUROFER is being developed by the Eurofusion programme [155, 156] and F82H [156] is the equivalent low-activation steel undergoing development in Japan. The compositions are listed in table 2.3.1. However, recent neutronic activation studies have revealed that these low-activation steels might not meet the low-activation criteria [137].

The creep rupture lifetimes of these steels are displayed in figure 2.3.1. It is

Table 2.3.1: Comparison between the compositions of structural steels for use in Generation IV and fusion reactors in wt%. T91 is also known as ASTM A213 or Mod 9Cr-1Mo.

	COMPOSITION (wt%)											
Steel	C	Si	Mn	Cr	Ni	Mo	W	V	Nb	B	N	Other
HT9	0.2	0.4	0.6	12.0	0.5	1.0	0.5	0.25	–	–	–	–
T91	0.1	0.4	0.4	9.0	0.1	1.0	–	0.2	0.08		0.07	–
T92 (NF616)	0.07	0.06	0.45	9.0	0.25	0.5	1.8	0.2	0.05	0.004	0.06	–
EUROFER	0.11	0.05	0.5	8.5	–	–	1.0	0.25	–	0.005	–	0.08 Ta
F82H	0.1	0.2	0.5	8.0	–	–	2.0	0.2	–	0.003	–	0.04 Ta

clear that T91 (Mod 9Cr-1Mo) has better mechanical properties at 650 °C compared to the fusion steels and HT9. Further, figure 2.3.2 provides a comparison of creep rupture strength at 100,000 hrs. It should be noted that a Generation III structural material called NF616 (also known as T92) with improved high temperature strength and increased creep rupture times [38], however, the candidacy as a Generation IV structural material has been curtailed somewhat due to the addition of boron (neutron absorber).

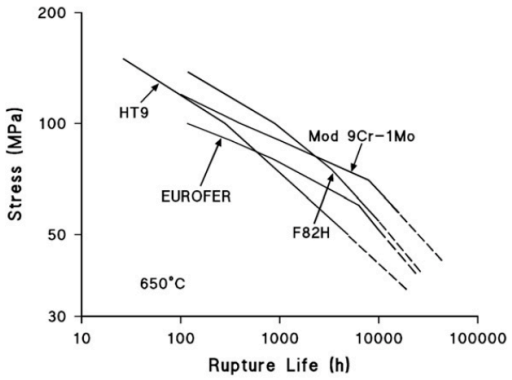

Figure 2.3.1: A direct comparison between creep rupture curves at 650 °C of EUROFER, F82H, HT9 and T91 (Mod 9Cr-1Mo). Reproduced with permission from Klueh et al. (2007) [38].

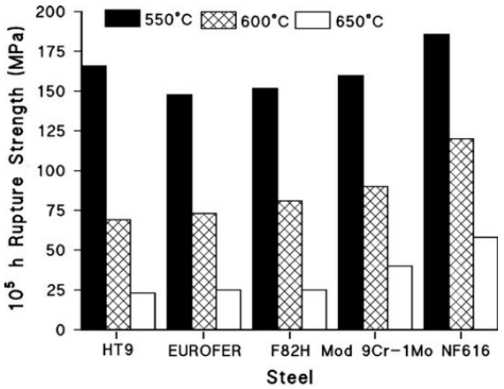

Figure 2.3.2: A direct comparison of the 100,000 hr rupture strengths between EUROFER, HT9, F82H, T91 (Mod 9Cr-1Mo) and NF616 (T92). Reproduced with permission from Klueh et al. (2007) [38].

2.4 Grade 91 (T91) Ferritic-Martensitic Steel

Grade 91 steel is a ferritic-martensitic steel with excellent high temperature strength, good thermal conductivity, and low thermal expansion. The ASTM Grade 91 ferritic-martensitic steel is commonly known by its form names: T91 [151], F91 [152], P91 [157], where T, F, and P indicate tube, forge and pipe form, respectively, or Grade 91 for pressure vessel steel. The differences between these forms is manufacturing method only (composition is the same). Other names that have been used are Mod 9Cr-1Mo (United States), 9Cr-1Mo-1V within the ASME BPVC code and 1.4903 X10CrMoVNb9-1 (Europe).

Grade 91 (referred to hereafter as T91) steel is a candidate for major structural component material of sodium [42], lead/lead-bismuth [158] and molten-salt cooled reactors, and could be a candidate for structural components (first-wall, divertor and breeder blanket structural supports) for fusion power reactors [148]. The attractive properties of T91 steel for these applications are: a) excellent swelling resistance [34, 38]; b) high thermal conductivity; c) existing supply chain due to the steels use in boiler tubes, heat exchangers and piping [159] and; d) both ASME BPVC Section III Division 5 [73] and French RCC-MRx nuclear code qualified [147]. T91 steel could become a suitable candidate for fusion reactors, as it possesses the required mechanical properties for the breeder blanket and divertor, neutron irradiation history [34, 42, 160–166], nuclear code qualification, and exhibits superior high temperature creep resistance (10^5 hr creep rupture strength is 160MPa at 550 ° C) when compared to EUROFER97 (10^5 hr creep rupture strength is 125 MPa at 550 °C) and F82H (10^5 hr creep rupture strength is 140 MPa at 550 °C) reduced-activation ferritic-martensitic steels [44]. However, T91 does not meet a ‘reduced-activation’ criterion [145] because the long-lived isotopes that are generated by the transmutation of niobium, molybdenum and nitrogen alloying additions [109, 137].

T91 steel was originally designed for the Clinch River Breeder Reactor Project

in the 1970s. The development was between Combustion Engineering Inc. and Oak Ridge National Laboratory [167]. Its mechanical and thermal properties make it an excellent potential material for sodium heat exchangers, and it is one of the most intensively studied steels in boiler service [168]. The material is considered as the 'Generation II' ferritic-martensitic steel [38].

2.4.1 ASTM T91 Standard

For the steel to be legally called T91 steel, it must meet the composition, manufacturing and form factors defined within the ASTM International A213 standard [151]. If the material does not meet this standard, it will not be considered nuclear-grade or nuclear code qualified. The size requirements are as follows: 3.2 mm $< d <$ 127 mm and 0.4 mm $< t <$ 12.7 mm; where d is the diameter and t is thickness of the tube. The manufacturing route is as follows and it must meet the conditions listed:

- The steel is fully austenitised between 1040 – 1080 °C and allows for vanadium and niobium carbides/nitrides to form.
- The steel is then air-cooled below 204 °C to transform it to martensite.
- The steel is reheated between 730 – 800 °C to allow for the formation of large $M_{23}C_6$ precipitates. These type of steels are over aged to allow the steels to operate for long times at high temperatures.
- The steel is then air cooled to room temperature.

The composition must be within the range defined in the ASTM International A213 standard [151], as defined in Table 2.3.1.

2.4.2 ASME BPVC Section III Division 5

T91/F91/P91/Grade 91 steel is nuclear code qualified in the ASME BPVC Section III Division 5 'High Temperature Reactors' [73] and the French RCC-MRx design

code [147]. The ASME BPVC nuclear code has seen the most development for T91 steel and has a mandatory use within the USA and Canada [169]. Section III Division 5 applies to nuclear installations when a ferritic-martensitic steel is at or above 370 °C. A Class A component is defined as any component within the reactor pressure boundary and a Class B component is defined as any component outside the reactor pressure boundary. It should be noted that the US Nuclear Regulatory Commission require the use of ASME nuclear design code for any nuclear reactor construction on US soil [170].

2.4.3 General Microstructure Properties of T91 Steel

The microstructure of T91 steel underpins the performance of the material at high temperatures. Thus, it is important to understand the basic ferritic-martensitic microstructure that this steel possesses. The following features of the microstructure enable T91 steel to have good high temperature properties and are as follows:

- A high number density of $M_{23}C_6$ carbides, 'M' stands for Cr and/or Mo. These carbides are $\sim$ 200 nm in diameter [130].
- A high number density of MX particles, where 'M' stands for V or Nb and 'X' stands for C or N. These MX particles are $\sim$30 – 50 nm in diameter [38].

A schematic of the ferritic-martensitic microstructure can be found in figure 2.4.1.

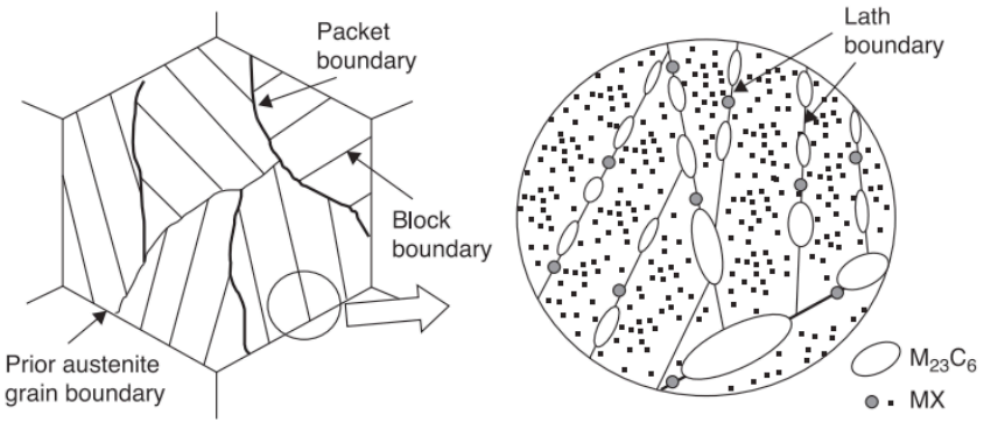

Figure 2.4.1: A schematic of the ferritic-martensitic microstructure. Reproduced with permission from Abe (2006) [171]

2.4.4 Neutron Irradiated T91 Steel

It should be noted that the author of this thesis provided scientific advice on the use of T91 steel for use in a nuclear reactor core to the UK's Office for Nuclear Regulation, and has been published in Ref. [42]. This section will provide an overview of the published work.

As outlined in section 2.2, high energy neutrons generated in a fast reactor will displace the lattice atoms within the structural materials. Interstitials and vacancies form, which is represented in the dpa term that affects the microstructure and mechanical properties. The properties change due to the agglomeration of these vacancies and interstitials, which ultimately embrittle and swell materials. In addition, these point defects enhance alloying element diffusion creating radiation-induced segregation and precipitation.

T91 steel has yet to be used as a component within nuclear reactor cores, thus the operational experience is limited. The majority of T91 steel irradiation experience is due to it being irradiated in the BOR-60, FFTF, ATR, and EBR-II reactors as test specimens [34, 42, 85, 86, 130, 160–166]. T. P. Davis' (2018) [42] Office for Nuclear Regulation report summaries the neutron irradiation properties of T91 steel for use

as a SFR fuel cladding material. This section will briefly cover the effect of neutron and ion irradiation on T91 steel properties. However, detailed microstructure changes will be discussed in research Chapters 4 and 5.

2.4.4.1 Mechanical Properties

T91 exhibits typical mechanical properties for a ferritic-martensitic steel in the unirradiated conditions. These typical values are as follows: the tensile strength is a minimum of 585 MPa, the yield strength is a minimum of 415 MPa, the elongation at 50 mm is 20%, and the hardness should be around 265 HV, as specified by the ASTM A213 standard [151]. Under irradiation, the yield strength increases due to radiation induced hardening [164] and ductility decreases due to radiation-induced microstructural changes [160] as a function of irradiation temperature [172].

Neutron irradiation produces point defects within the material's lattice, as discussed in section 2.2. These point defects form dislocation loops and voids as a function of temperature. All steels embrittle below $\sim$ 450°C due to the precipitation of nanoclusters and segregation of alloying (or trace) elements [16]. The embrittlement is a result of the microstructure dislocations becoming pinned on the radiation-induced features, such as Mn-Ni-Si precipitates (MNSP) [164, 165, 173–179] (often described as 'G-phase' – $Mn_6Ni_{16}Si_7$ [180]). However, above 500 °C the nanoclusters generally dissolve back into the matrix [181] and vacancies have the energy to diffuse and annihilate with interstitial atoms. This is called radiation-softening in T91 steel [38]. Charpy impact testing is used to determine the shift in ductile-to-brittle transition temperature (DBTT) [182, 183]. The DBTT is important as the component could become brittle under the operating conditions.

The change in yield stress, DBTT, fracture toughness and swelling are found in figures 2.4.2, 2.4.3, 2.4.4 and 2.4.5, respectively.

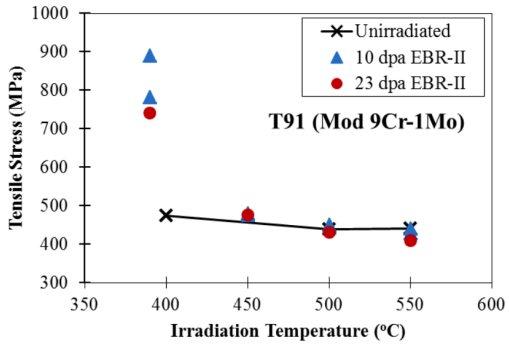

Figure 2.4.2: The yield stress (tensile stress) as a function of irradiation temperature for T91 steel. Below 450 °C, steels are known to embrittle, whereas above this temperature the alloy tends to soften. Collection of data presented in Ref. [42].

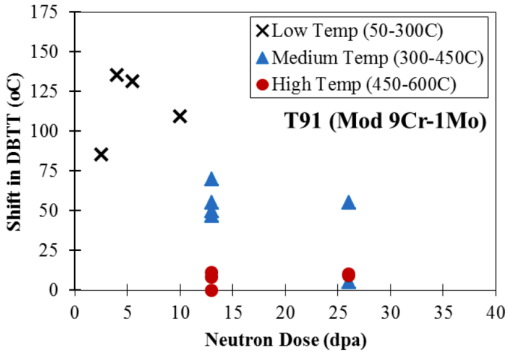

Figure 2.4.3: The shift in DBTT temperature for T91 steel as a function of irradiation dose. The red data points show little or no shift in DBTT. Collection of data presented in Ref. [42].

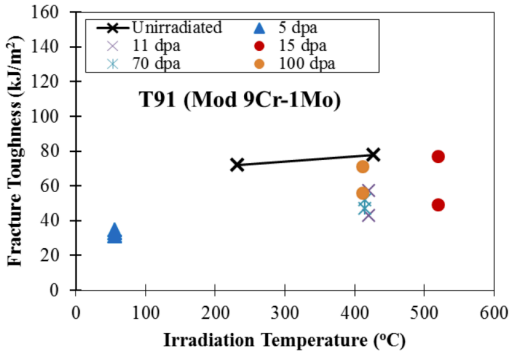

Figure 2.4.4: The fracture toughness of T91 steel as a function of irradiation dose and temperature. Collection of data presented in Ref. [42].

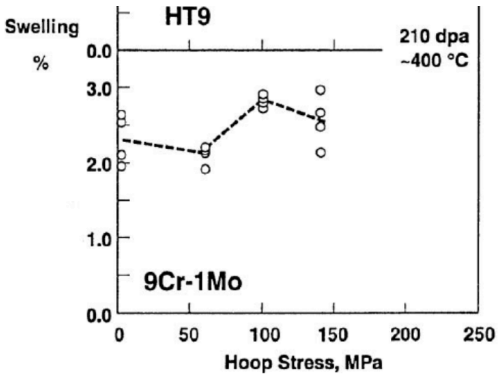

Figure 2.4.5: The swelling (%) of T91 steel (9Cr-1Mo) as a hoop stress tested at 400 °C and up to 208 dpa in the FFTF reactor. Reproduced with permission from Toloczko et al. (1994) [34].

2.4.4.2 Radiation-Induced Segregation

RIS of solute additions (Si, Mn, Ni, Cr, Cu, P) in ferritic-martensitic steels is an expected feature of radiation damage [9, 30, 44, 173, 178, 179, 184]. It is well known that chromium (Cr) segregates under heavy irradiation doses [130, 177, 185–187] which enriches the level of Cr above the solubility of Cr in Fe producing the α' phase

(face-centred-cubic (fcc)) [187, 188]. Further, many studies have reported the observation of G-phase [130], M_6C [189], and χ [164] phases as a result of neutron irradiation [177, 190].

Lu et al. [184] compiled and reviewed the literature on RIS and found conflicting results on the segregation of Cr under irradiating conditions; out of the total 15 experiments, 8 of which displayed grain boundary Cr enrichment and 7 displayed Cr depletion. The major discrepancy between these 15 studies derives from wide ranging the irradiation conditions (dose, dose rate, temperature, and ion), in fact no two data points were taken under the same conditions. It is clear that a systematic study of irradiation damage is required to understand and ultimately predict the effect of irradiation.

Wharry et al. [70] pursued this by producing a systematic RIS study in T91 steel. The authors studied 2 MeV proton irradiated T91 steel at 400 °C and 500 °C with a dose rate of 1.3 $\times 10^{-5}$ dpa/s. RIS at prior austenite grain boundaries (PAGB) was analysed with both TEM and APT. Cr, Ni and Si segregated to PAGBs and was found to saturate above 3 dpa, which is consistent with neutron irradiated ferritic-martensitic steels [191]. It was found that radiation induced hardening was primarily caused by the formation of MNSP. This is one of the first systematic approaches to determining the effect of RIS however, no attempt was made to compare it against neutron irradiation experiments.

Below 500 °C, Cr is known to segregate beyond the solid solution in Fe and precipitates to form a Cr-rich α' phase under irradiation [130, 185–187, 192]. α' has been observed under neutron irradiation where the dose rate is low (10^{-7} dpa/s). This phase is known to embrittle these steels [193]. Tissot et al (2017) [188] first claimed to observe α' formation after heavy ion irradiation. The injected interstitials could play a role in suppressing the formation of α' phase. Further, the authors determined that multi-step ion irradiation to reach high doses is not recommended as the technique suppresses α' formation.

It has also been shown that the carbides ($M_{23}C_6$) and MX particles coarsen at both high temperatures and under irradiating conditions [38, 130]. Further literature review and research conducted on RIS and RIP can be found in Chapter 4 and Chapter 5.

2.4.5 Summary of T91 Steel

T91 steel is a candidate for the SFR's fuel cladding material but there are outstanding knowledge gaps that inhibit the use today [42]. T91 steel has physical limitations due to the ferritic-martensitic matrix, which are:

- Above > 700 °C, the material will fail due to plastic deformation at low stresses of 10 MPa in under 1000 hours [38, 73]. This is due to the failure of the iron ferritic-martensitic matrix.
- When T91 steel is exposed to low temperatures (<100 °C), it could fail by brittle fracture when damaged by neutrons [42]. At these temperatures, the structural integrity of the fuel cladding will no longer meet the safety requirements of the reactor.

These intrinsic limitations present the need for a new type of steel to meet the demands of SFRs. These steels need to withstand very high doses (>100 dpa) at high temperatures (550 – 700 °C) and produce an insignificant degree of swelling. The most promising approach is based on using powder metallurgy to produce high strength, radiation resistant oxide dispersion strengthened (ODS) steels [44]. The next section will discuss this new branch of steels.

2.5 Oxide Dispersion Strengthened Steels

It should be noted that the author provided scientific advice on the use of ODS steels in nuclear reactor cores to the UK's Office for Nuclear Regulation, and has been published in Ref. [42]. This section will provide an overview of the published work.

The very first design procedure to reduce the effect of radiation damage on materials was to introduce cold-work in type 304 stainless steel to reduce swelling in the 1970s [194]. The process of cold-work introduces large dislocation densities compared to the annealed condition that provides increased trapping sites which delays the onset of void swelling. However, after approximately 1 dpa the dislocation densities in cold-worked austenitic steels generally relax and tend towards the void swelling values observed in non-cold-worked conditions [195]. Thus, cold-work addition to the treatment provides only a temporary engineered radiation resistance rather than a permanent solution to the challenging phenomenon. The main approach to design radiation-resistant materials is by engineering in high sink strength properties with the introduction of high density recombination centres for point defects (i.e. point defect sinks, such as grain boundaries and stable nanosized precipitation) [44].

It is the third approach that ODS steels use to resist radiation damage by promoting a high density recombination centres through the creation of nm-scale precipitates that are stable under high temperatures and neutron irradiation [41, 196–199]. The most common nm-scale precipitates include the elements Y, Ti, and O [199].

2.5.1 Introduction

ODS steels that contain 12-16 %wt Cr typically have high tensile strength, high creep resistance, and high fatigue strengths over a large operational temperature range [200]. They also have long-term thermal stability up to 900 °C [201] and high radiation damage tolerance (such as resistance to helium embrittlement [202]). The maximum operating temperatures are limited to the Cr concentration [41] within the

alloy; ODS steels that have 14% Cr are considered to operate between 650-850 °C, whereas 9% Cr is considered to operate between 550-650 °C. The increase in Cr provides a higher density of $M_{23}C_6$ carbides, which improve the high temperature operation window.

These properties generally derive from the inclusion of a small volume fraction (between 0.25–0.5 %) of Y_2O_3, which has an extremely high number density (5×10^{23} m^{-3}) with an average diameter between 2–8 nm [45, 196, 198, 203, 204]. These nanoscale particles are generally yttrium-titanium-oxygen ($Y_2Ti_2O_7$) pyrochlores. These Y-Ti-O nanoclusters are highly stable under extreme operating conditions, are chemically inert and resistant up to 900 °C [45], and oxide particles act as recombination points for the vacancies and interstitials generated by irradiation [44]. These steels have been described as radiation resistant [44, 45, 205].

ODS steels are the prime candidates for being the fuel cladding of SFRs and fusion structural materials [30, 41]. However, fabrication of these steels is extremely difficult due to yttrium being virtually insoluble in iron [206] (indicating that the traditional melting and forging processes are incompatible). Therefore, the only method at present to manufacture these steels is by powder processing and either by hot isostatic pressing (HIP) or through the field assisted sintering technique (FAST) (which is also known as Spark Plasma Sintering (SPS)) [207–209].

The challenges of developing ODS steels remain significant [210]. The challenges arise in the technological areas of joining, welding, uniformity, fabricability and scaling it up to the industrial production scale [42, 45, 199].

2.5.2 ODS Steel Fabrication Methods

Benjamin (1971) [211] first developed the process of mechanically alloying materials. Originally, the method added Ti, Mo and Y [210, 212] to increase the yield strength. The US breeder reactor program accelerated the development of these steels. It was found by adding titanium to the powder that it produced finer Y-Ti-O particles [213],

and Hf and Zr were found to further refine the size [214]. Due to the immiscibility of yttrium in iron [206], it is not possible to produce yttrium-containing steels via the traditional manufacturing routes so instead Y is mechanically introduced to the iron matrix. A typical ODS steels composition is found in Table 2.5.1, with W added for solid solution strengthening, Mn, Al and Si are impurities introduced by the mechanical milling process, and C is provided for Ti carbide formation.

The typical manufacturing method of ODS is as follows [203, 212]:

1. Produce the base alloy material in the form of a fine powder [210];
2. Mechanically mix yttrium oxide (Y_2O_3) powder with the fine alloying powder. Generally ball mill the combined powder up to 40 hr reduce the average particle size. This milling process is conducted under an inert atmosphere to reduce internal oxidation. Mechanically milling provides plastic deformation into the powder. Recent research indicates the atmosphere optimal composition should be either He or H [215];
3. 'Can' the powder and degas in a vacuum chamber;
4. HIP the can between 900 – 1300 °C and 100 – 200 MPa for 4 hours [210, 216].

HIPing is the most common method to produce ODS steel [210]. However, there are major scalability due to the small mechanically milled batch ($\approx$ kg) scale and high cost issues along with only producing simple geometries [44, 45] and thus possible unsuitability for industrialisation. Secondly, there is a current lack of industrial partners that could help speed up the process of manufacturing. Zoz Group in Germany have started a research project that investigates the scale-up of ODS steel manufacturing to the tonnage level [217]. Indira Gandhi Centre for Atomic Research, India, has also been developing the upscale of ODS steels [218].

FAST is an upcoming alternative method to manufacture ODS steel. The advantage is that sintering only takes 4 – 5 minutes rather than 4 hours at a high temperature

using the HIPing method (less time indicates a quicker batch process and possibly cheaper). The base alloy powder is gas atomised with pure Y. A sacrificial oxide, normally Fe_3O_4, is mechanically milled with the gas-atomised powder. It should be noted that vanadium oxide has proven to have advantages over Fe_3O_4 [219]. The powder is then packed into a graphite die. The die is then held under uniaxial pressure with a 1000 – 5000 A (electrical current) passed through the sample [208, 220]. The ohmic heating is enough to fully sinter the powder into a solid body within 5 minutes. The typical cooling rates are 2000 °C/min to achieve theoretical density [220].

Table 2.5.1: A typical ODS Steel composition, 14YWT (where Y, W and T reference yttrium, tungsten and titanium, with 14 referring to the Cr wt%). Composition taken from ref. [221].

COMPOSITION (wt%)									
Alloy	Cr	Mn	C	Ti	W	Y_2O_3	Al	Si	Fe
14YWT	13.34	0.33	0.09	0.21	2.66	0.3	0.11	0.18	Bal.

Producing ODS in raw billet form will be costly [45] and no single steel manufacturer in the world is producing this steel on a tonnage scale. The applications for this steel could expand into non-nuclear sectors, such as envisioning it being used as heat exchanger tubes in the petrochemical industry so they can run at higher temperatures to improve efficiencies. The manufacture scale up of this steel is possible and does produce a promising outlook [45] but does require further research and development.

2.5.3 Characterisation of the Microstructure

ODS steels are categorised by the amount of Cr: martensitic (body centre tetragonal (bct)) microstructure with 7-9 wt%Cr and fully ferritic bcc structure with 12-16 wt% Cr. By providing sufficient amounts of O and Ti during sintering, the Y_2O_3 will react and produce 2–8 nm diameter $Y_2Ti_2O_7$ pryochlore, Y_2TiO_5, or $YTiO_3$ [199, 204, 210, 216]. These Y-Ti-O particles have a fcc structure that is incoherent with the matrix,

as shown in figure 2.5.1. There is evidence that these Y-Ti-O particles have a core-shell of normally Cr [204]. The interfaces (see figure 2.5.1(d)) are coherent with the matrix and produce a significant amount of strain on the lattice.

The milling process introduces ultra-high dislocation densities. During sintering the pressure produced on the grain boundaries exceeds Zener pinning before the Y-Ti-O particles have fully consolidated. Thus, the grains which exceed the pinning force grow significantly and grains which are pinned grow insignificantly [222]. This scenario produces a bimodal grain structure, as shown in the 14YWT (Fe-14Cr-3W-0.2Ti-0.25Y_2O_3) electron backscatter detection (EBSD) map figure 2.5.2. The bimodality could become a drawback at high temperatures in terms of creep resistance. The non-uniformity of grains in ODS steels have been attributed to three effects:

1. By the non-uniform distribution of nano oxide Y-Ti-O particles [223];
2. By the inhomogeneous temperature distribution across the sample during sintering [207];
3. By the inhomogeneous dislocation density distribution across the powder after mechanically alloying it [224].

The consolidated Y-Ti-O particles produce high defect trap-sink strength, enhancing vacancy and interstitial diffusion, thus increasing the likelihood of recombination [30]. Y-Ti-O particles also stabilise the grain boundaries and trap helium nuclei (via transmutation). These features impact the mechanical properties of these steels allowing them to operate at higher temperatures, stresses, and dose (dpa) levels [45].

2.5.4 Mechanical properties

In general, ODS steels have a higher yield stress, higher creep resistance strength, poorer fracture toughness, reduced elongation properties, and a higher DBTT value compared to 9-12 % Cr ferritic-martensitic steels. In particular, ODS steels have

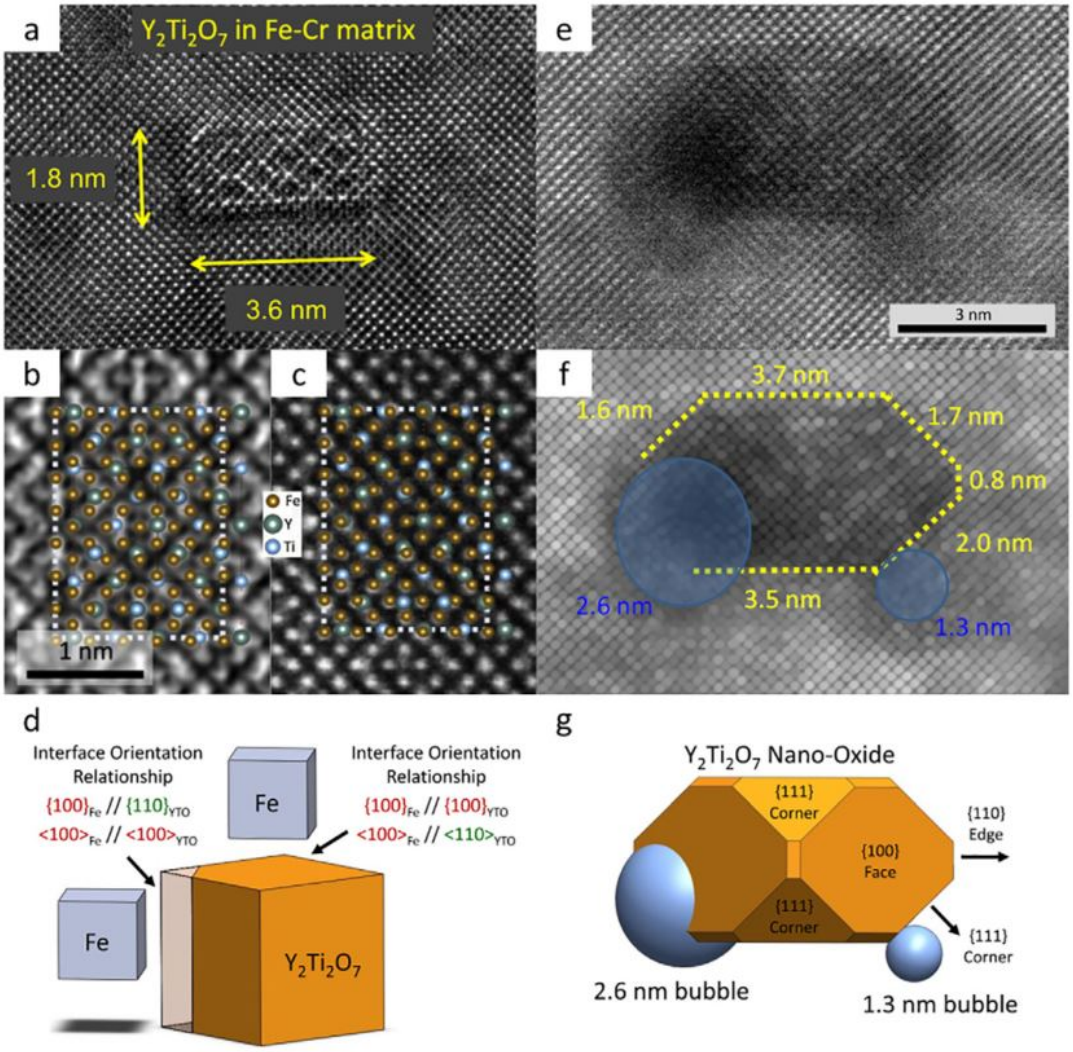

Figure 2.5.1: a) Transmission electron microscopy (TEM) micrograph of the $Y_2Ti_2O_7$ particles in a Fe-Cr matrix; b) Scanning TEM (STEM) showing the elemental distribution of these Y-Ti-O particles; c) pyrochlore structure shown using exit wave focal series images; d) description of the orientational relationship between the matrix and precipitate; e) actual and f) processed STEM images showing the dimensions of a pyrochlore; g) 3D representation of the STEM image f). Reproduced with permission from Wu et al. (2016) [204].

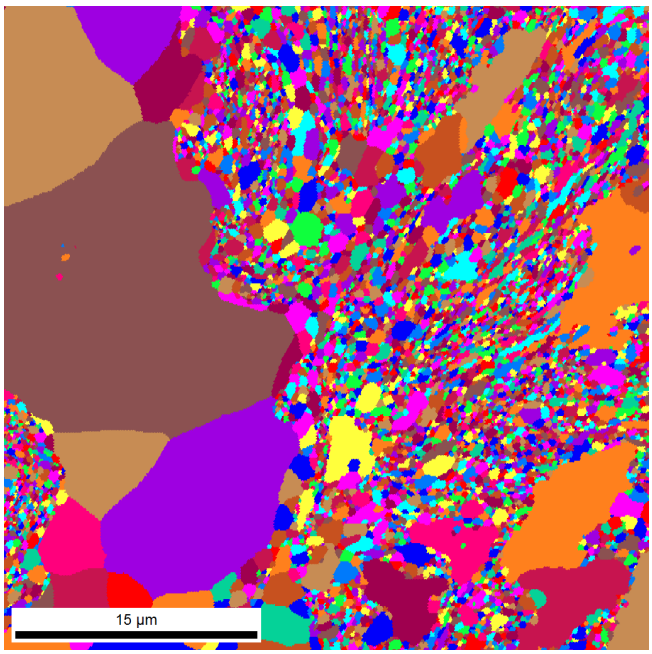

Figure 2.5.2: EBSD map of 14YWT (Fe-14Cr-3W-0.2Ti-0.25Y_2O_3) ODS alloy. The grain structure is bimodal. Reproduced with permission from C. Jones [221].

outperformed ferritic-martensitic steels by lasting longer (in hrs) at the same creep rupture stress (in MPa), as shown in figure 2.5.3. The fracture toughness of ODS steels are generally lower than ferritic-martensitic steels, as shown in figure 2.5.4, due to the high dislocation density and high nanosized precipitates density.

McClintock et al. (2009) [197] extensively studied the mechanical properties of both EUROFER (Fe-9Cr-1W-0.1C-0.2V), ODS-EUROFER (Fe-9Cr-1W-0.1C-0.2V-0.3Y_2O_3), 14WT (Fe-14Cr-3W-0.2Ti) and 14YWT (Fe-14Cr-3W-0.2Ti-0.25Y_2O_3) ODS alloy in both unirradiated and irradiated conditions. The authors used small sheet-type tensile specimens to determine the properties. There is a clear distinction between ODS and non-ODS material by their yield strength as a function of temperature, as shown in figure 2.5.5. Further, the elongation of these alloys is shown in figure 2.5.6. It is clear that ODS steel in the unirradiated condition has superior creep resistance and yield strength.

The inhomogeneity of Y-Ti-O particles [222] could impact predictability of the

steels performance [221]. There have been attempts made to quantify the heterogeneity of ODS steels by Czainski et al. (1994)[225]. However, the authors were unsuccessful in predicting the mechanical properties due to this heterogeneity in particle distribution. Further review into the inhomogeneity of ODS steels is the central focus of the study in Chapter 6.

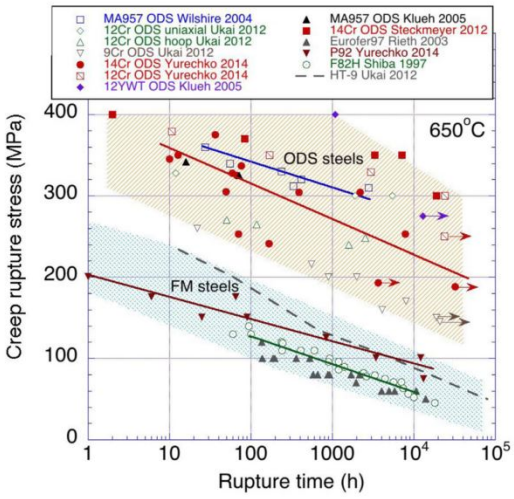

Figure 2.5.3: Creep behaviour of ferritic-martensitic steels and ODS steels at 650 °C. Reproduced with permission from Zinkle et al. [44].

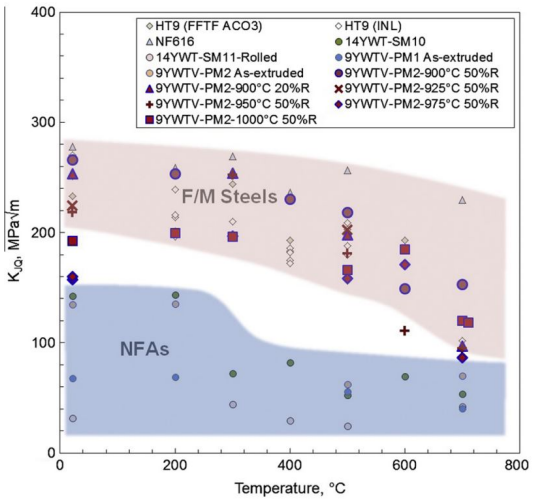

Figure 2.5.4: Temperature dependence of fracture toughness of both F/M steels and ODS (nanostructured ferritic alloys (NFAs)). Reproduced with permission from Byun et al. [226].

2.5.5 Effect of Neutron Irradiation

The promise of ODS steels is that they are radiation resistant due to the Y-Ti-O particles providing a high density of strong sinks.

McClintock et al. (2009) [197] neutron irradiated (1.5 dpa; 2.1 $\times 10^{21}$ n/cm^2 E$>$ 0.1 MeV) EUROFER, ODS-EUROFER, 14WT and 14YWT alloys, and compared their yield stress. The yield stress increased for EUROFER, ODS-EUROFER and 14YWT by 200 MPa and 14YWT increased by 100 MPa, as shown for EUROFER in figure 2.5.7 and ODS-EUROFER in figure 2.5.8. In addition, there was a loss of

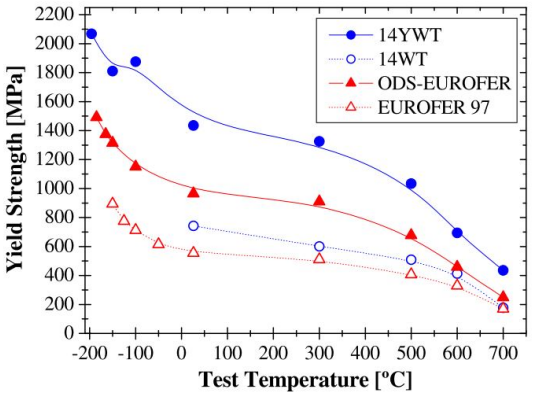

Figure 2.5.5: Yield strength as a function of temperature of unirradiated EUROFER, 14WT (non-ODS version of 14YWT without the Y_2O_3 powder milled) and 14YWT. Reproduced with permission from McClintock et al. [227].

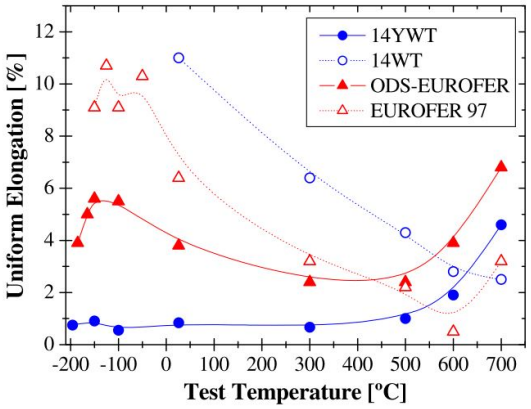

Figure 2.5.6: Uniform elongation as a function of temperature of unirradiated EUROFER, 14WT and 14YWT. Reproduced with permission from McClintock et al. [227].

ductility and fracture toughness. It should be noted that, as shown in figure 2.5.8, there was little change in the yield stress in the irradiated condition. It is this data that characterises the radiation resistance of these ODS steels.

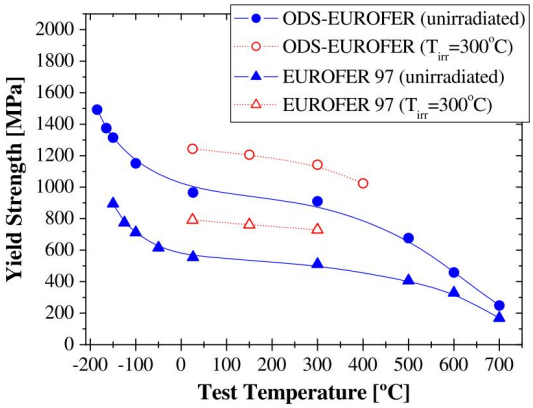

Figure 2.5.7: Yield strength as a function of temperature of neutron irradiated EUROFER and ODS-EUROFER steel to 1.5 dpa. Reproduced with permission from McClintock et al. [227].

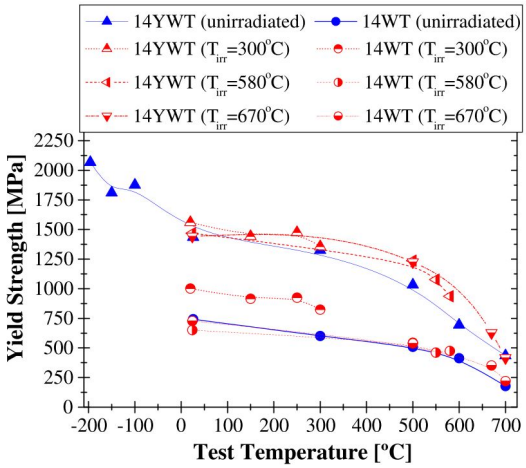

Figure 2.5.8: Yield strength as a function of temperature of neutron irradiated 14WT and 14YWT steel to 1.5 dpa Reproduced with permission from McClintock et al. [197].

The Y-Ti-O particle stability under high temperatures is not well understood [30, 44]. Yamashita et al. (2002) and (2004) [228, 229] reported that, after neutron irradiation, there was a loss of small (< 3nm) Y-Ti-O particles within the microstructure. On the contrary, Yamashita et al. (2007) [230] later reported that growth of the large particles from 75 to 85nm after neutron irradiation (JOYO reactor; 100 dpa up to 982 K) was observed and an increase in minimum particle size from 5.2 to 9.5 nm was detected. Furthermore, another study by Yamashita et al. (2013) [231] observed no change in Y-Ti-O particle size distribution from neutron irradiation to 30 dpa at 827 °C. The range in conclusions on the particle stability in ODS steels characterises the lack of solid understanding.

Further, ion irradiation of ODS steels have been conducted to determine the effects on the microstructure and mechanical properties. A square-root dependence for the Y-Ti-O particle size decrease with increasing ion dose was determined by Allen et al. (2005) [232], which is consistent with the ballistic mixing theory. However, later studies by Allen et al. (2008) [233] indicated that this square-root dependence was also a function of irradiation temperature.

One of the considerations in misunderstanding the particle size change is related to the limits of frequent TEM characterisation methods used in observing Y-Ti-O particles. Particles that are small (< 2nm) remain elusive in TEM images [44, 233], which can lead to inaccurate determinations of the change in nano size particles challenging. Atom probe tomography (APT) is capable of observing particles < 2nm at low and high doses. Thus, APT has shown promise in accurately determining the particle size distribution change as a function of irradiation [234–236]. The operational details of the APT method is found in chapter 3 section 3.1.

Jones (2016) [221] investigated the effect of nanoindentation hardness from proton irradiation in ODS steels. The author demonstrated that 14YWT ODS steels had a bimodal grain structure and bimodal nanohardness behaviour. The author ruled out that large precipitates (> 50 nm) was the cause of this bimodal hardness but failed

to determine what microstructural or metallurgical phenomena caused the bimodal properties.

An overarching issue within the ODS steel research community is there has been no consistency between ODS alloy batches (such as composition, manufacturing route, microstructure reproducibility); between all the literature reviewed in this section, not one ODS alloy was produced with the same parameters, method, and composition. By centralising on a ODS alloy composition and partnering with industry to manufacture these steels on a large scale, should begin a consistent and systematic supply of this material. It is this predictable, sustained supply of material that could accelerate the alloy system to be deployed in future SFRs and fusion reactors.

2.6 Summary of Knowledge Gaps

When T91 steel operates at low temperatures (300 – 400 °C) and is subjected to neutron irradiation, the material becomes embrittled. This embrittlement is caused by irradiation hardening primarily due to precipitation of supersaturated Cu impurities and/or Mn-Ni-Si solute atoms. However, detailed characterisation of these precipitates have not been conducted on neutron and ion irradiated T91 ferritic-martensitic steels at low (300 – 400 °C) temperatures.

For ODS steels, a bimodal grain structure after heat treatment and recrystallisation are a typical defining feature of ODS steels, comprising two distinctive regions of nanosized and microsized grain. Understanding and control of grain size bimodality, heterogeneity of the grain sizes and Y-Ti-O nanocluster densities are likely important characteristics in microstructure to control during the manufacture of these steels. Characterisation of the Y-Ti-O particles' influence on the deformation in ODS steels has not been conducted before. This type of study would provide an insight into the nature of these nano-sized particles on the deformation mechanics.

2.7 Thesis Theme and Objectives

The theme of this DPhil thesis is based on the role of precipitation, whether that is radiation-induced precipitation or oxide precipitation. The nucleation and evolution of the material's microstructure, and its effects on the mechanical properties by irradiation is important for the structural steels of reactor cores, as it determines the safety, structural integrity and allowable operational windows. This DPhil thesis will investigate the effect of neutron and ion irradiation on T91 steel's microstructure and mechanical properties and the microstructure of ODS steels. The detailed research chapters are as follows:

- Chapter 3 discusses the experimental methods that will be used within this thesis research.
- Chapter 4 discusses atom probe characterisation of segregation driven Cu and MNSP co-precipitation in neutron irradiated T91 ferritic-martensitic steel. The aim is to understand how neutron irradiation effects the microstructure, such as RIS and RIP, of candidate structural materials.
- Chapter 5 discusses nanocluster evolution and mechanical properties of ion irradiated T91 ferritic-martensitic steel. The aim is to understand the effect of low dose irradiation, and to investigate the usage of ion acceleration as a tool for understanding irradiation damage on the microstructure and mechanical properties.
- Chapter 6 discusses electron microscopy and atom probe tomography of nanoindentation deformation in oxide dispersion strengthened steels. The objective is to investigate heterogeneity of the Y-Ti-O particle distribution and its effect on the mechanical properties of ODS steels.

Chapter 3

Experimental Methods

This chapter will discuss the experimental methods used to conduct the studies within Chapters 4, 5, and 6. The three main techniques used for this thesis are: atom probe tomography (APT), electron backscatter diffraction (EBSD) ,and nanoindentation. Transmission electron microscopy (TEM) is discussed as the technique was applied by a collaborative researcher for the oxide dispersion strengthened steel research within Chapter 6 (details are provided within the chapter).

3.1 Atom Probe Tomography

APT is a technique combining a nanoscale position sensitive detector and a mass spectrometer, producing three-dimensional chemical mapping of the species' detected mass-to-charge-state ratio [237, 238]. The technique enables detailed analysis of 2D (interfaces) and 3D (precipitates) features in materials and is applied extensively in this thesis to study precipitates within materials. APT has a lateral spatial resolution of up to 0.2 nm [238], up to 0.06 nm depth spatial resolution [237], and 100 atomic parts per million sensitivity [239, 240]. Typical APT datasets acquired in this study have between 2 to 10 million ions, which can be reconstructed in 3D volumes that range from $25 \times 25 \times 75 \text{nm}^3$ to $150 \times 150 \times 500$ nm^3. The instrument used for

this project is the Local Electrode Atom Probe (LEAP) 5000XR® manufactured by CAMECA and located at the Department of Materials, University of Oxford, and LEAP 4000 HR® located at the Center for Advanced Energy Studies, Idaho National Laboratory.

3.1.1 Principles of Operation

Fundamentally, APT is based upon highly controlled field evaporation of ions from the apex of a needle-shaped materials specimen [237, 241]. APT is a destructive analysis technique which applies a high DC voltage to generate an intense electric field at the surface of a specimen, which is cryogenically cooled to between 30 – 60 K. The application of this DC voltage in combination with either a high voltage pulse or ultrashort laser pulse results in the ionization and removal of atoms from the tip. APT requires the material specimen to be very sharp with a tip apex of radius between 25 – 100 nm [238, 241]. Typical voltages applied to the APT samples (in high vacuum) ranged between 2 – 10 kV to generate an electric field at the apex. This electric field is defined as:

$$E_F = \frac{V}{k_f R} \tag{3.1.1}$$

where E_F is the electric field generated at the APT sample apex, V is the applied voltage, k_f is the geometric field factor (which is dependent on electrostatic environment including the specimen shape), and R is the radius of curvature at apex of the tip [237]. The strength of this electric field generated can lead to field evaporation of ions from the tip. Once evaporated, the (positively charged) ions accelerate towards the position sensitive detector that records both the ions' position and time-of-flight (TOF). This can be used to determine the mass-to-charge-state ratio of the ion. As the apex changes shape (i.e. R changes) due to the loss of ions, the voltage generally increases to maintain the required electric field at the apex, usually to enable a constant rate of field evaporation. A typical APT analysis will increase the applied DC voltage until either the sample fractures or a user-set voltage limit has been reached.

A highly simplified LEAP schematic is shown in figure 3.1.1.

The collection of this raw ion positional data from the detector must then be reversed-projected back to the ions original real space locations within the sample using an image reconstruction algorithm. The Integrated Visualisation & Analysis Software (IVAS) developed by CAMECA is used to reconstruct APT datasets [242, 243]. The detector position is used to calculate the original x and y coordinates from the apex and the z coordinate is based on the temporal order of ion detection combined with a geometrical correction [244]. Specifically, IVAS uses the reconstruction algorithms that is outlined in more detail by Gault et al. [243] and Geiser et al. [242].

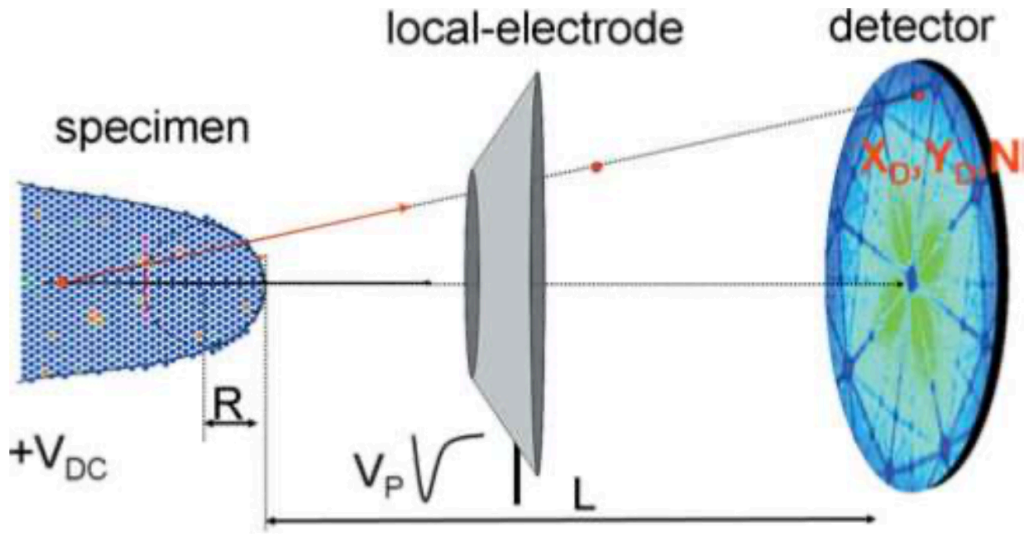

Figure 3.1.1: A typical LEAP schematic where X_D and Y_D are the coordinates of the ion which impacts on the position sensitive detector, N represents the atoms position within the detected atom sequence (not to scale). Reproduced with permission from Gault et al. (2010). [245].

3.1.2 Limitations and Artefacts of APT

The artefacts that arise from APT ultimately result in erroneous atomic positions within the reconstruction. Such artefacts and limitations arise due to the imperfections of materials, changes in field evaporation, whilst complex physics leads to trajectory

aberrations surface migration of ions, and chromatic aberrations [240, 246].

Trajectory artefacts are of concern when investigating materials with small scale (nm) precipitates [246, 247]. The trajectory aberrations arise from the relative difference in the electric fields needed to evaporate ions constituent within the precipitate compared to the surrounding matrix [248]. This results in the reconstruction of regions of low and high atomic density. This type of artefact is found when there is a change in crystallographic phases and crystallographic poles (here the electric field is discontinuous). The consequence of these artefacts is that the reconstructed precipitate could have a higher or lower density than the matrix, which may lead to erroneous conclusions in the data. An illustration of this phenomena is found in figure 3.1.2. The data analysis could be impacted due to the increase in difficulty of quantifying the phase chemistry, composition and density as both the matrix and precipitate atoms could be reconstructed in the incorrect volume [246]. Analysis within this thesis considers spatial trajectories and is addressed in section 3.1.6.

Overall, the key message is that the difference in the electric field required for evaporation causes local changes in the shape at the sample's apex (e.g. the shape is either flatter or increased curvature). This breaks the key assumption in the reconstruction algorithms (i.e. the point projection model assumes that the tip is perfectly hemispherical). When the tip deviates from this assumption, this results in aberrations where the atoms are reverse projected back to in the reconstruction. Crystallographic poles are similar as they arise from the crystallography at the surface, which is not smooth at the atomic scale but consists of steps and terraces. This can also result in subtle changes in the tip radius that result in the crystallographic poles that are seen in reconstructions of the APT data.

Another limitation to the APT technique is that segregation of solute elements to and on dislocations must be present in the material to observe them in the data. If no segregation occurs to dislocations, APT cannot detect their presence due to the combination of imperfect spatial resolution and limited detection efficiency.

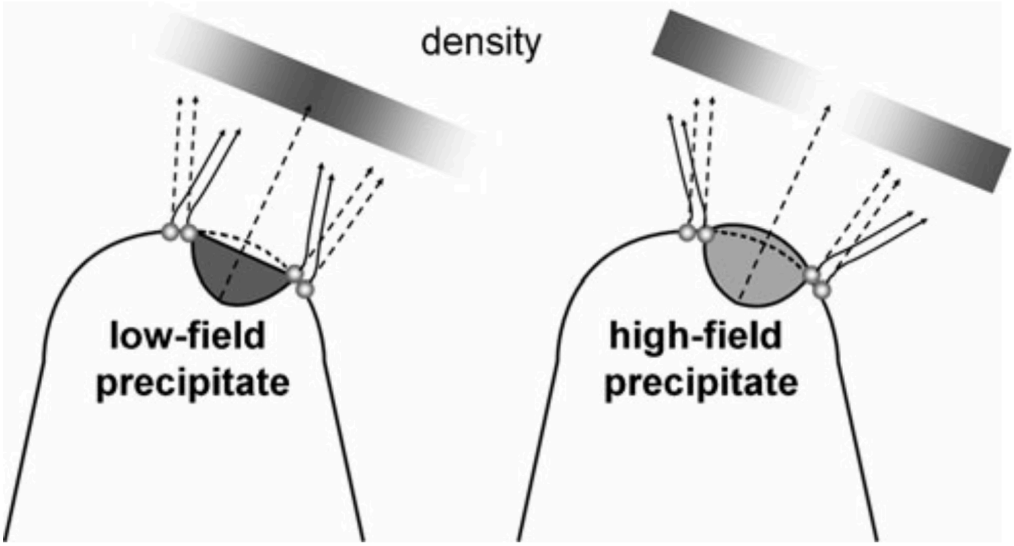

Figure 3.1.2: An illustration on how precipitates could be affected (such as the atomic density variation) by the trajectory aberrations in the APT. Reproduced with permission from Gault et al. (2012) [238].

3.1.3 Focused Ion Beam

Either electropolishing or focused-ion beam (FIB) techniques are required for sample preparation [241]. The FIB based methods enable specimens to be fabricated from either bulk or site specific region (such as a grain boundary, precipitate or irradiated depth) [241]. Within this thesis, only FIB APT sample preparation was used due to the nature of radioactive samples (i.e. FIB minimises the change of a radiological hazard occurring due to the small volume interaction). The typical FIB preparation for APT specimens used in this thesis is shown in figure 3.1.3. The effects of APT data collection on materials normally result in a fractured tip; however, figure 3.1.4 shows the apex after a successful APT run.

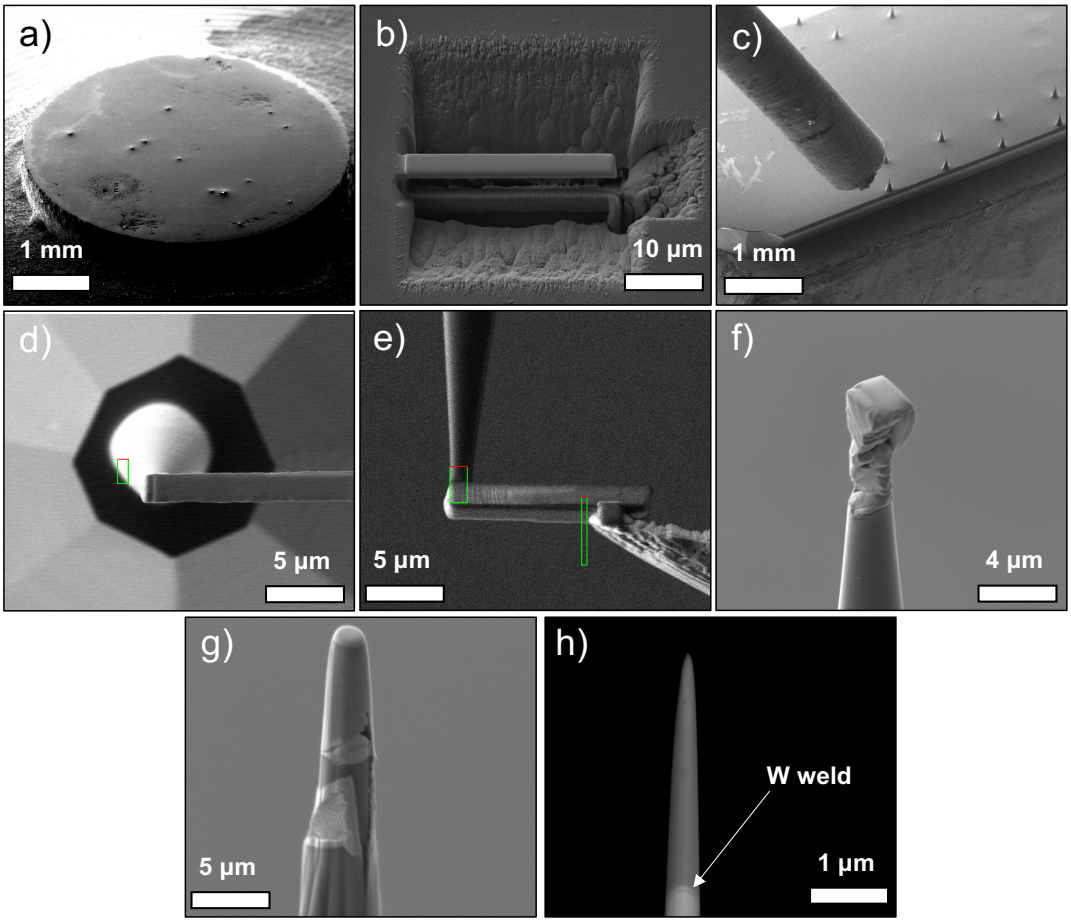

Figure 3.1.3: a) 3mm disc specimen inserted in the SEM vacuum chamber; b) the typical trench style cantilever lift-out method, as described in [241]; c) the pre-manufactured copper base and silicon posts to mount the cantilever via a manipulator arm (the gas inserted tube provides the W gas for welding); d) the cantilever placed on the top of a pre-manufactured silicon post; e) W gas is injected on the surface with a predefined FIB beam to weld the sample and W together to the silicon post; f) a typical wedge shape mounted on top of the silicon post; g) annular milling is performed with the FIB to provide a coarse APT tip; h) final FIB milling with 2 kV ions is performed to make a suitably thin tip (<100 nm apex) for APT.

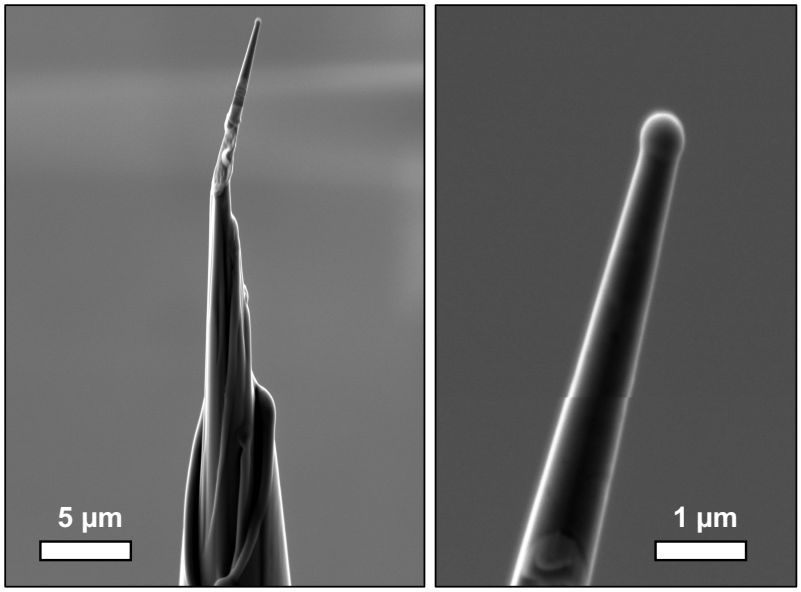

Figure 3.1.4: The apex of a ODS steel APT tip after a successful run (> 10 million ions collected). The apex has a spherical shape.

3.1.4 Cluster Searching

The definition of a cluster at the atomic scale within APT data is still a topic of much debate [237, 238, 243]. Two methods have emerged to identify and search for clusters in APT datasets: a) detect subtle non-random spatial distributions of elements, and b) identification and characterisation of individual clusters. The former used methods such as frequency distributions [238, 249, 250], nearest neighbour distance distributions [251, 252] and the pair correlation function [253]. The later uses techniques such as the maximum separation method [247], core linkage [251] isoconcentration surfaces, and proxigrams [83, 254–256]. These individual cluster search methods will be used in this thesis to characterise nanosized clusters in all steels investigated [130, 247, 257, 258].

3.1.5 Maximum Separation and Core Linkage

The Maximum Separation and Core Linkage methods are based on the assumption that two nearest neighbour solute atoms within a cluster are separated by a distance less than a pair of corresponding solute atoms in the matrix. The algorithms are implemented as follows [237, 238]:

1. Select the solute elements that are expected to be in the cluster. This is material system dependent;

2. Select an initial maximum separation distance, D_{Max}, which is the distance from each solute atom core wherein neighbouring atoms will be searched. Typical values range from 0.3 – 1 nm [238, 259];

3. A sweep of D_{Max} is conducted for all selected solute atoms within the system. If a solute atom lies within D_{Max}, it is tagged as connected to the original solute atom, as shown in figure 3.1.5(b);

4. The minimum number of atoms in a cluster, N_{Min} must be user-defined. This parameter determines the minimum number of ions a cluster should have to be called a cluster;

5. Randomise each dataset and perform a cluster search with the same parameters listed above. Styman et al. (2013) [260] developed this method and removed the random clusters from the real data.

6. The method was further developed by Vaumousse et al. (2003) [261] with the introduction of an envelope, L step, so as to incorporate matrix atoms into the defined cluster. All atoms within L distance of a cluster are now part of the cluster, as shown in figure 3.1.5(c);

7. The envelope method leaves am erroneous shell of matrix atoms around the surface of the defined cluster. The introduction of a step, called the erosion

step is performed. All matrix atoms within D_{Erosion} will be removed from the cluster, as shown in figure 3.1.5(d). This step improves the quantification of cluster size, shape, and composition.

8. Next, the introduction of a core-link process where the algorithm includes the above maximum separation method but adds an order, O, term [251]. O is the number of solute atoms that must be within D_{Max} for it to be defined as a cluster [238, 262]. Max separation uses $O = 1$ whereas the core-link method uses $O > 1$.

A limitation of this cluster searching method is the subjective aspect input by the initial selection of D_{Max} and N_{Min}. The outcome of the cluster search can be strongly influenced by the parameter selection [263]. Therefore, it is important to state the cluster search algorithm and all parameters selected to enable repeatability of the research.

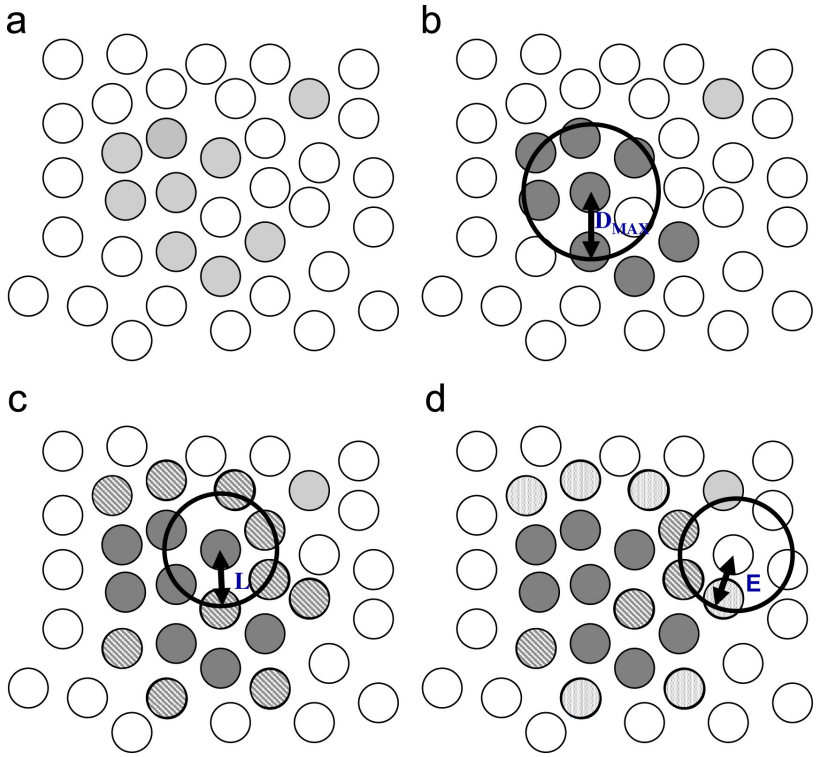

Figure 3.1.5: A schematic for the maximum separation and core-linkage method. (a) identified solute atoms are in the light grey colour. (b) sweep through D_{Max} and the core atoms tagged (dark grey colour). (c) Sweep through L and identify more core atoms (hatched grey) associated with the cluster. (d) atoms with a D_{Erosion} (labelled E in the schematic) from the matrix atoms are removed (dotted grey colour). Reproduced with permission from Hyde et al. (2011) [263].

3.1.6 Cluster Post Processing in APT

The search for MNSP is conducted by using the maximum separation method [247] and the core-link method [251]. The cluster search parameters are optimised following the method outlined by C. A. Williams et al. (2012) [259]. The cluster search used the IVAS implementation of the maximum separation method and the core-link method. After the cluster search, the size, number density, composition, and volume fraction of the identified MNSP are calculated using the solute ions. Partial edge clusters (defined as a cluster from the original material whose true extent is not completely contained within the reconstructed APT volume) are removed from the cluster search to avoid underestimation of the sizes. The algorithm used to detect and remove the edge clusters was developed by Jenkins et al (2020) [262]. The number density of clusters, N_d, was calculated by the following:

$$N_d = \frac{N_{\text{ClustersDetected}} - \frac{1}{2}N_{\text{EdgeClusters}}}{V_{\text{Dataset}}} \tag{3.1.2}$$

where $N_{\text{ClustersDetected}}$, is the number of clusters within the analysed reconstruction, $N_{\text{EdgeClusters}}$ is the number of clusters at the edge of the reconstruction, and V_{Dataset} is the volume of the reconstruction dataset (in m^3). The volume is determined by:

$$V_{\text{Dataset}} = \frac{N_{\text{Ranged}}\Omega}{\eta} \tag{3.1.3}$$

where Ω is taken as the volume of one Fe atom (1.178×10^{-2} nm^3), the number of Fe atoms contained in the bcc lattice per m^3, and η is the detection efficiency of the atom probe instrument used (LEAP 4000HR $\eta = 0.37$ and LEAP 5000XR $\eta = 0.52$). It is assumed that any cluster would have a Poisson distribution, thus the error follows $\sigma(N_d) = \sqrt{N_d}$. The volume fraction, f, of the MNSP is calculated by:

$$f = \frac{N_{\text{Ranged}}^{\text{Cluster}} - N_{\text{Fe}}^{\text{Ranged}}}{N_{\text{Total}}} \tag{3.1.4}$$

where $N_{\text{Ranged}}^{\text{Cluster}}$ is the number of ranged atoms within all clusters, $N_{\text{Fe}}^{\text{Ranged}}$ is the number of ranged Fe in all clusters and N_{Total} is the total number of ranged atoms within the dataset. Ranged atoms are user defined elements in the mass-spectrum of the APT dataset (examples are found in chapter 4 figure 4.4.1 and chapter 6 figure 6.4.2). The volume of each cluster is assumed to be spherical and with the atomic density of bcc-Fe.

The radius of the clusters was calculated by the assumption that they were spherical in volume. The radius was then calculated using the following relationship:

$$r = \sqrt[3]{\frac{\mathrm{N_{sol}}\Omega}{4\pi\eta}} \tag{3.1.5}$$

where $\mathrm{N_{sol}}$ is the number of solute ions in a cluster.

The atom probe mass-spectrum must be ranged by user assigned chemical identities to each peak. Steels that have Ni and Si alloying additions have overlapping mass-to-charge-state peaks at 29 Da with $^{58}Fe^{2+}$, $^{58}Ni^{2+}$ and $^{29}Si^{1+}$ with all three ion species potentially incorporated within the MNSP. The contribution of $^{58}Fe^{2+}$ to the 29 Da peak with the clusters has previously been claimed to be limited in other irradiated steels [264] and some authors have chosen not to include any ions originating from the 29 Da peak in their cluster searches [265]. Other researchers have utilised Scanning TEM (STEM)-Energy-dispersive X-ray spectroscopy (EDS) as evidence to claim that the exclusion of Fe from the defined MNSP in the APT data was reasonable [266]. The situation is further complicated by trajectory aberrations that affect the spatial resolution of the reconstructed atom maps, as discussed by Larson et al. [267], which can erroneously introduce Fe (matrix) into the defined MnNiSi cluster. Therefore, in this thesis, all cluster compositions will identify peak 29 as $^{58}Ni^{2+}$ (the $^{29}Si^{1+}$ peak did not match the expected natural isotope ratios) and the Fe ions will be removed from the cluster calculations.

All APT datasets investigated within this thesis are found in Tables 3.1.1, 3.1.2, and 3.1.3 for Chapters 4, 5, and 6 respectively. The data includes: APT run number,

irradiation conditions, total ions, temperature, pulse fraction, detection rate, voltage or laser mode, and cluster search parameters. The ion 'Fm' in tables 3.1.1 and 3.1.2 is actually Ni at peak 29 Da. This was differentiated to locate and deconvolve the peak at 29 Da, as discussed above. The contributions of 'Fm' was considered as Ni in all MNSP calculations. Overall, the total datasets collected by APT include **179** successful (> 2 million ions) runs. The total unsuccessful APT analyses is $\sim$ twice this number at **357**.

Table 3.1.1: APT experimental conditions for all neutron irradiated T91 steel investigated in Chapter 4. The cluster search parameters have been provided for all used datasets. T_{Irr} is the irradiation temperature, O is the order, and V is voltage-pulsing mode. 55 K temperature was chosen to maximise APT datasets whist at CAES, INL, USA

			APT Experimental Details					Cluster Search Parameters						
Run ID	T_{Irr} (°C)	Dose (dpa)	APT Mode	Temp (K)	Pulse Fraction (%)	Pulse Freq. (Hz)	Ion count ($\times 10^6$)	Ions Selected	D_{Max}	O	N_{min}	L (nm)	D_{Erosion} (nm)	Detected Clusters
R33_09642	327	2.14	V	55	20	200	3.4	Mn Ni Si P Cu Fm	0.8	1	25	0.4	0.4	22
R33_09649	327	2.14	V	55	20	200	10.1	Mn Ni Si P Cu Fm	0.7	1	43	0.35	0.35	38
R33_09665	327	2.14	V	55	20	200	3.8	Mn Ni Si P Cu Fm	0.7	1	37	0.35	0.35	43
R33_09666	327	2.14	V	55	20	200	5.4	Mn Ni Si P Cu Fm	1	6	30	0.5	0.5	32
R33_09693	327	2.14	V	55	20	200	18.0	Mn Ni Si P Cu Fm	0.85	1	35	0.43	0.43	71
R33_09694	327	2.14	V	55	20	200	6.8	Mn Ni Si P Cu Fm	1	1	45	0.5	0.5	39
R33_09698	327	2.14	V	55	20	200	12.5	Mn Ni Si P Cu Fm	0.8	1	25	0.4	0.4	38
R33_09806	377	8.82	V	55	20	200	12.4	Mn Ni Si P Cu Fm	0.9	4	40	0.45	0.45	86
R33_09809	377	8.82	V	55	20	200	5.0	Mn Ni Si P Cu Fm	0.8	4	40	0.4	0.4	21
R33_09811	377	8.82	V	55	20	200	3.7	Mn Ni Si P Cu Fm	0.8	5	35	0.4	0.4	11
R33_09813	377	8.82	V	55	20	200	10.5	Mn Ni Si P Cu Fm	0.7	4	35	0.35	0.35	11
R33_09814	377	8.82	V	55	20	200	21.8	Mn Ni Si P Cu Fm	0.8	15	40	0.4	0.4	11
R33_09815	377	8.82	V	55	20	200	5.0	Mn Ni Si P Cu Fm	0.8	1	40	0.4	0.4	24
R33_09837	377	8.82	V	55	20	200	5.6	Mn Ni Si P Cu Fm	0.8	4	20	0.4	0.4	32

Table 3.1.2: APT experimental conditions for all ion irradiated T91 steel investigated in Chapter 5. The cluster search parameters have been provided for all used datasets. T_{Irr} is the irradiation temperature, O is the order, and V is voltage-pulsing mode. 50 K temperature was chosen to maximise APT datasets.

			APT Experimental Details					Cluster Search Parameters						
Run ID	T_{Irr} (°C)	Dose (dpa)	APT Mode	Temp (K)	Pulse Fraction (%)	Pulse Freq. (Hz)	Ion count ($\times 10^6$)	Ions Selected	D_{Max}	O	N_{min}	L (nm)	D_{Erosion} (nm)	Detected Clusters
R83_07003	311	1.76	V	50	20	200	33.7	MnNiSiPFm	0.7	5	22	0.35	0.35	39
R5083_07649	311	1.93	V	50	20	200	3.4	MnNiSiPFm	0.7	5	20	0.35	0.35	10
R5083_07646	311	2.62	V	50	20	200	3.5	MnNiSiPFm	0.7	5	20	0.35	0.35	5
R5083_07647	311	2.62	V	50	20	200	8.2	MnNiSiPFm	0.7	5	20	0.35	0.35	18
R5083_07770	311	3.07	V	50	20	200	4.7	MnNiSiPFm	0.7	8	20	0.35	0.35	24
R5083_07773	311	4.1	V	50	20	200	7.8	MnNiSiPFm	0.7	5	20	0.35	0.35	12
R5083_07780	311	4.1	V	50	20	200	4.4	MnNiSiPFm	0.7	10	30	0.4	0.4	6

Table 3.1.3: APT experimental conditions for the ODS steel investigated in Chapter 6. The cluster search parameters have been provided for all used datasets. T_{Irr} is the irradiation temperature, O is the order, V is voltage-pulsing mode, and L is for laser-pulsing mode. The indent number and letters refer to the indentation in figure 6.4.4 and 6.4.5 in Chapter 6.

			APT Experimental Details					Cluster Search Parameters						
Run ID	Indent No.	Tip	M	Temp (K)	Laser Energy (pJ)	Pulse Freq. (Hz)	Ion count (10^6)	Ions Selected	D_{Max}	O	N_{min}	L (nm)	$D_{Erosion}$ (nm)	Detected Clusters
R83_06351	59 (C)	Left	L	50	40	200	33.5	Y Ti O TiO YO_2	0.9	0.45	10	0.45	1	956
R83_06348	59 (C)	Centre	L	50	40	200	38.8	Y Ti O TiO YO_2	1	0.5	20	0.5	1	634
R83_06398	59 (C)	Right	L	50	40	200	50.1	Y Ti O TiO YO_2	1.1	0.55	20	0.55	1	1118
Fractured	60 (D)	Left	L	50	40	200	–	–	–	–	–	–	–	–
Fractured	60 (D)	Centre	L	50	40	200	–	–	–	–	–	–	–	–
R83_06349	60 (D)	Right	L	50	40	200	4.9	Y Ti O TiO YO_2	1.1	0.55	15	0.55	1	144
R83_06285	61 (A)	Left	L	50	40	200	29.0	Y Ti O TiO YO_2	1.1	0.55	15	0.55	1	681
R83_06282	61 (A)	Centre	L	50	40	200	32.0	Y Ti O TiO YO_2	1	0.5	25	0.5	1	375
R83_06396	61 (A)	Right	V	50	40	200	3.5	Y Ti O TiO YO_2	1.1	0.55	10	0.55	1	68
R83_06284	62 (B)	Left	L	50	40	200	9.3	Y Ti O TiO YO_2	0.4	0.2	20	0.2	1	74
Fractured	62 (B)	Centre	L	50	40	200	–	–	–	–	–	–	–	–
R83_06393	62 (B)	Right	V	50	40	200	15.6	Y Ti O TiO YO_2	1.1	0.55	15	0.55	1	56

3.2 Electron Microscopy

This section will briefly discuss the electron-based microscopy methods used within this thesis research. The techniques used are: EBSD, Transmission Kikuchi Diffraction (TKD) and TEM. The latter was performed by Dr. J. C. Haley as part of a collaborative study discussed in Chapter 6; however, the technique will be described to provide the necessary understanding to interpret the data.

3.2.1 Electron-Backscatter Detection (EBSD)

EBSD is a technique built upon the scanning electron microscopy (SEM) method [268, 269]. The SEM uses a focused beam of electrons that scans the surface of samples in a vacuum chamber. The electrons interact with the material's surface, which can provide information on the surface topography, composition, and in the case of EBSD, crystal orientation. Advanced EBSD techniques can reveal information on the grain boundary misorientation [269, 270], texture [268], and phase morphology [269]. EBSD is used to characterise the grain size and morphology within this thesis. The basic principles of EBSD are shown in figure 3.2.1.

EBSD was conducted on a Zeiss Merlin with a beam energy of 15 keV. ESBD mapping within this study was conducted by a 100 µm by 100 µm area at 100 nm step size with a 17.3 mm working distance. The definition of a grain to reconstruct the EBSD map was that the grain boundary misorientation was set to $\geq 15°$.

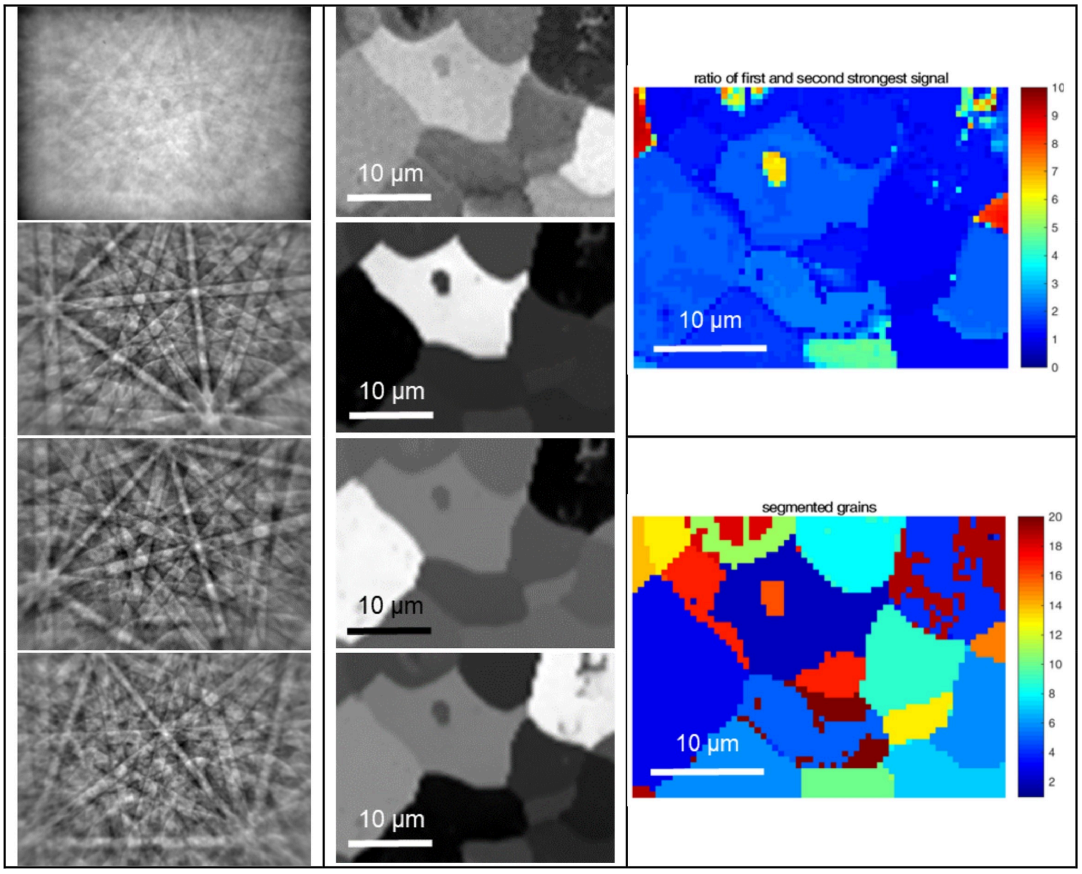

Figure 3.2.1: The basic principle of EBSD is as follows: the leftmost column shows four characteristic patterns from ferritic (body-centred cubic) steel. The central column show the spatial signal variations. The top right-hand side pattern shows the ratio between the strongest and second strongest components to the signal. The bottom right hand side pattern shows the grain morphology. Reproduced with permission from Wilkinson et al. (2019) [270]

3.2.2 Transmission Kikuchi Diffraction (TKD)

TKD is an advanced electron microscopy technique that improves the spatial resolution [270, 271] and has been under development since 2012. TKD is also known as transmission-EBSD, or t-EBSD. For TKD, the sample is mounted horizontally (or back-tilted) away from the EBSD detector. The consequence of this is that the samples bottom surface will be imaged (as the electrons will transcend through the sample). Electrons can only penetrate ~ 100 nm into the material, so the sample must

be thin.

TKD was used in this thesis to locate grain boundaries in APT samples and place the boundary on the tip for analysis. A schematic setup of the FIB/TKD is found in figure 3.2.2. A typical APT TKD milling method is found in figure 3.2.3. The TKD technique used on T91 steel that has been neutron irradiated to 2.14 dpa at 327 °C, as part of the research discussed in Chapter 4, is shown in figure 3.2.4.

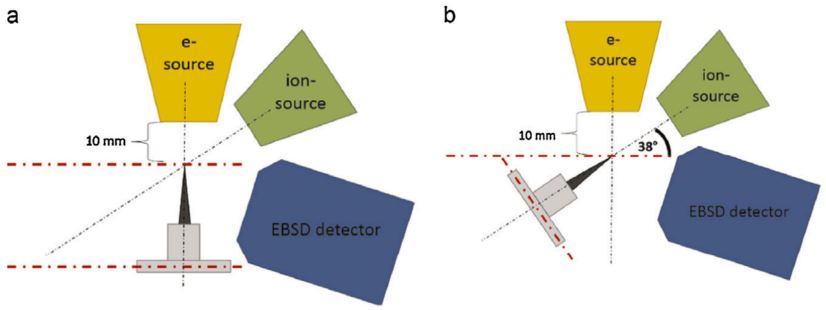

Figure 3.2.2: A schematic of both (a) FIB/TKD setup with a EBSD detector at 0° tilt and b) at 52 ° tilt. Reproduced with permission from Sneddon et al. (2016) [271].

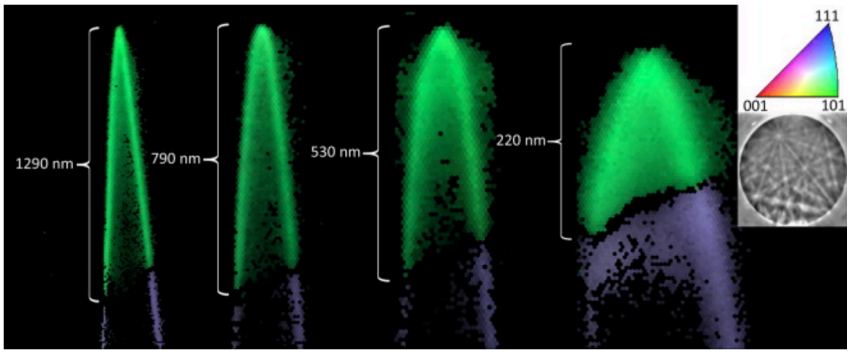

Figure 3.2.3: A novel technique for combining APT specimen with grain orientation in the first 220 nm. Removal of material from the tip is carefully performed with the FIB whilst periodically checking the position of the grain boundary. The iterative process is completed once the grain boundary is near the apex of the tip. Reproduced with permission from Babinsky et al. (2014) [272].

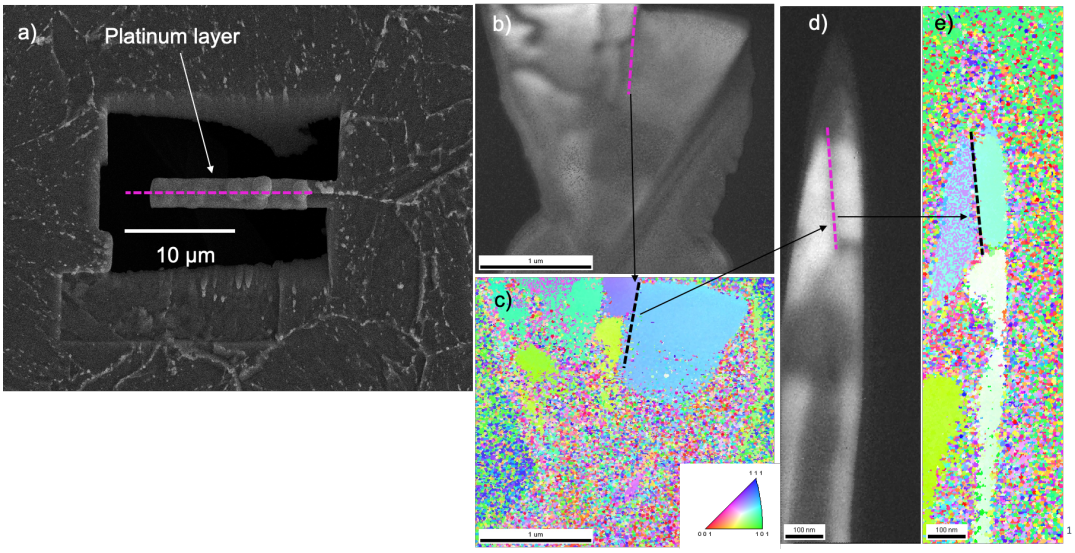

Figure 3.2.4: TKD technique used on T91 steel that has been neutron irradiated to 2.14 dpa at 327 °C, as part of the research discussed in Chapter 4. a) platinum layer has been deposited over a prior-austenite grain boundary (PAGB) (pink line); b) TKD spatial image of the APT tip prior to milling; c) the grain boundary orientation of the tip, with the PAGB labelled with a black dotted line. d) final FIB polishing and e) final FIB polish with identified PAGB.

3.2.3 Transmission Electron Microscopy

TEM is an electron-based microscopy technique that has been in use since the 1930s [273, 274]. TEM bombards material specimens with electrons of 200 to 300 keV in energy, and if the material is thin enough (50 – 100 nm, material dependent), the electrons will transmit through the sample. These transmitted electrons interact with either a digital TEM camera or phosphorous screen. When this happens in a crystalline material, they diffract via Bragg's Law [273, 275].

The material specimen can be rotated so the incoming electron beam can diffract upon particular crystallographic directions and form an image on the camera or screen. The choice of tilting angle and diffraction patterns can illuminate specific features of interest. This method is called the diffraction contrast-based technique [276].

Further, another common method used with TEMs is the scanning TEM (STEM)

capability [274]. Rather than pointing the electron beam at one spot, it is rather rastered across the sample. A detector is used to collect electrons that have diffracted from a spot on the sample. The angle and diffraction electrons detected will depend on the type of detector: annular dark-field (ADF), bright-field (BF), and high-angle annular dark-field (HAADF), collect weakly-diffracted, transmitted, and strongly-diffracted electrons, respectively [275, 276].

3.3 Micromechanical Testing

3.3.1 Introduction

The property 'hardness' is defined as the measure of a materials resistance to localised plastic deformation induced by either mechanical indentation or abrasion [277]. The Vickers hardness test is the most common method for collecting macroscale (mm to cm scale) hardness properties of materials [278]. The general indenter is diamond tip shape with a square base pyramidal geometry [279]. The main advantage of this shape enables indentation geometries that are independent of indentation depth [279]. Hardness is calculated by:

$$H = \frac{P}{A} \tag{3.3.1}$$

where P is the applied load to the indenter's tip and A is the surface contact area of the tip.

However, Vickers hardness testing raises radiological challenges with neutron irradiated materials and is incompatible with ion irradiation (as the ion beam only penetrates from few nm to μm) [125, 279–281]. Therefore, mechanical testing on the micro-to-nano-scale which can probe the penetration depth of these ion damaged layers is required on radioactive samples. Nanoindentation is one such micromechanical technique [280].

3.3.2 Nanoindentation

Nanoindentation has been developed to be a useful tool for measuring the mechanical properties within thin layers (nm to µm). However, nanoindentation prior to 1992 was labour intensive due to the estimation of the tip contact area. Oliver and Pharr (1992) [282] developed a new, simple method to calculate the tip area function through indentation. It is this method that is fundamental to modern day nanoindentation, and will be used within this thesis. The model is as follows:

First, the elastic modulus of the material is assumed to be independent of indentation depth. The contact stiffness is required to be determined per indentation depth to provide precise measurements. The load-frame compliance must be determined first where compliance is defined as the inverse of stiffness (where stiffness is the material's resistance to deformation in response to an applied force). By modelling the compliance as a series of springs, the specimen and load-frame compliance is:

$$C = C_s + C_f \tag{3.3.2}$$

where C_s and C_f are the specimen and load-frame compliance, respectively. Since C_s is the inverse of stiffness, S, the determination of the compliance is the inverse of the unloading displacement gradient, as shown in figure 3.3.1.

From elastic contact theory, Oliver and Pharr (1992) [282] derived an expression to determine C_s by:

$$C_s = \frac{\sqrt{\pi}}{2E_r\sqrt{A}} \tag{3.3.3}$$

where E_r is the reduced modulus (reduced due to the modulus contributions from the tip and specimen), and A the area between the tip and material's surface. The specimen modulus can be calculated by:

$$\frac{1}{E_r} = \frac{1-\nu^2}{E} + \frac{1-\nu_i^2}{E_i} \tag{3.3.4}$$

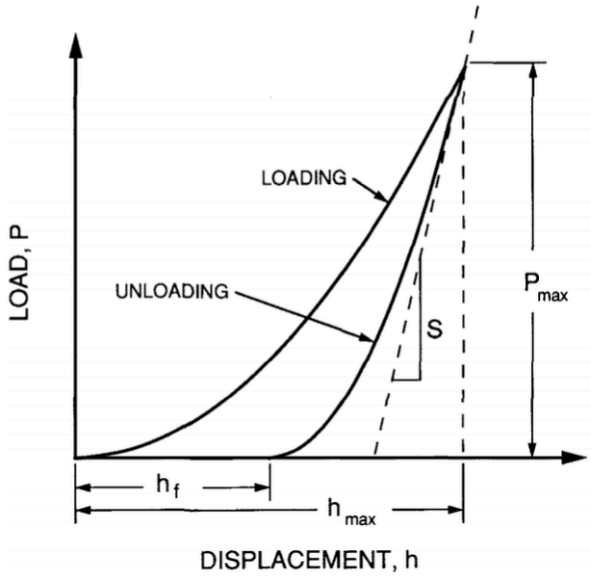

Figure 3.3.1: A schematic of a typical load-displacement curve for a single nanoindent. Reproduced with permission from Oliver and Pharr (1992) [282].

where E and E_i are the modulus of the specimen and diamond tip, respectively, and ν^2 and ν_i^2 are the Poisson's ratio for the specimen and diamond tip, respectively. Diamond has a modulus of 1141 GPa and Poisson ratio of 0.07 [282]. Combining equations 3.3.2 and 3.3.3 produces:

$$C = C_f + \frac{\sqrt{\pi}}{2E_r\sqrt{A}} \tag{3.3.5}$$

The original assumption is that the modulus was independent of indentation depth; therefore, a plot of C against $A^{\frac{1}{2}}$ should be linear. The constant at the intercept with the C axis should measure the load-frame compliance. Oliver and Pharr [282] determined for a Berkovich diamond tip geometry that the tip area function is:

$$A(h_c) = 24.5h_c^2 \tag{3.3.6}$$

where $h_c = h_{\max} - h_s$, as shown in figure 3.3.2, and h_s is displacement from the surface. This equation represents a perfect tip geometry [283].

However, due to imperfections and tip blunting during indentation, one must calibrate the tip area function. A Taylor mathematical series can be used to describe the deviations from the perfect Berkovich geometry. By rearranging equation 3.3.3 in terms of A

$$A = \frac{\pi}{4E_r^2}\frac{1}{C - C_f} \tag{3.3.7}$$

then estimation of the tip area function by fitting A with h_c data to a Taylor series by

$$A(h_c) = 24.5h_c^2 + C_1h_c + C_2h_c^{\frac{1}{2}} + C_3h_c^{\frac{1}{4}} + C_4h_c^{\frac{1}{8}} + C_5h_c^{\frac{1}{16}} + ... + C_8h_c^{\frac{1}{128}} \tag{3.3.8}$$

where $C_{1\to8}$ are constants. The first term is a perfect Berkovich tip shape and the following terms describe the deviation from the perfect shape.

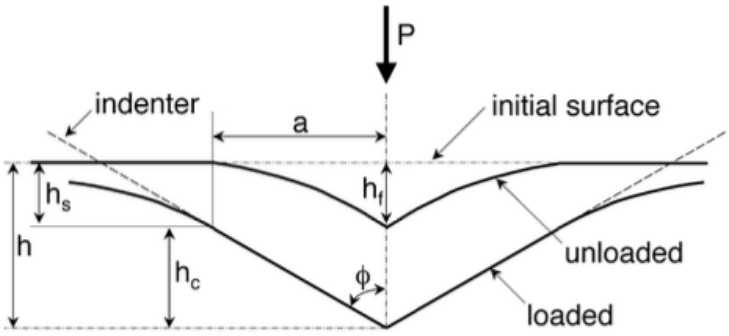

Figure 3.3.2: A schematic of Berkovich indentation cross-section. Reproduced with permission from Oliver and Pharr (1992) [282].

The tip area function must be calibrated before any indentation into interested material can be completed. The calibration material, such as fused-silica, is used regularly as it provides an accurate measurement of area functions. The modulus of fused silica is 72 GPa [284]. Once the tip area function has been calibrated, the indentation data used to investigate materials of interest can be estimated, such as hardness and modulus. The elastic modulus can be determined by rearranging equation 3.3.3 for E_r:

$$E_r = \frac{\sqrt{\pi}}{2\beta C\sqrt{A}} \tag{3.3.9}$$

where β is a new term, which is indenter tip specific. The Berkovich tip β value has been estimated to be between 1.0226 to 1.0850 [285]. The hardness, H_h, can be calculated at an indent depth, h, by:

$$H_h = \frac{P_h}{A_h} \tag{3.3.10}$$

This nanoindentation model provided by Oliver and Pharr (1992) [282] has been used with all nanoindentation experiments within this thesis. However, there are some known limits of this model; the contract area can reduce under 'sink-in', where the material could undergo plastic deformation; soft pile-up of material around the indenter tip is not accounted for within the model. Due to plastic deformation and work-hardening under indentation, ductile material can flow up the tip and deposit around the periphery. Overestimation of the materials contact area and stiffness can occur [286].

3.3.3 Continuous Stiffness Measurement

For all nanoindentation experiments conducted in this thesis, the Continuous Stiffness Measurement (CSM) model [283] has been used. CSM was introduced in 1987 [287] and the method introduces a small oscillating force, P to the indenter tip:

$$P = P_c \exp(i\omega t) \tag{3.3.11}$$

where P_c is a constant, ω is the oscillation frequency, and t is the time. The resultant displacement from this oscillating force can be characterised as

$$h(\omega) = h_o \exp(i\omega t + \phi) \tag{3.3.12}$$

where ϕ is the load with a phase shift.

Figure 3.3.3 shows a schematic of a CSM system. The overall system dynamics (schematic shown in figure 3.3.3(b)) can be described as (from Ref. [287]):

$$\left|\frac{P_c}{h(\omega)}\right| = \sqrt{\left(\left(S^{-1} + K_f^{-1}\right)^{-1} + K_s - m\omega^2\right)^2 \omega^2 C^2} \tag{3.3.13}$$

where $\left|\frac{P_c}{h(\omega)}\right|$ is the contact displacement signal, P_c is the force oscillation, $h(\omega)$ is the resulting displacement oscillation magnitude, S, K_f, K_s, and C are the contact stiffness, frame stiffness, and damping coefficient to the displacement sensing capacitor plate, respectively.

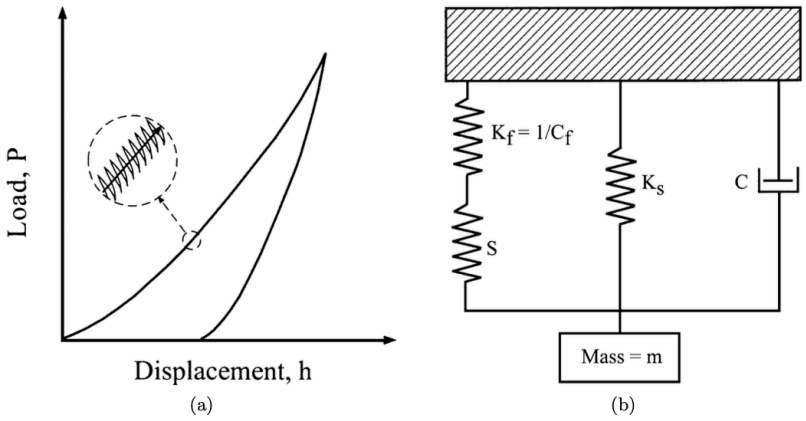

Figure 3.3.3: (a) A schematic of an ideal CSM indent load-displacement cycle. b) A system overview of determining the dynamics, where S, K_f, K_s, C_f, and C are the contact stiffness, frame stiffness, frame compliance, and damping coefficient to the displacement sensing capacitor plate, respectively. Reproduced with permission from Li et al. (2002) [283].

The material's stiffness as a function of tip displacement can be determined by equation 3.3.13 when the material's elastic modulus is assumed to be constant. The tip area function, as described by equation 3.3.8, and the aforementioned equation, when used together, can determine the material's modulus and hardness as a function of tip displacement. It is the latter which is sought when conducting nanoindentation experiments.

3.3.4 Summary

The nanoindentation technique provides an insight into the mechanical properties of irradiated materials in a reasonable time, whilst minimising the change of radiological hazards occurring, and provides useful properties. It is these factors that enable this technique to be a powerful tool in studying the changes in mechanical properties due to neutron or ion irradiation. In addition, nanoindentation can be used to target specific regions within the microstructure.

Chapter 4

Atom Probe Characterisation of Neutron Irradiated T91 steel

4.1 Preface

This first research chapter is heavily based on the following submitted paper [288]:

T. P. Davis, M. A. Auger, N. Almirall, P. A. J. Bagot, P. Hosemann, M. P. Moody, G. R. Odette, and D. E. J. Armstrong, "Atom Probe Characterisation of Segregation Driven Cu and Mn-Ni-Si co-precipitation in neutron irradiated T91 tempered-martensitic steel" Materialia, 14, 2020, 100946

The contributions to the paper are as follows: T. P. Davis provided conceptualisation, writing, scientific development, editing, atom probe data collection, analysis, and conclusions; M. A. Auger provided supervision and manuscript editing; N. Almirall provided assistance with manuscript editing; P. A. J. Bagot provided supervision and manuscript editing; M. P. Moody provided supervision and manuscript editing; P Hosemann provided manuscript editing; G.R. Odette provided manuscript editing and analysis; D. E. J. Armstrong provided supervision, funding, and manuscript editing. It should be noted that nanoindentation was planned on the two neutron irradiated

T91 steel specimens whilst conducting the APT at Idaho National Laboratory; however, due to equipment failure and the COVID-19 pandemic, nanoindentation was not completed.

4.2 Introduction

Neutron irradiation drives microstructural and microchemical change in tempered martensitic steels (TMS) such as T91; this change imposes detrimental effects on the mechanical properties of the steels. Reported microstructural features that result from neutron irradiation of 9-12 wt% Cr ferritic-martensitic alloys, such as T91, HT9 and Eurofer97, include the MNSPs [164, 165, 173–179] (often described as 'G-phase' – $Mn_6Ni_{16}Si_7$ [180]), Cr-rich alpha prime (α') ppts [164, 176, 186, 289, 290], voids, dislocation loops and evolved network dislocations, and solute segregation towards, and precipitation on, dislocations [177, 291–293]. These microstructural changes are due to the excess radiation defect generation and clustering, dislocation climb, RIS, and radiation enhanced diffusion (RED). These hardening features embrittle the steels, as manifested by elevations of DBTT, increases in yield stress, decreases in ductility and degradation of fracture toughness [42].

A number of characterization studies of the MNSPs that form during neutron irradiation of T91 steel have been reported previously [40, 85, 86, 164, 165, 173, 181]. MNSPs have been observed in ion [83, 177, 294, 295] and proton [70, 129, 130, 173, 296] irradiated T91 and HT9 steels also. In all cases, segregation of Mn, Ni, and Si was observed near or on dislocations and Cu precipitates between temperatures of $\sim$ 270°C to $\sim$ 450°C. Jiao et al. [166] investigated MNSPs in a T91 steel neutron irradiated to 17.1 dpa and 35.1 dpa at 376 °C to 524 °C in the Russian BOR60 sodium-cooled fast test reactor. The TEM study indicated that the average MNSP size was between 5.8 to 7.0 nm, with number densities from 2.4 to 3.6 $\times 10^{21}$ m^{-3}, corresponding to a volume fraction 0.037 to 0.043%. Impurity Cu precipitates [70]

and dislocations [181] enhance MNSP formation in 9Cr TMS, likely by promoting nucleation. Typical Mn-Ni-Si solute contents of these alloys are relatively low, lying either near, or below, the thermodynamic solvus boundary. Recent cluster dynamics modelling has showed that solute segregation is required for heterogeneous nucleation and growth of MNSPs on dislocations in T91 steel [181].

In addition to MNSP observation in Fe-Cr based alloys, neutron irradiation embrittlement of low alloy reactor pressure vessel (RPV) steels has been the subject of extensive basic research for 40 years [89, 297]. Embrittlement is caused by irradiation hardening primarily due to precipitation of supersaturated Cu impurities [87, 89, 298] and/or Mn-Ni-Si solute atoms [81, 257, 265, 299]. Supersaturated Cu can form Cu-rich precipitates (CRPs) under very long-term thermal aging near RPV service temperatures ($\sim 290°C$)[300]; however, Cu precipitation kinetics are highly accelerated by neutron irradiation due to RED [89, 257, 301]. The formation of so called late blooming MNSPs was first predicted by Odette in 1996 [297]. In Cu bearing steels, MNSPs form as appendages to CRPs and slowly grow to large fractions of the steel Mn+Ni+Si alloying element contents, which are typically 2 to 3 atomic (at.)% [89]. MNSPs also develop in low Cu steels, although even trace amounts of Cu are known to be catalysts for their formation [255]. The first experimental proof of MNSP formation in irradiated RPV steels was reported in 2004 [88]; since then, MNSPs have been widely observed [80, 81, 175, 257, 258, 300, 302, 303]. Notably, CRPs and MNSPs are predicted by thermodynamic and kinetic modelling [298, 304, 305]. Kinetic lattice Monte Carlo models recently showed that the co-precipitated morphology observed in APT reconstructions are the result of an interplay between interfacial energies, diffusion paths, such as through the Cu cluster, and ordering energies [298]. Both experiments and physical models show that MNSPs will dominate RPV integrity issues for life extension of light-water reactors [80, 81, 255]. RPV steel studies have also revealed significant solute segregation to loop and network dislocations. The segregated dislocations are a favoured nucleation sites for heterogeneous

nucleation of MNSPs, as are cascade generated solute cluster complexes. However, apparently random matrix homogeneous is frequently observed in RPV steels and is predicted by models at sufficiently high solute contents (supersaturations), particularly Ni. Although previously there has been little attention to the topic, recently solute segregation to dislocations in RPV steels has been characterized in some detail [257, 258, 306, 307].

Thus, the objective of this study is to build on the understanding of precipitation in RPV steels and the corresponding much more limited database for Fe-Cr alloy systems, including model binary alloys and TMS 9-12%Cr steels like T91 and HT9 [38, 42, 150, 177]. The major differences between these two alloy systems are that the solute contents of TMS are typically much higher than in RPV steels, while the dose (dpa) is much larger and the temperatures higher whilst in service. The primary significance of these differences is that solute segregation to, and heterogeneous nucleation of clusters, on dislocations is critically important in TMS alloys. Here, this study focuses on APT characterisation of TMS T91 steel, irradiated to 2.14 and 8.82 dpa at 327 and 377 °C, respectively, in the Advanced Test Reactor (ATR).

Further, low temperature investigations of T91 steel have practical importance because the 'cold' reactor coolant (liquid sodium, lead, or lead-bismuth) which enters the core could be within the 320 – 375 °C temperature range (the specific temperature range is reactor design dependent) [42], thus exposing the lower cladding tubes, wrapper and structural components to these conditions. It is within these conditions that the maximum embrittlement is observed in ferritic-martensitic steels [148].

4.3 Experimental Method

4.3.1 As-Received (AR) Material

For the material to be classified as 'T91' steel, it must meet the respective ASTM International standards [308–311]. The measured composition of T91 steel used in this study is given in table 4.3.1 and meets the required standard. The as-received (AR) APT composition measurement is given in Table 4.3.1 also (see section 4.3.3 for the experimental parameters). The C content is lower in the APT data, since it primarily resides in coarse carbides not sampled by the small APT analysis volumes. The other elements are generally similar with the exception of Ni, which is significantly higher in the APT data due to segregation and low sample volume. APT also detects trace amounts of dissolved Cu.

Table 4.3.1: T91 Bulk Chemical and APT Composition Measurement.

Element	Bulk (wt%)	Bulk (at%)	APT (at%)
C	0.07	0.32	0.02± 0.01
Mn	0.47	0.47	0.41± 0.02
P	0.02	0.04	0.02± 0.01
S	0.02	0.04	-
Si	0.28	0.55	0.54± 0.01
Cr	9.24	9.84	8.81± 0.17
Mo	0.96	0.55	0.41± 0.09
Ni	0.16	0.15	0.39± 0.02
V	0.21	0.21	0.10± 0.01
Al	-	-	0.04± 0.01
Cu	-	-	0.03± 0.01
Co	-	-	0.01± 0.01
Fe	Bal.	Bal.	89.25± 0.34

4.3.2 Neutron Irradiation

The neutron irradiated alloys were irradiated in the ATR: a) as part of the University of California Santa Barbara (UCSB) ATR-1 experiment and are included in the Nuclear Science User Facilities (NSUF) Library [312]; and, b) as part of the University of Illinois at Urbana-Champagne (UIUC)) experiments. Both of these irradiations were drop-in experiment, which did not include thermocouples to directly monitor temperatures. Rather, the temperatures were regulated by a combination of insulating helium/argon mixture gas gap and nuclear heating. The temperatures were estimated based on Abaqus thermal heat transfer and MCNP code [313] for nuclear heating analysis and the reactor lobe power history [312]. Specimen 0020-2008-139 from the UCSB-1 library and specimen 2008-92-387 from the UIUC library have similar compositions, and are believed to be from the same heat provided by Los Alamos National Laboratory (see composition in Table 4.3.1). The neutron history of these two samples is found in Table 4.3.2.

It should be noted that another T91 steel specimen was analysed with the APT at Idaho National Laboratory. The Sample ID was 1109-2008-139 and is part of the UCSB library. The conditions were 6.65 dpa at 320 °C. 38 APT datasets were collected (> 5 million ions), however, upon analysis the sample was contaminated with carbon (> 6 at% C) due to imperfect polishing in the hot-cells at INL. Therefore, this data was discarded.

Table 4.3.2: Irradiation Conditions for the T91 specimens in the ATR reactor [312].

Specimen ID	Steel	Temp (°C)	Neutron flux ($n/cm^2/s$)	Neutron fluence (n/cm^2)	Dose (dpa)
0020-2008-139	T91	327	1.21×10^{14}	1.57×10^{21}	2.14
2008-92-387	T91	377	2.30×10^{14}	$\sim 7.80 \times 10^{21}$	8.81

4.3.3 Atom Probe Tomography

AR T91 steel (the same steel batch as 0020-2008-139 and 2008-92-387 sample ID) was analysed using the atom probe tomography technique [237]. APT analysis on the as-received T91 steel was conducted with a CAMECA LEAP® 5000XR at the Department of Materials, University of Oxford. APT specimens were prepared by the lift-out technique [241] using a Zeiss Crossbeam 540 Analytical FIB-SEM.

The post neutron irradiation examination was conducted at the Microscopy and Characterization Suite located at the Center for Advanced Energy Studies (CAES) with support from the NSUF (US Department of Energy). APT analysis on the neutron irradiated T91 steel specimens were conducted with a CAMECA LEAP® 4000X HR. APT specimens were prepared by the lift-out technique using a FEI Quanta 3D FEG FIB Scanning Electron Microscope (SEM). All lift-out cantilevers were chosen at random across the specimens. A final FIB cleaning process was performed by using 2 kV Ga ions, in order to minimise FIB-induced damage [241]. After this process, the diameters of the specimens were approximately between 50 – 100 nm.

For both LEAP systems, the APT specimens were analysed at a stage temperature of 55 K, a voltage pulse fraction of 20%, a pulse rate of 200 kHz and the average detection rate was set to 1.0 %, as listed in table 3.1.1 in Chapter 3. The detection efficiency of the LEAP® 4000X HR and LEAP® 5000 XR were 37% and 52%, respectively. CAMECA IVAS® version 3.8.4 was used to reconstruct all atom probe datasets. Calibration of the final reconstructed APT maps used SEM micrographs of the final tip shape and crystallographic pole indexing. The cluster search for MNSP is outlined in 3.1.6 and values for the cluster search (D_{max}, N_{Min}, O, and number of clusters) are found in Chapter 3 Table 3.1.1. To capture the solute segregation to dislocations, 2.0 at% Si isosurface was created and a region of interests (ROI) was placed through the dislocation's core in both transverse and longitude direction to generate composition line profiles. This procedure was provided by N. Almirall et al [314].

4.4 Results

4.4.1 AR T91 Steel

A typical reconstruction of the AR T91 steel is presented in figure 4.4.2(a). The microstructure was homogeneous at the APT scale and presented no evidence of nanometric sized ppts by checking cluster searchers and visual inspection of the APT datasets.

4.4.2 Neutron Irradiated T91 Steel

The mass-to-charge-state (Da) spectrum of a typical neutron irradiated APT dataset (R33_09693 in table 3.1.1) is shown in 4.4.1 and all associated identification of the peaks is shown for reference.

The typical APT reconstruction in figure 4.4.2(b) of the neutron irradiated T91 steel at 2.14 dpa at 327 °C, shows the formation of Cu rich clusters (CRPs) as well as, segregation of Si, P and Ni to dislocations. The corresponding MNSPs on the dislocations were found to be appendages to CRPs (shown later in figures 4.4.5 and 4.4.7). No clustering of Mo, V, Co, Al, Fe or Cr was detected. The average composition of MNSPs was calculated for each dataset and is shown on a ternary projection of the Fe-Mn-Ni-Si phase diagram in figure 4.4.3. The average of 8 APT datasets of MNSP-CRP volume fraction, average radius, volume, composition and number density are summarised in table 4.4.1. ROI solute segregation profiles, both transverse and longitudinal (along) dislocations, are shown in figure 4.4.5. The longitudinal solute profile in figure 4.4.5(c), clearly shows the periodic formation of MNSPs-CRPs along the dislocation line. Enrichment of Ni, Si and P at a carbide interface is shown in figure 4.4.6.

A typical APT reconstruction of T91 neutron irradiated to 8.8 dpa is shown in figure 4.4.2(c). As seen in the close-up atom map, the MNSPs are appendages to CRPs,

as frequently observed in RPV steels [255, 305] and proton irradiated T91 [83]. No clustering of Mo, V, Co, Al, Fe or Cr was detected. The average compositions of the MNSPs were calculated for each tip dataset and are shown on a ternary phase diagram projection in figure 4.4.3. The averages of all 7APT datasets for this irradiation condition of MNSP volume fraction, average radius, volume, composition and number density are summarised in Table 4.4.1. The APT reconstruction in figure 4.4.2(c) and 4.4.4 suggests that the MNSP-CRP features have larger and better defined volumes in the neutron irradiated T91 steel to 8.82 dpa at 377 °C, along with less apparent segregation of Si, P and Ni to dislocations. Solute segregation to dislocation loops in figure 4.4.7 is shown as concentration profiles. The profile in figure 4.4.7(b) is a 1.0 at.% Cu isoconcentration surface marking a CRP. The longitudinal solute segregation profile, shown in figure 4.4.7(d), indicates the formation of MNSPs-CRPs at the edge of a dislocation loop.

The T91 MNSP number density, volume fraction and radii found in Table 4.4.1 and solute (Ni, Si, Mn, P and Cu) segregations to dislocations will be compared to the model of Ke et al. (2018) [181] in the next Section.

Table 4.4.1: The volume fraction, average radii, average volume, volume fraction and solute composition of MNSP in both neutron irradiation conditions using the cluster search, as outlined in Section 4.3.3.

	Irradiation Conditions	
	2.14 dpa at 327 °C	8.82 dpa at 377 °C
MNSP (only solute ions, excluding Fe)		
Number Density (#/cm^3)	(3.1± 0.7) $\times 10^{23}$	(1.5± 0.7) $\times 10^{23}$
Average Radii (nm)	1.1± 0.1	1.45± 0.2
Average Volume (nm^3)	5.8± 1.3	15.6± 5.4
Volume fraction (%)	0.26± 0.06	0.33± 0.14
MNSP solute compositions (Fig. 4.4.3)		
Mn (%)	16.49 ± 4.7	16.47 ± 4.4
Ni (%)	37.87 ± 6.33	36.80 ± 10.61
Si (%)	45.64 ± 7.62	46.73 ± 11.59

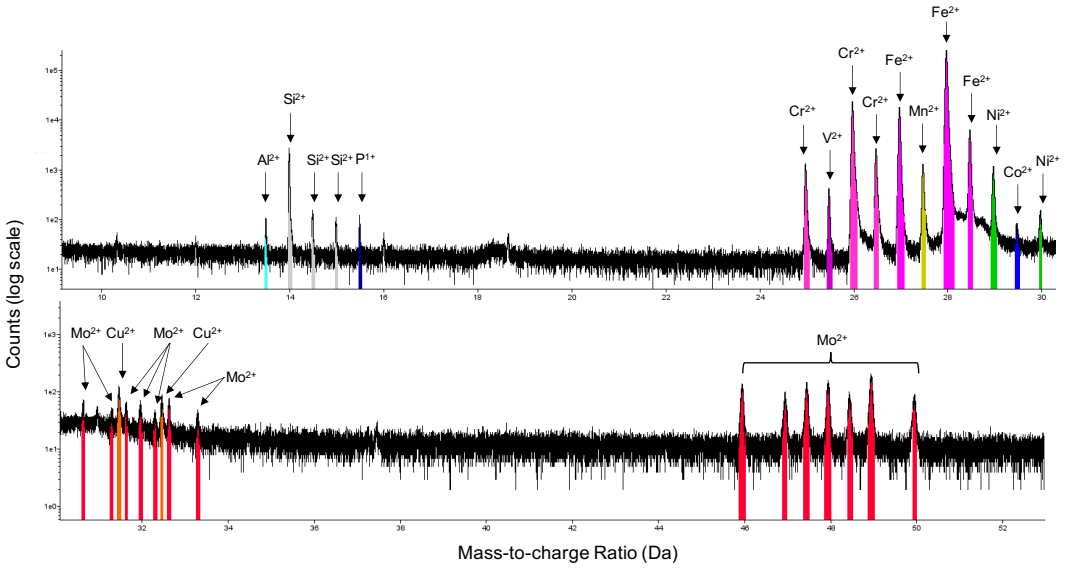

Figure 4.4.1: The mass-to-charge-state spectrum of a typical neutron irradiated T91 steel sample (R33_09693 in table 3.1.1). The peaks have been identified according to the natural isotopes and expected chemical additions. The peak at 29 Da has been identified as Ni, as discussed in section 3.1.6.

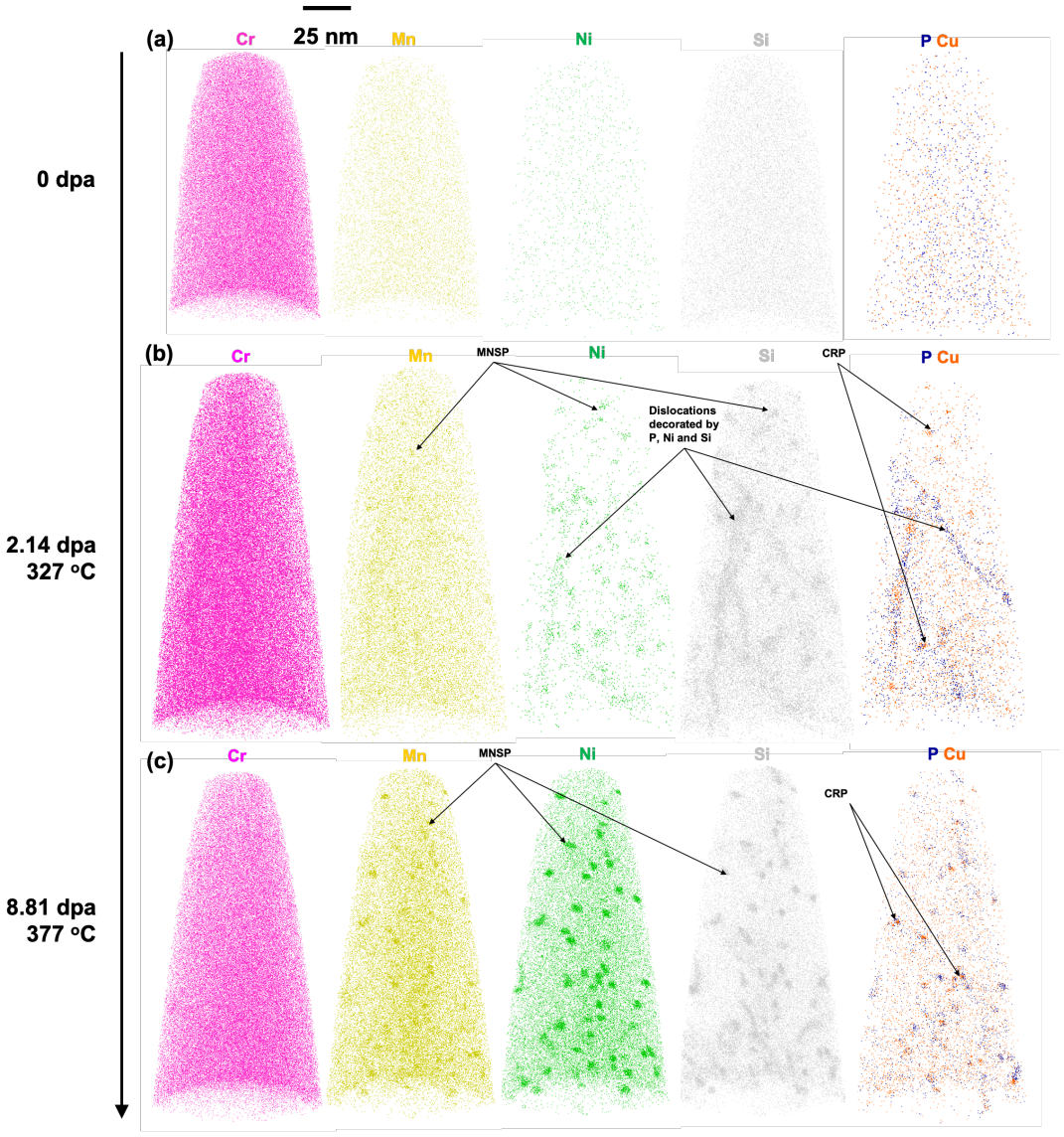

Figure 4.4.2: (a) APT reconstruction of the AR T91 steel, showing a homogeneous microstructure; (b) APT reconstruction of the neutron irradiated T91 steel to 2.14 dpa at 327 °C showing MNSPs and CRPs, as well as Ni/Si/P segregating to dislocations; (c) APT reconstruction of the neutron irradiated T91 steel to 8.82 dpa at 377 °C, showing better defined MNSPs and P/Cu precipitates, perhaps with somewhat less Ni/Si/P segregation. Cr appeared homogeneous in all conditions.

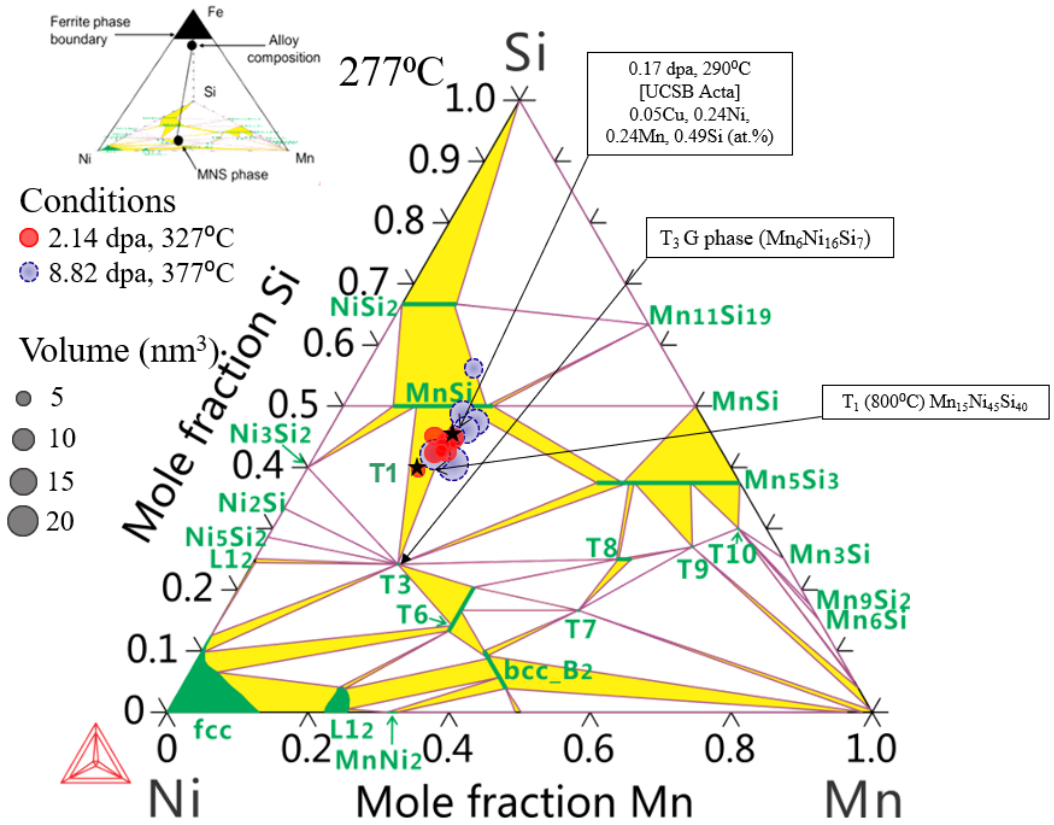

Figure 4.4.3: The averaged MNSP composition (in at%) of each APT dataset (over >5 million ions) for both 2.14 dpa and 8.82 dpa T91 irradiations displayed on an isothermal section of the Mn-Ni-Si ternary system projection of a Fe based phase diagram at 277 °C. The isothermal system is taken from refs [299, 303, 315]. The size of the data point is scaled to the MNSP average APT dataset volume (nm^3). The stoichiometric 'G-phase' phase, $Mn_6Ni_{16}Si_7$, is marked as T3. Low Ni containing RPV steel neutron irradiated to 0.17 dpa at 290 °C is provided by Almirall et al. (2019) [255] for comparison. Further, the Fe-Mn-Ni-Si phase diagram is provided in the top left to indicate the projection of Mn-Ni-Si phase diagram.

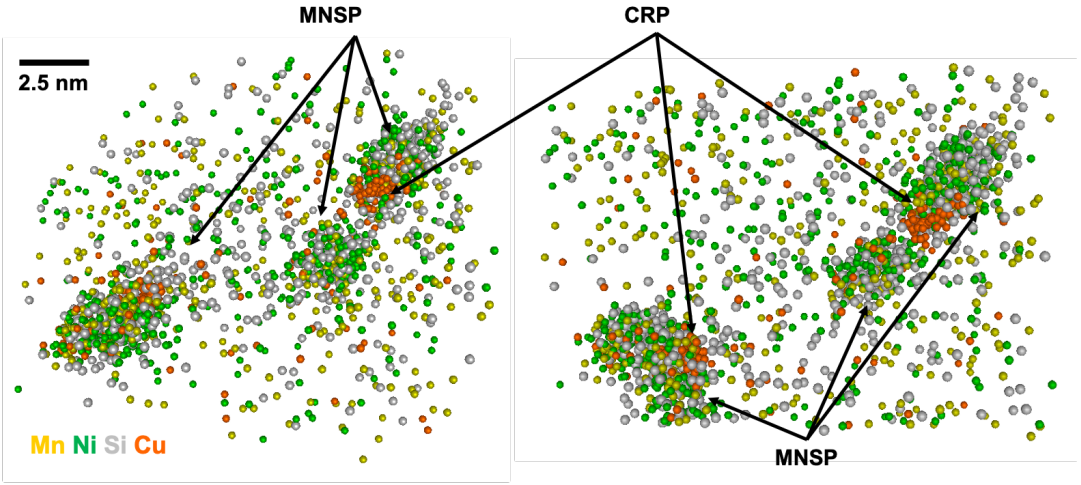

Figure 4.4.4: A close-up view of MNSP and CRP of the APT reconstruction shown in figure 4.4.2(c) (T91 neutron irradiated to 2.14 dpa at 327 °C).

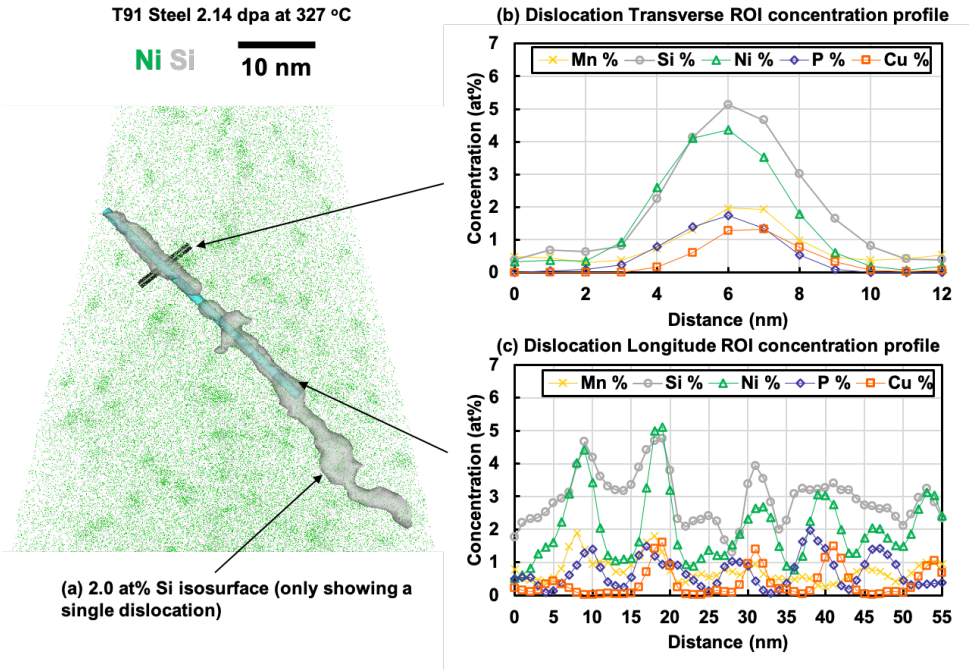

Figure 4.4.5: Solute segregation on a dislocation line in T91 steel irradiated to 2.14 dpa at 327 °C. (a) displays a 2.0 at.% Si isosurface. (b) is a 1D transverse ROI concentration profile at a random section of the dislocation and (c) is a 1D longitude ROI concentration profile inside the dislocation.

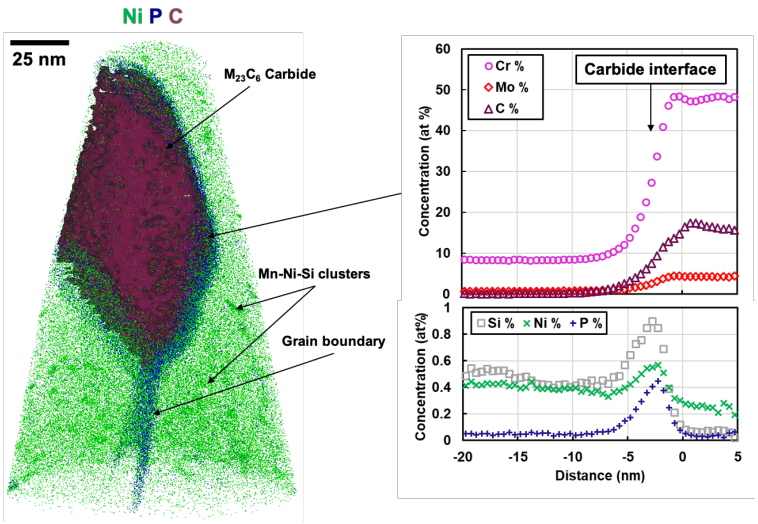

Figure 4.4.6: APT reconstruction of T91 neutron irradiated to 2.14 dpa at 327 °C. A chromium-based carbide can be seen with a grain boundary/interface that is decorated with Ni, Si and P. The concentration profile was produced using a proxigram from a 5 at% C isosurface.

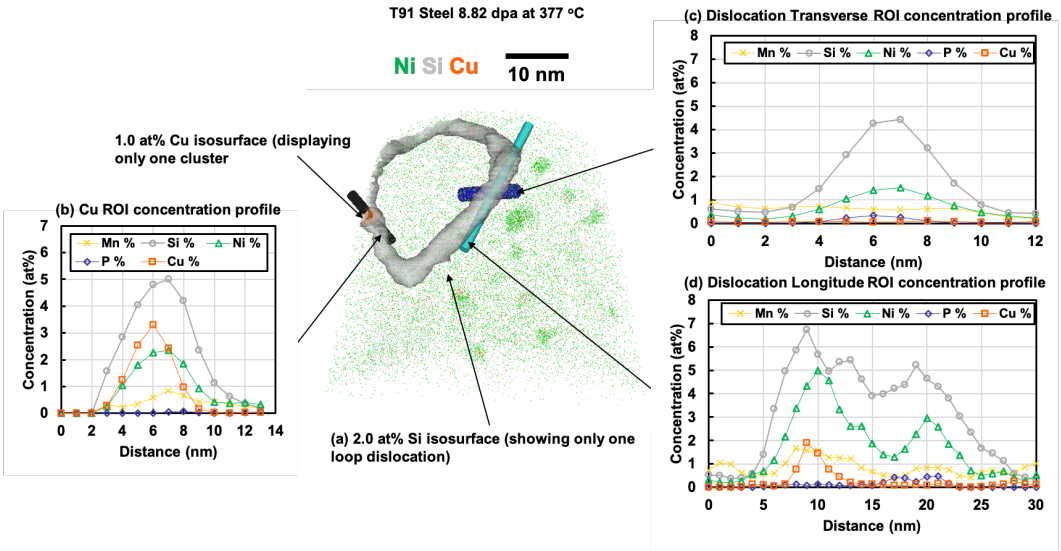

Figure 4.4.7: Solute segregation to a dislocation loop in a T91 steel irradiated to 8.82 dpa at 377 °C; (a) displays a 2.0 at% Si loop isoconcentration surface; (b) is a 1D concentration profile through the 1.0 at% Cu isoconcentration surface; (c) is a 1D transverse ROI concentration profile centered on a random section of the dislocation loop and (d) is a 1D longitude ROI concentration profile inside the random segment of the dislocation loop.

4.5 Discussion

The defining microstructural features of T91 steel are the martensitic lath microstructure, high network dislocation densities, $M_{23}C_6$ carbides, as well as somewhat finer scale vanadium nitrides (50 – 100 nm diameter) and molybdenum/niobium carbides (100 – 200 nm scale) [150]. The latter features provide the high creep strength [143] needed for elevated temperature boiler and nuclear applications [38]. Note that these performance-enabling microstructures are unstable in T91 under irradiation at temperatures more than 450 to 500 °C, as indicated by irradiation softening and non-hardening embrittlement [316]. At lower temperatures, the main effects of irradiation are hardening and embrittlement due to segregation and precipitation of solutes, as described in the previous Chapter 2 Section 2.4.4. It is well known, and the topic of a large literature, that a smaller amount of hardening is contributed by dislocation loops, as illustrated by Bhattacharyya et al. (2019) [290] for Fe-Cr binary alloys. Potential contributions from the evolution of network dislocations is rapidly emerging as an issue, but it is not close to being well quantified [89, 166, 292, 293]. Here, the focus is on using the high mass and spatial resolution of APT to investigate segregation and nanometric precipitates, which are absent prior to neutron irradiation.

Precipitate evolution under neutron irradiation is illustrated in figure 4.4.2(a) – (c). Cr remains homogeneously distributed in all conditions. The high number density nanosized MNSPs are likely to act as dispersed barrier obstacles dislocation glide, which results in hardening and shifts in DBTT [38, 42, 150, 182]. The decrease in number density and increase in size (and individual precipitate volume) in the higher dpa and temperature irradiation condition is expected based on the thermokinetics of segregation and precipitation; the slightly larger volume fraction at higher fluence and temperature (from 0.26 ± 0.06 to 0.33 ± 0.1) is probably within the uncertainties of the APT measurements. Note, RPV studies show that dispersed barrier hardening and embrittlement are primarily controlled by the square root of the precipitate

volume fraction [80, 81, 255]. The T91 volume fractions correspond to estimated hardening contributions of ∼168 to 186 MPa. This estimation uses the hardening contributions as function of MNSP volume developed by Almirall et al. [303].

The average composition of MNSP in both irradiated conditions, shown in figure 4.4.2 and Table 4.4.1, is significantly different than the most cited 'G-phase'. Rather, the MNSP compositions are closer to the Si(Mn,Ni) phase field in the Mn-NiSi ternary projection of the Fe matrix-based quaternary phase diagram (as shown in figure 4.4.3 where Si = 0.5 fraction). This phase field, calculated by Xiong et al. [299], is $Si_{0.5}Mn_xNi_{(1-x)}$ where x varies from $\sim$ 0.1 to 0.25. Note, the crystallographic structure of the precipitates in this study has not been characterised. Similar Si(Mn,Ni) phase compositions have been observed on dislocations in a low Ni (0.07 at.%) VVER-440 RPV steel [317]; and more recently in another low Ni RPV steel [303].

The T91 2.14 dpa at 327 °C carbide shown in figure 4.4.6 is likely a $M_{23}C_6$ phase with a composition of $\sim 48.2 \pm 0.5$ Cr, 16.7 ± 0.4 C, 4.3 ± 0.3 Mo, and 29.0 ± 0.5 Fe (in at.%); however the crystallography has not been determined. The composition line profile across the carbide/matrix interface in figure 4.4.6 shows enrichment of Ni, Si and P, which correlates well with previously analysed irradiated carbide interfaces [83, 130, 177].

Co-precipitation of CRPs and MNSPs, clearly seen in figure 4.4.5, is widely observed in RPV steels at high fluence, and has been extensively characterised [81, 257, 265, 299] and modelled [89, 298, 304, 305]. CRPs have been observed in neutron and ion irradiated T91 [166, 296] and HT9 [85, 177]. Indeed, Cu driven co-precipitation has also been exploited by some high strength steels to promote the formation of various intermetallic phases [318]. The corresponding sequence-of-events begins with the rapid precipitation of highly supersaturated Cu, with shells composed of the other solutes. After Cu is depleted from the matrix, Mn, Ni and Si continue to accumulate, so as to eventually form a separate appendage phase

[89, 255, 297, 298, 304, 305]. Even trace amounts of Cu act as a powerful catalyst for MNSP formation [255] due to the supersaturation of Cu in Fe. In the case of T91 co-precipitation takes place in highly solute segregated regions at dislocations, as previously been observed by APT in irradiated T91 steel [166, 177, 296].

The nominal transverse solute concentrations profile at line dislocations in figure 4.4.5(a,b) reaches 4-5% for Si and Ni, and 1 to 2% for Mn, P and Cu. Figure 4.4.5(c) presents longitudinal profiles that show periodic peaks of Mn, Ni, Si, Cu and P, indicating the formation of precipitates. Note, the Cu peaks are slightly displaced from those for Ni, and especially Mn, which is consistent with co-precipitation [298] where MNSP are found to be precipitated next to Cu. The Si enrichment is very high and more uniformly distributed along the dislocation lines. This may rationalise the $Si_{0.5}Mn_xNi_{(1-x)}$ precipitate compositions, which are near the Si(Mn,Ni) phase field, shown in figure 4.4.3. As seen in figure 4.4.7, generally similar solute segregation also occurs at dislocation loops. However, P does not appear to segregate to loops. Cu is localized in the precipitate regions of both dislocation features. Note, these solute compositions are nominal, and may be affected by APT artefacts like trajectory aberrations, as discussed in section 3.1.2.

This analysis highlights the parallels that can be drawn between the much more limited database on MNSPs in neutron irradiated for Fe-Cr alloy systems, including model binary alloys and 9-12%Cr steels like T91 and HT9, with the much more extensive literature on precipitate evolution in RPV steels [80, 175, 255, 257, 265, 297–303, 305, 315]. Notably, precipitates in some very low Ni RPV steels have compositions that fall near the Si(Mn,Ni) phase field [317]. The major difference between these alloy classes is that the typical Cu + Ni + Mn +Si solute contents in RPV steels are much higher ($\sim$ 3%) than in the 9Cr TMS alloys ($\leq$ 1%). Thus, while precipitation at segregated dislocations (loops and lines) occurs and is important in some RPV steels and irradiation conditions, local solute enrichment is probably necessary in alloys like T91. Note, segregation may be either thermally driven or RIS, or both.

The main thermodynamic driver for co-segregation is the local bonding interactions between the solutes, lowering their free energies near the dislocations. The other difference between RPV and 9Cr TMS, is that service conditions for the latter involves much higher temperatures and doses. This implies that TMS alloys will experience greater solute segregation compared to RPV.

Ke et al. (2018) created a combined solute segregation and cluster dynamics (CD) model that was used to predict the nucleation and growth of MNSPs in a subsaturated T91 steel as a function of dpa [181]. The model, which predicts the MNSP number density, volume fraction and mean radius (and size distribution), was calibrated using the results of a single proton irradiation at 400 °C to 7 dpa [83]. Figure 4.5.1 compares these predictions to the 8.8 dpa at 377 °C APT data in this study. Figure 4.5.1 shows that the model predictions are in remarkable agreement with the neutron results. The number density and radius are in almost exact agreement, while the volume fraction is slightly under predicted. Figure 4.5.2 compares the predictions of solute segregation to the observed values; the agreement is reasonable in the case of Si, but Ni segregation is under predicted. This is due to the fact that the model does not treat co-segregation of solutes (and solute-solute interactions in the semi dilute local micro-alloy regions at dislocations) that lower free energies in the segregated regions. Cu, Mn and P segregation that is observed in the T91 data is also shown but was not been modelled by Ke et al. (2019).

Notably, distinct α' precipitates were not observed in either irradiation conditions. The Cr solubility limit is $\sim 8.8 \pm 0.5$ at% [186, 187, 319, 320] at 300 °C. Thermal α' precipitation can occur but is sluggish. However, Cr precipitation is greatly accelerated by RED [320]. The absence of α' in T91 is due likely to the low, or absent, Cr supersaturation, depending on the temperature. Such low supersaturations are insufficient to form significant populations of small, discrete α' precipitates. Results in the literature on α' precipitates vary [186, 187, 289, 321]; for example, SANS [193] showed that a T91 alloy neutron irradiated to 0.7 dpa at 325 °C in the OSIRIS reactor

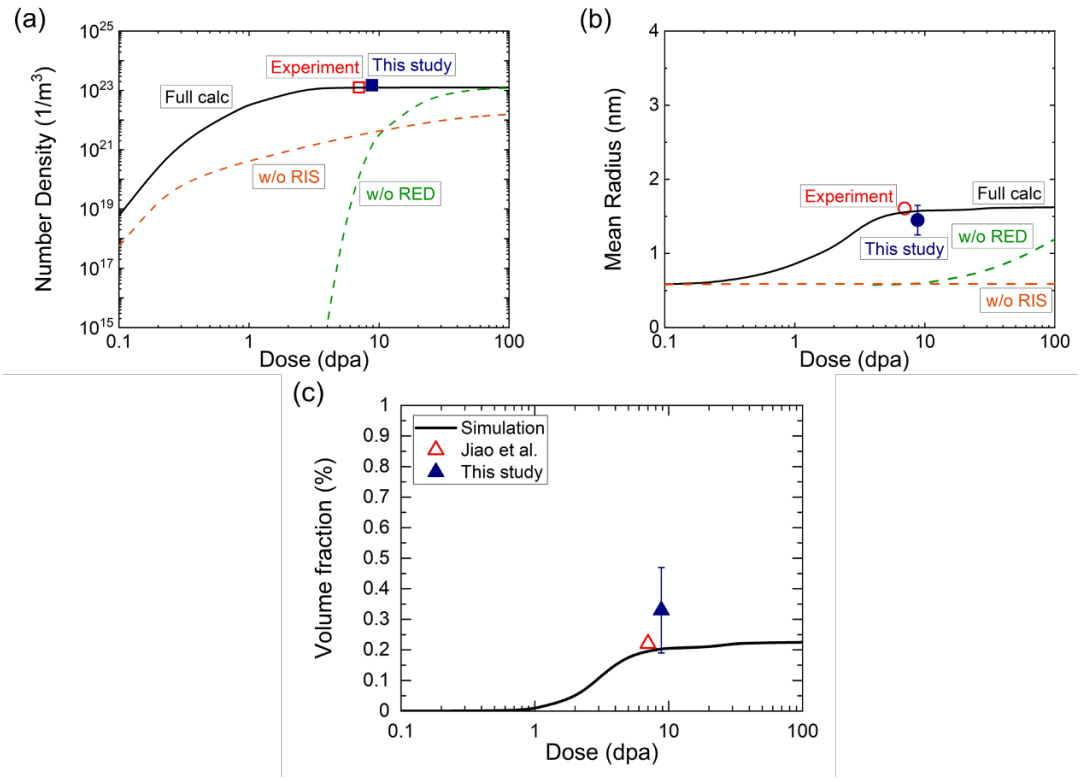

Figure 4.5.1: The comparison between the T91 MNSP (a) number densities, (b) radii, and (c) volume fraction with the model developed by Ke et al. (2018) [181]. Permission for reproducing Ke et al. (2018) [181] data has been granted.

contained a small volume fraction ($\sim$ 0.1%) of a high density (9.0×10^{23} m^{-3}) of α' precipitates with an average radius of 1.3 nm. Conversely, SANS and TEM did not observe α' in a T91 steel irradiated to 184 dpa since it was irradiated at a higher temperature of 413 °C in the Fast Flux Test Reactor [164].

While not the primary focus of this work, it is useful to briefly discuss the thermodynamics that appear to be at work here. As noted previously, the crystal structure of the MNSPs was not measured. However, the results show that the compositions fall near the Si(Mn,Ni) phase field (as calculated by Xiong et al. (2014) [299]), and as seen in figure 4.4.3. Further, H. Ke et al. (2017) [315] reported the existence of a $Mn_{15}Ni_{45}Si_{40}$ compound TI phase in the 800 °C Mn-Ni-Si isotherm, also shown in figure 4.4.3. These compositions bracket those found in this study, and at least one

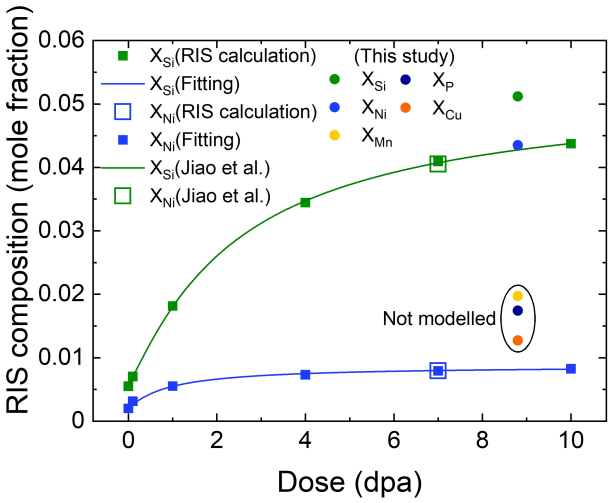

Figure 4.5.2: The comparison between T91 Si and Ni segregation to dislocations observed with predictions by Ke et al. (2018) [181]. The observed segregation of Cu, Mn and P is also shown but was not modelled in the original study by Ke et al. (2018) [181]. The 2.14 dpa data point was not included due to the lower temperature irradiation condition. Permission for reproducing Ke et al. (2018)) [181] data has been granted.

other on a similar T91 at 500°C and 3 dpa [322].

A full thermodynamic assessment of these phases is not yet available. However, the bulk and segregated alloy compositions can be compared to the thermodynamic solute product requirements for G-phase formation by the reaction:

$$16\mathrm{Ni}_s + 6\mathrm{Mn}_s + 7\mathrm{Si}_s \rightleftharpoons \mathrm{Ni}_{16}\mathrm{Mn}_6\mathrm{Si}_7 \tag{4.5.1}$$

where the subscript s denotes that the solutes are in solution. Thus, the reaction solute product, SP, is:

$$\mathrm{SP} = \{[X_{\mathrm{Ni}}]^{16} \times [X_{\mathrm{Mn}}]^{6} \times [X_{\mathrm{Si}}]^{7}\}^{\frac{1}{29}} \tag{4.5.2}$$

where X_i are the mole fractions of the dissolved Ni, Mn and Si. The equilibrium solute product (SP_e), or phase boundary, at 377 ° C is $\sim 5 \times 10^{-3}$ [299]. Fe is not considered as it is assumed it does not precipitate with Mn, Ni, and Si. The APT composition X_i values in table 4.3.1 yield an alloy solute product of $\sim 4.3 \times 10^{-3}$;

thus, the bulk system is nominally slightly undersaturated. In contrast, the local peak segregated X_i for Mn ∼0.01, Si ∼0.05 and Ni ∼0.02 , in figure 4.4.7(c) produces a local alloy SP of ∼ 0.044 (from eq. 4.5.2), which is highly supersaturated. The difference between the composition of G-phase, and that found in this work, is almost certainly due to the unusually high Si concentration in the segregated region. As shown by J. Ke et al. (2018) [181], RIS results in Ni and Si segregation, which is sufficient to drive precipitation. However, it should be noted that thermal segregation and precipitation, which is greatly accelerated by RED, could also be significant [323–325].

4.6 Conclusions

APT was used to understand the effect of neutron irradiation on solute segregation, CRP and MNSP co-precipitation in T91 steel. Two ATR irradiation conditions were investigated: 2.14 dpa at 327 °C and 8.82 dpa at 377 °C. The key observations are as follows:

- The compositions of all the MNSPs were similar and fell near the Si(Mn,Ni) phase field. While the structure of the precipitates has not been characterised, this composition range is distinctly different than that for the typically cited G-phase, which is consistent to the observations of MnSi precipitates in neutron irradiated low Ni % RPV steels;
- Co-precipitation of CRPs and MNSPs were observed, and the MNSPs appear as an appendage to the CRPs;
- Significant solute segregation (P, Si, Ni and Mn) to dislocation lines and loops is observed, with large enrichment factors for Si and Ni ∼ 10;
- MNSP and CRP form on the microalloy regions at dislocation lines and loops;

- CRP-MNSP number densities, sizes and volume fractions, as well as Si solute segregation to dislocations, are in good agreement with predictions of a previously reported model, combining solute segregation and CD mechanisms. Ni solute segregation to dislocations is under predicted in the modelling;
- α' formation was not observed in any atom probe data sets.

Overall, this study has provided an insight into the cluster composition, volume fractions and sizes, which may contribute to a better understanding of the embrittlement in T91 steel. Moreover, this study highlights how essential APT data is for reliable cluster dynamic modelling. If successful, then these models could predict real-world performance of critical reactor components, which, in turn, could lead to better understanding of how nuclear materials degrade in reactor cores.

However, neutron irradiation experiments are time consuming, expensive, and a radiological hazard to humans and the environment. Therefore, ion irradiation is used to study radiation damage (whether as a surrogate or in tandem with neutron irradiation) of materials under a controlled, quick, and safe environment. The next chapter investigates the use of ion irradiation to study RIS and RIP in T91 ferritic-martensitic steel, and effects on the mechanical properties via nanoindentation.

Chapter 5

Microstructure and Mechanical Properties of Ion Irradiated T91 Steel

5.1 Preface

The previous chapter investigated the RIS and RIP of neutron irradiated T91 ferritic-martensitic steel and reflected the realistic effects of neutron irradiation. However, conducting neutron irradiation experiments is time consuming (months to years), expensive (hundred thousand to millions of US dollars) and produce radioactive materials. Charged particle irradiation is a technique that has been developed for the simulation of neutron irradiation [71, 123, 127, 131]. Ion irradiation experiments have the added benefit of inducing little or no long-term radioactivity [131], they are low cost and generally quick (experiments can be conducted within a few hours). Therefore, the main objectives of this research chapter are based on applying ion irradiation as a tool to investigate RIS and RIP in T91 ferritic-martensitic steel at reactor relevant conditions. This second research chapter is heavily based on the submitted paper (Ref. [326]):

T. P. Davis, M. A. Auger, C. Hofer, P. A. J. Bagot, M. P. Moody, and D. E. J. Armstrong, 'Nanocluster evolution and mechanical properties of ion irradiated T91 ferritic-martensitic steel', Journal of Nuclear Materials, 2021, 547, 152842

The contributions to the paper are as follows: T. P. Davis provided conceptualisation, writing, scientific development, editing, atom probe data collection, analysis and conclusions; M. A. Auger provided supervision and manuscript editing; C. Hofer for figure 5.4.3; P. A. J. Bagot provided supervision, manuscript editing, and figure 5.4.3; M. P. Moody provided supervision and manuscript editing; D. E. J. Armstrong provided supervision, funding, and manuscript editing.

5.2 Introduction

Neutron irradiation is a driving force for microstructural and microchemical evolution. As discussed in Chapter 4 Section 4.2, one of the defining microstructural features that results from neutron irradiation of ferritic-martensitic steels is the formation of MNSPs [164, 166, 288], as shown in Chapter 4, α' formation (Cr-rich) [164], voids [34] and solute segregation towards dislocations [166]. These degrade the materials properties [163, 327], which is of concern for the safe operation of the material [42].

However, as aforementioned neutron irradiation experiments are time consuming, expensive, and induce radioactivity; thus, charged particle irradiation has been used to simulate neutron irradiation effects. In general, it is not possible to slow down irradiation damage to match that of neutron irradiation observed in nuclear reactors [142]; however, some researchers have introduced a "temperature shift" [106, 328] to compensate for the large difference between ion ($\sim 10^{-3} - 10^{-6}$ dpa/s) and neutron dose rates ($\sim 10^{-7} - 10^{-9}$ dpa/s). The effectiveness of this 'temperature shift' method to mimic neutron irradiation damage has been contested [142]. Nevertheless, within this study, heavy ions irradiation will be used as it is a useful experimental tool for fine control of fundamental scientific studies on the microstructure and mechanical

properties caused by irradiation [106, 125, 131].

It is known that α' does not nucleate under self-ion irradiation of Fe-Cr-based alloys unless the flux is $\leq 10^{10}$ ions/cm^2/s [188]. Previous studies on heavy ion and proton irradiated T91 steels [70, 83] have reported segregation of Cr, Si and Ni to dislocations, grain boundaries and matrix interfaces. Wharry and Was (2013) [296] produced a systematic study using STEM and energy dispersive x-ray spectroscopy (EDX) on proton irradiated T91 steel over a 300 – 700 °C temperature range, which revealed a peak in radiation-induced segregation (RIS) of Ni, Si and Cu between 400 – 500 °C. MNSP have also been observed with APT in T91 steel when subjected to proton-irradiation at 400 and 500 °C [70]. These studies reported that Cr, Si, Ni and Cu enrichment occurs at prior-austenite grain boundaries; however, attempts to de-convolute the synergies that were at play (temperature, dose, dose-rate, ion species etc.) was not done in that study.

Pareige et al. (2015) [173] confirmed that Cr, Si and P clusters were formed by the radiation-induced segregation and radiation-induced precipitation mechanisms, rather than a thermodynamic mechanism. Model Fe-9Cr alloys were used with varying controlled impurities of Si, P and Ni. It was suggested that P played a significant role in the appearance and stabilisation of point defect clusters. These clusters are thought to act as nucleation sites for Ni, Si and Cr. Gómez-Ferrer et al. (2019) [178] further investigated MNSP in model Fe-9Cr alloys to determine whether they are formed by irradiation or thermodynamics. APT was used to investigate the chemical segregation of Fe-9Cr model alloys irradiated with 5 MeV Fe^{2+} to 0.1 and 0.5 dpa at 300 °C. These model alloys had a controlled set of alloying additions (P, Ni and Si). The authors suggested that P was a faster diffuser than Ni and Si. It is worth noting that P precipitated up to a dose of 0.1 dpa and such P precipitates saturated in number density beyond 0.1 dpa. P forming a stable complex [329] which can act as a nucleation point for further clustering. At an increased dose (0.5 dpa), P, Ni and Si were shown to preferentially cluster together. These studies used model al-

loys to understand the fundamental influence of P, Ni and Si to the RIS mechanisms, which could underpin the understanding of MNSPs in real-world steels. Therefore, it then naturally follows to investigate the clustering dependence on irradiation dose on such a commercially used steel, as determined in Chapter 4 for neutron irradiated T91 commercial grade steel. Pareige et al. (2015) and Gómez-Ferrer et al. (2019) did not include any Mn alloying addition and it is known for T91 steel that Mn clusters with Ni and Si [42, 130, 164, 166, 173, 174, 288]. There has been no systematic study (same temperature and dose rate) to date on the fundamental microstructure precipitation and evolution in T91 steel caused by self-ion (iron) irradiation.

Furthermore, parallels can be drawn between the understanding of precipitation in reactor pressure vessel (RPV) steels as extensively done within Chapter 4 so the review for this will not be repeated. However, the single major difference between the RPV and Fe-Cr alloy systems is that the solute contents (Ni, Si, Mn, etc.) of the latter are typically much lower. Thus, embrittlement at high doses suggests that solute segregation to and heterogeneous nucleation on dislocations could be the cause rather than solute supersaturation (since the solute contents in Fe-Cr are low), as found with the research and conclusions found in Chapter 4. Therefore, the objectives of this study are:

1. To use APT and nanoindentation techniques to investigate the role and segregation of Mn, Ni, Si and P in self-ion irradiated T91 ferritic-martensitic steel;
2. To conduct the study at a single temperature and only vary the irradiation dose;
3. To investigate any links between MNSPs and changes in mechanical properties.
4. compare the cluster characterisation of ion and neutron irradiated steels.

5.3 Experimental Method

5.3.1 T91 Ferritic-Martensitic Steel

For the material to be classified as 'Grade 91', it must meet the manufacturing international standards. Eighty kg of ASTM F91 A182-16a [309] (cast number 381056) was purchased from Abbey Forged Products Ltd, United Kingdom, for the material used in this study (and future studies). ASTM A213 T91 was not chosen as the thin walled tube geometry was impractical, thus two forged F91 bars (⌀78 mm by 1000 mm) were delivered to the Department of Materials, University of Oxford. The steel herein will be referred as T91 in accordance with extensive literature referring to it by this name (regardless of manufacturing form) due to its primary application as tubing for fuel cladding and heat exchangers. The AR steel was normalised at 1040 °C, tempered at 730 °C and air cooled. In accordance with the British Standard EN 10204.3.1, the mechanical testing resulted in: 599 MPa 0.2% Proof Stress, 689 MPa Tensile stress, 21% elongation, and 220 HV hardness. The bulk and APT composition is given in Table 5.3.1. The composition and mechanical testing confirmed that the steel met the ASTM A213 standard. For the ion irradiations, ⌀3mm by 1mm discs of T91 steel samples were produced by electrical discharge machining and polished to a mirror finish by standard polishing techniques using silicon carbide grinding papers, diamond polish and colloidal silica suspension. AR T91 analysed using APT received the same thermal history as the T91 steel specimens exposed to ion irradiation (these cantilevers were taken on the backside of the ion irradiated samples). The motivation for this was to determine whether MNSPs were thermally activated, rather than irradiation enhanced.

Table 5.3.1: The measured bulk composition (wt. % and at. %) and averaged matrix APT composition measurement and the corresponding standard deviation (at. %) of ASTM F91 A182-16a [309]. The APT composition and associated errors were based on the difference between multiple mass spectrum ranges.

	C	Mn	P	S	Si	Cr	Mo	Nb	Cu
Bulk (wt %)	0.105	0.420	0.017	0.020	0.370	8.620	0.920	0.070	–
Bulk (at %)	0.483	0.422	0.030	0.034	0.727	9.151	0.529	0.042	
APT (at %)	0.04 ± 0.01	0.41 ± 0.01	0.07 ± 0.01	–	0.93 ± 0.01	7.99 ± 0.09	0.46 ± 0.04	–	0.02 ± 0.01
	N	Al	V	Ti	Zr	Ni	Co	Fe	
Bulk (wt%)	0.0485	0.01	0.212	0.002	0.005	0.250	–	Bal.	
Bulk (at %)	0.191	0.020	0.230	0.002	0.003	0.225	–	Bal.	
APT (at %)	–	0.02 ± 0.01	0.07 ± 0.01	–	–	0.47 ± 0.01	0.01 ± 0.01	89.53 ± 0.17	

5.3.2 Ion Irradiation

The ion irradiation was conducted using the Dalton Accelerator for Nuclear Experiments (DAFNE) at the Dalton Cumbrian Facility, University of Manchester, United Kingdom [330]. DAFNE is a 5 MV tandem Pelletron ion accelerator which used a Source of Negative Ions by Caesium Sputtering (SNICS) that produced Fe ions with a 4+ charge state. The stage charge was measured by an isolated wire which was attached to the target stage. The ion flux (in ions/cm^2/s) was calculated by the following expression:

$$\phi = \frac{I}{\epsilon q A} \tag{5.3.1}$$

where I is the current on the specimen target stage in Coulombs/s, ϵ is the charge state, $q = 1.602 \times 10^{-19}$ C, the charge of a single ion, and A is the beam area. The ion beam was rastered. The effects of a defocused and rastered ion beam on irradiation experiments has been researched by Getto et al. (2015) [294] indicating

that defocused beam produced better results.

T91 steel has been subjected to two ion irradiating conditions: low and high dose. The low dose experiment was irradiated with 5 MeV Fe^{4+} ions that had a 4.8×10^{11} ions/cm^2/s flux and a 3.5×10^{14} ions/cm^2 fluence at 301.1 $\pm$ 2.3 °C (average temperature over the experiment), which was 0.1 dpa at 240 nm depth from the surface calculated using SRIM 2008 software [105]. The beam spot size was 4.7 $\pm$ 0.5 cm^2 and total charge on the sample was 1.097 $\pm$ 0.010 mC. The high dose experiment was irradiated with Fe^{4+} ions that had a 4.4×10^{11} ions/cm^2/s flux and a 6.5×10^{15} ions/cm^2 fluence at 311.9 $\pm$ 5.2 °C (averaged over the experiment), which was 1.83 dpa at 240 nm depth from the surface, as shown in figure 5.3.1. The beam spot size was 6.50 $\pm$ 0.5 cm^2 and total charge on sample was 27.010 $\pm$ 0.010 mC. Best efforts were made to maintain the temperature at the target temperature of 300 °C and maintain similar ion flux. The SRIM calculation followed the recommendations provided by Stoller et al. [99]; 'Quick Kinchin-Pease calculation' was selected, displacement damage threshold values were selected from the ASTM E521 standard [97] (Fe and Cr displacement energies was set to 40 eV), and the lattice binding energy was set to zero. The dpa per second per ion penetration depth (in µm) was calculated by the following expression:

$$\text{dpa/s/µm} = \frac{\nu\phi}{N_f} \tag{5.3.2}$$

where ν is the integral of the second and third columns of the 'vacancy.txt' SRIM 2008 output file, ϕ is the ion flux (ions/cm^2/s) calculated by eq. 5.3.2 and N_f is the number density as a function of penetration depth (in µm). The ion irradiation dpa profiles as a function of depth from the surface were calculated by eq. 5.3.2 for both low and high dose irradiation experiments and is shown in figure 5.3.1.

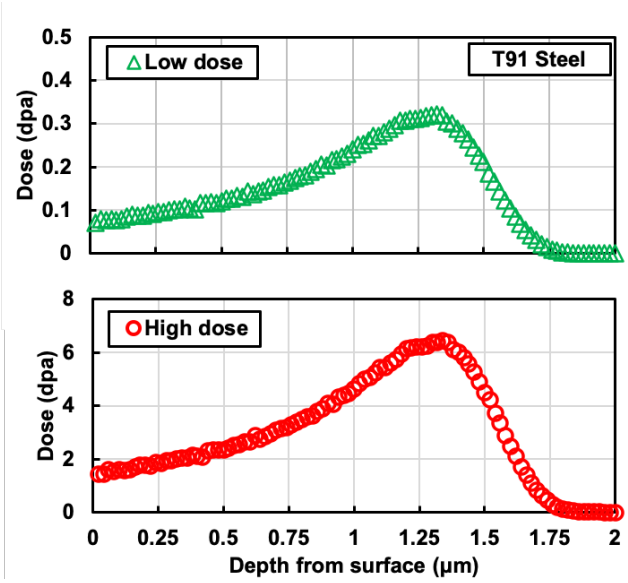

Figure 5.3.1: The Fe^{4+} heavy ion irradiation damage profiles of T91 steel as a function of depth at temperatures of 301.1 ± 2.3 °C (low dose, where the dpa was 0.1 dpa at 240 nm depth) and 311.9 ± 5.2 °C (high dose, where the dpa was 1.83 dpa at 240 nm depth).

5.3.3 Atom Probe Tomography

The majority of atom probe analysis was conducted with a CAMECA LEAP® 5000 XR at the Department of Materials, University of Oxford, with supplementary experiments targeting grain boundaries on a CAMECA LEAP® 3000X HR at the Department of Materials Science, Montanuniversität Leoben (only TKD figures). Atom probe specimens were prepared by the lift-out technique [241] using a Zeiss NVision 40 FIB-SEM. Cleaning of the specimens was performed on all samples using 2 kV Ga ions to minimise FIB-induced damage. All atom probe samples had tip diameters that were approximately between 50 – 100 nm. For samples prepared in Leoben, matchsticks (∼0.5 mm diameter) of AR T91 were electropolished using 25% perchloric acid in acetic acid. Finished specimens were transferred to a ThermoFisher Versa 3D dual-beam FIB system to determine if any grain boundaries were suitably close to the tip (within ∼ 200 – 300 nm). Where present, Ga-ion sharpening was used to locate identified boundaries closer to the actual tip apex, and to shape the

final sample. TKD scans were carried out between each milling step to determine the grain boundary misorientation angles. There was no need to change stage tilt or rotation, since suitable patterns were obtained in the same position as used for milling, ensuring fast, repeated scanning. The patterns were recorded with an EDAX Hikari XP electron backscatter diffraction (EBSD) system at an acceleration voltage of 30 kV. Data analysis was conducted using the software OIM Analysis 7 from EDAX. All suitable APT samples were analysed at a stage set-point temperature of 50-55K. A voltage pulse fraction of 20% was selected with a pulse rate of 200 kHz and the average detection rate was set to 0.5 %. For specimens prepared with grain boundaries, laser pulsing was used to improve yield, running at a pulse energy of 0.6 nJ and a rate of 160 kHz. CAMECA IVAS 3.8.4 was used to reconstruct all atom probe datasets contributed to this study. Calibration of the final reconstructed APT maps used SEM micrographs/TKD orientation maps of the final tip shape and crystallographic pole indexing.

It should be noted that all ion irradiated lift-out cantilevers were made perpendicular to the surface to capture a 'uniform' damage profile parallel to the APT tips.

For MNSP cluster search in the APT data, the same procedure used in Chapter 4 and Ref [258, 262, 288] was used within this ion irradiation study. The cluster search algorithm for MNSP is outlined in 3.1.6. The values for the cluster search ($D_{\max}$, N_{Min}, O, and number of clusters) are found in Chapter 3 Table 3.1.1. All APT and cluster search parameters can be found in Chapter 3 table 3.1.2.

5.3.4 Nanoindentation

An Agilent G200 nanoindentor was used to measure hardness of T91 steel by indenting a colloidal-silica polished surface to a 2 µm indentation depth at room temperature (21 °C). The methodology is outlined in the experimental methods found in Chapter 3 Section 3.3. A continuous stiffness measurement system with a 2 nm 39 Hz harmonic displacement was used to measure the modulus and hardness as a function of

indentation depth. A Berkovich tip was used and the tip area coefficients were calculated from the average load-displacement data of sixteen 2 µm indents into fused silica. Thus, using the known area function and contact stiffness as a function of tip displacement, the hardness of T91 steel was calculated as a function of tip displacement.

5.4 Results

5.4.1 AR T91 Steel

The matrix volume composition reported by the atom probe reconstructions for the AR T91 steel is found in Table 5.3.1. The grain structure of T91 is shown in figure 5.4.1. A typical reconstruction volume of AR T91 steel is shown in figure 5.4.2. This ion map shows two grain boundaries decorated with P, Mn, Si, Mo and C, as expected due to the typical normalisation and tempering treatments for this type of steel. Analysis of the grain boundaries using TKD and APT is shown in figure 5.4.3. The 38° boundary was likely a prior-austenite grain boundary due to the impurity level, whereas the 50° boundary was likely a martensite lath (due to no segregation of impurities and solute elements). No visual clustering of Si, Mn, Ni, Cu, Cr, Mo, or V was detected with the APT data, while prior-austenite grain boundaries were slightly enriched with P, Mo, Ni and C, which was expected for ferritic-martensitic steels. These AR solute microstructure details provide a useful baseline for the starting microstructure before irradiation. Finally, the AR T91 steel nanoindentation hardness and modulus were found to be 4.08 ± 0.25 GPa and 174 ± 42.1 GPa, respectively (calculated between 230 to 250 nm in the load-displacement curve), which is shown within a later figure under the irradiation results section (see figure 5.4.8).

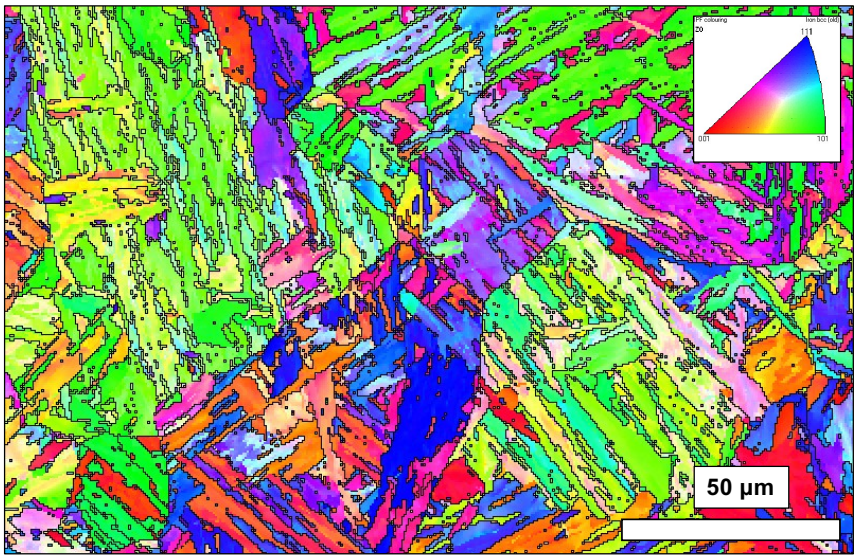

Figure 5.4.1: AS T91 steel typical grain structure. The average prior austenite grain size and martensitic lath grain size were $\sim 40-60$ µm and $\sim 2-10$ µm, respectively.

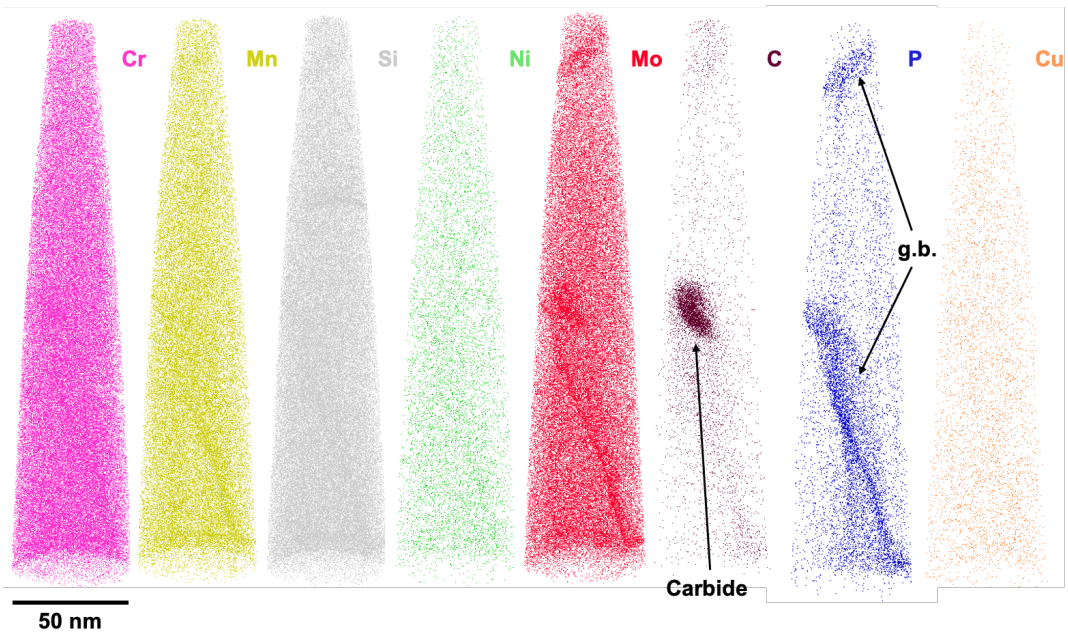

Figure 5.4.2: : Atom probe reconstructions of AR T91 steel, showing segregation of Mn, Si, Ni and P species to a grain boundary and a Mo-based carbide.

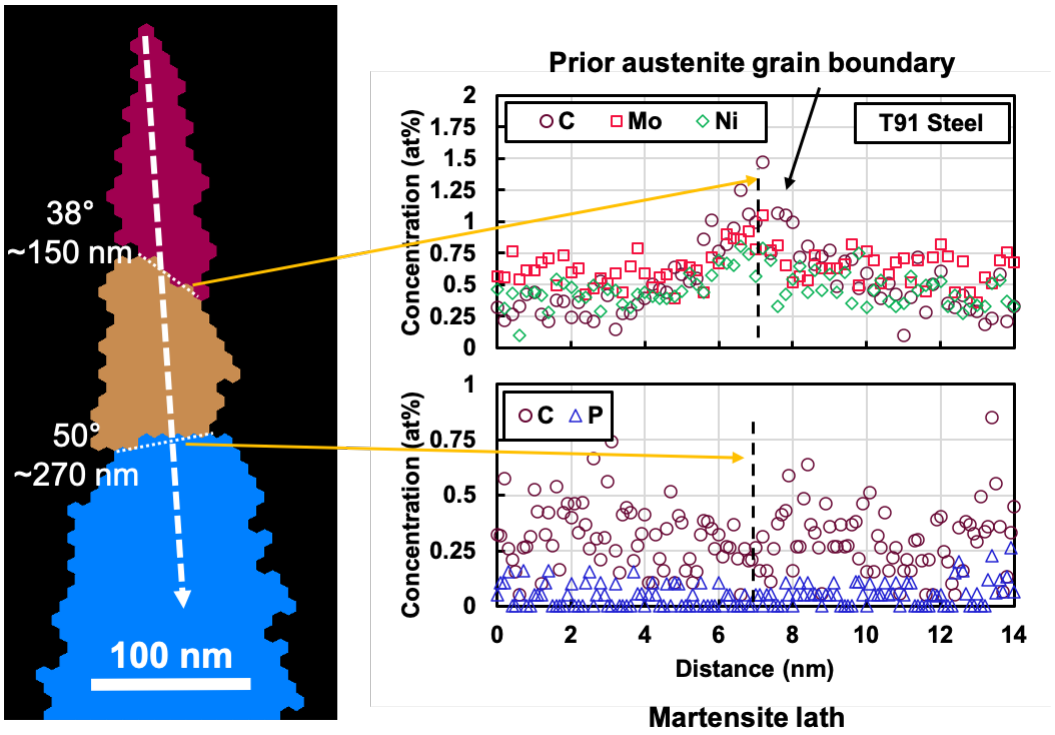

Figure 5.4.3: AR T91 steel grain boundary analysis. The 38° boundary was likely a prior-austenite grain boundary due to the increase in solute atoms (Mo, C and Ni), whereas the 50° boundary was likely a martensite lath (due to the no observed increase in C and P, and displaying compliance to the Kurdjumov–Sachs orientational relationship). The dotted vertical lines on the concentration profiles represent the relevant position of the grain boundaries (white dotted lines) in the APT dataset.

5.4.2 Ion Irradiation Damage Profiles

The ion irradiation dose (dpa) damage profiles as a function of depth from the surface were calculated by equation 5.3.2 for both 'low' and 'high' dose irradiation experiments and are shown in figure 5.3.1. The irradiation dose (dpa) was taken as the average between 200 nm to 250 nm depth from the surface. To capture the low dose ion irradiation microstructural effects in APT, careful FIB milling was performed 100 nm below the irradiated surface. This region was damaged to 0.12 dpa, as shown from the ion damage profile in figure 5.3.1. The motivation behind this was to determine whether Si/P plays a significant role in the initial irradiation stages during 5 MeV

Fe^{4+} ion irradiation at 300 °C.

APT reconstructions of the T91 steel ion irradiated to the 'low' and 'high' doses are shown in figure 5.4.4(a)-(c). The range of dose damages examined can be explored by selecting specific depths from the sample surface for APT analysis, as damage is strongly dependent on irradiation depth. P/Si-rich clusters can be seen after irradiation to 0.12 dpa at 301.1 ± 2.3°C in figure 5.4.4(a). Increasing the irradiation dose to 2.62 dpa at 311.9 ± 5.2°C reveals the formation of MNSP, as seen in figure 5.4.4(b) and (c). Solute (Si, Ni and P) segregation to line dislocations can be seen in figure 5.4.4(b). The formation of P/Si-rich clusters is further revealed by a 1.0 % at. P isosurface and corresponding proxigram, as shown in figure 5.4.5. The extent of P segregation to clusters is between 3 -4 at % at the core, which is significant considering the bulk P was 0.065 at%, as shown in Table 5.3.1. The average MNSP composition as a function of irradiation dose can be seen in figure 5.4.6 on a Mn, Ni and Si ternary projection of a Fe based phase (similar approach taken in Chapter 4 and Ref. [288]), and the composition values were calculated using the method outlined in Chapter 3 Section 3.1.6. MNSPs are a defining irradiation-induced feature in ferritic-martensitic steels (such as T91 steel) and are observed in figure 5.4.4(b) and (c) APT reconstructions at 2.62 dpa and 4.1 dpa. By visual inspection of the reconstruction, these MNSP were enriched with P, but not Cu. MNSP's were not detected below a dose of 1.76 dpa, indicating there was a threshold value of dose. The average volume fraction, size, number density, cluster diameter and cluster composition are found in Table 5.4.1, and the methods used to calculate these values are outlined in Chapter 3 Section 3.1.6.

The presence of dislocation loops was observed by Si decoration in the 1.0 at % Si isosurface shown in figure 5.4.7. The dislocation loops had an average diameter of 13 ± 3 nm.

The nanohardness of T91 steel as a function of irradiated dose is shown in figure 5.4.8. The 'low' dose nanoindentation depth value was measured at 0.10 dpa and the

'high' dose nanoindentation depth value measured at 1.81 dpa. The nanohardness increase from AR condition to 0.10 dpa and 1.83 dpa was 13.1 % and 21.4 %, respectively. The exact nanohardness values for 0 dpa, 0.10 dpa and 1.83 dpa were 4.1 ± 0.3 GPa, 4.6 ± 0.2 GPa, and 5.1 ± 0.3 GPa, respectively.

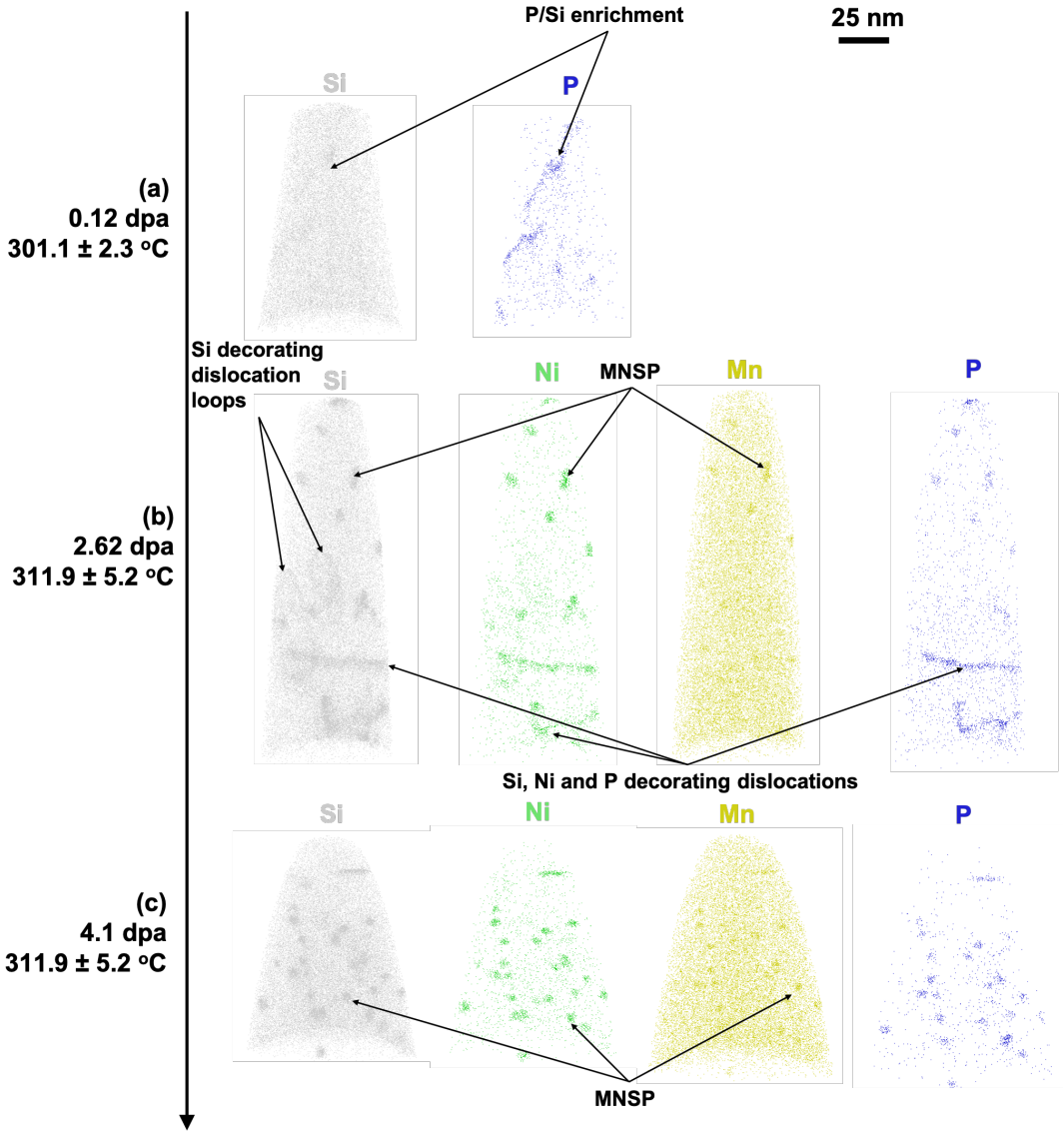

Figure 5.4.4: APT point cloud data from a dose range of T91 steel Fe^{4+} ion irradiated to (a) 0.12 dpa at temperatures of 301.1 ± 2.3°C for the 'low' dose and to (b) 2.62 dpa and (c) 4.1 dpa at 311.9 ± 5.2°C for the 'high' dose. Ni and Si were not displayed for (a) as they were uniformly distrusted in every APT dataset.

Table 5.4.1: The volume fraction, average radii, average volume, volume fraction and composition of MSNP as a function of ion irradiation dose at 311.9 ± 5.2 °C.The composition of the clusters is plotted in figure 5.4.6.

MNSP (only solute ions, excluding Fe)							
Ion dose (dpa)	Number Density (#/m^3)	Average Diameter (nm)	Average Volume (nm^3)	Vol. fraction (%)	Mn (at %)	Ni (at %)	Si (at %)
1.76	(2.7 ± 0.5) 10^{23}	1.2 ± 0.1	8.5 ± 2.5	0.17 ± 0.05	13.3 ± 3.4	36.7 ± 10.6	50.0 ±13.4
1.93	(2.4 ± 0.5) 10^{23}	0.8 ± 0.2	17.1 ± 5.0	0.41 ± 0.10	10.9 ± 1.6	42.0 ± 2.3	47.1 ± 2.7
2.62	(1.4 ± 0.5) 10^{23}	1.2 ± 0.2	23.4 ± 5.0	1.80 ± 0.15	9.2 ± 4.1	33.9 ± 5.7	56.9 ± 7.8
3.07	(1.8 ± 0.5) 10^{23}	1.0 ± 0.2	6.2 ± 3.0	0.26 ± 0.10	10.1 ± 4.9	27.3 ± 13.1	62.6 ± 17.3
4.10	(1.1 ± 0.5) 10^{23}	2.0 ± 0.2	15.2 ± 5.0	0.33 ± 0.10	10.6 ± 4.5	39.5 ± 7.7	49.9 ± 8.3

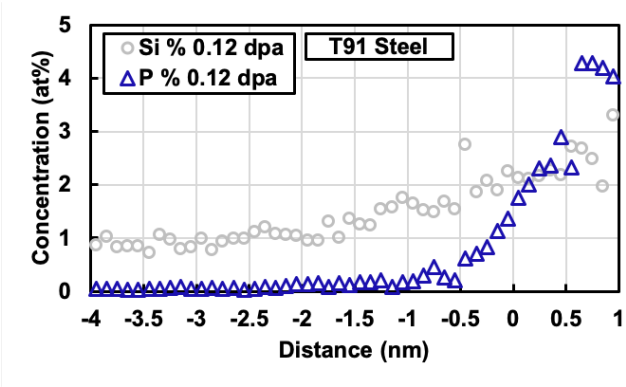

Figure 5.4.5: Proxigrams of 1.0 at.% P isosurfaces from P/Si enrichment clusters, as shown in figure 5.4.4(a) at 0.12 dpa.

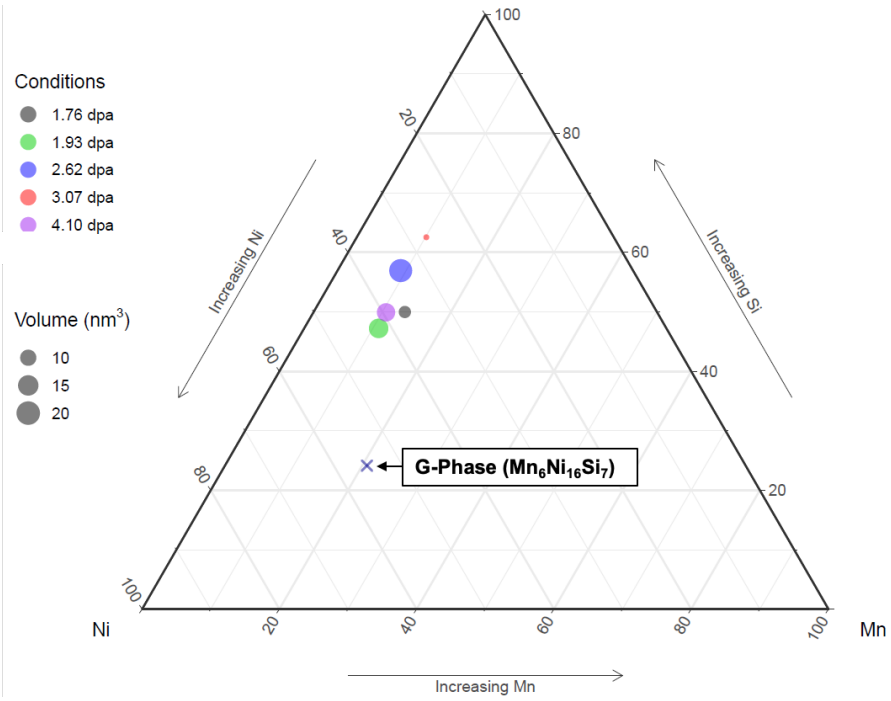

Figure 5.4.6: The Mn-Ni-Si MNSP composition (in at%) for each ion irradiation dose represented Mn, Ni, and Si ternary projection of a Fe based phase diagram. The size of the data point is scaled to the MNSP average volume (nm^3) per APT dataset and values are in Table 5.4.1. The 'G-phase' stoichiometric phase has been provided for reference [180].

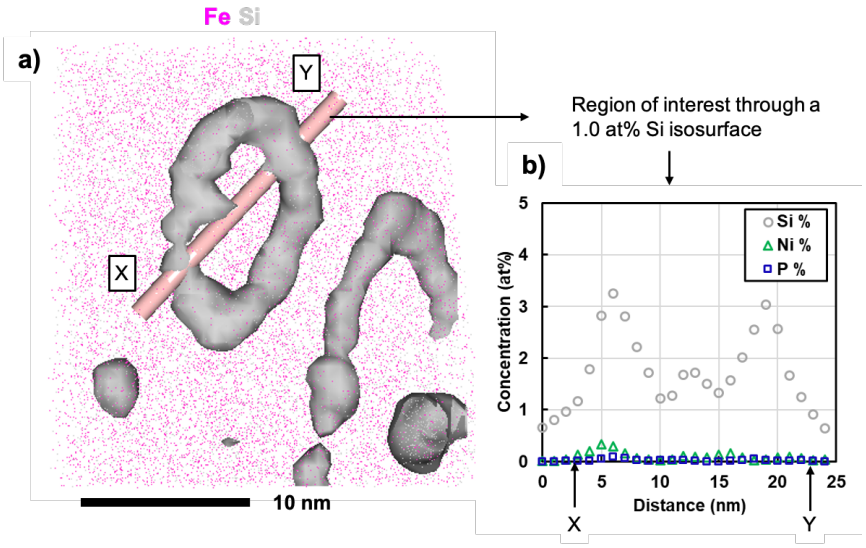

Figure 5.4.7: a) Segregation of Si to a dislocation loop in T91 steel irradiated to 2.62 dpa at 311.9 ± 5.2°C. b) 1D line profile of the concentration (at%) across the cylinder in a) highlighting the silicon enrichment.

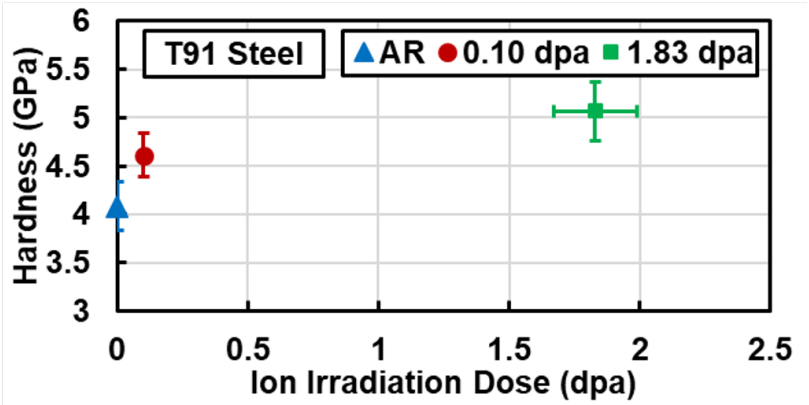

Figure 5.4.8: Nanoindentation hardness of the AR T91 steel and ion irradiated T91 steel to 0.10 and 1.83 dpa.

5.5 Discussion

The primary aim of this study was to investigate the role that minor alloying elements and impurities have on a real-world nuclear-grade steel, such as T91 steel. Multiple AR T91 steel atom probe reconstructions were analysed, with the typical resulting microstructures shown in figures 5.4.2 and 5.4.3, exhibiting no visual clustering of solute elements. The AR results shown in this study provide the baseline microstructure before any comparison can be made once exposed to ion irradiation. Any changes to the grain boundaries and matrix regions can thus be a guide to the exposure of ion irradiation rather than thermal effects on their own. The limitation of this analysis is due to the sampling of grain boundaries is very limited.

The role The results shown in figures 5.4.4(a) and 5.4.5 indicate that, at 0.12 dpa, Si/P segregate and form clusters, in agreement with the work of Gómez-Ferrer et al. (2019) [178]. RIS is the likely mechanism behind the segregation, as it was confirmed that no clustering of P and Si was observed in the AR T91 material undergoing the same heat treatment, as shown in figure 5.4.2. This is also in agreement with previous studies on the role of P and Si at low heavy ion doses in steels [173]. No segregation of Ni was observed at these low doses, which is also in agreement with similar studies on Fe-15Cr alloys by Gómez-Ferrer et al. (2019) [178]. The findings within the study suggests that the low dose irradiation dynamics are dominated by P and Si and they are independent of whether the material is a model Fe-Cr alloy or a commercial-grade Fe-Cr steel. This systematic study of 'low' dose ion irradiation at a single temperature has shown that both P and Si dominate the early stages of segregation and clustering. These clusters could provide the nucleation sites for the MNSP observed at high doses, as discussed in the following sections. This line of argumentation can be reinforced by the diffusion constants of P and Si with a ferritic matrix. For example, the P diffusion constant is much greater than Si due to the low solubility of interstitial P within the ferritic matrix [331]. Whereas Si is a substitutional element

within the ferritic iron matrix (and thus has a lower diffusion constant compared to P).

MNSPs were observed once the irradiation dose surpassed 1.76 dpa, with the composition (as a ratio between Mn-Ni-Si) shown in figures 5.4.4 (c) and 5.4.6, and data listed in Table 5.4.1. For increasing ion irradiation dose, the average diameter of MNSPs grew from 2.4 nm to 4.0 nm , as shown by the data in Table 5.4.1. The average volume size and volume fraction appear to be uncorrelated (which could be related to the sampling size limitation), while the overall composition of the cluster population remains approximately constant rather than tending towards the theoretical 'G-phase' composition. This is shown in the ternary Mn-Ni-Si phase diagram provided in figure 5.4.6. The average composition of MNSP did not correlate with the G-phase composition. MnSi(Ni) phase has been observed on dislocations in VVER-440 RPV steel that had low nickel (0.07 at.%) [257]. The T91 steel investigated in this study had 0.225 at. % Ni bulk content, whereas most RPV steels investigated within the literature are between 0.7 – 1.9 at.% Ni [80].

The Mn, Ni, Si and P solute evolution is similar to that in model Fe-Cr alloys with P/Si/Ni impurities used to study their individual effects [173, 178]. However, the Fe-Cr binary alloy investigated within those studies did not contain Mn, an alloying element that has shown clear influence on the formation of MNSP in Fe-Cr and RPV steels. Wharry et al. (2011) [70] reported that the MNSP number density was between $5 - 7 \times 10^{22}$ m^{-3} with a diameter of 3 – 5 nm in 2 MeV proton irradiated T91 steel for up to 10 dpa at 400 °C. The number density reported within this study is $1.1 - 2.7 \times 10^{23}$ m^{-3} with an average diameter 1.3 – 4.0 nm (as provided in Table 5.4.1). The major difference between these two studies is Wharry et al. (2011) conducted the experiment at 400 °C whereas this study was conducted at 311.9 $\pm$ 5.2 °C; as expected with an increase in temperature, the number density of the MNSP would decrease due to the increase in the rate of solute diffusion.

Ion damage cascades form dislocation loops [292] at 300 °C. At the 'high' dose,

Si segregated to the periphery of dislocations as shown in figure 5.4.7(a). These Si-decorated dislocations have either a line and/or loop formation, and these loops have an average diameter of 13 $\pm$ 3 nm. Si has been observed to segregate, along with Ni, to dislocations lines and loops in ferritic-martensitic steels [332]. Conversely, Cr has been predicted by modelling to decorate loops in irradiated Fe-Cr alloys [333] but this has not been observed in the current work. Additionally, not all of the dislocations (loop and line type) observed in the APT datasets had P-enriched peripheries; line dislocations were decorated with P and Ni, as shown in figure 5.4.4(c) following 2.62 dpa irradiation, but loop dislocations were observed as decorated only with Si (shown in the same figure for 2.62 dpa). A suggestion to explain this result is that these Si-enriched loop dislocations were introduced by irradiation displacement damage rather than by the manufacturing process.

Prior to irradiation, pre-existing dislocations would become the first to be decorated with P due to the large diffusion affinity to form stable complexes [329]. From the low dose irradiation at 0.12 dpa, P has already clustered and, thus, becomes depleted within the matrix. The formation of loop dislocations by displacement damage would form within this now P-depleted matrix. It is therefore not possible for P to decorate the newly formed dislocation loop. This provides a feasible explanation for the observation of no P decorated dislocation loops following irradiation at 300 °C.

The nanohardness increase from AR condition to 0.10 dpa and 1.83 dpa was 13.1 % and 21.4 %, respectively, as shown in figure 5.4.8. For comparison, Hardie et al. (2015) [334] ion irradiated Fe-12%Cr binary alloy with Fe ions at 320 °C at 2 MeV to 6.18 dpa and showed that the hardness increased from 1.31 GPa (unirradiated) to 1.9 GPa (irradiated) with a Berkovich tip. It is well known that irradiation damage produces dislocation loops, increasing the dislocation density [292]. In addition to the dislocation density, the APT results show, even at low doses, that the formation of P and Si clusters likely contributes to hardening of the steel. These clusters act as dislocation motion barriers; however, direct observation of this pinning would

involve utilising TEM to image the plastic zone beneath the nanoindent (which is beyond this study, however Chapter 6 and subsequent publication Davis et al. (2020) [335] performed a similar study that examined the dislocations becoming pinned by nanoparticles beneath nanoindents; the size of the nanoparticles were 2 – 5 nm, which is comparable to the size of the MNSP observed within this study).

The hardness response as a function of irradiation dose was not linear, as shown in figure 5.4.8. The number density of MNSP remained within the same order of magnitude and did not increase with dose. The increase in hardness from the AR condition can be attributed to dislocation pinning on these irradiated-induced MNSP and dislocation loops becoming entangled during deformation. The density of these clusters should not be expected to increase after further irradiation as the matrix has been depleted of Mn, Ni and Si to form new clusters. This would lead to the observed tail-off in hardening from 0.1 dpa to 1.83 dpa as shown in figure 5.4.8. Any further increase in hardness with irradiation dose would be a resultant of solute segregation towards dislocations rather than the nucleation of more MNSPs within the matrix. Furthermore, the single major difference between Fe-Cr and RPV alloy systems is that the solute contents of Fe-Cr ferritic-martensitic steels are typically much lower than in low alloy RPV steels, while the dpa doses are much higher and the temperatures higher. This indicates that the significance of solute segregation to and heterogeneous nucleation on dislocations are critically important. This study highlights that solute segregation to and on dislocations in T91 steel occur under heavy ion irradiation at 311.9 ± 5.2 °C based on a small volume analysed with APT.

Direct comparisons of ion irradiated T91 steel can be made with neutron irradiated T91 analysed in Chapter 4 and Ref. [288]. These comparisons are as follows:

- First, the batch of steel used in the neutron and ion irradiation experiments were different, and considering the clustering dynamics is highly sensitive to solute additions (Ni, Si, Mn and Cu), these differences are shown in table 5.5.1. The notable difference is that the ion irradiated T91 steel has just under double the

amount of Si, a known fast diffusing solute addition. Ni and Mn additions are in similar quantities, with Cu impurities a third greater for neutron irradiated T91 steel.

Table 5.5.1: Comparison between solute elements in the two batches of T91 steel for the neutron and ion irradiation experiments. The full APT-measured compositions can be found in tables 4.3.1 and 5.3.1 for neutron and ion irradiation experiments, respectively.

	Solute Additions (at %)		
	Neutron	Ion	Δ
Ni	0.39 ± 0.02	0.47 ± 0.01	–0.08
Mn	0.41 ± 0.02	0.41 ± 0.01	0
Si	0.54 ± 0.01	0.93 ± 0.01	–0.39
Cu	0.03 ± 0.01	0.02 ± 0.01	0.01

- Regarding nucleation sites for MNSP, it should be noted that Cu impurities were detected in all APT datasets; however, no evidence of clustering was observed for the ion irradiated conditions. This observation is the opposite compared to that of the heavily CRPs in the neutron irradiated T91 steel discussed in Chapter 4 and Ref. [288]. The damage rate (dpa/s) were vastly different to the ion irradiated T91 steel in this study ($\sim 10^{-4}$ dpa/s) compared to neutron irradiation of T91 steel in chapter 4 ($\sim 10^{-7}$ dpa/s), which could have suppressed Cu clustering in the ion irradiated experiments due to possibly extra ballistic mixing.

- It appears that both for neutron and ion irradiated T91 steels, the formation of MNSP appears to lie within the MnSi(Ni) phase field as shown in figures 4.4.3 and 5.4.6. The combination of these conditions can be found in figure 5.5.1 further indicating similarities in composition of MNSP. In addition, this finding indicates that the near double amount of Si solute addition for the ion irradiated T91 steel had slighly increased the Si amount in MNSP (as shown by the Si increase in figure 5.5.1).

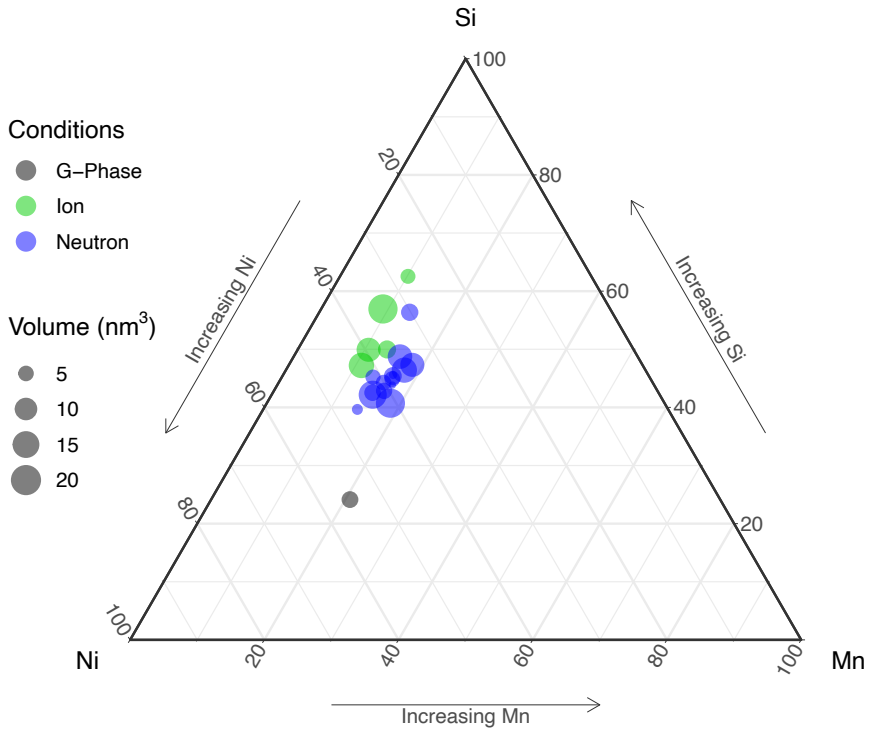

Figure 5.5.1: The Mn-Ni-Si MNSP composition (in at%) for neutron and ion irradiation dose represented Mn, Ni, and Si ternary projection of a Fe based phase diagram. The size of the data point is scaled to the MNSP average volume (nm^3) per APT dataset and values are in tables 4.4.1 and 5.4.1 for neutron and ion irradiation experiments, respectively. The 'G-phase' stoichiometric phase has been provided for reference [180].

- In comparison to the neutron irradiation MNSP cluster data from Chapter 4 Table 4.4.1, the MNSP number density was found to be $1.5 - 3.1 \times 10^{23}$ m^{-3}, which is a similar result. Further, the number density is in agreement with the modelling discussed in Chapter 4 figure 4.5.1.

- Along with the finding in Chapter 4 it should be noted that there was no observation of α' precipitation in any of the APT datasets. This was as expected because the kinetics do not enable the formation due to the high dose rate used in this study [188].

Such a direct comparison for T91 steel between ion and neutron irradiation con-

ditions has not been reported in literature to-date. The indication between the comparisons of these results shows the applicability of ion irradiation to understand RIP and RIS of T91 steel due to the similarities in the formation on MNSP in number densities and composition at similar temperatures (300 – 377 °C) and doses (1 – 8 dpa).

5.6 Conclusions

Overall, this ion irradiation study has provided an insight into how minor alloying elements and impurities evolve as a function of irradiation dose whilst maintaining the temperature and irradiation dose rate as fixed parameters by using APT and nanoindentation. The key findings from this were:

- Prior to irradiation, the AR T91 steel state showed no clustering of Mn, Ni, Si and P, with minor enrichment of impurities and alloying elements at the prior-austenite gain boundaries;
- MNSPs were observed at a ion dose of 1.76 dpa at 300 °C;
- The MNSP had a significant different composition to the typical cited 'G-Phase', which had a composition that fell near the MnSi(Ni) phase field and similar to that observed for the case of neutron irradiation of T91;
- The average diameter of MNSPs grew with dose, as expected;
- Dislocation loops were decorated with Si when irradiated to 2.62 dpa at 311.9 ± 5.2 °C;
- At 0.12 dpa, formation of Si/P-rich clusters were observed and increased the nanohardness by 13.1% from the AR condition. The hardness did not increase linearly as a function of dose but rather tailed off between 0.1 to 1.83 dpa.

- The direct comparison for T91 steel between ion and neutron irradiation conditions has not been reported in literature to-date. The findings show that ion irradiation can be used to study RIP and RIS of T91 steel to understand the fundamental mechanism before conducting neutron irradiation experiments.

Overall, this study has demonstrated the usefulness of ion irradiation to observe and understand the role of solute ions and impurities in commercial grade ferritic-martensitic steels, particularly when part of a controlled study varying irradiation over a number of dose conditions. Further, strong evidence has been presented for the viability of using ion irradiation as tool to understand RIP and RIS in T91 steels (and similar steels) to assist the understanding of neutron irradiation experiments. The APT and nanoindentation techniques have shown that, when applied in tandem, they can provide insight into how microstructural changes under irradiation can explain observed changes in mechanical properties.

Chapter 6

Characterisation of Deformation in Oxide Dispersion Strengthened Steels

6.1 Preface

This research chapter is heavily based on the published paper [335]:

T. P. Davis, J. C. Haley, S. Connolly, M. A. Auger, M. J. Gorley, P. S. Grant, P. A. J. Bagot, M. P. Moody, and D. E. J. Armstrong, "Electron microscopy and atom probe tomography of nanoindentation deformation in oxide dispersion strengthened steels", Materials Characterization, 167, 110477, 2020

The contributions to this paper are as follows: T. P. Davis provided conceptualisation, writing, scientific development, editing, atom probe data collection, analysis and conclusions; J. Haley provided TEM (Figs 6.4.8, 6.4.9, 6.4.10, 6.4.11, and 6.4.12) and interpretation of TEM micrographs, and writing up TEM sections; S. Connolly provided nanoindentation data for nanocrystalline Fe; M. A. Auger provided supervision and manuscript editing; M. J. Gorley provided ODS steel and manuscript editing; P. S. Grant provided manuscript editing and ODS steel; P. A. J. Bagot provided supervision; M. P. Moody provided supervision and manuscript editing; D. E. J. Armstrong

provided supervision, conceptualisation, data interpretation, and manuscript editing;

6.2 Introduction

As discussed in Chapter 1 Section 1.1.3, the fuel cladding materials of sodium-cooled fast reactors will experience intense neutron irradiation, high temperatures, and corrosive environments, which excludes the use of existing Generation II/III/III+ fuel cladding materials such as zirconium alloys used in current PWRs [64]. The fuel cladding's primary function is to provide a physical barrier between the fuel and coolant; any failure of this material could result in contaminated coolants and components and system outages. Furthermore, increasing the primary coolant temperature and maximising the fuel burn up fraction are two methods that could significantly improve the efficiency, optimise resource use, reduce nuclear waste, and increase the economic viability of sodium-cooled fast reactors [336]. Unfortunately, these methods would also exclude the use of established ferritic-martensitic steels , such as HT9 [42], T91 [42] (as discussed in Chapter 2.4.5) or EP-450 [337], due to their limited high temperature creep resistance, and austenitic stainless steels, such as Type 316 [42], 15-15Ti (1.4970) [32] or D9 [338], due to their extensive void swelling. New structural materials are therefore required to meet the demands of high temperature coolants, high fuel burn up fraction methods and tolerate the associated increase in neutron flux [339].

Reduced-activation ferritic-martensitic (RAFM) steels, such as F82H [156, 340] and EUROFER97 [155], are possible candidate structural materials for the breeder blanket, divertor, and other structural components within nuclear fusion power reactors. However, like the sodium-cooled fast reactor, nuclear fusion demands the development of new materials that can withstand greater irradiation damage and higher operational temperatures than RAFM steels [30].

ODS steels (sometimes called 'nanostructured ferritic alloys' (NFAs)) are candi-

dates for both the fuel cladding material of sodium-cooled fast reactors and structural materials for nuclear fusion power stations [142], as they have shown high radiation damage tolerance (>100 displacements-per-atom (dpa)),high temperature mechanical strength (600-800 °C) and high temperature creep resistance [41]. ODS steels contain a high density ($\sim 10^{23}$ m^{-3}) of yttrium-titanium-oxygen (Y-Ti-O) nano-oxides, typically sized <2 nm in radius, which improve the high temperature strength and creep resistance of ferritic steels [45], as discussed in chapter 2 section 2.5 in detail. These Y-Ti-O nano-oxides have the added benefit of reducing the mean-free path of irradiation induced lattice defects (interstitial and vacancy clusters and point defects). Thus, they are also effective sinks for such defects to recombine and for helium [142]. Furthermore, the nano-oxides are sources of grain refinement due to the pinning of grain boundaries during heat treatment, which further increases the sink density. This combination of nano-oxides and fine grain structure are the source of ODS steels' exceptional tolerance to radiation damage.

During ODS steel powder consolidation, the mechanisms controlling microstructural evolution throughout recrystallisation are not well understood [222]. A bimodal grain structure after heat treatment and recrystallisation are a typical defining feature of ODS steels, comprising two distinctive regions of nanosized and microsized grains [212, 341]. There are some reports of ODS steels with a "homogeneous" nanograin structure [342]; however, the majority of studies acknowledge grain size bimodality even for alloys with relatively high mechanical or radiation resistance performance. Previous studies [341, 343] have investigated the bimodal grain size distributions in Fe-14Cr (wt. %) ODS steels by using EBSD, TKD, nanoindentation and APT. Short powder milling times have been found to increase the heterogeneity of the Y-Ti-O particle size distribution, which is thought to increase the bimodality of the final grain structure [341]. García-Junceda et al. (2016) [341] found that ZrO_2 added to Fe-14Cr-5Al-3W-0.4Ti-0.25Y_2O_3 (wt. %) acted to refine the bimodal grain structure.

Consequently, understanding and control of grain size bimodality, heterogeneity

of the grain sizes and Y-Ti-O nanocluster densities are likely important characteristics to control in the manufacture of ODS steels. Heintze et al. (2019) [343] showed that while hardening in ODS steels during self-ion irradiation was a function of grain size, the hardening during dual self-ion and helium-ion irradiation was a function of both the grain size and the Y-Ti-O particle density. This suggested that the tolerance of ODS steels to transmutation gases (hydrogen and helium) during neutron irradiation may be strongly dependent on the Y-Ti-O nanocluster density, and thus any large spatial variations in the particle density could lead to variations in these unique properties.

How the heterogeneity of Y-Ti-O nanoclusters and grain sizes influence the deformation micromechanics is also poorly understood, although a bimodality in microscale mechanical properties [222, 343] is thought to be related to the bimodality of the grain-sizes and Y-Ti-O particle distribution. Critically, it is this bimodality of mechanical properties that challenges the predictability of ODS steels performance as a fuel cladding material in sodium-cooled fast reactors and its use as a structural material for nuclear fusion reactors. A detailed characterisation to understand how these Y-Ti-O particles influence the deformation and mechanical properties would provide an insight into predicting the properties of this unique branch of steels.

In this study, a Fe-14Cr-3W-0.2Ti-0.25Y_2O_3 (nominal wt. %) ODS steel (referred to hereafter as 14YWT), typical in the field, was produced using powder milling followed by hot isostatic pressing (HIP) consolidation. This batch of material has been studied previously by Gorley (2014) [210] and Burrows (2014) [216], who provided useful additional data on the manufacturing and microstructure characterisation. Here, APT, EBSD, and transmission electron microscopy (TEM) were used to characterise the local nanoindentation deformation and its correlation with the microstructural features observed at room temperature. Although the operational temperature of ODS steels are at high temperatures for nuclear systems, room temperature (21 °C) mechanical properties should not be disregarded. The steel would be

exposed at room temperatures during transport, storage and decommissioning. Thus, the mechanical properties at room temperature could provide better understanding into the handling of these materials. The study was restricted to room temperature and unirradiated conditions to focus on the microstructure characterisation of deformation in ODS steels. Another focus of this study was to demonstrate the use of three techniques (APT, electron microscopy and nanoindentaion) and show how they complement each other when used to characterise the microstructure of nanostructured materials. It should be noted that ion irradiation of ODS steels was planned; however, due to the COVID-19 pandemic, ion irradiation was not completed.

6.3 Experimental Methods

6.3.1 ODS Steel Manufacturing

Given the difficulty of dispersing fine-scale oxides in liquid alloys and the preference for oxides < 5 nm diameter that can only be achieved by in-situ precipitation, mechanical milling of pre-alloyed powders and Y_2O_3 followed by powder consolidation under vacuum and heat treatment has emerged as the standard, preferred route to manufacturing of ODS steels. The ODS steel used here was milled in the Department of Materials, University of Oxford, and then HIP consolidated at the University of Birmingham, UK [210, 216].

14YWT was produced by mechanically alloying of gas-atomised Fe-14Cr-3W-0.2Ti (wt. %) powder with $0.25Y_2O_3$ (wt. %) powder using AISI 52-100 steel (low Ni) pots and stainless steel balls at 250 rpm in an Ar atmosphere for 60 hours with a ball-to-powder ratio of 10:1 and a ball diameter of 10 mm. The milled powder was then degassed and packed into a mild steel can, evacuated, sealed and HIPed at 150 MPa and 1150 °C for 4 hours [210]. The chemical composition of 14YWT is listed in Table 6.3.1. A slice of the consolidated alloy that had undergone the HIP technique was cut from the can using a diamond saw and then polished to a colloidal silica

finish for microscopy, nanoindentation and focused ion beam (FIB) lift out for TEM and APT.

For comparison to 14YWT, a pure nanocrystalline iron (Fe) was produced by high-pressure torsion to provide the nanocrystalline grain structure as a baseline. This nanocrystalline iron material was used as a reference for grain boundary attribution to nanohardness measurements.

Table 6.3.1: Measured composition of 14YWT by X-ray fluorescence and LECO analysis (London & Scandinavian Metallurgical Co Limited.)

Element	Bulk (wt%)	Bulk (at%)	APT (at%)
Cr	13.34	14.21	14.686 ± 0.402
W	2.66	0.80	0.592 ± 0.054
Ti	0.21	0.24	0.186 ± 0.010
Y_2O_3	0.30	0.05	-
Al	0.11	0.23	-
Mn	0.33	0.34	0.279 ± 0.010
Si	0.18	0.36	0.404 ± 0.018
C	0.09	0.42	0.016 ± 0.001
N	-	-	0.063 ± 0.012
Fe	Bal.	Bal.	Bal.

6.3.2 Characterisation Techniques

6.3.2.1 Electron Backscatter Detection

EBSD was used on both the nanocrystalline Fe and 14YWT materials to determine the grain size distributions, a Zeiss Crossbeam 540 FIB/SEM and an Oxford Instruments EBSD detector were used to measure the diffraction patterns (voltage at 20 kV). Reconstruction of the maps was conducted using Oxford Instrument's Aztec version 3.3 SP1 and HKL Channel 5 version 5.12.67.0 software.

6.3.2.2 Nanoindentation

The methodology of nanoindentation is discussed in Chapter 3 Section 3.3. An Agilent G200 nanoindentor was used to measure hardness and modulus of the material by indenting a colloidal-silica polished surface to a 250 nm indentation depth at room temperature (21 °C). A continuous stiffness measurement system with a 2 nm 39 Hz harmonic displacement was used to measure the modulus and hardness as a function of indentation depth. A Berkovich tip was used and the tip area coefficients were calculated from the average load-displacement data of sixteen 2 µm indents into fused silica. Thus, using the known area function and contact stiffness as a function of tip displacement, both the modulus and hardness of 14YWT and pure nanocrystalline Fe were calculated as a function of tip displacement.

One hundred 250 nm indents were made in 14YWT, arranged in a 10 by 10 grid with 15 µm between each indent, as shown in figure 6.4.4. The hardness and modulus values were determined between 125 to 225 nm from the load-displacement curve, as shown in figure 6.4.3.

6.3.2.3 Atom Probe Tomography

APT analysis was conducted with a CAMECA LEAP® 5000XR at the Department of Materials, University of Oxford. Atom probe specimens were prepared by the lift-out technique [23] using a Zeiss NVision 40 FIB-SEM. Cleaning of the specimens was performed using 2 kV Ga ions to minimise FIB-induced damage. All atom probe specimens had tip diameters that were approximately between 50 – 100 nm.

The atom probe tips were cooled down to 50 K. A 355 nm wavelength Nd:YAG laser at 40 pJ and 200 kHz was used to sputter atoms from the tip under ultra-high vacuum, at an average detection rate of 0.5 %. The detection efficiency of the LEAP 5000XR is 52% [344]. CAMECA IVAS® 3.8.2 software was used to reconstruct 3D chemical atomic maps. Reconstruction of all the atom probe data sets utilised the SEM tip profiles and pole indexing techniques. A maximum separation method [247]

cluster algorithm was used on all APT datasets to determine the density, radius and composition of Y-Ti-O particles. Solute ions (TiO, Y and YO_2 (YO was not detected within the datasets; if YO was detected, it would have been included in the cluster search)) were selected for all the particle searches. The average APT compositional measurement across seven datasets is provided in Table 6.3.1.

6.3.2.4 Transmission Electron Microscopy

J. Haley provided the TEM micrographs (Figs 6.4.8, 6.4.9, 6.4.10, 6.4.11, and 6.4.12), interpretation, and analysis.

TEM was conducted using a Jeol 2100L with a LaB_6 electron source and 200kV accelerating voltage. STEM and EDX were conducted on a Jeol ARM200F with a cold field-emission gun source and 200kV accelerating voltage, and a 100 mm^2 Centurion EDX detector. A Zeiss Auriga dual-beam FIB microscope was used to produce a single cross-section foil through two indents using the lift-out method [241]. Cleaning of the tips was performed on all samples using 2 kV Ga ions to minimise FIB-induced damage.

To image the dislocation network beneath the indents, conventional TEM (C-TEM) kinematical two-beam conditions, and zone-axis bright-field STEM techniques were used. C-TEM not optimised for imaging dislocations in highly deformed foils since the distortions in the lattice can significantly reduce the contrast from the localised strain fields of dislocations. In STEM, such distortions have much less effect on the contrast of dislocations due to the highly converged probe typically used [345]. STEM also significantly reduces the elastic contrast in the background by smearing out thickness-dependent contrast [346], allowing for improved contrast of dislocation networks over wide areas of deformed foils.

Porosity is a concern in the production of ODS steels [210]; this is problematic for TEM analysis since light particles (such as Y) appear with a similar contrast to micro-pores in both C-TEM and STEM. Thus, chemical analysis is often necessary

for distinguishing nanoscale oxides from cavities. High angle annular dark-field was therefore used alongside EDX mapping in order to confirm oxide particles from various parts of the microstructure and across a wide range of scales. Hyperspy [347] was used to extract qualitative element maps from the EDX spectrum images.

6.4 Results

6.4.1 Nanocrystalline Fe

S. Connolly provided the nanoindentation data for nanocrystalline Fe.

The grain structure from the EBDS analysis of the pure nanocrystalline iron material is shown in figure 6.4.1. The average grain size was 150±50 nm with an average nanohardness of 7.5±0.3 GPa and modulus of 245±10 GPa. The average hardness and modulus were determined from 16 indents at 1000 nm depth.

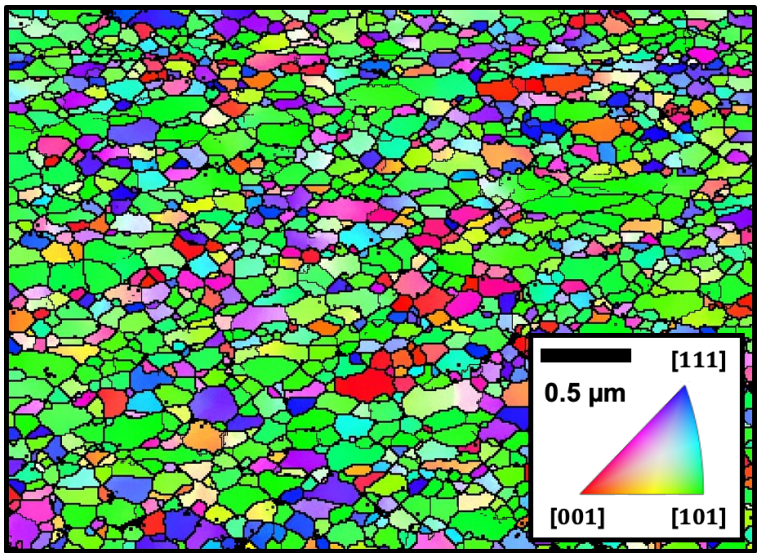

Figure 6.4.1: Microstructure of the nanocrystalline iron material using EBSD. An inverse pole key is shown for the crystallographic directions.

6.4.2 ODS Nanoindentation

OThe average hardness and modulus were found to be 5.8±1.1 GPa and 239±12 GPa, respectively. An EBSD map was produced after the indentation to determine the crystallographic directions and grain sizes of the grain structure, which had a bimodal grain distribution, as shown in figure 6.4.5. The microstructure was fully ferritic. There were two distant grain size distributions: 0 – 1 µm and 1 – 20 µm grain diameter ranges with averages of 0.53±0.16 µm and 2.60±1.8 µm, respectively. It should be noted that no indentation sized effect was observed with both the nanocrystalline and 14YWT materials, which allowed for the comparison between each dataset.

6.4.3 ODS EBSD and APT

The mass-to-charge (Da) spectrum of a typical ODS 14YWT APT datasets (R83_06348 in table 3.1.3) is shown in figure 6.4.2 and all associated identification of the peaks is shown for reference.

Four indents in the 14YWT labelled A, B, C and D are highlighted in figure 6.4.5(b), with their corresponding hardness values; the indents were chosen based on their range of hardness values, showing a range of values, and lack of obvious grain boundary strengthening from local nanocrystalline grains, minimising the Hall-Petch effect. APT sample tips were taken underneath each identified indent to determine the nano-oxide distribution within the plastic zone produced by the nanoindentation. APT tips were made from the left, centre and right side of each indent, where sufficient data was collected. Indent A's APT Y and TiO atom maps are reconstructed, along with a 2.0 at% tungsten isosurface to highlight the grain boundary, as shown in figure 6.4.6. Further, a proxigram [348] was calculated across this isosurface and shows the enrichment of tungsten at the grain boundary, as seen in figure 6.4.7.

For all four indents listed in figure 6.4.5-b), the density and average size of the nano-oxides were calculated using the method outlined in Section 6.3.2 and the re-

sults listed in Table 6.4.1. The Y-Ti-O dispersion within each indent investigated was calculated by the maximum separation method cluster algorithm. The density and average size of each indent have been calculated using the IVAS software implementation of the algorithm. Solute ions, TiO, Y, and YO_2, were selected for the algorithm. The optimal maximum separation parametrisation for cluster analysis was found for all APT datasets and the results are found in chapter 3 table 3.1.3. Values that are missing in Table 6.4.1 were due to the atom probe tip fracturing before any significant amount of data could be collected.

As shown in Table 6.4.1, the number density of Y-Ti-O of indent B and C (which have the same nanohardness of 6.4 ± 0.1) are within the same order of magnitude but, for indent B, the density is between 2 – 4 times higher than that of indent C. Whereas the Guinier radius of Y-Ti-O was approximately the same (except half for indent B LT, which could be a resultant of a small APT dataset). Generally across all indents, the Guinier radius was similar in size. Between a low hardness indent D and a high hardness indent C, the number density of Y-Ti-O particles are within the same order of magnitude and value.

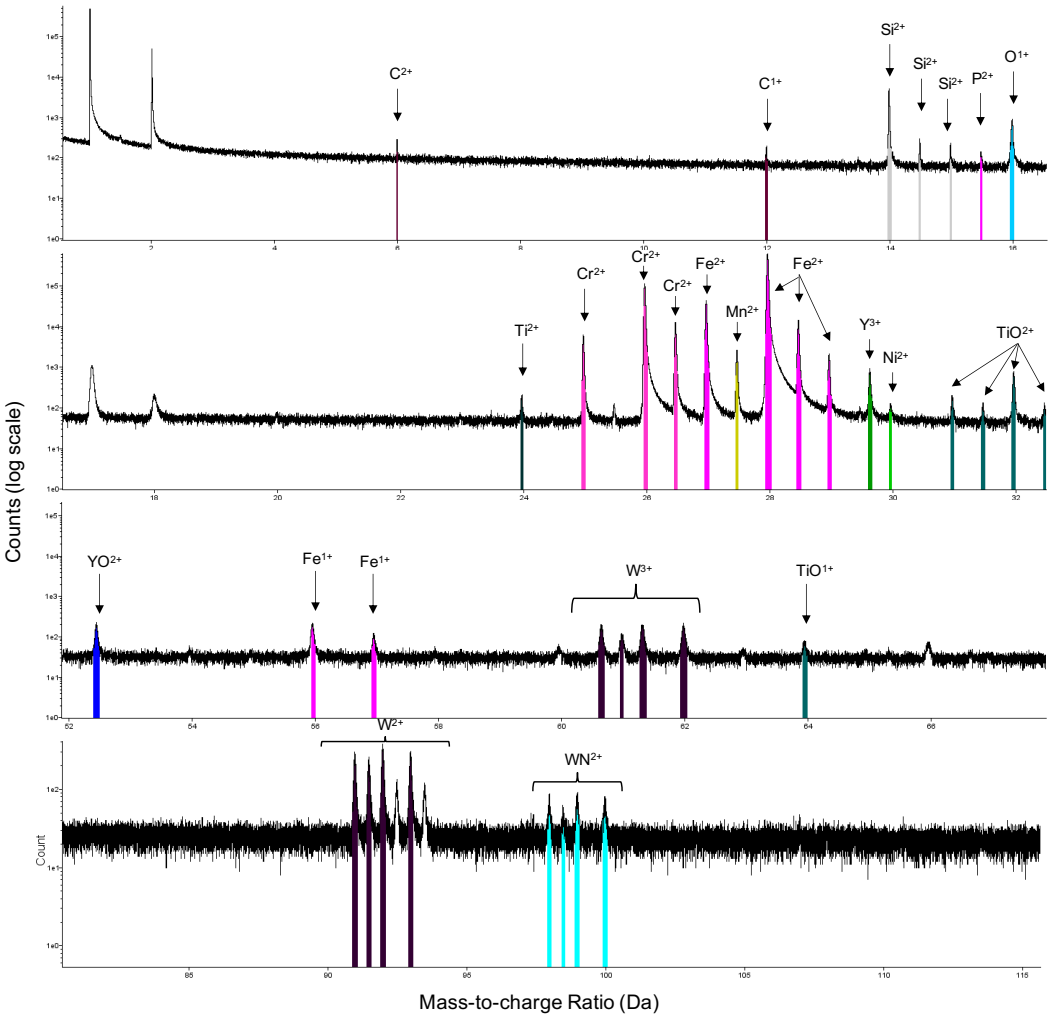

Figure 6.4.2: The mass-to-charge spectrum of a typical neutron 14YWT ODS steel sample (R83_06348 in table 3.1.3). The peaks have been identified according to the natural isotopes and expected chemical additions.

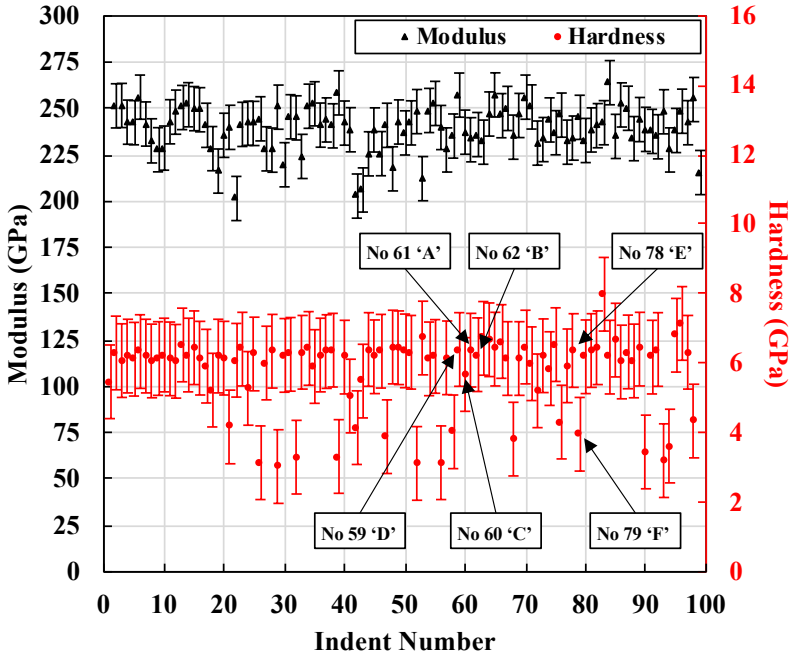

Figure 6.4.3: The hardness and modulus values of 14YWT for all the indents. The values were determined between 125 to 225 nm from the load-displacement curve. For reference, the nanocrystalline Fe's hardness and modulus were 7.5±0.3 GPa and modulus of 245±10 GPa, respectively.

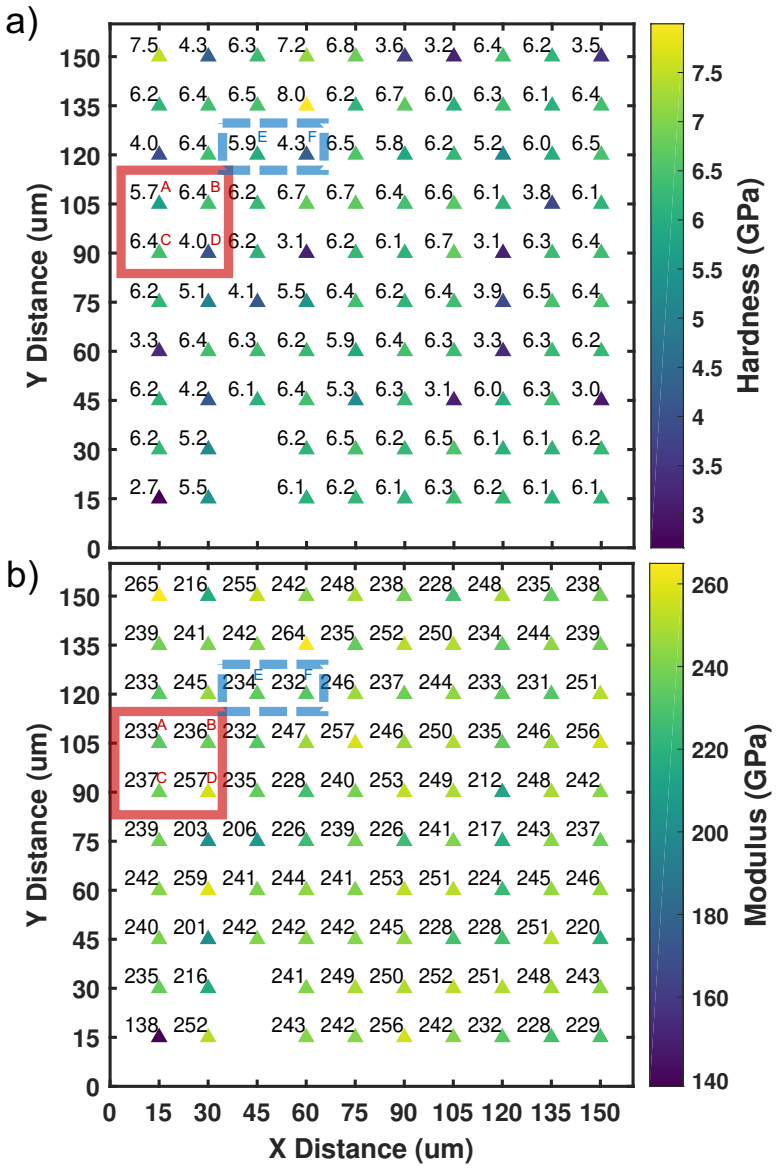

Figure 6.4.4: a) the x and y relative coordinates of the 100 array nanoindents, hardness values in GPa, the APT indent locations are labelled A-D inside a red solid line box, and the TEM indent locations are labelled E-F inside a blue dashed line box. b) the x and y relative coordinates of the 100 array nanoindents, modulus values in GPa, the APT indent locations are labelled A-D inside a red solid line box, and the TEM indent locations are labelled E-F inside a blue dashed line box.

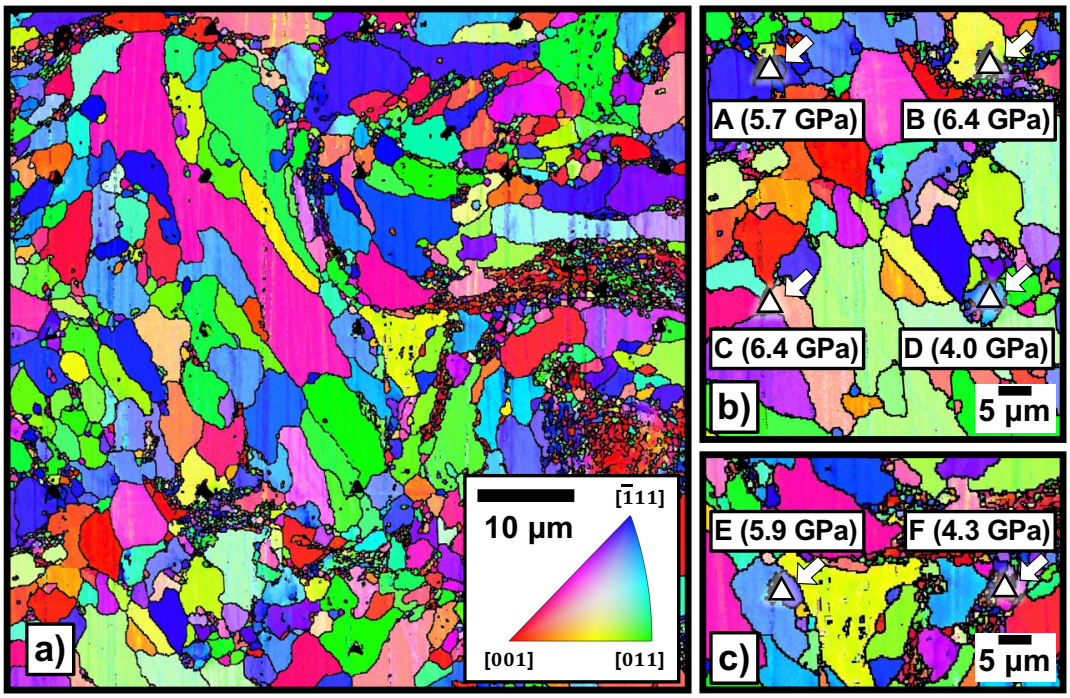

Figure 6.4.5: a) EBSD map section of the region containing 100 indents showing a bimodal grain structure in 14YWT. b) Identification of the four A-D indents that were investigated with APT with their respective hardness values. (c) Identification of indents E and F lifted out for TEM analysis with their respective hardness values. The indents of interest are highlighted triangles in b) and c). An inverse pole key is shown for the crystallographic directions.

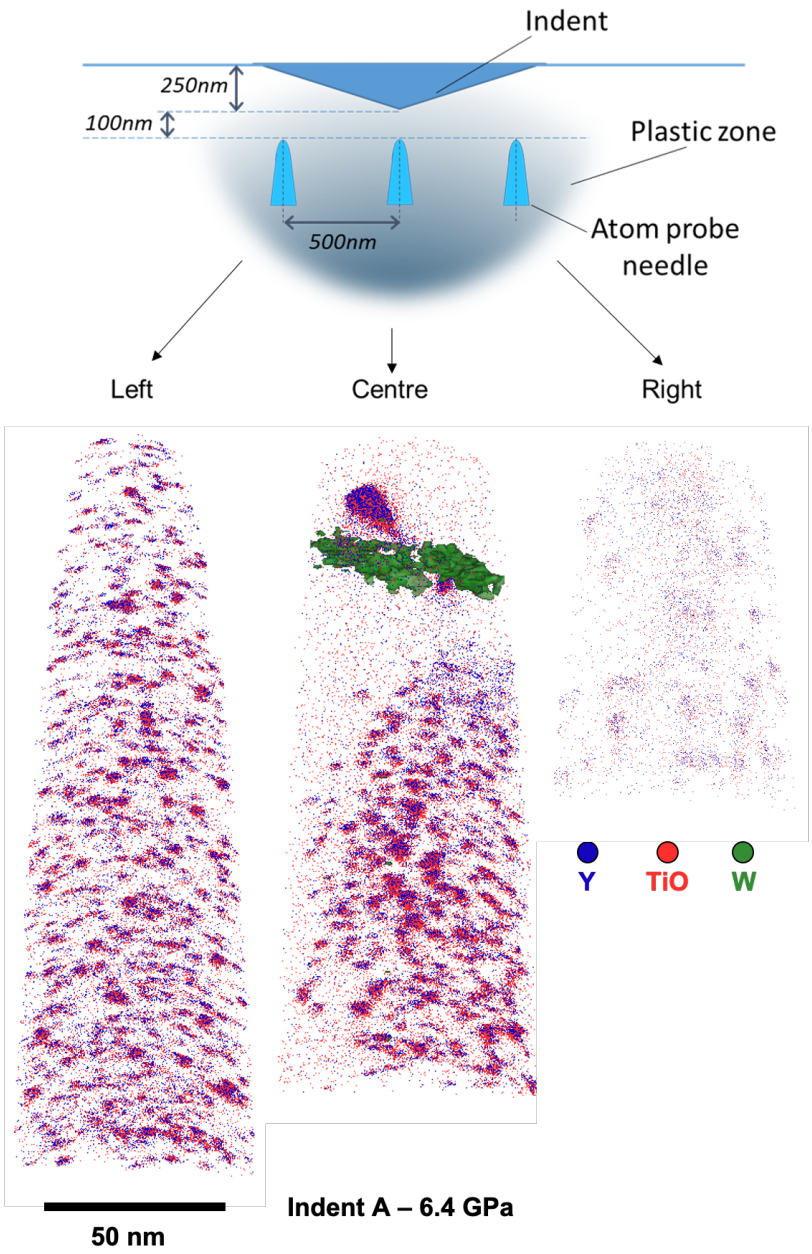

Figure 6.4.6: APT reconstruction of the material underneath indent A in figure 6.4.5(b). The distribution of Y, W and TiO has been displayed for each tip (left, centre and right). A 2.0 at% isosurface of W for the centre tip has been displayed to demonstrate the enrichment of W at grain boundaries. The inhomogeneous distribution of Y and TiO can be seen in this case (right side).

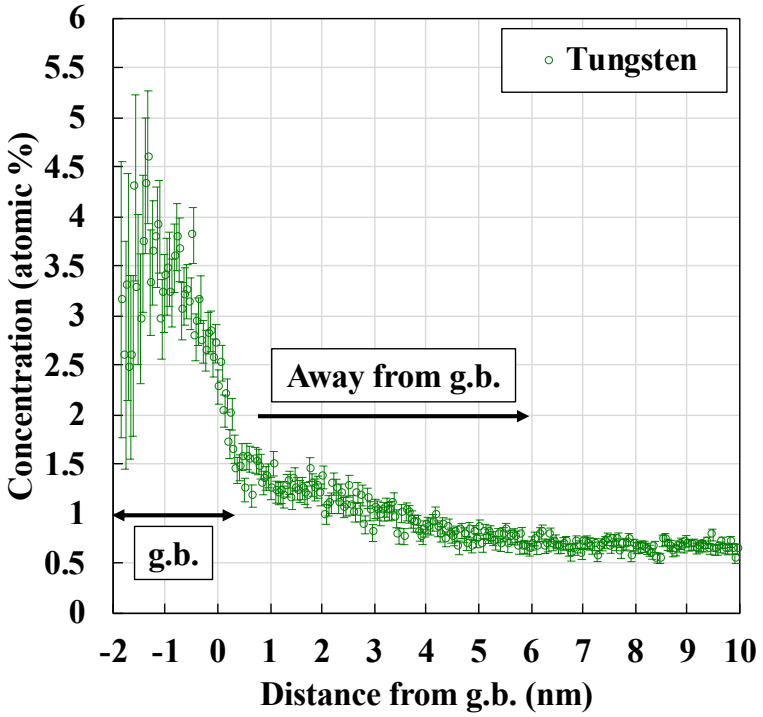

Figure 6.4.7: APT proxigram across the grain boundary (g.b.) with a 2.0 at% W isosurface shown in figure 6.4.6.

Table 6.4.1: Summary of hardness values in indents A, B, C and D in Fig 3-b) and nanocluster analysis from APT of the plastic zone volumes beneath each indent. Vacant data indicates that the atom probe tip fractured before sufficient data was acquired. LT, CT, and RT are the left tip, centre tip, and right tip, respectively.

		Indent			
		A	B	C	D
Hardness (GPa)		5.7 ± 0.2	6.4 ± 0.1	6.4 ± 0.1	4.0 ± 0.1
Number	LT	$(1.5 \pm 0.1) \times 10^{24}$	$(4.7 \pm 0.1) \times 10^{23}$	$(1.6 \pm 0.1) \times 10^{24}$	–
Density of	CT	$(7.2 \pm 0.1) \times 10^{23}$	–	$(1.2 \pm 0.1) \times 10^{24}$	–
Y-Ti-O (#/m^3)	RT	$(1.2 \pm 0.1) \times 10^{24}$	$(2.1 \pm 0.2) \times 10^{23}$	$(1.2 \pm 0.1) \times 10^{24}$	$(1.7 \pm 0.1) \times 10^{24}$
Guinier radius	LT	2.0 ± 0.2	1.0 ± 0.2	1.9 ± 0.2	–
of Y-Ti-O	CT	2.2 ± 0.3	–	2.1 ± 0.2	–
(nm)	RT	2.0 ± 0.2	2.6 ± 0.2	2.3 ± 0.2	2.0 ± 0.2

6.4.4 TEM of ODS

Two further indents in 14YWT, labelled E and F, were chosen for TEM analysis based on their wide differences in hardness (similar to that seen in indents A-D), despite the lack of obvious differences in local surface grain boundary morphology. These indents are highlighted in figure 6.4.6(c), along with their corresponding hardness values. TEM was used to examine the material beneath indents E and F in order to assess the mechanisms behind the differences in hardness. Figure 6.4.8 shows a low magnification C-TEM image of each indent.

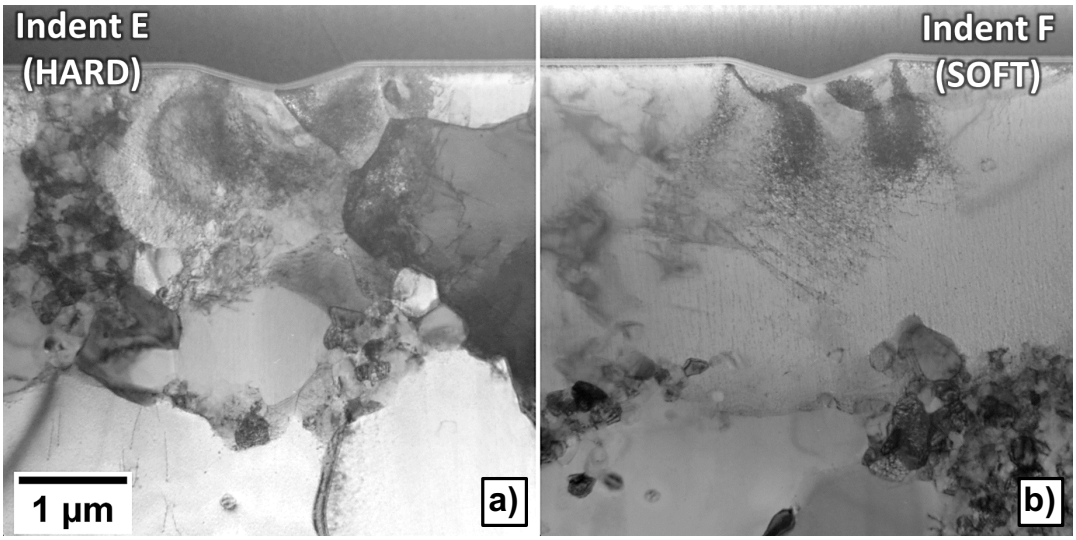

Figure 6.4.8: Bright field TEM micrographs of cross-sections taken from indents (a) E and (b) F in figure 6.4.5(c).

The plastic zone of indent E is clearly shown in figure 6.4.9(b), extending approximately 1.5 µm below the deepest point of the indent. Many dislocations were pinned against small defects in the matrix, presumably oxide particles; an example of such a dislocation is shown in figure 6.4.9(d). HAADF revealed that the larger grain beneath the indent contained an abrupt change in the visible density of oxide nanoclusters (the dark spots) midway through this large grain, as shown in figure 6.4.9(a). There was also a pile-up of dislocations at this particle interface, which did not coincide with any grain boundary, in figure 6.4.9(b).

HAADF was used to image the region immediately beneath the tip of indent E, as shown in figure 6.4.10(a,b). The inset corresponding to figure 6.4.10(c) EDX maps indicated that the dark spots were yttrium oxide (likely close to Y_2O_3 stoichiometry), as expected, but with a Ti-rich shell. It should be noted that titanium-rich shells were not found in the atom probe data. The grain boundary was comparatively enriched with Cr and W; Al and Mn were also weakly present and assumed contamination through the various stages of powder handling in production or as an impurity already linked to the Fe powder used. No cavities were found under indent E, and this was verified by detecting yttrium within the EDX scans.

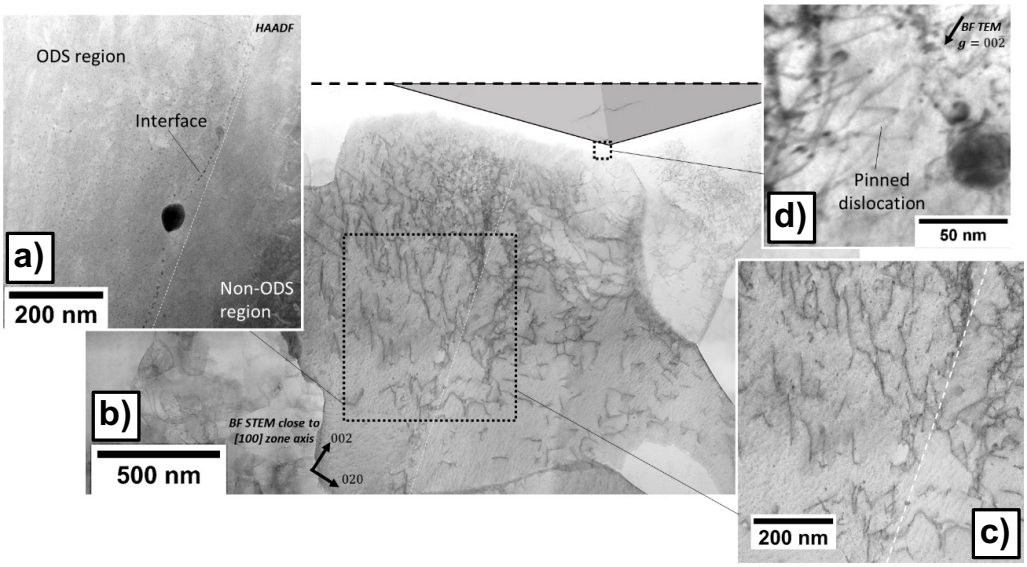

Figure 6.4.9: TEM and STEM micrographs of a dislocation network beneath indent E. (a) The HAADF image shows an abrupt change in oxide particle density in the region indicated (labelled ODS and non-ODS regions); (b) the BF STEM shows a pile up of dislocations at this interface. (c) A white dashed line indicates this interface. d) A typical example of a pinned dislocation is also shown.

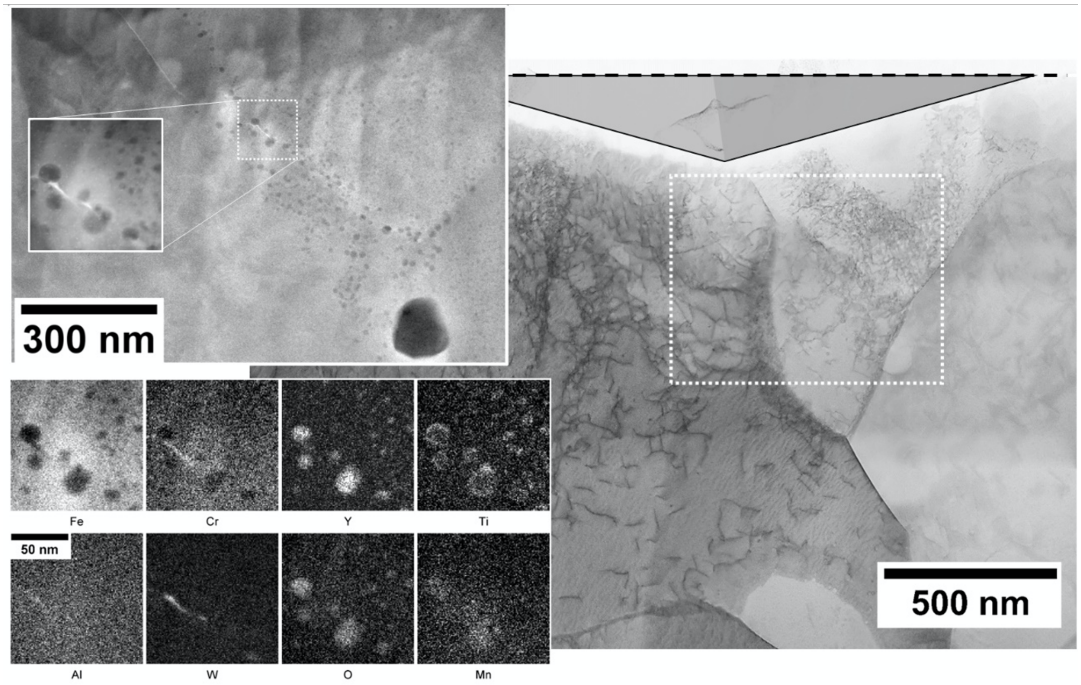

Figure 6.4.10: (a)-(b) STEM micrographs and (c) qualitative EDX element maps (L-α lines) from a region immediately beneath the tip of indent E.

The plastic zone of indent F is clearly shown in figure 6.4.11(a). Dislocations were more artificially extended to a greater length than those in figure 6.4.9-b) and figure 6.4.10(b) since the foil was orientated close to a 110 plane, on which two variants of the $\langle 111 \rangle$-type screw dislocations would lie. HAADF again revealed a fine distribution of dark spots near the tip of the indent. Due to their small size, EDX maps were only acquired from single clusters here as shown in figure 6.4.11(c).

HAADF was used to image the region immediately beneath the tip of indent F, as also shown in figure 6.4.12(a,b). HAADF and EDX were used to examine if the Y-Ti-O distributions were different in the nanograins and larger grains. It has been shown through the HAADF micrographs in figure 6.4.12(a,b) that large ODS particles were contained within nanograined regions. Since the largest ODS particles were generally found on or near grain boundaries, it could be inferred that the nano-grains should have a higher fraction of the large ODS particles since the grain boundaries are in closer proximity to each other. No cavities were found under indent F, and this was

verified by detecting yttrium within the EDX scans.

STEM-based estimates of the Y-Ti-O density for those regions that were qualitatively homogeneous within large grains ranged from $\sim 7 \times 10^{22}$ m^{-3} (measured from the centre of a large grain beneath indent E) to $\sim 1 \times 10^{23}$ m^{-3} (measured immediately beneath indent F). For both these measurements, the particles diameters were 3 ± 1 nm. In the nanograined regions, the Y-Ti-O nanoparticle density was calculated as $\sim 5 \times 10^{22}$ m^{-3}, with larger diameters of 7 ± 2 nm.

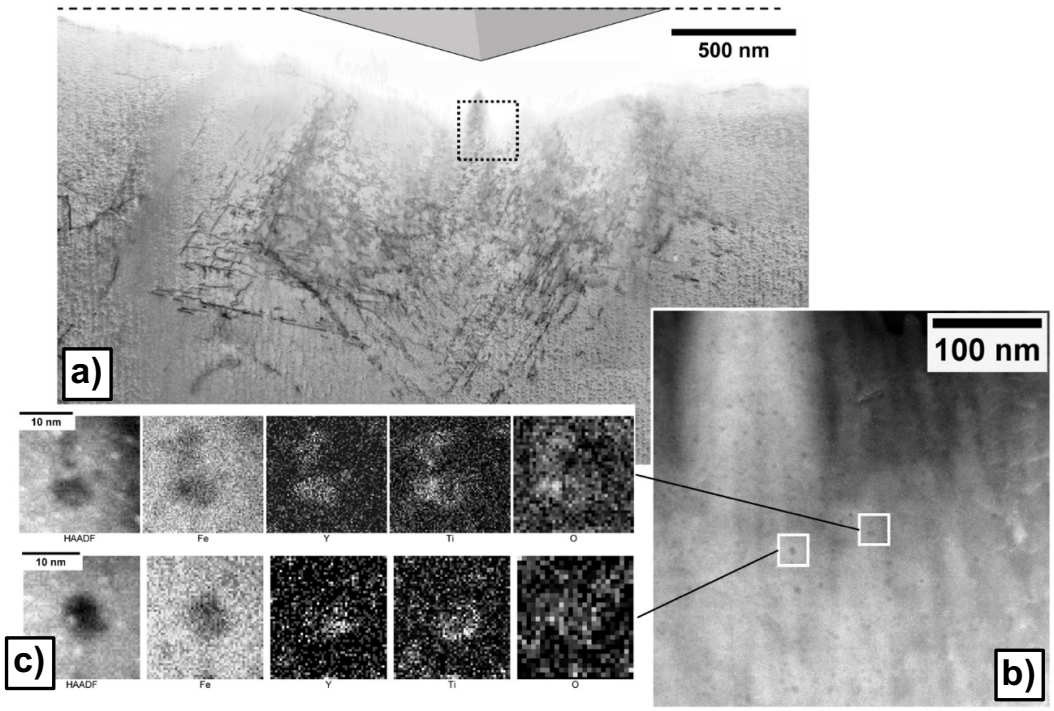

Figure 6.4.11: (a)-(b) STEM micrographs and (c) qualitative EDX element maps (L-α lines) from a region immediately beneath the tip of indent F. Note: The white dots visible in the HAADF images besides the EDX maps are carbon contaminants on the foil surface and are unrelated to the microstructure.

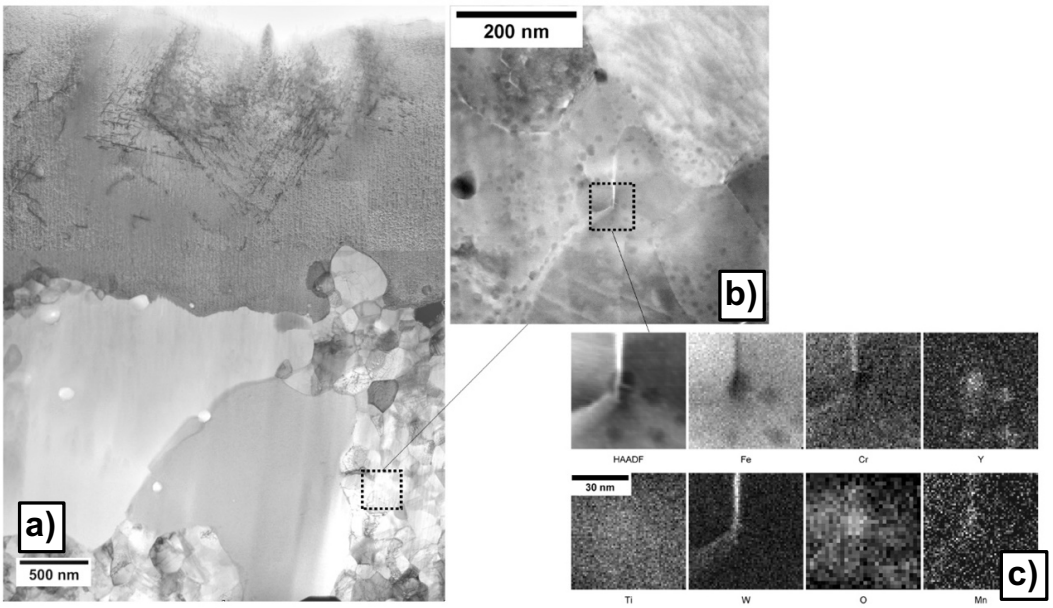

Figure 6.4.12: (a)-(b) STEM micrographs and (c) qualitative EDX element maps (L-α lines) from a nanograin region beneath the plastic zone of indent F.

The Y-Ti-O number density measurements from APT (at near atomic resolution) were generally much larger ($\sim 10^{23}$ – 10^{24} #/m^3) than those obtained by STEM ($\sim 10^{21}$ – 10^{22} #/m^3) , which may indicate that HAADF did not resolve the smallest Y-Ti-O clusters, and this reflects the difficulty in quantifying a high density of $\sim$1 nm sized clusters in a 2D projection of a TEM foil. The APT-based number density measurements were thus considered a more reliable estimate of the ODS particle density.

6.5 Discussion

The rationalisation of how the Y-Ti-O particles influence the deformation mechanisms in and around the nanoindents must consider various facets. The 14YWT hardness showed a bimodal distribution, and this might simply relate to the spatial heterogeneity in Y-Ti-O particle number density (i.e. if the nano-oxide dispersion is non-uniform), then the associated dispersion hardening will also be non-uniform

[223, 349]. However, the hardness values of indents B and C were both 6.4±0.1 GPa, despite different APT number densities of Y-Ti-O particles of $5.8 \pm 0.1 \times 10^{23}$ m^{-3} and $1.3 \pm 0.1 \times 10^{24}$ m^{-3}, respectively (taking an average of left, centre and right APT tips). Further, the Guinier radius was 1.8±0.2 nm and 2.1±0.2 nm respectively (again taking an average of the left, centre and right tips). In contrast, indent D exhibited a hardness of 4.0±0.1 GPa and a number density of Y-Ti-O particles of 1.7×10^{24} m^{-3}; in other words, the hardness increased from 4.0±0.1 GPa (indent D) to 6.4±0.1 GPa (indent C), whilst the Y-Ti-O particle number density remained near-constant and equal to $1.7 \pm 0.2 \times 10^{24}$ m^{-3}. Thus, the limited volume probed could suggest that the dominant hardening mechanism was not Y-Ti-O based dispersion hardening.

14YWT had an average hardness and modulus of 5.8±1.1 GPa and 239±12 GPa, respectively, with two very different grain size distributions of 0 – 1 µm and 1 – 20 µm grain diameter ranges with an average of 0.53±0.16 µm and 2.60±1.8 µm, respectively. For comparison, the nanocrystalline iron exhibited on average a hardness 7.5±0.3 GPa, and modulus of 245±10 GPa with an average grain size of 150±50 nm.

The TEM analysis showed that the plastic zone extended to 2 µm below each indent (8 times the indenter depth of 250 nm). The plastic zone beneath indent F (the softer of the two indents) was mostly contained within a single grain, except for a small grain at the surface, allowing dislocations to propagate unconstrained through the grain. The microstructure beneath indent E (the harder indent) was mostly polycrystalline. The plastic zone extended to a nano-grained region on the left-hand side of the indent, and beyond the grain-boundaries between the larger grains on the right-hand side and below the indent. Evidently in this case, the dislocations were more constrained by the grain boundaries.

The grain structure alone can be suggested as the pre-dominant hardening mechanism, however the role of ODS particles on dislocations must be considered. These nano-oxides were captured in conventional two-beam bright field conditions, and in

zone-axis bright field STEM. HAADF, complemented by EDX maps, was also used to examine the oxide nanoclusters. Further thinning of the foils was conducted after capturing the images in figure 6.4.8(a,b), which resulted in the loss of the protective platinum layer and some of the near-surface material, as is noticeable in subsequent micrographs.

The softer indent, indent F, examined by STEM appeared to contain a relatively homogeneous distribution of Y-Ti-O beneath the indent, as shown in figure 6.4.11(b), whereas the harder indent E contained a more obviously heterogeneous distribution with large depletion zones absent of TEM-visible clusters, as shown in figure 6.4.10(a,b). This finding, alongside the APT results, implies that the majority of hardening is likely to arise from the grain refinement, rather than by dislocation pinning on the Y-Ti-O particles (as shown in figure 6.4.9(d)).

Generally, the Y-Ti-O dispersion strengthening contribution has been explained, and quantified, by the Orowan by-pass mechanism with a key assumption that the particles are impenetrable. Shen et al. [350] performed such a calculation but did not provide evidence that this assumption was reasonable. The dislocation TEM analysis within the plastic zone of a nanoindent within 14YWT, as shown by figure 6.4.9, indicated that the dislocations were straight, rather than bowed around the Y-Ti-O particles; this implies that the Y-Ti-O were partially cut. Within the limitations of this study (room temperature), the results suggest that Y-Ti-O particles were partially penetrable at room temperature, which could explain their minimal contribution to strengthening. It should be noted that the dispersion strengthening is also dependent on the inter-particle distance. However, the TEM analysis conducted within this study was unable to resolve particles smaller than 3 nm and the distances between Y-Ti-O ppts in the APT data would be subjected to reconstruction aberrations, thus potentially providing misleading distance between particle results. The determination of the inter-particle spacing was not calculated within this study. The investigation of the particle/matrix interface coherency was beyond the scope of this study (it has

been investigated in previous literature [351]).

Another feature was the enrichment of W at grain boundaries, as shown in figure 6.4.11(c) and figure 6.4.12(c). This enrichment was confirmed by APT analysis of two grain boundaries in the datasets, with an average composition of 3.5 at % W, as shown in figure 6.4.7. It should be noted that the bulk W in 14YWT was 0.80 at%. The enrichment could strengthen the grain boundaries. In addition, the combined STEM and APT analysis suggests that the Y-Ti-O dispersion was not uniform in general. W enrichment at the grain boundaries has been shown to provide some strengthening. This indicates that W enrichment observed in 14YWT could have strengthened the grain boundaries (thus, this has shown to increase creep resistance) [352, 353].

Overall, the major hardening mechanism was due to grain boundary refinement, rather than directly to the number density or homogeneity of Y-Ti-O particle distribution. This finding is consistent with the high hardness measurement of 7.5±0.25 GPa for the pure nanocrystalline Fe with an average grain size of 150±50 nm. There is no doubt that the high hardness in the nanocrystalline Fe is caused by the very fine grain structure and had high dislocation density. It is noted that another common feature of 14YWT grain boundaries was the larger Y-Ti-O particle densities close to the boundaries (see figure 6.4.10(a,c) and figure 6.4.12(b,c)). It is not possible to separate the strengthening effects of these larger Y-Ti-O particles from the grain boundaries themselves in this study. Furthermore, model alloys and pure iron produced by high-pressure torsion can provide a suitable baseline for the effects of grain refinement.

It should be noted that the studies were conducted at room temperature. High temperature mechanical properties and their relation to the microstructure is vitally important for the use of these steels in high temperature application, such as fuel cladding in sodium-cooled fast reactors.

It has been common practice to compare 14YWT to ‘non-ODS’ variants, which

have the same composition but no addition of Y_2O_3 powder [197, 210]. Inevitably, the alloys have very different final ferritic grain structures because there is no grain refinement/pinning effect from the Y-Ti-O particles during recrystallization. These studies then highlight differences in mechanical properties between the alloys; the results here suggest these differences, at least at room temperature, may be more due to the effect of grain refining than by direct effects of dispersion hardening.

6.6 Conclusions

In the development of new fuel cladding materials for sodium-cooled fast reactors and structural materials for nuclear fusion power reactors, 14YWT steel is regarded as promising candidate. In this study, 14YWT has been investigated using a combination of TEM and EBSD microscopy, APT and nanoindentation at room temperature to contribute to a comprehensive understanding of the factors controlling its hardness, as a proxy measurement for its likely macro-scale mechanical properties. The findings were as follows:

- The average number density and diameter of Y-Ti-O particles had a relatively small effect on the hardness, suggesting that the dominant hardening mechanism may relate more strongly to other microstructural features.
- TEM imaging of the plastic zone beneath nano-indents suggested that the dominant strengthening mechanism was grain boundary hardening due to grain refinement, rather than dislocation pinning on the Y-Ti-O particles. This is consistent with the high hardness measurement of pure nanocrystalline Fe.
- Grain boundaries were enriched with W, which is also thought to improve the grain boundary strength.
- As is typical for this alloy class, the distribution of Y-Ti-O particles was comparatively non-uniform, with number densities ranging from $10^{23} - 10^{24}$ m^{-3}

as measured by APT.

- The Y-Ti-O particle diameter varied from region to region, with large (few microns to 10s of microns) grains containing particles of 1-3 nm, as well as nano-grained regions ($\sim$ 100 nm) containing particles sized on typically $\sim$7 nm, and up to $\sim$15 nm.
- Overall, the presence of nano-oxides, Y-Ti-O, may have an indirect effect on the hardness through the effect of grain refinement.

Overall the results suggest that for the alloy studied here in terms of hardening it is the grain boundary pinning effect of Y-Ti-O clusters (and associated grain refinement) during recrystallization that underpins the excellent yield strength of ODS alloys, and not direct dispersion strengthening effects, despite various types of microstructural inhomogeneity at the grain diameter and Y-Ti-O nanoparticle scale. The balance between grain boundary and dispersion strength will vary with temperature, and from alloy to alloy. Although nanoparticles/clusters may be less important in strengthening, they retain their importance in conferring radiation resistance. Furthermore, this study demonstrated how electron microscopy, APT and nanoindentation techniques complement each other when characterising a material.

The next and final chapter of this thesis provides the overarching conclusion and possible future work.

Chapter 7

Thesis Summary

The expansion of nuclear fission energy to tackle climate change is seen as a key stepping-stone to meet the Paris Agreement on Climate Change. The drive to improve the reliability, safety and scalability of future reactor designs (>2030s) by way of 'Generation IV' type fission reactors has driven the research and development within this industry [3, 13, 26]. However, the fuel cladding material of Generation IV nuclear reactor's experiences intense neutron irradiation, high temperatures, corrosive, and erosive environments, which excludes existing Generation II/III/III+ cladding materials (i.e. zircalloy-2/4) [9]. One of the leading structural and fuel cladding material for lead-cooled and sodium-cooled fast reactors is T91 ferritic/martensitic stainless steel for the short term solution (5-10 years) [42]. ODS steels are regarded as the fuel cladding material for the long-term deployment of Generation IV nuclear reactors [42] and structural materials for fusion power stations [44].

Neutron irradiation drives microstructural and microchemical changes in tempered martensitic steels like T91 ferritic-martensitic steel, and these changes impose detrimental effects on the steel's mechanical properties. As such, this evolution could limit the lifetime and performance of reactor structural components. ODS steels are engineered using nanoclusters (before irradiation) to improve the material's radiation resistance by including large radiation defect sinks. The overarching theme of this

thesis was the evaluation of the role of nanoclusters within steels for nuclear applications, and each chapter discussed this role, as described below:

- Chapter 4 investigated the formation and evolution of solute nanocluster precipitation in T91 steel under neutron irradiation. The MNSP nanoclusters degrade the materials properties, which is of major concern to design engineers, nuclear reactor operators, and nuclear regulators [42].
- Chapter 5 investigated the use of ion irradiation to simulate and study the formation and evolution of solute nanocluster precipitation in T91 steel. The objective was to understand the effect of low dose irradiation, and to investigate the usage of ion acceleration as a tool to understand irradiation damage, on the microstructure of candidate structural materials for nuclear applications.
- Chapter 6 investigated the successor type steel over T91 by engineering in Y-Ti-O nanoclusters before irradiation. The objective was to understand the effect that these nanoclusters imposed on the microstructure and mechanical properties.

Overall, the thesis investigated how nanoclusters can be designed for positive applications, whereas nanocluster formation under irradiation conditions can enable premature failure during the operation of a nuclear reactor.

7.1 Contribution to Science

This thesis provides original contributions to the understanding of nuclear reactor core materials, and the main findings can be found in sections 4.6, 5.6, and 6.6. The three main major unique contributions to science provided by this thesis provides are:

- Detailed characterisation of the MNSP and solute segregation to dislocations in T91 steel that was neutron irradiated to 2.14 dpa at 327 °C and 8.82 dpa

at 377 °C. The compositions of all the MNSPs were similar and fell near the Si(Mn,Ni) phase field, which was not observed beforehand. This composition range is distinctly different than that for the typically cited G-phase, which is consistent with the observations of Si(Mn,Ni) precipitates in neutron irradiated low Ni % RPV steels. CRP-MNSP number densities, sizes and volume fractions, as well as Si solute segregation to dislocations, was in remarkable agreement with model predictions of a previously reported simulation, combining solute segregation and CD mechanisms. This is further real evidence for the success of modelling MNSP in T91 steel. Moreover, the research highlights parallels which can be drawn between the much more limited database on MNSPs in neutron irradiated Fe-Cr alloy systems with that of the extensive literature on precipitate evolution in RPV steels. This link has not been provided before.

- Detailed characterisation of the MNSP and solute segregation to dislocations in T91 steel that was ion irradiated between 0.12 dpa to 4.1 dpa at 300 °C and the impact on mechanical properties were discussed. The insight that ion irradiation provides in understanding the fundamental mechanisms behind radiation damage to the microstructure was not apparent after the case for neutron irradiation. This study has demonstrated the usefulness of ion irradiation to observe and understand the role of solute ions and impurities in commercial grade ferritic-martensitic steels, and provide meaningful comparisons to neutron irradiated T91 steels with the same APT methodology. Furthermore, the study highlights that when APT and nanoindentation are applied in tandem, they provide a powerful insight into the role of radiation-induced precipitation and radiation-induced segregation. Moreover, the direct comparison for T91 steel between ion and neutron irradiation conditions has not been reported in literature to-date. The findings show that ion irradiation can be used to study RIP and RIS of T91 steel to understand the fundamental mechanism before

conducting neutron irradiation experiments.

- Throughout ODS steel literature, the assumption is consistently held that Y-Ti-O nano-oxides contribute to major alloy strengthening. The combination of TEM and EBSD microscopy, APT, and nanoindentation provided a useful tool to investigate which microstructural features control and/or affect the mechanical properties. Two major findings arose: 1) the presence of Y-Ti-O nano-oxides may have an indirect effect on the hardness by grain refinement and 2) the dominant strengthening mechanism in 14YWT ODS steel was grain boundary hardening due to grain refinement, rather than dislocation pinning on the Y-Ti-O particles.

7.2 Contribution to Nuclear Engineering

The previous section discussed the contribution to science and the fundamental materials understanding of RIS and RIP exposed to ion and neutron irradiation of T91 steels, and ODS steel's Y-Ti-O effect on the mechanical properties. This section will discuss the overall contribution to the nuclear engineering field and how this work provides an insight to the effect of radiation damage to engineers.

This research provides a scientific understanding to the formation and evolution of MNSP, which embrittle the material by impeding dislocation motion. It is the latter that increases the yield strength, decreases the fracture toughness and increases the DBTT. It is these factors that are of importance to nuclear engineers, such as the DBTT will determine the failure mechanism of the material [42]. Therefore, the contribution could provide lower limits on the use of T91 steel in a reactor core, such as the minimum temperature the steel should experience in a neutron field. These limits is what provides the safety margin for operates, strengths the nuclear safety cases, and ultimately provides the operating licence that vendors seek [42].

The ODS steel research provides characterisation of the Y-Ti-O particle and effect

on dislocations, which ultimately underpin how this branch of steels have such a high strength.

7.3 Suggestions for Future Work

The conclusions provide possible directions for further investigations, which may include the following:

- Conduct a greater array of ion irradiation conditions of T91 steel that covers the entire expected operational temperatures of fuel cladding in SFRs. This ranges from 300 – 650 °C. The higher temperatures are of interest as this is where the steel would be most spent during its operational lifetime. Rather than radiation embrittlement being the major factor to the steels degradation, the higher temperatures would enable the creep mechanism to dominate the failure mechanisms [42, 64]. The future work here could focus around the effect of RIS on the creep mechanisms seen in T91 steel and alike materials (EUROFER97, F82H, and T92).

- Use the combination of APT, EBSD, nanoindentation, and TEM to understand the pinning of dislocation ability MNSP in neutron and ion irradiated T91 steel (and similar TMS alloys), and to understand the effect that these radiation-induced precipitates have on the microstructure.

- Investigate the radiation-induced segregation around dislocation lines and loops further, as it appears that the high dose damage in T91 steels is dominated by these features. Specifically the temperatures range to investigate should be between 300 – 450 °C due to the embrittlement nature shown in mechanical data and high dose range (>10 dpa). It is these condition ranges that would determine the steels failure at these doses due to the expected time fuel cladding rods are in the reactor core [9].

- Conduct similar ion irradiation experiments outlined in Chapter 5 and apply them to the ODS steel investigated in chapter 6. The features of interest would be whether ion irradiation at these temperature and dose ranges effect the Y-Ti-O character (diameter, density, and composition) or do they remain unaffected (and thus could be considered 'radiation resistant').

- For ODS steel to become an engineering material, the challenge is upscaling the production from kg batches, which have inhomogeneous microstructures and mechanical properties, to tonnage scales with predictable properties. Further study could investigate possible solutions to this challenge, as it appears the most limiting factor about ODS steels when deploying them in test reactors (and eventually commercial nuclear reactors).

Bibliography

[1] V. Masson-Delmotte, P. Zhai, H.-O. Portner, D. Roberts, J. Skea, P.R. Shukla, A. Pirani, W. Moufouma-Okia, C. Pean, R. Pidcock, S. Connors, J.B.R. Matthews, Y. Chen, X. Zhou, M.I. Gomis, E. Lonnoy, T. Maycock, M. Tignor, and T. Waterfield. Summary for policymakers. In *Global Warming of 1.5°C. An IPCC Special Report on the impacts of global warming of 1.5°C above pre-industrial levels and related global greenhouse gas emission pathways, in the context of strengthening the global response to the threat of climate change, sustainable development, and efforts to eradicate poverty*. World Meteorological Organization, Geneva, Switcherland, 2018.

[2] John Cook, Dana Nuccitelli, Sarah A Green, Mark Richardson, Bärbel Winkler, Rob Painting, Robert Way, Peter Jacobs, and Andrew Skuce. Quantifying the consensus on anthropogenic global warming in the scientific literature. *Environmental Research Letters*, 8(2):024024, may 2013. URL http://dx.doi.org/10.1088/1748-9326/8/2/024024.

[3] T. P. Davis. Dispelling misconceptions of nuclear energy technology: How generation iv nuclear reactors could become the key to achieving the paris agreement and the united kingdom's net zero co_2 emissions target by 2050. In *St Anne's Academic Review 9*. St Anne's College, Oxford, United Kingdom, 2019. URL http://st-annes-mcr.org.uk/staar/publications/staar-9-2019/davis-2019-dispelling-misconceptions-of-nuclear-energy-technology/.

[4] Dieter Lüthi, Martine Le Floch, Bernhard Bereiter, Thomas Blunier, Jean-Marc Barnola, Urs Siegenthaler, Dominique Raynaud, Jean Jouzel, Hubertus Fischer, Kenji Kawamura, and et al. High-resolution carbon dioxide concentration record 650,000–800,000 years before present. *Nature*, 453(7193):379–382, 2008. URL http://dx.doi.org/10.1038/06949.

[5] Jeremy D. Shakun, Peter U. Clark, Feng He, Shaun A. Marcott, Alan C. Mix, Zhengyu Liu, Bette Otto-Bliesner, Andreas Schmittner, and Edouard Bard. Global warming preceded by increasing carbon dioxide concentrations during the last deglaciation. *Nature*, 484(7392):49–54, 2012. URL http://dx.doi.org/10.1038/nature10915.

[6] Carolyn W. Snyder. Evolution of global temperature over the past two million years. *Nature*, 538(7624):226–228, 2016. URL http://dx.doi.org/10.1038/nature19798.

[7] United Kingdom Government. The climate change act 2008 (2050 target amendment) order 2019. *UK Parliament*, 2019. URL https://www.legislation.gov.uk/uksi/2019/1056/pdfs/uksi_20191056_en.pdf.

[8] David MacKay. *Sustainable energy–without the hot air*. UIT, Cambridge, England, 2009. ISBN 978-0954452933.

[9] Steven J. Zinkle and Jeremy T. Busby. Structural materials for fission & fusion energy. *Materials Today*, 12(11):12–19, 2009. ISSN 13697021. URL http://dx.doi.org/10.1016/S1369-7021(09)70294-9.

[10] International Energy Agency. World energy outlook 2018. *International Energy Agency*, 2018. URL https://www.iea.org/reports/world-energy-outlook-2018.

[11] B. Gates. What i learned at work this year. *GatesNotes*, 2018. URL https://www.gatesnotes.com/About-Bill-Gates/Year-in-Review-2018.

[12] Massachusetts Institute of Technology. The future of nuclear energy in a carbon-constrained world: An interdisciplinary mit study. *MIT Energy Initiative*, 2018. URL http://energy.mit.edu/wp-content/uploads/2018/09/The-Future-of-Nuclear-Energy-in-a-Carbon-Constrained-World.pdf.

[13] Generation IV International Forum. Sodium-Cooled Fast Reactor (SFR). 2018. URL https://www.gen-4.org/gif/jcms/c_42152/sodium-cooled-fast-reactor-sfr.

[14] A.A. Harms. *Principles of Fusion Energy: An Introduction to Fusion Energy for Students of Science and Engineering*. World Scientific, 2000. ISBN 9789810243357.

[15] K.L. Murty and I. Charit. *An Introduction to Nuclear Materials: Fundamentals and Applications*. Physics Textbook. Wiley, 2013. ISBN 9783527412013. URL https://books.google.co.uk/books?id=N0ThLZxv4XoC.

[16] G. S. Was. *Fundamentals of Radiation Materials Science: Metals and Alloys*. Springer Berlin Heidelberg, 2007. ISBN 9783540494720.

[17] Pascal Yvon. *Structural materials for generation IV nuclear reactors*. Woodhead Publishing is an imprint of Elsevier, Duxford, UK, 2017. ISBN 978-0-08-100906-2.

[18] Igor Pioro. *Handbook of generation IV nuclear reactors*. Woodhead Publishing is an imprint of Elsevier, Duxford, UK, 2016. ISBN 9780081001493.

[19] S.M. Goldberg and R. Rosner. *Nuclear Reactors: Generation to Generation*. American Academy of Arts and Sciences, 2010.

[20] Nuclear Regulatory Commission. Peach Bottom Atomic Power Station, Units 2 & 3 – Subsequent License Renewal Application. 2020. URL https://www.nrc.gov/reactors/operating/licensing/renewal/applications/peach-bottom-subsequent.html.

[21] Juliana P. Duarte, José de Jesús Rivero Oliva, and Paulo Fernando F. Frutuoso e Melo. Generation iv nuclear systems: State of the art and current trends with emphasis on safety and security features. In Amir Zacarias Mesquita, editor, *Current Research in Nuclear Reactor Technology in Brazil and Worldwide*, chapter 7. IntechOpen, Rijeka, 2013. URL http://dx.doi.org/10.5772/53140.

[22] Hosik Yoo, Jang hoon Seo, Na-Young Lee, Jung hyun Lee, Moon sung Koh, and Seung-Ho Ahn. Methodology for evaluating proliferation resistance of nuclear systems and its case study. *Progress in Nuclear Energy*, 100:309 – 315, 2017. ISSN 0149-1970. URL https://doi.org/10.1016/j.pnucene.2017.06.017.

[23] H. György and Sz. Czifrus. Burnup calculation of the generation iv reactors. *Progress in Nuclear Energy*, 81:150 – 160, 2015. ISSN 0149-1970. URL https://doi.org/10.1016/j.pnucene.2015.01.015.

[24] R.S. El-Emam and I. Khamis. Advances in nuclear hydrogen production: Results from an iaea international collaborative research project. *International Journal of Hydrogen Energy*, 44(35):19080 – 19088, 2019. ISSN 0360-3199. URL https://doi.org/10.1016/j.ijhydene.2018.04.012. A Special Issue with the Papers Selected from the 7th World Hydrogen Technologies Convention.

[25] Charles Forsberg, Stephen Brick, and Geoffrey Haratyk. Coupling heat storage to nuclear reactors for variable electricity output with baseload reactor operation. *The Electricity Journal*, 31(3):23 – 31, 2018. ISSN 1040-6190. URL https://doi.org/10.1016/j.tej.2018.03.008.

[26] T. P. Davis. Could generation iv nuclear reactors strengthen russia's growing sphere of influence? In *The 2019 UK PONI Papers*. Royal United Services Institute, London, United Kingdom, 2019.

[27] Moltex Energy Ltd. Moltex Energy: Safer, Cheaper, Cleaner. 2020. URL https://www.moltexenergy.com/.

[28] Terrestrial Energy Inc. Terrestrial Energy. 2020. URL https://www.terrestrialenergy.com/.

[29] Advanced Reactor Concepts LLC. ARC – Advanced Reactor Concepts, LLC. 2020. URL https://www.terrestrialenergy.com/.

[30] S J Zinkle and L L Snead. Designing Radiation Resistance in Materials for Fusion Energy. *Annu. Rev. Mater. Res*, 44:241–67, 2014. ISSN 1531-7331. URL http://dx.doi.org/10.1146/annurev-matsci-070813-113627.

[31] M.B. Chadwick and et al. ENDF/B-VII.1 Nuclear Data for Science and Technology: Cross Sections, Covariances, Fission Product Yields and Decay Data. *Nuclear Data Sheets*, 112(12):2887 – 2996, 2011. ISSN 0090-3752. URL https://doi.org/10.1016/j.nds.2011.11.002. Special Issue on ENDF/B-VII.1 Library.

[32] Catherine Andrieux, François Baqué, Bernard Bonin, Bernard Boullis, Céline Cabet, Frank Carré, Philippe Dufour?, François Gauché, Jean-Paul Grouiller, Joël Guidez (Topic Editor), Jean-Philippe Jeannot, Christian Latgé, Marion Le Flem, Pierre Le Coz, Laurent Martin, Michel Masson, Gilles Mathonnière, Jean-Guy Nokhamzon, Michel Pelletier, Gilles Rodriguez, Manuel Saez, Jean-Louis Séran, Frédéric Varaine, and Alain Zaetta. *Sodium-Cooled Nuclear Reactors Monograph*. CEA, 2016. ISBN 9782281140552. URL http://www.materials.cea.fr/en/PDF/Sodium-Cooled%20Nuclear%20Reactor_CEA-en.pdf.

[33] R.L. Klueh and J.M. Vitek. The resistance of 9 Cr-1 MoVNb and 12 Cr-1 MoVW steels to helium embrittlement. *Journal of Nuclear Materials*, 117: 295 – 302, 1983. ISSN 0022-3115. URL https://doi.org/10.1016/0022-3115(83)90037-5.

[34] M.B. Toloczko, F.A. Garner, and C.R. Eiholzer. Irradiation creep and swelling of the US fusion heats of HT9 and 9Cr-1Mo to 208 dpa at 400°C. *Journal of Nuclear Materials*, 212-215:604 – 607, 1994. ISSN 0022-3115. URL https://doi.org/10.1016/0022-3115(94)90131-7.

[35] E.A. Little and D.A. Stow. Void-swelling in irons and ferritic steels: Ii. an experimental survey of materials irradiated in a fast reactor. *Journal of Nuclear Materials*, 87(1):25 – 39, 1979. ISSN 0022-3115. URL https://doi.org/10.1016/0022-3115(79)90123-5.

[36] C. Fazio and F. Balbaud. 2 - Corrosion phenomena induced by liquid metals in Generation IV reactors. In Pascal Yvon, editor, *Structural Materials for Generation IV Nuclear Reactors*, pages 23 – 74. Woodhead Publishing, 2017. URL https://doi.org/10.1016/B978-0-08-100906-2.00002-1.

[37] L.C Walters. Thirty years of fuels and materials information from EBR-II. *Journal of Nuclear Materials*, 270(1):39 – 48, 1999. ISSN 0022-3115. URL https://doi.org/10.1016/S0022-3115(98)00760-0.

[38] R. L. Klueh and A. T. Nelson. Ferritic/martensitic steels for next-generation reactors. *Journal of Nuclear Materials*, 371(1-3):37–52, 2007. ISSN 00223115. URL http://dx.doi.org/10.1016/j.jnucmat.2007.05.005.

[39] B.H. Sencer, J.R. Kennedy, J.I. Cole, S.A. Maloy, and F.A. Garner. Microstructural analysis of an HT9 fuel assembly duct irradiated in FFTF to 155dpa at 443°C. *Journal of Nuclear Materials*, 393(2):235 – 241, 2009. ISSN 0022-3115. URL https://doi.org/10.1016/j.jnucmat.2009.06.010.

[40] Gary S. Was, Janelle P. Wharry, Brian Frisbie, Brian D. Wirth, Dane Morgan, Julie D. Tucker, and Todd R. Allen. Assessment of radiation-induced segregation mechanisms in austenitic and ferritic-martensitic alloys. *Journal of Nuclear Materials*, 411(1-3):41–50, 2011. ISSN 00223115. URL http://dx.doi.org/10.1016/j.jnucmat.2011.01.031.

[41] P. Dubuisson, Y. de Carlan, V Garat, and M Blat. ODS Ferritic/martensitic alloys for Sodium Fast Reactor fuel pin cladding. *Journal of Nuclear Materials*, 428(1-3):6–12, 2012. URL http://dx.doi.org/10.1016/j.jnucmat.2011.10.037.

[42] T.P. Davis. Review of the iron-based materials applicable for the fuel and core of future Sodium Fast Reactors (SFR). *Office for Nuclear Regulation*, ONR-RRR-088:1–52, 2018. URL http://www.onr.org.uk/documents/2018/onr-rrr-088.pdf.

[43] Tae Kyu Kim, Sanghoon Noh, Suk Hoon Kang, Jin Ju Park, Hyun Ju Jin, Min Ku Lee, Jinsugn Jang, and Chang Kyu Rhee. Current status and future prospective of advanced radiation resistant oxide dispersion strengthened steel (arros) development for nuclear reactor system applications. *Nuclear Engineering and Technology*, 48(2):572 – 594, 2016. ISSN 1738-5733. URL https://doi.org/10.1016/j.net.2015.12.005.

[44] S J Zinkle, J L Boutard, D T Hoelzer, A Kimura, R Lindau, G R Odette, M Rieth, L Tan, and H Tanigawa. Development of next generation tempered and ODS reduced activation ferritic / martensitic steels for fusion energy applications. *Nuclear Fusion*, 092005, 2017.

[45] G. Robert Odette. On the status and prospects for nanostructured ferritic alloys for nuclear fission and fusion application with emphasis on the underlying science. *Scripta Materialia*, 143:142–148, 2018. ISSN 13596462. URL http://dx.doi.org/10.1016/j.scriptamat.2017.06.021.

[46] ITER. Fuelling the Fusion Reaction. 2016. URL https://www.iter.org/sci/fusionfuels.

[47] ITER. ITER Technical Basis: ITER EDA Documentation Series 24. *Interntaional Atomic Energy Agency*, 2002.

[48] M Keilhacker, A Gibson, C Gormezano, and P H Rebut. The Scientific Success of JET. *Nuclear Fusion*, 41(12):1925, 2001. ISSN 0029-5515. URL http://dx.doi.org/10.1088/0029-5515/41/12/217.

[49] F Romanelli, P Barabaschi, D Borba, G Federici, L Horton, R Neu, D Stork, and H Zohm. Fusion electricity: A roadmap to the realization of fusion energy. 2012. URL https://www.euro-fusion.org/fileadmin/user_upload/Archive/wp-content/uploads/2013/01/JG12.356-web.pdf.

[50] M. Turnyanskiy, R. Neu, R. Albanese, R. Ambrosino, C. Bachmann, S. Brezinsek, T. Donne, T. Eich, G. Falchetto, G. Federici, D. Kalupin, X. Litaudon, M.L. Mayoral, D.C. McDonald, H. Reimerdes, F. Romanelli, R. Wenninger, and J.-H. You. European roadmap to the realization of fusion energy: Mission for solution on heat-exhaust systems. *Fusion Engineering and Design*, 96-97: 361 – 364, 2015. ISSN 0920-3796. URL https://doi.org/10.1016/j.fusengdes.2015.04.041. Proceedings of the 28th Symposium On Fusion Technology (SOFT-28).

[51] National Academies of Sciences, Engineering, and Medicine. *Final Report of the Committee on a Strategic Plan for U.S. Burning Plasma Research*. The National Academies Press, Washington, DC, 2019. ISBN 978-0-309-48743-6. URL https://dx.doi.org/10.17226/25331.

[52] T. Muroga, S. Fukada, and T. Hayashi. Overview of fusion engineering research in japan focusing on activities in nifs and universities. *Fusion Science and Technology*, 75(7):559–574, 2019. URL http://dx.doi.org/10.1080/15361055.2019.1603499.

[53] E. Gibney. UK hatches plan to build world's first fusion power plant . *Nature*, 2019. URL https://doi.org/10.1038/d41586-019-03039-9.

[54] Y. Wu. Conceptual design of the china fusion power plant fds-ii. *Fusion Engineering and Design*, 83(10):1683 – 1689, 2008. ISSN 0920-3796. URL https://doi.org/10.1016/j.fusengdes.2008.06.048. Proceedings of the Eight International Symposium of Fusion Nuclear Technology.

[55] Timothy Jackson. Is fusion feasible? an assessment of the methodology and policy implications. *Energy Policy*, 17(4):407 – 412, 1989. ISSN 0301-4215. URL https://doi.org/10.1016/0301-4215(89)90011-6.

[56] Judy Clark and Gordon MacKerron. Great expectations: A review of nuclear fusion research. *Energy Policy*, 17(1):49 – 56, 1989. ISSN 0301-4215. URL https://doi.org/10.1016/0301-4215(89)90121-3.

[57] Colin Sweet. Criteria for the assessment of fusion power. *Energy Policy*, 17 (4):413 – 419, 1989. ISSN 0301-4215. URL https://doi.org/10.1016/0301-4215(89)90012-8.

[58] T.E.G. Nicholas, T.P. Davis, F. Federici, J. Leland, B.S. Patel, C. Vincent, and S.H. Ward. Re-examining the role of nuclear fusion in a renewables-based energy mix. *Energy Policy*, 149:112043, 2021. ISSN 0301-4215. URL https://doi.org/10.1016/j.enpol.2020.112043.

[59] K.S. Krane. *Introductory Nuclear Physics*. Wiley, 1987. ISBN 9780471805533.

[60] National Nuclear Data Centre. Nuclear Levels and Gammas Search, 2020. URL http://www.nndc.bnl.gov/nudat2/.

[61] Yuki Koga, Hideaki Matsuura, Yuma Ida, Ryo Okamoto, Kazunari Katayama, Teppei Otsuka, Minoru Goto, Shigeaki Nakagawa, Satoru Nagasumi, Etsuo Ishitsuka, and Yosuke Shimazaki. Study on lithium rod test module and irradiation method for tritium production using high temperature gas-cooled reactor. *Fusion Engineering and Design*, 136:587 – 591, 2018. ISSN 0920-3796. URL https://doi.org/10.1016/j.fusengdes.2018.03.029. Special Issue: Proceedings of the 13th International Symposium on Fusion Nuclear Technology (ISFNT-13).

[62] Richard J. Pearson, Armando B. Antoniazzi, and William J. Nuttall. Tritium supply and use: a key issue for the development of nuclear fusion energy. *Fusion Engineering and Design*, 136:1140 – 1148, 2018. ISSN 0920-3796. URL https://doi.org/10.1016/j.fusengdes.2018.04.090. Special Issue: Proceedings of the 13th International Symposium on Fusion Nuclear Technology (ISFNT-13).

[63] A. Moeslang, V. Heinzel, H. Matsui, and M. Sugimoto. The IFMIF test facilities design. *Fusion Engineering and Design*, 81(8-14):863–871, 2006. ISSN 0920-3796. URL http://dx.doi.org/10.1016/j.fusengdes.2005.07.044. Proceedings of the Seventh International Symposium on Fusion Nuclear Technology (ISFNT-7) Part BProceedins of the Seventh International Symposium on Fusion Nuclear Technology.

[64] S.J. Zinkle and G.S. Was. Materials challenges in nuclear energy. *Acta Materialia*, 61(3):735–758, feb 2013. ISSN 1359-6454. URL http://dx.doi.org/10.1016/J.ACTAMAT.2012.11.004.

[65] G. Federici, W. Biel, M. R. Gilbert, R. Kemp, N. Taylor, and R. Wenninger. European DEMO design strategy and consequences for materials. *Nuclear Fusion*, 57(9), 2017. ISSN 17414326. URL http://dx.doi.org/10.1088/1741-4326/57/9/092002.

[66] R Aymar, P Barabaschi, and Y Shimomura. The ITER design. *Plasma Physics and Controlled Fusion*, 44(5):519–565, apr 2002. URL http://dx.doi.org/10.1088/0741-3335/44/5/304.

[67] ITER. Aerial photo of ITER 28 Feburary 2020). 2020. URL https://www.iter.org/album/Media/4%20-%20Aerial.

[68] ITER. Perfect fit photo of ITER 26 May 2020). 2020. URL https://www.iter.org/album/Construction.

[69] R.E. Stoller. 1.11 - primary radiation damage formation. In Rudy J.M. Konings, editor, *Comprehensive Nuclear Materials*, pages 293 – 332. Elsevier, Oxford, 2012. ISBN 978-0-08-056033-5. URL http://dx.doi.org/10.1016/B978-0-08-056033-5.00027-6.

[70] Janelle P. Wharry, Zhijie Jiao, Vani Shankar, Jeremy T. Busby, and Gary S. Was. Radiation-induced segregation and phase stability in ferritic-martensitic alloy T 91. *Journal of Nuclear Materials*, 417(1-3):140–144, 2011. ISSN 00223115. URL http://dx.doi.org/10.1016/j.jnucmat.2010.12.052.

[71] P. Hosemann, D. Frazer, M. Fratoni, A. Bolind, and M. F. Ashby. Materials selection for nuclear applications: Challenges and opportunities. *Scripta Materialia*, 143:181–187, 2018. ISSN 13596462. URL http://dx.doi.org/10.1016/j.scriptamat.2017.04.027.

[72] J. R. Hawthorne. Irradiation embrittlement. In C.L. Briant and S.K. Banerji, editors, *Embrittlement of Engineering Alloys*, volume 25 of *Treatise on Materials Science and Technology*, pages 461 – 524. Elsevier, 1983. URL https://doi.org/10.1016/B978-0-12-341825-8.50016-7.

[73] American Society of Mechanical Engineers (ASME). *Section III Division 5 'High Temperature Reactors'*. ASME, 2019.

[74] R.E. Stoller, G.R. Odette, and B.D. Wirth. Primary damage formation in bcc iron. *Journal of Nuclear Materials*, 251:49–60, 1997. ISSN 00223115. URL http://dx.doi.org/10.1016/S0022-3115(97)00256-0.

[75] J.F. Bates, F.A. Garner, and F.M. Mann. The effect of solid transmutation products on swelling in 316 stainless steel. *Journal of Nuclear Materials*, 104:

999 – 1003, 1981. ISSN 0022-3115. URL https://doi.org/10.1016/0022-3115(82)90730-9.

[76] M.R. Gilbert and J.-Ch. Sublet. Neutron-induced transmutation effects in W and W-alloys in a fusion environment. *Nuclear Fusion*, 51(4):043005, 2011. ISSN 0029-5515. URL http://dx.doi.org/10.1088/0029-5515/51/4/043005.

[77] M.R. Gilbert, S.L. Dudarev, S. Zheng, L.W. Packer, and J. Sublet. An integrated model for materials in a fusion power plant: transmutation, gas production, and helium embrittlement under neutron irradiation. *Nuclear Fusion*, 52 (8):083019, 2012. URL http://stacks.iop.org/0029-5515/52/i=8/a=083019.

[78] L K Mansur. Theory and experimental background on dimensional changes in irradiated alloys. *Journal of Nuclear Materials*, 216:97–123, 1994.

[79] F.A. Garner and M.B. Toloczko. Irradiation creep and void swelling of austenitic stainless steels at low displacement rates in light water energy systems. *Journal of Nuclear Materials*, 251:252 – 261, 1997. ISSN 0022-3115. URL https://doi.org/10.1016/S0022-3115(97)00260-2. Proceedings of the International Workshop on Defect Production, Accumulation and Materials Performance in an Irradiation Environment.

[80] Peter B. Wells, Takuya Yamamoto, Brandon Miller, Tim Milot, James Cole, Yuan Wu, and G. Robert Odette. Evolution of manganese-nickel-silicon-dominated phases in highly irradiated reactor pressure vessel steels. *Acta Materialia*, 80:205–219, 2014. ISSN 13596454. URL http://dx.doi.org/10.1016/j.actamat.2014.07.040.

[81] N. Almirall, P. B. Wells, S. Pal, P. D. Edmondson, T. Yamamoto, K. Murakami, and G. R. Odette. The mechanistic implications of the high temperature, long time thermal stability of nanoscale Mn-Ni-Si precipitates in irradiated reactor pressure vessel steels. *Scripta Materialia*, 181:134–139, 2020. ISSN 13596462. URL http://dx.doi.org/10.1016/j.scriptamat.2020.02.027.

[82] J.T Busby, G.S Was, and E.A Kenik. Isolating the effect of radiation-induced segregation in irradiation-assisted stress corrosion cracking of austenitic stainless steels. *Journal of Nuclear Materials*, 302(1):20 – 40, 2002. ISSN 0022-3115. URL https://doi.org/10.1016/S0022-3115(02)00719-5.

[83] Zhijie Jiao, Vani Shankar, and Gary S. Was. Phase stability in proton and heavy ion irradiated ferritic–martensitic alloys. *Journal of Nuclear Materials*, 419(1-3):52–62, dec 2011. ISSN 0022-3115. URL http://dx.doi.org/10.1016/J.JNUCMAT.2011.08.020.

[84] Z. Jiao and G.S. Was. Novel features of radiation-induced segregation and radiation-induced precipitation in austenitic stainless steels. *Acta Materialia*, 59(3):1220 – 1238, 2011. ISSN 1359-6454. URL https://doi.org/10.1016/j.actamat.2010.10.055.

[85] Ce Zheng, Elaina R. Reese, Kevin G. Field, Emmanuelle Marquis, Stuart A. Maloy, and Djamel Kaoumi. Microstructure response of ferritic/martensitic steel HT9 after neutron irradiation: effect of dose. *Journal of Nuclear Materials*, 523:421–433, 2019. ISSN 00223115. URL http://dx.doi.org/10.1016/j.jnucmat.2019.06.019.

[86] Ce Zheng, Elaina R. Reese, Kevin G. Field, Tian Liu, Emmanuelle A. Marquis, Stuart A. Maloy, and Djamel Kaoumi. Microstructure response of ferritic/martensitic steel HT9 after neutron irradiation: Effect of temperature. *Journal of Nuclear Materials*, 528:151845, 2020. ISSN 00223115. URL http://dx.doi.org/10.1016/j.jnucmat.2019.151845.

[87] G.R. Odette. On the dominant mechanism of irradiation embrittlement of reactor pressure vessel steels. *Scripta Metallurgica*, 17(10):1183 – 1188, 1983. ISSN 0036-9748. URL https://doi.org/10.1016/0036-9748(83)90280-6.

[88] G.R. Odette, T. Yamamoto, and B. D. Wirth. Late Blooming Phases and Dose Rate Effects in RPV Steels: Integrated Experiments and Models. *Proceeding of the Second International Conference on Multiscale Modeling*, 2004.

[89] G. R. Odette, T. Yamamoto, T. J. Williams, R. K. Nanstad, and C. A. English. On the history and status of reactor pressure vessel steel ductile to brittle transition temperature shift prediction models. *Journal of Nuclear Materials*, 526: 151863, 2019. ISSN 00223115. URL http://dx.doi.org/10.1016/j.jnucmat.2019.151863.

[90] Tetsuo Shoji, Shun ichi Suzuki, and K.S Raja. Current status and future of iascc research. *Journal of Nuclear Materials*, 258-263:241 – 251, 1998. ISSN 0022-3115. URL https://doi.org/10.1016/S0022-3115(98)00304-3.

[91] John A. Brinkman. On the nature of radiation damage in metals. *Journal of Applied Physics*, 25(8):961–970, 1954. URL http://dx.doi.org/10.1063/1.1721810.

[92] David J. Bacon and Tomas Diaz de la Rubia. Molecular dynamics computer simulations of displacement cascades in metals. *Journal of Nuclear Materials*, 216:275 – 290, 1994. ISSN 0022-3115. URL https://doi.org/10.1016/0022-3115(94)90016-7.

[93] T. P. Davis, E. Davies, N. A. Houti, O. Larkin, A. Potts and M. J. Lloyd. Modelling the Damage Evolution of Neutron Irradiated Reactor Pressure Vessel Steels Coupled with a Feasibility Study on a Positron Annihilation Spectroscopy Experiment. *University of Birmingham*, 2015.

[94] M.J. Norgett, M.T. Robinson, and I.M. Torrens. A proposed method of calculating displacement dose rates. *Nuclear Engineering and Design*, 33(1):50 – 54, 1975. ISSN 0029-5493. URL http://dx.doi.org/10.1016/0029-5493(75)90035-7.

[95] Peter Vajda. Anisotropy of electron radiation damage in metal crystals. *Rev. Mod. Phys.*, 49:481–521, Jul 1977. URL http://dx.doi.org/10.1103/RevModPhys.49.481.

[96] S.J. Zinkle and C. Kinoshita. Defect production in ceramics. *Journal of Nuclear Materials*, 251:200 – 217, 1997. ISSN 0022-3115. URL https://doi.org/10.1016/S0022-3115(97)00224-9. Proceedings of the International Workshop on Defect Production, Accumulation and Materials Performance in an Irradiation Environment.

[97] ASTM E521. Standard Practice for Neutron Radiation Damage Simulation by Charged-Particle. *Annual Book of ASTM Standards*, E521 - 96(Reapproved), 1996. URL http://dx.doi.org/10.1520/E0521-96R09E01.

[98] K. Nordlund, J. Wallenius, and L. Malerba. Molecular dynamics simulations of threshold displacement energies in Fe. *Nuclear Instruments and Methods in Physics Research Section B: Beam Interactions with Materials and Atoms*, 246(2):322 – 332, 2006. ISSN 0168-583X. URL https://doi.org/10.1016/j.nimb.2006.01.003.

[99] R.E. Stoller, M.B. Toloczko, G.S. Was, A.G. Certain, S. Dwaraknath, and F.A. Garner. On the Use of SRIM for Computing Radiation Damage Exposure. *Nuclear Instruments and Methods in Physics Research Section B: Beam Interactions with Materials and Atoms*, 310:75–80, 2013. ISSN 0168583X. URL http://dx.doi.org/10.1016/j.nimb.2013.05.008.

[100] G H Kinchin and R S Pease. The displacement of atoms in solids by radiation. *Reports on Progress in Physics*, 18(1):1, 1955. URL http://stacks.iop.org/0034-4885/18/i=1/a=301.

[101] Federico Puente Espel, Maria N. Avramova, Kostadin N. Ivanov, and Stefan Misu. New developments of the MCNP/CTF/NEM/NJOY code system – Monte Carlo based coupled code for high accuracy modeling. *Annals of Nuclear Energy*, 51:18 – 26, 2013. ISSN 0306-4549. URL https://doi.org/10.1016/j.anucene.2012.06.031.

[102] C.J. Werner. MCNP Users Manual – Code Version 6.2. *Los Alamos National Laboratory*, A-UR-17-29981, 2017.

[103] J. F. Ziegler. Interactions of Ions in Matter - SRIM. 2013. URL http://www.srim.org.

[104] ASTM E693-17. Standard Practice for Characterizing Neutron Exposures in Iron and Low Alloy Steels in Terms of Displacements Per Atom (DPA). *Annual Book of ASTM Standards*, 2017. URL http://dx.doi.org/10.1520/E0693-17.

[105] J.F. Ziegler, J.P. Biersack, and M.D. Ziegler. *SRIM, the Stopping and Range of Ions in Matter*. SRIM Company, 2008. ISBN 9780965420716.

[106] G. S. Was, Z. Jiao, E. Getto, K. Sun, A. M. Monterrosa, S. A. Maloy, O. Anderoglu, B. H. Sencer, and M. Hackett. Emulation of reactor irradiation damage using ion beams. *Scripta Materialia*, 88:33–36, 2014. ISSN 13596462. URL http://dx.doi.org/10.1016/j.scriptamat.2014.06.003.

[107] F. A. Garner, H. L. Heinisch, R. L. Simons, and F. M. Mann. Implications of neutron spectrum and flux differences on fission-fusion correlations at high neutron fluence. *Radiation Effects and Defects in Solids*, 113(1-3):229–255, 1990. URL http://dx.doi.org/10.1080/10420159008213068.

[108] K. Nordlund, A. E. Sand, F. Granberg, S.J. Zinkle, R.E. Stoller, and Etal. Primary Radiation Damage in Materials. *OCDE / Nuclear Science*, page NEA/NSC/DOC(2015)9, 2015.

[109] M. R. Gilbert, J-Ch. Sublet, and R. A. Forrest. Handbook of activation, transmutation and radiation dmagae properties of the elements simulated using FISPACT-II and TENDL-2014. *Culham Centre for Fusion Energy*, CCFE-R(15)(December), 2015. URL http://fispact.ukaea.uk/documentation-2/.

[110] N. Soneda. *Irradiation Embrittlement of Reactor Pressure Vessels (RPVs) in Nuclear Power Plants*. Woodhead Publishing Series in Energy. Elsevier Science, 2014. ISBN 9780857096470. URL https://books.google.co.uk/books?id=A_TCAgAAQBAJ.

[111] T. Hirai, H. Maier, M. Rubel, Ph. Mertens, R. Neu, E. Gauthier, J. Likonen, C. Lungu, G. Maddaluno, G.F. Matthews, R. Mitteau, O. Neubauer, G. Piazza, V.Philipps, B. Riccardi, C. Ruset, and I. Uytdenhouwen. R and d on full tungsten divertor and beryllium wall for jet iter-like wall project. *Fusion Engineering and Design*, 82(15):1839 – 1845, 2007. ISSN 0920-3796. URL https://doi.org/10.1016/j.fusengdes.2007.02.024. Proceedings of the 24th Symposium on Fusion Technology.

[112] R.A. Pitts, S. Carpentier, F. Escourbiac, T. Hirai, V. Komarov, S. Lisgo, A.S. Kukushkin, A. Loarte, M. Merola, A. Sashala Naik, R. Mitteau, M. Sugihara, B. Bazylev, and P.C. Stangeby. A full tungsten divertor for iter - physics issues and design status. *Journal of Nuclear Materials*, 438:S48 – S56, 2013. URL http://www.sciencedirect.com/science/article/pii/S0022311513000160. Proceedings of the 20th International Conference on Plasma-Surface Interactions in Controlled Fusion Devices.

[113] Patrick Lorenzetto, Stefano Banetta, Boris Bellin, Bruno Boireau, Philippe Bucci, Tindaro Cicero, Denis Conchon, Georges Dellopoulos, Stephen Hardaker, Paul Marshall, Patrice Nogué, Marcos Pérez, Leticia Ruiz Gutierrez, Fernando Samaniego, Paul Sherlock, and Francesco Zacchia. Eu contribution to the procurement of the iter blanket first wall. *Fusion Engineering and Design*, 109-111:661 – 665, 2016. ISSN 0920-3796. URL https://doi.org/10.1016/j.fusengdes.2016.02.024. Proceedings of the 12th International Symposium on Fusion Nuclear Technology-12 (ISFNT-12).

[114] D. Stork, P. Agostini, J.L. Boutard, D. Buckthorpe, E. Diegele, S.L. Dudarev, C. English, G. Federici, M.R. Gilbert, S. Gonzalez, A. Ibarra, Ch. Linsmeier, A. Li Puma, G. Marbach, P.F. Morris, L.W. Packer, B. Raj, M. Rieth, M.Q. Tran, D.J. Ward, and S.J. Zinkle. Developing structural, high-heat flux and plasma facing materials for a near-term demo fusion power plant: The eu assessment. *Journal of Nuclear Materials*, 455(1):277 – 291, 2014. ISSN 0022-3115. URL https://doi.org/10.1016/j.jnucmat.2014.06.014. Proceedings of the 16th International Conference on Fusion Reactor Materials (ICFRM-16).

[115] M. J. Makin and J. V. Sharp. A Model of "Lattice" Hardening in Irradiated Copper Crystals with the External Characteristics of "Source" Hardening. *Physica Status Solidi (b)*, 9(1):109–118, 1965. ISSN 1521-3951. URL http://dx.doi.org/10.1002/pssb.19650090114.

[116] G.R. Odette. A model for in-reactor stress rupture of austenitic stainless steels. *Journal of Nuclear Materials*, 122(1–3):435 – 441, 1984. ISSN 0022-3115. URL http://dx.doi.org/10.1016/0022-3115(84)90636-6.

[117] F.A. Garner, M.L. Hamilton, C.R. Eiholzer, M.B. Toloczko, and A.S. Kumar. Irradiation and thermal creep of a titanium-modified austenitic stainless steel and its dependence on cold work level. *Journal of Nuclear Materials*, 191-194, Part B:813–817, 1992. URL http://dx.doi.org/10.1016/0022-3115(92)90585-9.

[118] Y. Dai, G.R. Odette, and T. Yamamoto. 1.06 - The Effects of Helium in Irradiated Structural Alloys. In Rudy J.M. Konings, editor, *Comprehensive Nuclear*

Materials, pages 141 – 193. Elsevier, Oxford, 2012. ISBN 978-0-08-056033-5. URL http://dx.doi.org/10.1016/B978-0-08-056033-5.00006-9.

[119] D.S Gelles. On quantification of helium embrittlement in ferritic/martensitic steels. *Journal of Nuclear Materials*, 283-287:838 – 840, 2000. ISSN 0022-3115. URL https://doi.org/10.1016/S0022-3115(00)00379-2. 9th Int. Conf. on Fusion Reactor Materials.

[120] F. Bergner, G. Hlawacek, and C. Heintze. Helium-ion microscopy, helium-ion irradiation and nanoindentation of Eurofer 97 and ODS Eurofer. *Journal of Nuclear Materials*, 2017. ISSN 0022-3115. URL https://doi.org/10.1016/j.jnucmat.2017.07.054.

[121] M. Bossant N. Soppera, E. Dupont and O. Cabellos. JANIS Book of proton-induced cross-sections. *OECD NED Data Bank*, 2017.

[122] C. Abromeit. Aspects of simulation of neutron damage by ion irradiation. *Journal of Nuclear Materials*, 216:78 – 96, 1994. ISSN 0022-3115. URL https://doi.org/10.1016/0022-3115(94)90008-6.

[123] J Gan and G.S Was. Microstructure evolution in austenitic Fe-Cr-Ni alloys irradiated with potons: comparison with neutron-irradiated microstructures. *Journal of Nuclear Materials*, 297(2):161 – 175, 2001. ISSN 0022-3115. URL http://dx.doi.org/10.1016/S0022-3115(01)00615-8.

[124] Gary S. Was and Todd R. Allen. *Radiation Effects in Solids – Chapter 4: Radiation Damage from Difference Particle Types*. Springer Netherlands, Dordrecht, 2007. ISBN 978-1-4020-5295-8. URL https://dx.doi.org/10.1007/978-1-4020-5295-8_4.

[125] Peter Hosemann. Small-scale mechanical testing on nuclear materials: Bridging the experimental length-scale gap. *Scripta Materialia*, 143:161–168, 2018. ISSN 13596462. URL http://dx.doi.org/10.1016/j.scriptamat.2017.04.026.

[126] T Fukuda, T Aoki, Y Isobe, T Furuya, A Hasegawa, and K Abe. Microchemical and microstructural changes of austenitic steels caused by proton irradiation following helium implantation. *Journal of Nuclear Materials*, 258-263:1694 – 1699, 1998. ISSN 0022-3115. URL https://doi.org/10.1016/S0022-3115(98)00338-9.

[127] G. S. Was and et al. Emulation of neutron irradiation effects with protons: Validation of principle. *Journal of Nuclear Materials*, 300(2-3):198–216, 2002. ISSN 00223115. URL http://dx.doi.org/10.1016/S0022-3115(01)00751-6.

[128] Bulent H. Sencer, Gary S. Was, Mitsuyuki Sagisaka, Yoshihiro Isobe, Gillian M. Bond, and Frank A. Garner. Proton irradiation emulation of PWR neutron damage microstructures in solution annealed 304 and cold-worked 316 stainless steels. *Journal of Nuclear Materials*, 323(1):18 – 28, 2003. ISSN 0022-3115. URL https://doi.org/10.1016/j.jnucmat.2003.07.007.

[129] G. Gupta, Z. Jiao, A.N. Ham, J.T. Busby, and G.S. Was. Microstructural evolution of proton irradiated T91. *Journal of Nuclear Materials*, 351(1):162 – 173, 2006. ISSN 0022-3115. URL https://doi.org/10.1016/j.jnucmat.2006.02.028. Proceedings of the Symposium on Microstructural Processes in Irradiated Materials.

[130] Z. Jiao and G. S. Was. Segregation behavior in proton- and heavy-ion-irradiated ferritic-martensitic alloys. *Acta Materialia*, 59(11):4467–4481, 2011. URL http://dx.doi.org/10.1016/j.actamat.2011.03.070.

[131] Gary S. Was. Challenges to the use of ion irradiation for emulating reactor irradiation. *Journal of Materials Research*, 30(9):1158–1182, 2015. ISSN 20445326. URL http://dx.doi.org/10.1557/jmr.2015.73.

[132] G.S. Was and R.S Averback. 1.07 - radiation damage using ion beams. In Rudy J.M. Konings, editor, *Comprehensive Nuclear Materials*. Elsevier, Oxford, 2012. ISBN 978-0-08-056033-5. URL http://dx.doi.org/10.1016/B978-0-08-056033-5.00027-6.

[133] A. Souidi, M. Hou, C.S. Becquart, L. Malerba, C. Domain, and R.E. Stoller. On the correlation between primary damage and long-term nanostructural evolution in iron under irradiation. *Journal of Nuclear Materials*, 419(1):122 – 133, 2011. ISSN 0022-3115. URL https://doi.org/10.1016/j.jnucmat.2011.08.049.

[134] Kai Nordund, Sand Andrea, and et al. Primary radiation damage in materials. review of current understanding and proposed new standard displacement damage model to incorporate in cascade defect production efficiency and mixing effects. *IAEA*, pages NEA–NSC–DOC–2015–9, 2015.

[135] F.A. Garner. Impact of the injected interstitial on the correlation of charged particle and neutron-induced radiation damage. *Journal of Nuclear Materials*, 117:177 – 197, 1983. ISSN 0022-3115. URL https://doi.org/10.1016/0022-3115(83)90023-5.

[136] W.G. Johnston, J.H. Rosolowski, A.M. Turkalo, and T. Lauritzen. The depth distribution of void swelling produced by 5 MeV Ni ions. *Journal of Nuclear Materials*, 62(2):167 – 180, 1976. ISSN 0022-3115. URL https://doi.org/10.1016/0022-3115(76)90014-3.

[137] M. R. Gilbert, T. Eade, T. Rey, R. Vale, C. Bachmann, U. Fischer, and N. P. Taylor. Waste implications from minor impurities in European DEMO materials. *Nuclear Fusion*, 59(7), 2019. ISSN 17414326. URL http://dx.doi.org/10.1088/1741-4326/ab154e.

[138] M. Rieth and et al. Recent progress in research on tungsten materials for nuclear fusion applications in europe. *Journal of Nuclear Materials*, 432(1–3): 482 – 500, 2013. ISSN 0022-3115. URL http://dx.doi.org/10.1016/j.jnucmat.2012.08.018.

[139] Alan Xu, Christian Beck, David E J Armstrong, Krishna Rajan, George D W Smith, Paul A J Bagot, and Steve G. Roberts. Ion-irradiation-induced clustering in W-Re and W-Re-Os alloys: A comparative study using atom probe tomography and nanoindentation measurements. *Acta Materialia*, 87:121–127, 2015. ISSN 13596454. URL http://dx.doi.org/10.1016/j.actamat.2014.12.049.

[140] Alan Xu, David E.J. Armstrong, Christian Beck, Michael P. Moody, George D.W. Smith, Paul A.J. Bagot, and Steve G. Roberts. Ion-irradiation induced clustering in W-Re-Ta, W-Re and W-Ta alloys: An atom probe tomography and nanoindentation study. *Acta Materialia*, 124:71–78, 2017. ISSN 13596454. URL http://dx.doi.org/10.1016/j.actamat.2016.10.050.

[141] Jaime Marian, Tuan Hoang, Michael Fluss, and Luke L. Hsiung. A review of helium–hydrogen synergistic effects in radiation damage observed in fusion energy steels and an interaction model to guide future understanding. *Journal of Nuclear Materials*, 462(Supplement C):409 – 421, 2015. ISSN 0022-3115. URL https://doi.org/10.1016/j.jnucmat.2014.12.046.

[142] S. J. Zinkle and L. L. Snead. Opportunities and limitations for ion beams in radiation effects studies: Bridging critical gaps between charged particle and neutron irradiations. *Scripta Materialia*, 143:154–160, 2018. ISSN 13596462. URL http://dx.doi.org/10.1016/j.scriptamat.2017.06.041.

[143] K. Kimura, H. Kushima, and K. Sawada. Long-term creep deformation property of modified 9Cr-1Mo steel. *Materials Science and Engineering A*, 510-511(C):58–63, 2009. ISSN 09215093. URL http://dx.doi.org/10.1016/j.msea.2008.04.095.

[144] G. Kurita, T. Tuda, M. Azumi, S. Ishida, S. Takeji, A. Sakasai, M. Matsukawa, T. Ozeki, and M. Kikuchi. Ferromagnetic and resistive wall effects on the beta limit in a tokamak. *Nuclear Fusion*, 43(9):949, 2003. URL http://stacks.iop.org/0029-5515/43/i=9/a=319.

[145] M. J. Gorley. Critical assessment 12: Prospects for reduced activation steel for fusion plant. *Materials Science and Technology*, 31(8):975–980, 2015. URL http://dx.doi.org/10.1179/1743284714Y.0000000732.

[146] W. K. Sowder and Richard W. Barnes. ASME division 4 fusion energy devices. *International Conference on Nuclear Engineering, Proceedings, ICONE*, 4(1): 1–3, 2012. URL http://dx.doi.org/10.1115/ICONE20-POWER2012-54015.

[147] AFCEN. *RCC-MRx: Design and Construction Rules for Mechanical Components in high-temperature structures, experimental reactors and fusion reactors*. AFCEN, 2018. URL https://www.afcen.com/en/106-rcc-mrx.

[148] C. Cabet, F. Dalle, E. Gaganidze, J. Henry, and H. Tanigawa. Ferritic-martensitic steels for fission and fusion applications. *Journal of Nuclear Materials*, 523:510–537, sep 2019. ISSN 0022-3115. URL http://dx.doi.org/10.1016/J.JNUCMAT.2019.05.058.

[149] S. Hamada, P.J. Maziasz, M.P. Tanaka, M. Suzuki, and A. Hishinuma. Temperature dependence of swelling in type 316 stainless steel irradiated in hfir. *Journal of Nuclear Materials*, 155-157:838 – 844, 1988. ISSN 0022-3115. URL https://doi.org/10.1016/0022-3115(88)90426-6.

[150] Ronald L Klueh and Donald R Harries. *High-Chromium Ferritic and Martensitic Steels for Nuclear Applications*. ASTM, 2001. ISBN 0803120907. URL http://dx.doi.org/10.1520/mono3-eb.

[151] ASTM. A213 Standard Specifications: Seamless Ferritic and Austenitic Alloy-Steel Boiler, Superheater, and Heat-Exchanger Tubes. *ASTM InternationalASTM International*, A213, 2006.

[152] ASTM. A182 Standard Specification for Forged or Rolled Alloy-Steel Pipe Flanges , Forged Fittings , and Valves and Parts for High-Temperature Service. *ASTM International*, (October 2002):1–4, 2004. URL http://dx.doi.org/10.1520/A0182.

[153] A. Zeman, L. Debarberis, J. Kočík, V. Slugeň, and E. Keilová. Microstructural analysis of candidate steels pre-selected for new advanced reactor systems. *Journal of Nuclear Materials*, 362(2):259 – 267, 2007. ISSN 0022-3115. URL https://doi.org/10.1016/j.jnucmat.2007.01.068. E-MRS 2006: Symposium N.

[154] R.J. Kurtz, A. Alamo, E. Lucon, Q. Huang, S. Jitsukawa, A. Kimura, R.L. Klueh, G.R. Odette, C. Petersen, M.A. Sokolov, P. Spatig, and J.-W. Rensman. Recent progress toward development of reduced activation ferritic/martensitic

steels for fusion structural applications. *Journal of Nuclear Materials*, 386-388:411 – 417, 2009. ISSN 0022-3115. URL https://doi.org/10.1016/j.jnucmat.2008.12.323. Fusion Reactor Materials.

[155] A. A.F. Tavassoli, A. Alamo, L. Bedel, L. Forest, J. M. Gentzbittel, J. W. Rensman, E. Diegele, R. Lindau, M. Schirra, R. Schmitt, H. C. Schneider, C. Petersen, A. M. Lancha, P. Fernandez, G. Filacchioni, M. F. Maday, K. Mergia, N. Boukos, Baluc, P. Spätig, E. Alves, and E. Lucon. Materials design data for reduced activation martensitic steel type EUROFER. *Journal of Nuclear Materials*, 329-333(1-3 PART A):257–262, 2004. ISSN 00223115. URL http://dx.doi.org/10.1016/j.jnucmat.2004.04.020.

[156] L. Tan, Y. Katoh, A. A.F. Tavassoli, J. Henry, M. Rieth, H. Sakasegawa, H. Tanigawa, and Q. Huang. Recent status and improvement of reduced-activation ferritic-martensitic steels for high-temperature service. *Journal of Nuclear Materials*, 479:515–523, 2016. ISSN 00223115. URL http://dx.doi.org/10.1016/j.jnucmat.2016.07.054.

[157] ASTM. A335 Specficiation for Seamless Ferritic Alloy-Steel Pipe for High-Temperature Service. *ASTM International*, A335-15a, 2015.

[158] A Alemberti, M L Frogheri, S Hermsmeyer, L Ammirabile, V Smirnov, M Takahashi, C F Smith, Y Wu, and I S Hwang. Lead-cooled Fast Reactor (LFR) Risk and Safety Assessment White Paper. *GENIV International Forum*, April:17, 2014. URL https://www.gen-4.org/gif/upload/docs/application/pdf/2014-11/rswg{_}lfr{_}white{_}paper{_}final{_}8.0.pdf.

[159] Savoy Piping Inc. ASTM A2143 T91 Tubes, Savoy Pip. Inc., 2020. URL https://www.savoypipinginc.com/alloy-steel-pipestubes-tubing-manufacturer/astm-a213-T5_seamless-alloy-steel-pipe.html.

[160] R.L. Klueh and J.M. Vitek. Elevated-temperature tensile properties of irradiated 9 Cr-1 MoVNb steel. *Journal of Nuclear Materials*, 132(1):27 – 31, 1985. ISSN 0022-3115. URL https://doi.org/10.1016/0022-3115(85)90389-7.

[161] W-L Hu and D S Gelles. The Ductile-to-Brittle Transition Behavior of Martensitic Steels Neutron Irradiated to 26 dpa. In F A Garner, C H Henager, and N Igata, editors, *Influence of Radiation on Material Properties: 13th International Symposium (Part II)*, pages 83–97. ASTM International, West Conshohocken, PA, jan 1987. ISBN 978-0-8031-5017-1. URL http://dx.doi.org/10.1520/STP25642S.

[162] Huang Fan-Hsiung and Margaret L. Hamilton. The fracture toughness database of ferritic alloys irradiated to very high neutron exposures. *Journal of Nuclear Materials*, 187(3):278–293, 1992. ISSN 00223115. URL http://dx.doi.org/10.1016/0022-3115(92)90508-I.

[163] J. J. Kai and R. L. Klueh. Microstructural analysis of neutron-irradiated martensitic steels. *Journal of Nuclear Materials*, 230(2):116–123, 1996.

[164] J. Van Den Bosch, O. Anderoglu, R. Dickerson, M. Hartl, P. Dickerson, J. A. Aguiar, P. Hosemann, M. B. Toloczko, and S. A. Maloy. SANS and TEM of ferritic-martensitic steel T91 irradiated in FFTF up to 184 dpa at 413 °c. *Journal of Nuclear Materials*, 440(1-3):91–97, 2013. ISSN 00223115. URL http://dx.doi.org/10.1016/j.jnucmat.2013.04.025.

[165] L. Tan, B. K. Kim, Y. Yang, K. G. Field, S. Gray, and M. Li. Microstructural evolution of neutron-irradiated T91 and NF616 to □4.3 dpa at 469 °C. *Journal of Nuclear Materials*, 493:12–20, 2017. ISSN 00223115. URL http://dx.doi.org/10.1016/j.jnucmat.2017.05.041.

[166] Z. Jiao, S. Taller, K. Field, G. Yeli, M. P. Moody, and G. S. Was. Microstructure evolution of T91 irradiated in the BOR60 fast reactor. *Journal of Nuclear Materials*, 504:122–134, 2018. ISSN 00223115. URL http://dx.doi.org/10.1016/j.jnucmat.2018.03.024.

[167] R.W Swindeman, M.L Santella, P.J Maziasz, B.W Roberts, and K Coleman. Issues in replacing cr–mo steels and stainless steels with 9cr–1mo–v steel. *International Journal of Pressure Vessels and Piping*, 81(6):507 – 512, 2004. ISSN 0308-0161. URL https://doi.org/10.1016/j.ijpvp.2003.12.009. The 7th International Conference on Operating Pressure Equipment.

[168] S. J. Brett. UK experience with modified 9Cr (grade 91) steel. *VTT Symposium (Valtion Teknillinen Tutkimuskeskus)*, 1(246):48–60, 2007. ISSN 03579387. URL http://dx.doi.org/10.1179/174892407x266707.

[169] R Wright and Sam Sham. Status of metallic structural materials for molten salt reactors, 05 2018. URL http://dx.doi.org/10.2172/1467482.

[170] Nuclear Regulatory Commission. 50.55a Codes and standards). *NRC Regulations (10 CFR)*, 2020. URL https://www.nrc.gov/reading-rm/doc-collections/cfr/part050/part050-0055a.html.

[171] F. Abe. 1 - grade 91 heat-resistant martensitic steel. In Ahmed Shibli, editor, *Coal Power Plant Materials and Life Assessment*, pages 3 – 51. Woodhead Publishing, 2014. ISBN 978-0-85709-431-5. URL https://doi.org/10.1533/9780857097323.1.3.

[172] S. J. Zinkle. Radiation-induced effects on microstructure. In Konings, R.J.M. and Allen, T.R. and Stoller, R.E. and Yamanaka, S., editor, *Comprehensive Nuclear Materialsk*, volume 1, chapter 1.03. Elsevier, 1 edition, 2012.

[173] C. Pareige, V. Kuksenko, and P. Pareige. Behaviour of P, Si, Ni impurities and Cr in self ion irradiated Fe-Cr alloys - Comparison to neutron irradiation. *Journal of Nuclear Materials*, 456:471–476, 2015. ISSN 00223115. URL http://dx.doi.org/10.1016/j.jnucmat.2014.10.024.

[174] O. Anderoglu, J. Van Den Bosch, P. Hosemann, E. Stergar, B. H. Sencer, D. Bhattacharyya, R. Dickerson, P. Dickerson, M. Hartl, and S. A. Maloy. Phase stability of an HT-9 duct irradiated in FFTF. *Journal of Nuclear Materials*, 430(1-3):194–204, 2012. ISSN 00223115. URL http://dx.doi.org/10.1016/j.jnucmat.2012.06.038.

[175] S. Rogozhkin, A Nikitin, N. Orlov, A Bogachev, O. Korchuganova, A Aleev, A Zaluzhnyi, T. Kulevoy, R. Lindau, A Moslang, and P Vladimirov. Evolution of microstructure in advanced ferritic-martensitic steels under irradiation: the origin of low temperature radiation embrittlement S. *MRS Advances*, 2(21-22): 1143–1155, 2017. ISSN 1098-6596. URL http://dx.doi.org/10.1017/CBO9781107415324.004.

[176] M. J. Swenson and J. P. Wharry. Nanocluster irradiation evolution in Fe-9%Cr ODS and ferritic-martensitic alloys. *Journal of Nuclear Materials*, 496:24–40, 2017. ISSN 00223115. URL http://dx.doi.org/10.1016/j.jnucmat.2017.08.045.

[177] Ce Zheng, Maria A. Auger, Michael P. Moody, and Djamel Kaoumi. Radiation induced segregation and precipitation behavior in self-ion irradiated Ferritic/Martensitic HT9 steel. *Journal of Nuclear Materials*, 491:162–176, 2017. ISSN 00223115. URL http://dx.doi.org/10.1016/j.jnucmat.2017.04.040.

[178] B. Gómez-Ferrer, C. Heintze, and C. Pareige. On the role of Ni, Si and P on the nanostructural evolution of FeCr alloys under irradiation. *Journal of Nuclear Materials*, 517:35–44, 2019. ISSN 00223115. URL http://dx.doi.org/10.1016/j.jnucmat.2019.01.040.

[179] B. Gómez-Ferrer, C. Dethloff, E. Gaganidze, L. Malerba, C. Hatzoglou, and C. Pareige. Nano-hardening features in high-dose neutron irradiated Eurofer97 revealed by atom-probe tomography. *Journal of Nuclear Materials*, 537: 152228, 2020. ISSN 00223115. URL http://dx.doi.org/10.1016/j.jnucmat.2020.152228.

[180] K. P. Gupta. The Mn-Ni-Si (manganese-nickel-silicon) system. *Journal of Phase Equilibria and Diffusion*, 27(5):529–534, 2006. ISSN 15477037. URL http://dx.doi.org/10.1361/154770306X136520.

[181] Jia Hong Ke, Huibin Ke, G. Robert Odette, and Dane Morgan. Cluster dynamics modeling of Mn-Ni-Si precipitates in ferritic-martensitic steel under irradiation. *Journal of Nuclear Materials*, 498:83–88, 2018. ISSN 00223115. URL http://dx.doi.org/10.1016/j.jnucmat.2017.10.008.

[182] R.L. Klueh, K. Ehrlich, and F. Abe. Ferritic/martensitic steels: promises and problems. *Journal of Nuclear Materials*, 191-194:116 – 124, 1992. ISSN 0022-3115. URL https://doi.org/10.1016/S0022-3115(09)80018-4. Fusion Reactor Materials Part A.

[183] R. L. Klueh. Elevated temperature ferritic and martensitic steels and their application to future nuclear reactors. *International Materials Reviews*, 50(5): 287–310, 2005. URL http://dx.doi.org/10.1179/174328005X41140.

[184] Z. Lu, R.G. Faulkner, G. Was, and B.D. Wirth. Irradiation-induced grain boundary chromium microchemistry in high alloy ferritic steels. *Scripta Materialia*, 58(10):878 – 881, 2008. ISSN 1359-6462. URL https://doi.org/10.1016/j.scriptamat.2008.01.004.

[185] Kevin G. Field, Brandon D. Miller, Heather J M Chichester, Kumar Sridharan, and Todd R. Allen. Relationship between lath boundary structure and radiation induced segregation in a neutron irradiated 9 wt.% Cr model ferritic/martensitic steel. *Journal of Nuclear Materials*, 445(1-3):143–148, 2014. ISSN 00223115. URL http://dx.doi.org/10.1016/j.jnucmat.2013.10.056.

[186] Mukesh Bachhav, G. Robert Odette, and Emmanuelle A. Marquis. α' precipitation in neutron-irradiated Fe-Cr alloys. *Scripta Materialia*, 74:48–51, 2014. ISSN 13596462. URL http://dx.doi.org/10.1016/j.scriptamat.2013.10.001.

[187] Mukesh Bachhav, G. Robert Odette, and Emmanuelle A. Marquis. Microstructural changes in a neutron-irradiated Fe-15 at.%Cr alloy. *Journal of Nuclear Materials*, 454(1):381–386, 2014. ISSN 00223115. URL http://dx.doi.org/10.1016/j.jnucmat.2014.08.026.

[188] O. Tissot, C. Pareige, E. Meslin, B. Décamps, and J. Henry. Influence of injected interstitials on α' precipitation in fe–cr alloys under self-ion irradiation. *Materials Research Letters*, 5(2):117–123, 2017.

[189] X. Jia and Y. Dai. Microstructure in martensitic steels T91 and F82H after irradiation in SINQ Target-3. *Journal of Nuclear Materials*, 318(Supplement C):207 – 214, 2003. ISSN 0022-3115. URL https://doi.org/10.1016/S0022-3115(03)00101-6. Fifth International Workshop on Spallation Materials Technology.

[190] P.J. Maziasz. Formation and stability of radiation-induced phases in neutron-irradiated austenitic and ferritic steels. *Journal of Nuclear Materials*, 169:95 – 115, 1989. ISSN 0022-3115. URL https://doi.org/10.1016/0022-3115(89)90525-4.

[191] S. Yamashita, Y. Yano, Y. Tachi, and N. Akasaka. Effect of high dose/high temperature irradiation on the microstructure of heat resistant 11Cr ferritic/martensitic steels. *Journal of Nuclear Materials*, 386-388:135 – 139, 2009. ISSN 0022-3115. URL https://doi.org/10.1016/j.jnucmat.2008.12.082. Fusion Reactor Materials.

[192] M. Matijasevic and A. Almazouzi. Effect of Cr on the mechanical properties and microstructure of Fe–Cr model alloys after n-irradiation. *Journal of Nuclear Materials*, 377(1):147 – 154, 2008. URL https://doi.org/10.1016/j.jnucmat.2008.02.061.

[193] M. H. Mathon, Y. De Carlan, G. Geoffroy, X. Averty, A. Alamo, and C. H. De Novion. A SANS investigation of the irradiation-enhanced α-α' phases separation in 7-12 Cr martensitic steels. *Journal of Nuclear Materials*, 312 (2-3):236–248, 2003. ISSN 00223115. URL http://dx.doi.org/10.1016/S0022-3115(02)01630-6.

[194] J.O. Stiegler and E.E. Bloom. The effect of thermo-mechanical treatments on void formation in irradiated stainless steel. *Journal of Nuclear Materials*, 41 (3):341 – 344, 1971. ISSN 0022-3115. URL http://dx.doi.org/10.1016/0022-3115(71)90171-1.

[195] S.J. Zinkle, P.J. Maziasz, and R.E. Stoller. Dose dependence of the microstructural evolution in neutron-irradiated austenitic stainless steel. *Journal of Nuclear Materials*, 206(2):266 – 286, 1993. ISSN 0022-3115. URL http://dx.doi.org/10.1016/0022-3115(93)90128-L.

[196] M. J. Alinger, G. R. Odette, and D. T. Hoelzer. The development and stability of Y-Ti-O nanoclusters in mechanically alloyed Fe-Cr based ferritic alloys. *Journal of Nuclear Materials*, 329-333(1-3 PART A):382–386, 2004. ISSN 00223115. URL http://dx.doi.org/10.1016/j.jnucmat.2004.04.042.

[197] D A Mcclintock, D T Hoelzer, M A Sokolov, and R K Nanstad. Mechanical properties of neutron irradiated nanostructured ferritic alloy 14YWT. *Journal of Nuclear Materials*, 388:307–311, 2009. URL http://dx.doi.org/10.1016/j.jnucmat.2008.12.104.

[198] A. Hirata, T. Fujita, Y. R. Wen, J. H. Schneibel, C. T. Liu, and M. W. Chen. Atomic structure of nanoclusters in oxide-dispersion-strengthened steels. *Nature Materials*, 10(12):922–926, 2011. ISSN 1476-1122. URL http://dx.doi.org/10.1038/nmat3150.

[199] G. R. Odette. Recent progress in developing and qualifying nanostructured ferritic alloys for advanced fission and fusion applications. *JOM*, 66(12):2427–2441, Dec 2014. ISSN 1543-1851. URL https://doi.org/10.1007/s11837-014-1207-5.

[200] Cunningham, N.J. *Study of the Structure, Composition, and Stability of Yttrium-Ti-Oxygen nm-Scale Features in Nano-Structured Ferritic Alloys*. PhD thesis, University of California, Santa Barbara, 2012.

[201] N. Cunningham, Y. Wu, D. Klingensmith, and G.R. Odette. On the remarkable thermal stability of nanostructured ferritic alloys. *Materials Science and Engineering: A*, 613(Supplement C):296 – 305, 2014. ISSN 0921-5093. URL https://doi.org/10.1016/j.msea.2014.06.097.

[202] P.D. Edmondson, C.M. Parish, Y. Zhang, A. Hallén, and M.K. Miller. Helium bubble distributions in a nanostructured ferritic alloy. *Journal of Nuclear Materials*, 434(1):210 – 216, 2013. ISSN 0022-3115. URL https://doi.org/10.1016/j.jnucmat.2012.11.049. Special Section on Spent Nuclear Fuel.

[203] I. Hilger, M. Tegel, M.J. Gorley, P.S. Grant, T. Weißgärber, and B. Kieback. The structural changes of Y_2O_3 in ferritic ODS alloys during milling. *Journal of Nuclear Materials*, 447(1):242 – 247, 2014. ISSN 0022-3115. URL https://doi.org/10.1016/j.jnucmat.2014.01.026.

[204] Yuan Wu, Jim Ciston, Stephan Kräemer, Nathan Bailey, G. Robert Odette, and Peter Hosemann. The crystal structure, orientation relationships and interfaces of the nanoscale oxides in nanostructured ferritic alloys. *Acta Materialia*, 111:108 – 115, 2016. ISSN 1359-6454. URL https://doi.org/10.1016/j.actamat.2016.03.031.

[205] Shigeharu Ukai and Masayuki Fujiwara. Perspective of ODS alloys application in nuclear environments. *Journal of Nuclear Materials*, 307-311(Part 1):749 – 757, 2002. ISSN 0022-3115. URL https://doi.org/10.1016/S0022-3115(02)01043-7.

[206] S. Kardellass, C. Servant, N. Selhaoui, A. Iddaoudi, M. Ait Amar, and L. Bouirden. A thermodynamic assessment of the iron-yttrium system. *Journal of Alloys and Compounds*, 583:598–606, 2014. ISSN 09258388. URL http://dx.doi.org/10.1016/j.jallcom.2013.07.010.

[207] Thierry Grosdidier, Gang Ji, and Sébastien Launois. Processing dense hetero-nanostructured metallic materials by spark plasma sintering. *Scripta Materialia*, 57(6):525 – 528, 2007. ISSN 1359-6462. URL https://doi.org/10.1016/j.scriptamat.2007.05.022.

[208] Hongtao Zhang, Yina Huang, Huanpo Ning, Ceri A. Williams, Andrew J. London, Karl Dawson, Zuliang Hong, Michael J. Gorley, Chris R.M. Grovenor, Gordon J. Tatlock, Steve G. Roberts, Michael J. Reece, Haixue Yan, and Patrick S. Grant. Processing and microstructure characterisation of oxide dispersion strengthened fe–14cr–0.4ti–0.25y2o3 ferritic steels fabricated by spark plasma sintering. *Journal of Nuclear Materials*, 464:61 – 68, 2015. ISSN 0022-3115. URL https://doi.org/10.1016/j.jnucmat.2015.04.029.

[209] I. Hilger, X. Boulnat, J. Hoffmann, C. Testani, F. Bergner, Y. De Carlan, F. Ferraro, and A. Ulbricht. Fabrication and characterization of oxide dispersion strengthened (ODS) 14Cr steels consolidated by means of hot isostatic pressing, hot extrusion and spark plasma sintering. *Journal of Nuclear Materials*, 472(Supplement C):206 – 214, 2016. ISSN 0022-3115. URL https://doi.org/10.1016/j.jnucmat.2015.09.036.

[210] Michael Gorley. *Powder processing of oxide dispersion strengthened steels for nuclear applications*. PhD thesis, University of Oxford, 2014.

[211] J.S. Benjamin. Composite metal powder. US Patent 3,591,362, 1971.

[212] M.J. Alinger, G.R. Odette, and D.T. Hoelzer. On the role of alloy composition and processing parameters in nanocluster formation and dispersion strengthening in nanostuctured ferritic alloys. *Acta Materialia*, 57(2):392 – 406, 2009. ISSN 1359-6454. URL https://doi.org/10.1016/j.actamat.2008.09.025.

[213] Okuda, T. and et al. Development of Oxide Dispersion Strengthened (ODS) Ferritic Alloys With Excellent High Temperature Creep Strength and Neutron Irradiation Resistance. *New Materials Processes for the Future*, pages 1616–1621, 1989.

[214] Y. Uchidi and et al. Effect of minor alloying element on dispersing nanoparticles in ods steel. *MRS Proceedings*, 981:0981–JJ07–09, 2011.

[215] M. A. Auger, V. de Castro, T. Leguey, S. Lozano-Perez, P. A J Bagot, M. P. Moody, and S. G. Roberts. Effect of the milling atmosphere on the microstructure and mechanical properties of a ODS Fe-14Cr model alloy. *Materials Science and Engineering A*, 671:264–274, 2016. ISSN 09215093. URL http://dx.doi.org/10.1016/j.msea.2016.06.054.

[216] Christopher Burrows. *The Irradiation Resistance of Oxide Dispersion Strengthened Steels*. PhD thesis, University of Oxford, 2014.

[217] Zoz Group. Zoz launching PM2000. *Zoz Group*, 2017. URL http://gmbh.zoz.de/wp-content/uploads/ZG-1702-PM2000-relaunch-E.pdf.

[218] A.J. London, S. Santra, S. Amirthapandian, B.K. Panigrahi, R.M. Sarguna, S. Balaji, R. Vijay, C.S. Sundar, S. Lozano-Perez, and C.R.M. Grovenor. Effect of ti and cr on dispersion, structure and composition of oxide nano-particles in model ods alloys. *Acta Materialia*, 97:223 – 233, 2015. ISSN 1359-6454. URL https://doi.org/10.1016/j.actamat.2015.06.032.

[219] S Miran, P Franke, A Möslang, and H J Seifert. Casting technology for ODS steels – the internal oxidation approach. *IOP Conference Series: Materials Science and Engineering*, 228(1):012021, 2017. URL http://stacks.iop.org/1757-899X/228/i=1/a=012021.

[220] Zuhair A. Munir, Dat V. Quach, and Manshi Ohyanagi. Electric current activation of sintering: A review of the pulsed electric current sintering process. *Journal of the American Ceramic Society*, 94(1):1–19, 2011. ISSN 1551-2916. URL http://dx.doi.org/10.1111/j.1551-2916.2010.04210.x.

[221] Christopher Jones. *A Micromechanical Investigation of Proton Irradiated Oxide Dispersion Strengthened Steels*. PhD thesis, University of Oxford, 2016.

[222] Isabell Hilger, Frank Bergner, and Thomas Weibarber. Bimodal Grain Size Distribution of Nanostructured Ferritic ODS Fe – Cr Alloys. *Journal of the American Ceramic Society*, 3581(36126):3576–3581, 2015. URL http://dx.doi.org/10.1111/jace.13833.

[223] N. Sallez, X. Boulnat, A. Borbély, J.L. Béchade, D. Fabrègue, M. Perez, Y. de Carlan, L. Hennet, C. Mocuta, D. Thiaudière, and Y. Bréchet. In situ characterization of microstructural instabilities: Recovery, recrystallization and abnormal growth in nanoreinforced steel powder. *Acta Materialia*, 87: 377 – 389, 2015. ISSN 1359-6454. URL https://doi.org/10.1016/j.actamat.2014.11.051.

[224] X.L. Wang, C.T. Liu, U. Keiderling, A.D. Stoica, L. Yang, M.K. Miller, C.L. Fu, D. Ma, and K. An. Unusual thermal stability of nano-structured ferritic

alloys. *Journal of Alloys and Compounds*, 529:96 – 101, 2012. ISSN 0925-8388. URL https://doi.org/10.1016/j.jallcom.2012.02.143.

[225] A Czainski, Z Garncarek, and R Piasecki. Quantitative characterization of inhomogeneity in thin metallic films using Garncarek's method. *Journal of Physics D: Applied Physics*, 27(3):616, 1994. URL http://stacks.iop.org/0022-3727/27/i=3/a=030.

[226] Thak Sang Byun, Ji Hyun Yoon, Sung Hun Wee, David T. Hoelzer, and Stuart A. Maloy. Fracture behavior of 9Cr nanostructured ferritic alloy with improved fracture toughness. *Journal of Nuclear Materials*, 449(1):39 – 48, 2014. ISSN 0022-3115. URL https://doi.org/10.1016/j.jnucmat.2014.03.007.

[227] D.A. McClintock, M.A. Sokolov, D.T. Hoelzer, and R.K. Nanstad. Mechanical properties of irradiated ods-eurofer and nanocluster strengthened 14ywt. *Journal of Nuclear Materials*, 392(2):353 – 359, 2009. ISSN 0022-3115. URL https://doi.org/10.1016/j.jnucmat.2009.03.024. Nuclear Fuels and Structural Materials 2.

[228] S. Yamashita, K. Oka, S. Ohnuki, N. Akasaka, and S. Ukai. Phase stability of oxide dispersion-strengthened ferritic steels in neutron irradiation. *Journal of Nuclear Materials*, 307-311:283 – 288, 2002. ISSN 0022-3115. URL https://doi.org/10.1016/S0022-3115(02)01077-2.

[229] S Yamashita, N Akasaka, and S Ohnuki. Nano-oxide particle stability of 9–12Cr grain morphology modified ODS steels under neutron irradiation. *Journal of Nuclear Materials*, 329-333:377 – 381, 2004. ISSN 0022-3115. URL https://doi.org/10.1016/j.jnucmat.2004.04.041. Proceedings of the 11th International Conference on Fusion Reactor Materials (ICFRM-11).

[230] S. Yamashita, N. Akasaka, S. Ukai, and S. Ohnuki. Microstructural development of a heavily neutron-irradiated ods ferritic steel (ma957) at elevated temperature. *Journal of Nuclear Materials*, 367-370:202 – 207, 2007. ISSN 0022-3115. URL https://doi.org/10.1016/j.jnucmat.2007.03.145. Proceedings of the Twelfth International Conference on Fusion Reactor Materials (ICFRM-12).

[231] Shinichiro Yamashita, Yasuhide Yano, Satoshi Ohtsuka, Tsunemitsu Yoshitake, Takeji Kaito, Shin ichi Koyama, and Kenya Tanaka. Irradiation behavior evaluation of oxide dispersion strengthened ferritic steel cladding tubes irradiated in JOYO. *Journal of Nuclear Materials*, 442(1):417 – 424, 2013. ISSN 0022-3115. URL https://doi.org/10.1016/j.jnucmat.2013.04.051.

[232] T. R. Allen, J. Gan, J. I. Cole, S. Ukai, S. Shutthanandan, and S. Thevuthasan. The stability of 9cr-ods oxide particles under heavy-ion irradiation. *Nuclear Science and Engineering*, 151(3):305–312, 2005.

[233] T.R. Allen, J. Gan, J.I. Cole, M.K. Miller, J.T. Busby, S. Shutthanandan, and S. Thevuthasan. Radiation response of a 9 chromium oxide dispersion strengthened steel to heavy ion irradiation. *Journal of Nuclear Materials*, 375 (1):26 – 37, 2008. ISSN 0022-3115. URL https://doi.org/10.1016/j.jnucmat.2007.11.001.

[234] A.G. Certain, K.G. Field, T.R. Allen, M.K. Miller, J. Bentley, and J.T. Busby. Response of nanoclusters in a 9Cr ODS steel to 1 dpa, 525°C proton irradiation. *Journal of Nuclear Materials*, 407(1):2 – 9, 2010. ISSN 0022-3115. URL https://doi.org/10.1016/j.jnucmat.2010.07.002. Proceedings of the Symposium on Microstructural Processes in Irradiated Materials and on Reactor Pressure Vessel (RPV) Embrittlement and Fusion Materials: Measuring, Modeling and Managing Irradiation Effects.

[235] P. Pareige, M.K. Miller, R.E. Stoller, D.T. Hoelzer, E. Cadel, and B. Radiguet. Stability of nanometer-sized oxide clusters in mechanically-alloyed steel under ion-induced displacement cascade damage conditions. *Journal of Nuclear Materials*, 360(2):136 – 142, 2007. ISSN 0022-3115. URL https://doi.org/10.1016/j.jnucmat.2006.09.011.

[236] R. Schäublin, A. Ramar, N. Baluc, V. de Castro, M.A. Monge, T. Leguey, N. Schmid, and C. Bonjour. Microstructural development under irradiation in European ODS ferritic/martensitic steels. *Journal of Nuclear Materials*, 351 (1):247 – 260, 2006. ISSN 0022-3115. URL https://doi.org/10.1016/j.jnucmat.2006.02.005. Proceedings of the Symposium on Microstructural Processes in Irradiated Materials.

[237] M. K. Miller and R. G. Forbes. Atom probe tomography. *Materials Characterization*, 60(6):461–469, 2009. ISSN 10445803. URL http://dx.doi.org/10.1016/j.matchar.2009.02.007.

[238] B. Gault, M.P. Moody, J.M. Cairney, and S.P Ringer. *Atom probe microscopy*. Springer, New York, 2012. ISBN 9781461434351.

[239] M.K. Miller and E.A. Kenik. Atom probe tomography: A technique for nanoscale characterization. *Microscopy and Microanalysis*, 10(3):336–341, 2004. URL http://dx.doi.org/10.1017/S1431927604040577.

[240] A. Cerezo, T. J. Godfrey, S. J. Sijbrandij, G. D. W. Smith, and P. J. Warren. Performance of an energy-compensated three-dimensional atom probe. *Review of Scientific Instruments*, 69(1):49–58, 1998. URL http://dx.doi.org/10.1063/1.1148477.

[241] M.K. Miller, K.F. Russell, K. Thompson, R. Alvis, and D.J. Larson. Review of atom probe FIB-based specimen preparation methods. *Microscopy and microanalysis : the official journal of Microscopy Society of America, Microbeam Analysis Society, Microscopical Society of Canada*, 13(6):428–436, 2007. ISSN 1431-9276. URL http://dx.doi.org/10.1017/S1431927607070845.

[242] BP Geiser, DJ Larson, E Oltman, S Gerstl, D Reinhard, TF Kelly, and TJ Prosa. Wide-field-of-view atom probe reconstruction. *Microscopy and Microanalysis*, 15(S2):292–293, 2009.

[243] Baptiste Gault, D Haley, Frederic de Geuser, Michael P Moody, Emmanuelle A Marquis, David J Larson, and Brian P Geiser. Advances in the reconstruction of atom probe tomography data. *Ultramicroscopy*, 111(6):448–457, 2011.

[244] Baptiste Gault, Frederic Danoix, Khalid Hoummada, Dominique Mangelinck, and Harald Leitner. Impact of directional walk on atom probe microanalysis. *Ultramicroscopy*, 113:182–191, 2012.

[245] Baptiste Gault, Michael P. Moody, Frederic De Geuser, Alex La Fontaine, Leigh T. Stephenson, Daniel Haley, and Simon P. Ringer. Spatial resolution in atom probe tomography. *Microscopy and Microanalysis*, 16(1):99–110, 2010. URL http://dx.doi.org/10.1017/S1431927609991267.

[246] Emmanuelle A. Marquis and Francois Vurpillot. Chromatic aberrations in the field evaporation behavior of small precipitates. *Microscopy and Microanalysis*, 14(6):561–570, 2008. URL http://dx.doi.org/10.1017/S1431927608080793.

[247] J. M. Hyde and C. A. English. Symposium R: Microstructural Processes in Irradiated Materials,. In *MRS 2000 Fall Meeting*, 2000.

[248] A. Cerezo and L. Davin. Aspects of the observation of clusters in the 3-dimensional atom probe. *Surface and Interface Analysis*, 39(2□3):184–188, 2007. URL http://dx.doi.org/10.1002/sia.2486.

[249] Leigh T. Stephenson, Anna V. Ceguerra, Tong Li, Tanaporn Rojhirunsakool, Soumya Nag, Rajarshi Banerjee, Julie M. Cairney, and Simon P. Ringer. Point-by-point compositional analysis for atom probe tomography. *MethodsX*, 1:12 – 18, 2014. ISSN 2215-0161. URL https://doi.org/10.1016/j.mex.2014.02.001.

[250] M. K. Miller. *Atom probe field ion microscopy*. Clarendon Press Oxford University Press, Oxford New York, 1996. ISBN 9780198513872.

[251] Leigh T. Stephenson, Michael P. Moody, Peter V. Liddicoat, and Simon P. Ringer. New techniques for the analysis of fine-scaled clustering phenomena within Atom Probe Tomography (APT) data. *Microscopy and Microanalysis*, 13(6):448–463, 2007. ISSN 14319276. URL http://dx.doi.org/10.1017/S1431927607070900.

[252] T. Philippe, F. De Geuser, S. Duguay, W. Lefebvre, O. Cojocaru-Mirédin, G. Da Costa, and D. Blavette. Clustering and nearest neighbour distances in atom-probe tomography. *Ultramicroscopy*, 109(10):1304 – 1309, 2009. ISSN 0304-3991. URL https://doi.org/10.1016/j.ultramic.2009.06.007.

[253] T. Philippe, S. Duguay, and D. Blavette. Clustering and pair correlation function in atom probe tomography. *Ultramicroscopy*, 110(7):862 – 865, 2010. ISSN 0304-3991. URL https://doi.org/10.1016/j.ultramic.2010.03.004.

[254] O. Dmitrieva, D. Ponge, G. Inden, J. Millán, P. Choi, J. Sietsma, and D. Raabe. Chemical gradients across phase boundaries between martensite and austenite in steel studied by atom probe tomography and simulation. *Acta Materialia*, 59(1):364 – 374, 2011. ISSN 1359-6454. URL https://doi.org/10.1016/j.actamat.2010.09.042.

[255] N. Almirall, P. B. Wells, T. Yamamoto, K. Wilford, T. Williams, N. Riddle, and G. R. Odette. Precipitation and hardening in irradiated low alloy steels with a wide range of Ni and Mn compositions. *Acta Materialia*, 179:119–128, 2019. ISSN 13596454. URL http://dx.doi.org/10.1016/j.actamat.2019.08.027.

[256] Yinbin Miao, Kun Mo, Zhangjian Zhou, Xiang Liu, Kuan-Che Lan, Guangming Zhang, Michael K. Miller, Kathy A. Powers, Zhi-Gang Mei, Jun-Sang Park, Jonathan Almer, and James F. Stubbins. On the microstructure and strengthening mechanism in oxide dispersion-strengthened 316 steel: A coordinated electron microscopy, atom probe tomography and in situ synchrotron tensile investigation. *Materials Science and Engineering: A*, 639:585 – 596, 2015. ISSN 0921-5093. URL https://doi.org/10.1016/j.msea.2015.05.064.

[257] M. K. Miller, K. F. Russell, M. A. Sokolov, and R. K. Nanstad. APT characterization of irradiated high nickel RPV steels. *Journal of Nuclear Materials*, 361(2-3 SPEC. ISS.):248–261, 2007. ISSN 00223115. URL http://dx.doi.org/10.1016/j.jnucmat.2006.12.015.

[258] Benjamin M. Jenkins, James O. Douglas, Nathan Almirall, Nick Riddle, Paul A.J. Bagot, Jonathan M. Hyde, G. Robert Odette, and Michael P. Moody. The Effect of Composition Variations on the Response of Steels Subjected to

High Fluence Neutron Irradiation. *Materialia*, 11(May):100717, 2020. ISSN 25891529. URL http://dx.doi.org/10.1016/j.mtla.2020.100717.

[259] Ceri A. Williams, Daniel Haley, Emmanuelle A. Marquis, George D.W. Smith, and Michael P. Moody. Defining clusters in APT reconstructions of ODS steels. *Ultramicroscopy*, 132:271–278, 2013. ISSN 03043991. URL http://dx.doi.org/10.1016/j.ultramic.2012.12.011.

[260] Paul D. Styman, Jonathan M. Hyde, Keith Wilford, and George D.W. Smith. Quantitative methods for the apt analysis of thermally aged rpv steels. *Ultramicroscopy*, 132:258 – 264, 2013. ISSN 0304-3991. URL https://doi.org/10.1016/j.ultramic.2012.12.003. IFES 2012.

[261] D. Vaumousse, A. Cerezo, and P.J. Warren. A procedure for quantification of precipitate microstructures from three-dimensional atom probe data. *Ultramicroscopy*, 95:215 – 221, 2003. ISSN 0304-3991. URL https://doi.org/10.1016/S0304-3991(02)00319-4. IFES 2001.

[262] Benjamin M. Jenkins, Andrew J. London, Nick Riddle, Jonathan M. Hyde, Paul A.J. Bagot, and Michael P. Moody. Using alpha hulls to automatically and reproducibly detect edge clusters in atom probe tomography datasets. *Materials Characterization*, 160:110078, feb 2020. ISSN 1044-5803. URL http://dx.doi.org/10.1016/J.MATCHAR.2019.110078.

[263] J.M. Hyde, E.A. Marquis, K.B. Wilford, and T.J. Williams. A sensitivity analysis of the maximum separation method for the characterisation of solute clusters. *Ultramicroscopy*, 111(6):440 – 447, 2011. ISSN 0304-3991. URL https://doi.org/10.1016/j.ultramic.2010.12.015. Special Issue: 52nd International Field Emission Symposium.

[264] P. D. Styman, J. M. Hyde, D. Parfitt, K. Wilford, M. G. Burke, C. A. English, and P. Efsing. Post-irradiation annealing of Ni-Mn-Si-enriched clusters in a neutron-irradiated RPV steel weld using Atom Probe Tomography. *Journal of Nuclear Materials*, 459:127–134, 2015. ISSN 00223115. URL http://dx.doi.org/10.1016/j.jnucmat.2015.01.027.

[265] Kristina Lindgren, Magnus Boåsen, Krystyna Stiller, Pål Efsing, and Mattias Thuvander. Evolution of precipitation in reactor pressure vessel steel welds under neutron irradiation. *Journal of Nuclear Materials*, 488:222–230, 2017. ISSN 00223115. URL http://dx.doi.org/10.1016/j.jnucmat.2017.03.019.

[266] P. D. Edmondson, C. M. Parish, and R. K. Nanstad. Using complimentary microscopy methods to examine Ni-Mn-Si-precipitates in highly-irradiated reactor pressure vessel steels. *Acta Materialia*, 134:31–39, 2017. ISSN 13596454. URL http://dx.doi.org/10.1016/j.actamat.2017.05.043.

[267] D. J. Larson, B. Gault, B. P. Geiser, F. De Geuser, and F. Vurpillot. Atom probe tomography spatial reconstruction: Status and directions. *Current Opinion in Solid State and Materials Science*, 17(5):236–247, 2013. ISSN 13590286. URL http://dx.doi.org/10.1016/j.cossms.2013.09.002.

[268] Angus J. Wilkinson and Peter B. Hirsch. Electron diffraction based techniques in scanning electron microscopy of bulk materials. *Micron*, 28(4):279 – 308, 1997. ISSN 0968-4328. URL https://doi.org/10.1016/S0968-4328(97)00032-2.

[269] FJ Humphreys. Review grain and subgrain characterisation by electron backscatter diffraction. *Journal of materials science*, 36(16):3833–3854, 2001.

[270] Angus J Wilkinson, David M Collins, Yevhen Zayachuk, Rajesh Korla, and Arantxa Vilalta-Clemente. Applications of multivariate statistical methods and simulation libraries to analysis of electron backscatter diffraction and transmission kikuchi diffraction datasets. *Ultramicroscopy*, 196:88 – 98, 2019. ISSN 0304-3991. URL https://doi.org/10.1016/j.ultramic.2018.09.011.

[271] Glenn C. Sneddon, Patrick W. Trimby, and Julie M. Cairney. Transmission Kikuchi diffraction in a scanning electron microscope: A review. *Materials Science and Engineering R: Reports*, 110:1–12, 2016. ISSN 0927796X. URL http://dx.doi.org/10.1016/j.mser.2016.10.001.

[272] K. Babinsky, R. De Kloe, H. Clemens, and S. Primig. A novel approach for site-specific atom probe specimen preparation by focused ion beam and transmission electron backscatter diffraction. *Ultramicroscopy*, 144:9 – 18, 2014. ISSN 0304-3991. URL https://doi.org/10.1016/j.ultramic.2014.04.003.

[273] David Williams. *Transmission electron microscopy : a textbook for materials science*. Springer, New York, 2009. ISBN 978-0-387-76500-6.

[274] S.J. Pennycook and P.D. Nellist. *Scanning Transmission Electron Microscopy: Imaging and Analysis*. Springer New York, 2011. ISBN 9781441972002. URL https://books.google.co.uk/books?id=N_98Hef0ZTYC.

[275] S. Van Aert, J. Verbeeck, R. Erni, S. Bals, M. Luysberg, D. Van Dyck, and G. Van Tendeloo. Quantitative atomic resolution mapping using high-angle annular dark field scanning transmission electron microscopy. *Ultramicroscopy*, 109(10):1236 – 1244, 2009. URL http://www.sciencedirect.com/science/article/pii/S0304399109001259".

[276] Samuel A. Briggs, Kumar Sridharan, and Kevin G. Field. Correlative microscopy of neutron-irradiated materials. *Advanced Materials and Processes*, 174(10), 12 2016. ISSN 0882-7958.

[277] W.D. Callister and D.G. Rethwisch. *Callister's Materials Science and Engineering*. Wiley, 2020. ISBN 9781119453918.

[278] G. Gottstein. *Physical Foundations of Materials Science*. Springer Berlin Heidelberg, 2013. ISBN 9783662092910.

[279] A.C. Fischer-Cripps. *Nanoindentation*. Mechanical Engineering Series. Springer New York, 2011. ISBN 9781441998729.

[280] Christopher D. Hardie and Steve G. Roberts. Nanoindentation of model fe–cr alloys with self-ion irradiation. *Journal of Nuclear Materials*, 433(1):174 – 179, 2013. ISSN 0022-3115. URL https://doi.org/10.1016/j.jnucmat.2012.09.003.

[281] Andrew J. Bushby, Steve G. Roberts, and Christopher D. Hardie. Nanoindentation investigation of ion-irradiated fe–cr alloys using spherical indenters. *Journal of Materials Research*, 27(1):85–90, 2012. URL http://dx.doi.org/10.1557/jmr.2011.304.

[282] W.C. Oliver and G.M. Pharr. An improved technique for determining hardness and elastic modulus using load and displacement sensing indentation experiments. *Journal of Materials Research*, 7(6):1564–1583, 1992. URL http://dx.doi.org/10.1557/JMR.1992.1564.

[283] Xiaodong Li and Bharat Bhushan. A review of nanoindentation continuous stiffness measurement technique and its applications. *Materials Characterization*, 48(1):11 – 36, 2002. ISSN 1044-5803. URL https://doi.org/10.1016/S1044-5803(02)00192-4.

[284] Ben D. Beake and James F. Smith. High-temperature nanoindentation testing of fused silica and other materials. *Philosophical Magazine A*, 82(10):2179–2186, 2002. URL http://dx.doi.org/10.1080/01418610208235727.

[285] W.C. Oliver and G.M. Pharr. Measurement of hardness and elastic modulus by instrumented indentation: Advances in understanding and refinements to methodology. *Journal of Materials Research*, 19(1):3–20, 2004. URL http://dx.doi.org/10.1557/jmr.2004.19.1.3.

[286] J.G. Swadener, E.P. George, and G.M. Pharr. The correlation of the indentation size effect measured with indenters of various shapes. *Journal of the Mechanics and Physics of Solids*, 50(4):681 – 694, 2002. ISSN 0022-5096. URL https://doi.org/10.1016/S0022-5096(01)00103-X.

[287] J B Pethica and W C Oliver. Tip surface interactions in STM and AFM. *Physica Scripta*, T19A:61–66, jan 1987. URL http://dx.doi.org/10.1088/0031-8949/1987/t19a/010.

[288] T.P. Davis, N. Almirall, M.A Auger, P.A.J Bagot, P. Hosemann, M.P. Moody, G.R. Odette, and D.E.J Armstrong. Atom Probe Characterisation of Cu and Mn-Ni-Si co-precipitation in neutron irradiated T91 ferritic-martensitic steel. *Materialia*, 14:100946, 2020. URL https://doi.org/10.1016/j.mtla.2020.100946.

[289] Elaina R. Reese, Mukesh Bachhav, Peter Wells, Takuya Yamamoto, G. Robert Odette, and Emmanuelle A. Marquis. On α' precipitate composition in thermally annealed and neutron-irradiated Fe- 9-18Cr alloys. *Journal of Nuclear Materials*, 500:192–198, 2018. ISSN 00223115. URL http://dx.doi.org/10.1016/j.jnucmat.2017.12.036.

[290] Dhriti Bhattacharyya, Takuya Yamamoto, Peter Wells, Emmanuelle Marquis, Mukesh Bachhav, Yuan Wu, Joel Davis, Alan Xu, and G. Robert Odette. Microstructural changes and their effect on hardening in neutron irradiated Fe-Cr alloys. *Journal of Nuclear Materials*, 519:274–286, 2019. ISSN 00223115. URL http://dx.doi.org/10.1016/j.jnucmat.2019.03.022.

[291] V. Kuksenko, C. Pareige, C. Genevois, and P. Pareige. Characterisation of Cr, Si and P distribution at dislocations and grain-boundaries in neutron irradiated Fe-Cr model alloys of low purity. *Journal of Nuclear Materials*, 434(1-3):49–55, 2013. ISSN 00223115. URL http://dx.doi.org/10.1016/j.jnucmat.2012.11.027.

[292] J.C. Haley, S. de Moraes Shubeita, P. Wady, A.J. London, G.R. Odette, S. Lozano-Perez, and S.G. Roberts. Microstructural examination of neutron, proton and self-ion irradiation damage in a model Fe9Cr alloy. *Journal of Nuclear Materials*, page 152130, 2020. ISSN 00223115. URL http://dx.doi.org/10.1016/j.jnucmat.2020.152130.

[293] J. C. Haley, F. Liu, E. Tarleton, A. C.F. Cocks, G. R. Odette, S. Lozano-Perez, and S. G. Roberts. Helical dislocations: Observation of vacancy defect bias of screw dislocations in neutron irradiated Fe–9Cr. *Acta Materialia*, 181:173–184, 2019. ISSN 13596454. URL http://dx.doi.org/10.1016/j.actamat.2019.09.031.

[294] E. Getto, Z. Jiao, A. M. Monterrosa, K. Sun, and G. S. Was. Effect of irradiation mode on the microstructure of self-ion irradiated ferritic-martensitic alloys. *Journal of Nuclear Materials*, 465:116–126, 2015. ISSN 00223115. URL http://dx.doi.org/10.1016/j.jnucmat.2015.05.016.

[295] Stephen Taller, Zhijie Jiao, Kevin Field, and Gary S. Was. Emulation of fast reactor irradiated T91 using dual ion beam irradiation. *Journal of Nuclear Materials*, 527:151831, 2019. ISSN 00223115. URL http://dx.doi.org/10.1016/j.jnucmat.2019.151831.

[296] Janelle P. Wharry and Gary S. Was. A systematic study of radiation-induced segregation in ferritic-martensitic alloys. *Journal of Nuclear Materials*, 442 (1-3):7–16, 2013. ISSN 00223115. URL http://dx.doi.org/10.1016/j.jnucmat.2013.07.071.

[297] G. R. Odette. Radiation induced microstructural evolution in reactor pressure vessel steels. *Materials Research Society Symposium - Proceedings*, 373:137–148, 1995. ISSN 02729172. URL http://dx.doi.org/10.1557/proc-373-137.

[298] Shipeng Shu, Peter B. Wells, Nathan Almirall, G. Robert Odette, and Dane D. Morgan. Thermodynamics and kinetics of core-shell versus appendage co-precipitation morphologies: An example in the Fe-Cu-Mn-Ni-Si system. *Acta Materialia*, 157:298–306, 2018. ISSN 13596454. URL http://dx.doi.org/10.1016/j.actamat.2018.07.037.

[299] Wei Xiong, Huibin Ke, Ramanathan Krishnamurthy, Peter Wells, Leland Barnard, G. Robert Odette, and Dane Morgan. Thermodynamic models of low-temperature Mn–Ni–Si precipitation in reactor pressure vessel steels. *MRS Communications*, 4(3):101–105, 2014. ISSN 2159-6859. URL http://dx.doi.org/10.1557/mrc.2014.21.

[300] Paul D. Styman, Jonathan M. Hyde, Andrew Morley, Keith Wilford, Nick Riddle, and George D.W. Smith. The effect of Ni on the microstructural evolution of high Cu reactor pressure vessel steel welds after thermal ageing for up to 100,000 h. *Materials Science and Engineering A*, 736(April):111–119, 2018. ISSN 09215093. URL http://dx.doi.org/10.1016/j.msea.2018.08.063.

[301] G. R. Odette and G. E. Lucas. Recent progress in understanding reactor pressure vessel steel embrittlement. *Radiation Effects and Defects in Solids*, 144 (1-4):189–231, 1998. ISSN 10420150. URL http://dx.doi.org/10.1080/10420159808229676.

[302] N. Almirall, P. B. Wells, H. Ke, P. Edmondson, D. Morgan, T. Yamamoto, and G. R. Odette. On the elevated temperature thermal stability of nanoscale Mn-Ni-Si precipitates formed at lower temperature in highly irradiated reactor pressure vessel steels. *Scientific Reports*, 9(June):1–12, 2019. ISSN 20452322. URL http://dx.doi.org/10.1038/s41598-019-45944-z.

[303] N. Almirall, P.B. Wells, T. Yamamoto, K. Yabuuchi, A. Kimura, and G.R. Odette. On the use of charged particles to characterize precipitation in irradiated reactor pressure vessel steels with a wide range of compositions. *Journal of Nuclear Materials*, page 152173, may 2020. ISSN 0022-3115. URL http://dx.doi.org/10.1016/J.JNUCMAT.2020.152173.

[304] G.R. Odette and B.D. Wirth. A computational microscopy study of nanostructural evolution in irradiated pressure vessel steels. *Journal of Nuclear Materials*, 251:157–171, nov 1997. ISSN 0022-3115. URL http://dx.doi.org/10.1016/S0022-3115(97)00267-5.

[305] Mahmood Mamivand, Peter Wells, Huibin Ke, Shipeng Shu, G. Robert Odette, and Dane Morgan. CuMnNiSi precipitate evolution in irradiated reactor pressure vessel steels: Integrated Cluster Dynamics and experiments. *Acta Materialia*, 180:199–217, 2019. ISSN 13596454. URL http://dx.doi.org/10.1016/j.actamat.2019.09.016.

[306] E. Meslin, A. Barbu, L. Boulanger, B. Radiguet, P. Pareige, K. Arakawa, and C.C. Fu. Cluster-dynamics modelling of defects in α-iron under cascade damage conditions. *Journal of Nuclear Materials*, 382(2-3):190–196, dec 2008. ISSN 0022-3115. URL http://dx.doi.org/10.1016/J.JNUCMAT.2008.08.010.

[307] G. Bonny, D. Terentyev, E.E. Zhurkin, and L. Malerba. Monte Carlo study of decorated dislocation loops in FeNiMnCu model alloys. *Journal of Nuclear Materials*, 452(1-3):486–492, sep 2014. ISSN 0022-3115. URL http://dx.doi.org/10.1016/J.JNUCMAT.2014.05.051.

[308] ASTM International. A213/A213M - 19a: Standard Specification for Seamless Ferritic and Austenitic Alloy-Steel Boiler, Superheater and Heat-Exchanger Tubes. Technical report, ASTM, 2019. URL https://doi.org/10.1520/A0213{_}A0213M-19A.

[309] ASTM International. A182/A182M-19a: Standard Specification for Forged or Rolled Alloy-Steel Pipe Flanges, Forged Fittings, and Valves and Parts for High-Temperature Service. Technical report, ASTM, 2019. URL https://doi.org/10.1520/A0182{_}A0182M-19A.

[310] ASTM International. A335/A335-19a: Specification for Seamless Ferritic Alloy-Steel Pipe for High-Temperature Service. Technical report, ASTM, 2019. URL http://dx.doi.org/10.1520/A0335{_}A0335M-19A.

[311] ASTM International. A387/A387M-17a: Standard Specification for Pressure Vessel Plates, Alloy Steel, Chromium-Molybdenum. Technical report, ASTM, 2017. URL https://doi.org/10.1520/A0387{_}A0387M-17A.

[312] J W Nielsen. As-Run Physics Analysis for the UCSB–1 Experiment in the Advanced Test Reactor. *Idaho National Laboratory*, September, 2015. URL https://doi.org/10.2172/1235196.

[313] C J Werner. MCNP User's Manual Code Version 6.2 (LA-UR-17-29981). Technical report, Los Alamos National Laboratory, 2017.

[314] Nathan Almirall and G. Robert Odette. Private Communication, 2020.

[315] Huibin Ke, Peter Wells, Philip D. Edmondson, Nathan Almirall, Leland Barnard, G. Robert Odette, and Dane Morgan. Thermodynamic and kinetic modeling of Mn-Ni-Si precipitates in low-Cu reactor pressure vessel steels. *Acta Materialia*, 138:10–26, 2017. ISSN 13596454. URL http://dx.doi.org/10.1016/j.actamat.2017.07.021.

[316] Takuya Yamamoto, G. Robert Odette, Hirotatsu Kishimoto, Jan Willem Rensman, and Pifeng Miao. On the effects of irradiation and helium on the yield stress changes and hardening and non-hardening embrittlement of □8Cr tempered martensitic steels: Compilation and analysis of existing data. *Journal of Nuclear Materials*, 356(1-3):27–49, 2006. ISSN 00223115. URL http://dx.doi.org/10.1016/j.jnucmat.2006.05.041.

[317] M. K. Miller, K. F. Russell, J. Kocik, and E. Keilova. Embrittlement of low copper VVER 440 surveillance samples neutron-irradiated to high fluences. *Journal of Nuclear Materials*, 282(1):83–88, 2000. ISSN 00223115. URL http://dx.doi.org/10.1016/S0022-3115(00)00240-3.

[318] Argha Dutta, N Gayathri, P Mukherjee, Santu Dey, Sudipta Mandal, Tapatee Kundu Roy, Apu Sarkar, S Neogy, and Archna Sagdeo. An approach in the analysis of microstructure of proton irradiated T91 through XRDLPA using synchrotron and laboratory source. *Journal of Nuclear Materials*, 514: 161–170, 2019. ISSN 0022-3115. URL https://doi.org/10.1016/j.jnucmat.2018.11.038.

[319] F. Bergner, A. Ulbricht, and C. Heintze. Estimation of the solubility limit of Cr in Fe at 300 °C from small-angle neutron scattering in neutron-irradiated Fe-Cr alloys. *Scripta Materialia*, 61(11):1060–1063, 2009. ISSN 13596462. URL http://dx.doi.org/10.1016/j.scriptamat.2009.08.028.

[320] K. C. Russell. Phase stability under irradiation. *Progress in Materials Science*, 28(3-4):229–434, 1984. ISSN 00796425. URL http://dx.doi.org/10.1016/0079-6425(84)90001-X.

[321] V. Kuksenko, C. Pareige, and P. Pareige. Cr precipitation in neutron irradiated industrial purity Fe-Cr model alloys. *Journal of Nuclear Materials*, 432(1-3): 160–165, 2013. ISSN 00223115. URL http://dx.doi.org/10.1016/j.jnucmat.2012.07.021.

[322] S.B. Adisa, R. Blair, and M.J. Swenson. Comparison of microstructure evolution in Fe2+ or neutron-irradiated T91 at 500°C. *Materialia*, 12(March): 100770, 2020. ISSN 25891529. URL http://dx.doi.org/10.1016/j.mtla.2020.100770.

[323] M. I. Pascuet, G. Monnet, G. Bonny, E. Martínez, J. J.H. Lim, M. G. Burke, and L. Malerba. Solute precipitation on a screw dislocation and its effects on dislocation mobility in bcc Fe. *Journal of Nuclear Materials*, 519(April):265–273, 2019. ISSN 00223115. URL http://dx.doi.org/10.1016/j.jnucmat.2019.04.007.

[324] G. Bonny, C. Domain, N. Castin, P. Olsson, and L. Malerba. The impact of alloying elements on the precipitation stability and kinetics in iron based alloys: An atomistic study. *Computational Materials Science*, 161(February): 309–320, 2019. ISSN 09270256. URL http://dx.doi.org/10.1016/j.commatsci.2019.02.007.

[325] M. I. Pascuet, E. Martínez, G. Monnet, and L. Malerba. Solute effects on edge dislocation pinning in complex alpha-Fe alloys. *Journal of Nuclear Materials*, 494:311–321, 2017. ISSN 00223115. URL http://dx.doi.org/10.1016/j.jnucmat.2017.07.049.

[326] T. P. Davis, M. A. Auger, C. Hofer, P.A.J. Bagot, M. P. Moody, and D.E.J. Armstrong. Nanocluster evolution and mechanical properties of ion irradiated T91 ferritic-martensitic steel'. *Journal of Nuclear Materials*, 547:152842, 2021. URL https://doi.org/10.1016/j.jnucmat.2021.152842.

[327] R L Klueh and J M Vitek. Elevated-Temperature tensile properties of irradaited 9Cr-1MoVNb Steel. *Journal of Nuclear Materials*, 132:27–31, 1985.

[328] L. K. Mansur. Correlation of neutron and heavy-ion damage. II. The predicted temperature shift if swelling with changes in radiation dose rate. *Journal of Nuclear Materials*, 78(1):156–160, 1978. ISSN 00223115. URL http://dx.doi.org/10.1016/0022-3115(78)90514-7.

[329] C. Domain and C. S. Becquart. Diffusion of phosphorus in α-Fe: An ab initio study. *Physical Review B - Condensed Matter and Materials Physics*, 71(21): 1–13, 2005. ISSN 10980121. URL http://dx.doi.org/10.1103/PhysRevB.71.214109.

[330] P. T. Wady, A. Draude, S. M. Shubeita, A. D. Smith, N. Mason, S. M. Pimblott, and E. Jimenez-Melero. Accelerated radiation damage test facility using a 5 MV tandem ion accelerator. *Nuclear Instruments and Methods in Physics Research, Section A: Accelerators, Spectrometers, Detectors and Associated Equipment*, 806:109–116, 2015. ISSN 01689002. URL http://dx.doi.org/10.1016/j.nima.2015.09.088.

[331] W.F. Gale and T.C. Totemeier. *Smithells Metals Reference Book*. Elsevier Science, 2003. ISBN 9780080480961.

[332] G. Bonny, A. Bakaev, D. Terentyev, E. Zhurkin, and M. Posselt. Atomistic study of the hardening of ferritic iron by Ni-Cr decorated dislocation loops. *Journal of Nuclear Materials*, 498:430–437, 2018. ISSN 00223115. URL http://dx.doi.org/10.1016/j.jnucmat.2017.11.016.

[333] D. Terentyev and A. Bakaev. Radiation-induced strengthening and absorption of dislocation loops in ferritic Fe-Cr alloys: The role of Cr segregation. *Journal of Physics Condensed Matter*, 25(26), 2013. ISSN 09538984. URL http://dx.doi.org/10.1088/0953-8984/25/26/265702.

[334] Christopher D. Hardie, Steve G. Roberts, and Andy J. Bushby. Understanding the effects of ion irradiation using nanoindentation techniques. *Journal of Nuclear Materials*, 462:391 – 401, 2015. ISSN 0022-3115. URL https://doi.org/10.1016/j.jnucmat.2014.11.066.

[335] Thomas P. Davis, Jack C. Haley, Sarah Connolly, Maria A. Auger, Michael J. Gorley, Patrick S. Grant, Paul A.J. Bagot, Michael P. Moody, and David E.J. Armstrong. Electron microscopy and atom probe tomography of nanoindentation deformation in oxide dispersion strengthened steels. *Materials Characterization*, 167:110477, 2020. ISSN 1044-5803. URL https://doi.org/10.1016/j.matchar.2020.110477.

[336] F. Delage, J. Carmack, C. B. Lee, T. Mizuno, M. Pelletier, and J. Somers. Status of advanced fuel candidates for Sodium Fast Reactor within the Generation IV International Forum. *Journal of Nuclear Materials*, 441(1-3):515–519, 2013. ISSN 00223115. URL http://dx.doi.org/10.1016/j.jnucmat.2012.09.036.

[337] A. V. Tselishchev, V. S. Ageev, Yu P. Budanov, A. G. Ioltukhovskii, N. M. Mitrofanova, M. V. Leontieva-Smirnova, I. A. Shkabura, L. M. Zabud'Ko, A. V. Kozlov, V. V. Mal'Tsev, and A. V. Povstyanko. Development of structural steel for fuel elements and fuel assemblies of sodium-cooled fast reactors. *Atomic Energy*, 108(4):274–280, 2010. ISSN 10634258. URL http://dx.doi.org/10.1007/s10512-010-9289-9.

[338] F. A. Garner, M. B. Toloczko, and B. H. Sencer. Comparison of swelling and irradiation creep behavior of fcc-austenitic and bcc-ferritic/martensitic alloys at high neutron exposure. *Journal of Nuclear Materials*, 276(1):123–142, 2000. ISSN 00223115. URL http://dx.doi.org/10.1016/S0022-3115(99)00225-1.

[339] K. L. Murty and I. Charit. Structural materials for Gen-IV nuclear reactors: Challenges and opportunities. *Journal of Nuclear Materials*, 383(1-2):189–195, 2008. ISSN 00223115. URL http://dx.doi.org/10.1016/j.jnucmat.2008.08.044.

[340] A. A.F. Tavassoli. Present limits and improvements of structural materials for fusion reactors - A review. *Journal of Nuclear Materials*, 302(2-3):73–88, 2002. ISSN 00223115. URL http://dx.doi.org/10.1016/S0022-3115(02)00794-8.

[341] Andrea García-Junceda, Mónica Campos, Nerea García-Rodríguez, and José Manuel Torralba. On the Role of Alloy Composition and Sintering Parameters in the Bimodal Grain Size Distribution and Mechanical Properties of ODS Ferritic Steels. *Metallurgical and Materials Transactions A: Physical Metallurgy and Materials Science*, 47(11):5325–5333, 2016. ISSN 10735623. URL http://dx.doi.org/10.1007/s11661-016-3538-z.

[342] Jeoung Han Kim, Thak Sang Byun, and D. T. Hoelzer. Tensile fracture characteristics of nanostructured ferritic alloy 14YWT. *Journal of Nuclear Materials*, 407(3):143–150, 2010. ISSN 00223115. URL http://dx.doi.org/10.1016/j.jnucmat.2010.09.054.

[343] C. Heintze, I. Hilger, F. Bergner, T. Weissgärber, and B. Kieback. Nanoindentation of single- (Fe) and dual-beam (Fe and He) ion-irradiated ODS Fe-14Cr-based alloys: Effect of the initial microstructure on irradiation-induced hardening. *Journal of Nuclear Materials*, 518:1–10, 2019. ISSN 00223115. URL http://dx.doi.org/10.1016/j.jnucmat.2019.02.037.

[344] Tomas L. Martin, Andrew J. London, Benjamin Jenkins, Sarah E. Hopkin, James O. Douglas, Paul D. Styman, Paul A.J. Bagot, and Michael P. Moody. Comparing the Consistency of Atom Probe Tomography Measurements of Small-Scale Segregation and Clustering between the LEAP 3000 and LEAP 5000 Instruments. *Microscopy and Microanalysis*, 23(2):227–237, 2017. ISSN 14358115. URL http://dx.doi.org/10.1017/S1431927617000356.

[345] Yoji Miyajima, Masatoshi Mitsuhara, Satoshi Hata, Hideharu Nakashima, and Nobuhiro Tsuji. Quantification of internal dislocation density using scanning transmission electron microscopy in ultrafine grained pure aluminium fabricated by severe plastic deformation. *Materials Science and Engineering: A*, 528(2):776–779, 2010. ISSN 0921-5093. URL https://doi.org/10.1016/j.msea.2010.09.058.

[346] Chad M Parish, Kevin G Field, Alicia G Certain, and Janelle P Wharry. Application of STEM characterization for investigating radiation effects in BCC Fe-based alloys. *Journal of Materials Research*, 30(9):1275–1289, 2015. ISSN 0884-2914. URL http:/dx.doi.org/10.1557/jmr.2015.32.

[347] Francisco de la Peña, Tomas Ostasevicius, Vidar Tonaas Fauske, Pierre Burdet, Eric Prestat, Petras Jokubauskas, Magnus Nord, Katherine E. MacArthur, Mike Sarahan, Duncan N. Johnstone, Joshua Taillon, Alberto Eljarrat, Vadim

Migunov, Jan Caron, Tom Furnival, Stefano Mazzucco, Thomas Aarholt, Michael Walls, Tom Slater, Florian Winkler, Ben Martineau, Gaël Donval, Robert McLeod, Eric R. Hoglund, Ivo Alxneit, Ida Hjorth, Trond Henninen, Luiz Fernando Zagonel, Andreas Garmannslund, and 5ht2. HyperSpy v1.4. *HyperSpy*, sep 2018. URL http://dx.doi.org/10.5281/ZENODO.1407391.

[348] Olof C. Hellman, Justin A. Vandenbroucke, Järg Rüsing, Dieter Isheim, and David N. Seidman. Analysis of Three-dimensional Atom-probe Data by the Proximity Histogram. *Microscopy and Microanalysis*, 6(05):437–444, 2000. ISSN 1431-9276. URL http://dx.doi.org/10.1007/s100050010051.

[349] Xavier Boulnat, Michel Perez, Damien Fabregue, Thierry Douillard, Marie Hélène Mathon, and Yann De Carlan. Microstructure evolution in nano-reinforced ferritic steel processed by mechanical alloying and spark plasma sintering. *Metallurgical and Materials Transactions A: Physical Metallurgy and Materials Science*, 45(3):1485–1497, 2014. ISSN 10735623. URL http://dx.doi.org/10.1007/s11661-013-2107-y.

[350] Jingjie Shen, Yanfen Li, Feng Li, Huilong Yang, Zishou Zhao, Sho Kano, Yoshitaka Matsukawa, Yuhki Satoh, and Hiroaki Abe. Microstructural characterization and strengthening mechanisms of a 12Cr-ODS steel. *Materials Science and Engineering A*, 673:624–632, 2016. ISSN 09215093. URL http://dx.doi.org/10.1016/j.msea.2016.07.030.

[351] Tianyi Chen, Jonathan G. Gigax, Lloyd Price, Di Chen, S. Ukai, Eda Aydogan, S. A. Maloy, F. A. Garner, and Lin Shao. Temperature dependent dispersoid stability in ion-irradiated ferritic-martensitic dual-phase oxide-dispersion-strengthened alloy: Coherent interfaces vs. incoherent interfaces. *Acta Materialia*, 116:29–42, 2016. ISSN 13596454. URL http://dx.doi.org/10.1016/j.actamat.2016.05.042.

[352] T. Narita, S. Ukai, S. Ohtsuka, and M. Inoue. Effect of tungsten addition on microstructure and high temperature strength of 9CrODS ferritic steel. *Journal of Nuclear Materials*, 417(1-3):158–161, 2011. ISSN 00223115. URL http://dx.doi.org/10.1016/j.jnucmat.2011.01.060.

[353] Joon Sik Park, Sung Joon Kim, and Chong Soo Lee. Effect of W addition on the low cycle fatigue behavior of high Cr ferritic steels. *Materials Science and Engineering A*, 298(1-2):127–136, 2001. ISSN 09215093. URL http://dx.doi.org/10.1016/S0921-5093(00)01291-0.